

SEISMIC PERFORMANCE, CAPACITY AND RELIABILITY OF  
STRUCTURES AS SEEN THROUGH INCREMENTAL DYNAMIC  
ANALYSIS

A DISSERTATION  
SUBMITTED TO THE DEPARTMENT OF CIVIL AND ENVIRONMENTAL ENGINEERING  
AND THE COMMITTEE ON GRADUATE STUDIES  
OF STANFORD UNIVERSITY  
IN PARTIAL FULFILLMENT OF THE REQUIREMENTS  
FOR THE DEGREE OF  
DOCTOR OF PHILOSOPHY

Dimitrios Vamvatsikos  
July 2002

© Copyright by Dimitrios Vamvatsikos 2002  
All Rights Reserved

I certify that I have read this dissertation and that in my opinion it is fully adequate, in scope and quality, as a dissertation for the degree of Doctor of Philosophy.

---

C. Allin Cornell  
(Principal Adviser)

I certify that I have read this dissertation and that in my opinion it is fully adequate, in scope and quality, as a dissertation for the degree of Doctor of Philosophy.

---

Gregory G. Deierlein

I certify that I have read this dissertation and that in my opinion it is fully adequate, in scope and quality, as a dissertation for the degree of Doctor of Philosophy.

---

Eduardo Miranda

Approved for the University Committee on Graduate Studies:

# Abstract

Incremental Dynamic Analysis (IDA) is an emerging structural analysis method that offers thorough seismic demand and limit-state capacity prediction capability by using a series of nonlinear dynamic analyses under a suite of multiply scaled ground motion records. Realization of its opportunities is enhanced by several innovations, such as choosing suitable ground motion intensity measures and representative structural demand measures. In addition, proper interpolation and summarization techniques for multiple records need to be employed, providing the means for estimating the probability distribution of the structural demand given the seismic intensity. Limit-states, such as the dynamic global system instability, can be naturally defined in the context of IDA. The associated capacities are thus calculated such that, when properly combined with Probabilistic Seismic Hazard Analysis, they allow the estimation of the mean annual frequencies of limit-state exceedance.

IDA is resource-intensive. Thus the use of simpler approaches becomes attractive. The IDA can be related to the computationally simpler Static Pushover (SPO), enabling a fast and accurate approximation to be established for single-degree-of-freedom systems. By investigating oscillators with quadrilinear backbones and summarizing the results into a few empirical equations, a new software tool, SPO2IDA, is produced here that allows direct estimation of the summarized IDA results. Interesting observations are made regarding the influence of the period and the backbone shape on the seismic performance of oscillators. Taking advantage of SPO2IDA, existing methodologies for predicting the seismic performance of first-mode-dominated, multi-degree-of-freedom systems can be upgraded to provide accurate estimation well beyond the peak of the SPO.

The IDA results may display quite large record-to-record variability. By incorporating elastic spectrum information, efficient intensity measures can be created that reduce such dispersions, resulting in significant computational savings. By employing either a single optimal spectral value, a vector of two or a scalar combination of several spectral values, significant efficiency is achieved. As the structure becomes damaged, the evolution of such optimally selected spectral values is observed, providing intuition about the role of spectral shape in the seismic performance of structures.

# Acknowledgements

Ah, at last, the single unedited part of my thesis. It may appear in the first pages, but it was actually the last to be written. It is meant to acknowledge all these wonderful people who made it possible for me to come to Stanford and made my life here richer.

So where do I start? There is a long line of teachers, professors and mentors that apparently conspired to put me here, at the end of my PhD. There were at least a couple of teachers in my early years that tried to make me overcome my low self-esteem and make me believe in myself. I remember Mr. Leventis, who pushed me hard to read, write and understand literature, skills that came very handy later. And Mr. Danasis, my tutor in English, who drilled me hard and taught me this language. He will probably be very unhappy if any syntax error has crept into my thesis. Probably one of the most memorable is the late Mr. Koutoulakis, my math teacher for two years in high school. He taught me well and he actively encouraged me to participate in the national mathematical competitions. I never believed I could do it, but he did! Then came Mr. Fanourakis and for three years he taught me mathematics, logic and how to construct proofs. You can still see his insistence for precision and clarity when I am using symbols like  $\in$  or  $\infty$  in my formulas. This guy practically got me through the entrance exams for civil engineering college. I was convinced at the time that I would become a practicing engineer and I still remember when he told my mother that I had better turn into research. I did not believe it then, but maybe he was right after all.

Then came the college years and my meeting with Prof. Vardoulakis. What a great guy. Research flowed around him, ideas were popping in and out of his office and I can surely say that he steered me towards research when he asked me if I knew what a middle-age crisis is. He went on to say that this is what would happen to me if I submitted to the “background noise” in my surroundings that was convincing me to go against my true heart’s desire. He said that he just knew I was meant for a PhD, and I had better get it early rather than when I became forty. Under his and Prof. Georgiadis’s tutoring I got my first glimpse of research, and I have to admit I liked it. A lot.

Well, maybe it was all these guys that seemed to know me better than I knew myself. Maybe it was just my lusting for California through the scenes in Top Gun. Maybe it was destiny that I could not escape, nor delay, that just made me want to come here. And when I met Danai, she did not believe that I was serious about it. Almost a year after meeting her and a few months before leaving college, I got this letter from Prof. Borja, incorrectly addressed to Alec Zimmer (who later became a great buddy during my masters year), opening the gateway for an MS at Stanford. And so I left, leaving behind friends, family and girlfriend to pursue a degree that was supposedly going to last only a year. How clueless I was, even then.

Upon arriving at Stanford, I decided I did not want anything to do with all these silly probability classes and tried to convince Steve Winsterstein that I had no use for the (required) class he was teaching. He got me to come to the first lecture and I have to admit he was the one that seduced me to the other side. Have you noticed how probability flows around us and binds all things together? Well, something like that, but then it got better. I got to meet master Yoda. At that welcome BBQ

of the department I first said “hi” to Allin, (aka Prof. Cornell). After a few more months, I was looking for a way to stay longer at Stanford (or Berkeley). It was when talking to Prof. Armen Der Kiureghian at Berkeley and he asked me whether I had worked with Allin that I somehow got the idea that I had better do it. The rest is history.

If I start talking about Allin, my thesis will get too thick, and I will probably make him uncomfortable when he reads this. It suffices to say that I will never be able to pay him back for all he did for me, and I will surely miss those weekly meetings and the resulting indecipherable notes. His enthusiasm for research is contagious, simply too difficult to resist.

Many thanks for Professor Eduardo Miranda and Greg Deierlein who spend time to revise this document, and make it look even better. It is just great having your signatures on the front pages!

And all along these characters have been many many friends and colleagues, probably too many to be listed here without fear of leaving someone out. So, many thanks to the RMS team, the Blume gang, and of course all my friends at Stanford who took the time to listen to my research problems and propose ideas and venues that I had never thought of before.

Hi mom, hi dad, thanks for being patient with me. Lot’s of hugs to you Danai, it took a while but I made it, and you have waited for me all these years. And yes, I do love you so it is in ink now, ok? Ahhh, girls...

Lot’s of thanks to you, Stanford Greeks (nothing to do with fraternities), for keeping me in the Hellenic Association board for 4 years and not letting me give up having parties even when I really needed to work. I am going to miss those extended lunch hours at the greek corner of Tressider. Not to mention the ski trips, the nights out, the weekend soccer games, the dinners or so many other happy occasions.

So what now? The future is not set. I can only leave hoping that I will stay in touch with everyone, remain true to the principles that I have been taught and I will do even more and better research. But I will settle for what I have now, and just hope that my upcoming military duty will not rust my brain.

So I guess it is time to turn off my trusted *Nausika* (that is my computer of course) and bid you all goodbye. For now. The time has come to raise the sails and see what lies beyond the horizon.

Yours,

Dimitrios Vamvatsikos,  
Stanford, Thursday, July 18th, 2002.

# Contents

<b>Abstract</b>	<b>iv</b>
<b>Acknowledgements</b>	<b>v</b>
<b>1 Introduction</b>	<b>1</b>
1.1 Motivation . . . . .	1
1.2 Objectives and scope . . . . .	2
1.3 Organization and outline . . . . .	2
<b>2 Incremental Dynamic Analysis</b>	<b>5</b>
2.1 Abstract . . . . .	5
2.2 Introduction . . . . .	5
2.3 Fundamentals of single-record IDAs . . . . .	7
2.4 Looking at an IDA curve: Some general properties . . . . .	9
2.5 Capacity and limit-states on single IDA curves . . . . .	13
2.6 Multi-record IDAs and their summary . . . . .	15
2.7 The IDA in a PBEE framework . . . . .	18
2.8 Scaling legitimacy and <i>IM</i> selection . . . . .	18
2.9 The IDA versus the <i>R</i> -factor . . . . .	20
2.10 The IDA versus the Nonlinear Static Pushover . . . . .	21
2.11 IDA Algorithms . . . . .	23
2.12 Conclusions . . . . .	24
<b>3 Applied Incremental Dynamic Analysis</b>	<b>26</b>
3.1 Abstract . . . . .	26
3.2 Introduction . . . . .	26
3.3 Model and ground motion records . . . . .	27
3.4 Performing the Analysis . . . . .	28
3.5 Postprocessing . . . . .	29
3.5.1 Generating the IDA curves by Interpolation . . . . .	30
3.5.2 Defining Limit-States on an IDA curve . . . . .	32
3.5.3 Summarizing the IDAs . . . . .	33
3.5.4 PBEE calculations . . . . .	35
3.5.5 Taking advantage of the data: SPO versus IDA . . . . .	37
3.6 Discussion of choices and their influence on IDA . . . . .	40
3.6.1 Numerical convergence . . . . .	40
3.6.2 Choice of Tracing Algorithm . . . . .	41
3.6.3 Interpolation issues . . . . .	42

3.6.4	Sensitivity of the limit-state capacities to their definition . . . . .	44
3.6.5	Summarization given <i>IM</i> or <i>DM</i> . . . . .	46
3.6.6	Sensitivity to the record suite size . . . . .	48
3.7	Conclusions . . . . .	49
3.8	Acknowledgements . . . . .	50
<b>4</b>	<b>SPO2IDA for SDOF systems</b>	<b>51</b>
4.1	Abstract . . . . .	51
4.2	Introduction . . . . .	51
4.3	Methodology . . . . .	52
4.4	Moderate period pinching model . . . . .	55
4.4.1	Fitting the hardening branch of the IDA . . . . .	55
4.4.2	Fitting the negative branch of the IDA . . . . .	56
4.4.3	Fitting the residual part of the IDA . . . . .	57
4.4.4	Joining the pieces: The SPO2IDA tool . . . . .	58
4.4.5	Illustrative Results and Observations . . . . .	60
4.4.6	SPO2IDA error estimates for moderate periods . . . . .	60
4.5	Extension to all-periods pinching model . . . . .	62
4.5.1	Fitting the hardening branch of the IDA . . . . .	62
4.5.2	Fitting the negative branch of the IDA . . . . .	63
4.5.3	Fitting the residual part of the IDA . . . . .	64
4.5.4	Illustrative Results and Observations . . . . .	64
4.5.5	SPO2IDA error estimates for all periods . . . . .	65
4.6	From the IDA to the inelastic displacement ratios . . . . .	66
4.7	Influence of other SDOF parameters . . . . .	67
4.8	Conclusions . . . . .	69
4.9	Acknowledgments . . . . .	69
4.10	Appendix: The SPO2IDA algorithm . . . . .	70
<b>5</b>	<b>SPO2IDA for MDOF systems</b>	<b>72</b>
5.1	Abstract . . . . .	72
5.2	Introduction . . . . .	72
5.3	IDA fundamentals . . . . .	73
5.4	SPO2IDA for SDOF systems . . . . .	74
5.5	SPO2IDA for MDOF Systems . . . . .	74
5.5.1	Defining the SPO . . . . .	75
5.5.2	Estimating the IDA elastic stiffness . . . . .	77
5.5.3	Putting it all together . . . . .	77
5.6	Application to a 5-story braced frame . . . . .	79
5.7	Application to a 20-story moment frame . . . . .	79
5.8	Limit-state capacity estimation using the MDOF SPO2IDA . . . . .	83
5.9	Sensitivity to user choices . . . . .	84
5.10	Conclusions . . . . .	85
5.11	Acknowledgements . . . . .	86
<b>6</b>	<b>Elastic spectral shape for capacities</b>	<b>87</b>
6.1	Introduction . . . . .	87
6.2	Methodology . . . . .	89
6.3	Using a single spectral value . . . . .	91
6.4	Using a vector of two spectral values . . . . .	95
6.4.1	Postprocessing IDAs with vector <i>IMs</i> . . . . .	95

6.4.2	Collapsing a vector to a scalar . . . . .	101
6.4.3	Investigating the vector of two spectral values . . . . .	101
6.5	Using a power-law form with two or three spectral values . . . . .	103
6.6	Using all spectral values . . . . .	111
6.7	Conclusions . . . . .	115
<b>7</b>	<b>Conclusions</b>	<b>117</b>
7.1	Summary . . . . .	117
7.2	Limitations and Future Work . . . . .	119
7.3	Overall Conclusions . . . . .	120
	<b>Bibliography</b>	<b>121</b>

# List of Tables

3.1	The set of twenty ground motion records used. . . . .	27
3.2	Sequence of runs generated by the hunt & fill tracing algorithm for record #14. . . . .	28
3.3	Summarized capacities for each limit-state. . . . .	33
3.4	MAFs of exceedance for each limit-state, calculated both numerically from Equation (3.11) and with the approximate analytical form (3.12), using either a global or a local fit to the <i>IM</i> -hazard curve. . . . .	37
3.5	Comparing the sensitivity to parameters of the stepping versus the hunt & fill algorithm. . . . .	41
3.6	Median <i>IM</i> and <i>DM</i> capacities for each limit-state, shown versus the bootstrapped standard error and the 90% confidence interval on the median estimate. . . . .	48
3.7	MAFs for each limit-state, calculated both numerically and with the approximate analytical form (global or local fit). The bootstrapped standard error and 90% confidence interval on the MAF estimate are also presented. Additionally, we test the hypothesis that the approximate $\lambda_{LS}$ is equal to the exact at the 95% confidence level. . . . .	49
4.1	The suite of thirty ground motion records used. . . . .	53
4.2	Coefficients and functions needed for the IDA hardening part in Equation (4.1). . . . .	56
4.3	Coefficients and functions needed for the flatline of the IDA softening part in Equation (4.2). . . . .	57
4.4	Coefficients and functions needed for fitting the IDA residual part in Equation (4.4). . . . .	58
4.5	Average fractile-demand and fractile-capacity errors for moderate periods and a variety of backbone shapes, as caused by the fitting in SPO2IDA and by the record-to-record variability in IDA. . . . .	61
4.6	Coefficients needed for the IDA hardening part in Equation (4.7). . . . .	63
4.7	Coefficients needed for the flatline of the IDA softening part in Equation (4.8). . . . .	63
4.8	Coefficients needed for fitting the IDA residual part in Equation (4.9). . . . .	64
4.9	Average fractile-demand and fractile-capacity errors for short, moderate and long periods and a variety of backbone shapes, as caused by the fitting in SPO2IDA and by the record-to-record variability in IDA. . . . .	65
5.1	Comparing the real and estimated 16%, 50% and 84% $S_a^c(T_1, 5\%)$ capacities over three limit-states for each of the studied structures. Note that the 5-story reaches global collapse quite early, so the GI and CP limit-states coincide. . . . .	83
5.2	Comparing the real and estimated 16%, 50% and 84% $\theta_{max}$ -value of capacity for the CP limit-state for each of the studied structures. . . . .	83
5.3	Comparing the median IDA elastic $\theta_{roof}$ and $\theta_{max}$ stiffnesses, as estimated by several different methods for the three structures. . . . .	85

# List of Figures

2.1	An example of information extracted from a single-record IDA study of a $T_1 = 4$ sec, 20-story steel moment-resisting frame with ductile members and connections, including global geometric nonlinearities (P- $\Delta$ ) subjected to the El Centro, 1940 record (fault parallel component). . . . .	6
2.2	IDA curves of a $T_1 = 1.8$ sec, 5-story steel braced frame subjected to 4 different records. . . . .	9
2.3	IDA curves of peak interstory drifts for each floor of a $T_1 = 1.8$ sec 5-story steel braced frame. Notice the complex “weaving” interaction where extreme softening of floor 2 acts as a fuse to relieve those above (3,4,5). . . . .	10
2.4	Ductility response of a $T = 1$ sec, elasto-plastic oscillator at multiple levels of shaking. Earlier yielding in the stronger ground motion leads to a lower absolute peak response. . . . .	11
2.5	Structural resurrection on the IDA curve of a $T_1 = 1.3$ sec, 3-story steel moment-resisting frame with fracturing connections. . . . .	12
2.6	Two different rules producing multiple capacity points for a $T_1 = 1.3$ sec, 3-story steel moment-resisting frame with fracturing connections. The <i>DM</i> rule, where the <i>DM</i> is $\theta_{max}$ , is set at $C_{DM} = 0.08$ and the <i>IM</i> rule uses the 20% slope criterion. . . . .	14
2.7	An IDA study for thirty records on a $T_1 = 1.8$ sec, 5-story steel braced frame, showing (a) the thirty individual curves and (b) their summary (16%, 50% and 84%) fractile curves (in log-log scale). . . . .	17
2.8	Roof ductility response of a $T_1 = 1$ sec, MDOF steel frame subjected to 20 records, scaled to 5 levels of $S_a(T_1, 5\%)$ . The unscaled record response and the power-law fit are also shown for comparison (from Bazzurro et al., 1998). . . . .	19
2.9	IDA curves for a $T_1 = 2.2$ sec, 9-story steel moment-resisting frame with fracturing connections plotted against (a) <i>PGA</i> and (b) $S_a(T_1, 5\%)$ . . . . .	19
2.10	The median IDA versus the Static Pushover curve for (a) a $T_1 = 4$ sec, 20-story steel moment-resisting frame with ductile connections and (b) a $T_1 = 1.8$ sec, 5-story steel braced frame. . . . .	22
3.1	The numerically-converging dynamic analysis points for record #14, Table 3.2, are interpolated, using both a spline and a piecewise linear approximation. . . . .	31
3.2	The limit-states, as defined on the IDA curve of record #14. . . . .	31
3.3	All twenty IDA curves and the associated limit-state capacities. The <i>IO</i> limit is at the intersection of each IDA with the $\theta_{max} = 2\%$ line, the <i>CP</i> limit is represented by the dots, while <i>GI</i> occurs at the flatlines. . . . .	34
3.4	The summary of the IDA curves and corresponding limit-state capacities into their 16%, 50% and 84% fractiles. . . . .	34
3.5	Hazard curve for the Van Nuys Los Angeles site, for $S_a(2.37s, 5\%)$ . . . . .	35

3.6	The median peak interstory drift ratios for all stories at several specified $S_a(T_1, 5\%)$ levels. . . . .	38
3.7	The IDA curves of the odd stories for record #1. . . . .	38
3.8	The SPO curve generated from an inverse-triangle (maximum force at roof) load pattern versus the median IDA. . . . .	39
3.9	Linearly interpolated IDA curve for record #14, traced with a different total number of converging runs. . . . .	43
3.10	Spline-interpolated IDA curve for record #14, traced with a different total number of converging runs. . . . .	43
3.11	The sensitivity of the fractile (16%, 50% and 84%) $S_a(T_1, 5\%)$ and $\theta_{\max}$ capacities for the CP limit-state to the elastic stiffness fraction used (20% is the standard by FEMA, 2000a). The results are less sensitive if the $\theta_{\max} = 10\%$ limit is used. . .	45
	(a) Resulting $S_a(T_1, 5\%)$ and $\theta_{\max}$ capacities when the $\theta_{\max} = 10\%$ limit <i>is not imposed</i> . . . . .	45
	(b) Resulting $S_a(T_1, 5\%)$ and $\theta_{\max}$ capacities when the $\theta_{\max} = 10\%$ limit <i>is imposed</i> . . . . .	45
3.12	Summarization into fractiles of $IM$ given $DM$ versus fractiles of $DM$ given $IM$ . .	46
3.13	Two stripes, one given $DM$ and one given $IM$ , converging on the same median (the star). The records are No.18,5,19,6,9,10,13 from the highest to the lowest $IM$ at $\theta_{\max} = 4\%$ . . . . .	47
4.1	The backbone to be investigated and its five controlling parameters. . . . .	52
4.2	Generating the fractile IDA curves and capacities from dynamic analyses versus estimating them by SPO2IDA for an SPO with $a_h = 0.3$ , $\mu_c = 2$ , $a_c = -2$ , $r = 0.5$ , $\mu_f = 5$ . . . . .	54
	(a) Thirty IDA curves and flatline capacities . . . . .	54
	(b) Summarization into fractile IDAs, given $R$ or $\mu$ . . . . .	54
	(c) The fractile IDAs from (b) versus the SPO curve . . . . .	54
	(d) The fractile IDAs, as estimated by SPO2IDA . . . . .	54
4.3	An elastic-hardening-negative backbone and the two extremes of its “equivalent” set. . . . .	56
4.4	Demonstrating SPO2IDA: the median demand and collapse capacity as the SPO changes. . . . .	59
	(a) Increasing $\mu_c$ helps performance . . . . .	59
	(b) Increasing $a_h$ has negligible effects if same $\mu_{eq}$ . . . . .	59
	(c) The milder the negative slope, $a_c$ , the better . . . . .	59
	(d) $a_c$ is changing, but constant $r_{eq}$ anchors capacity . . . . .	59
	(e) Higher plateau $r$ benefits demand and capacity . . . . .	59
	(f) Increasing the fracturing ductility $\mu_f$ helps . . . . .	59
4.5	Median IDAs for a backbone with $a_h = 0.2$ , $\mu_c = 2$ , $a_c = -0.5$ , $r = 0.5$ , $\mu_f = 6$ but varying periods. . . . .	65
4.6	Comparing estimates of mean $C_\mu$ ratios generated by SPO2IDA for the special elastic-perfectly-plastic case versus the real data and results from Miranda (2000) for $\mu = 1.5, 2, 3, 4, 5, 6$ . . . . .	66
	(a) Results from IDA versus SPO2IDA . . . . .	66
	(b) Results from Miranda (2000). . . . .	66
4.7	Viscous damping has negligible influence, as shown for moderate periods for a backbone with $a_h = 0.3$ , $\mu_c = 2$ , $a_c = -2$ , $r = 0.5$ , $\mu_f = 5$ . . . . .	67
4.8	The different effect of the hysteresis model on oscillators with elastic-perfectly-plastic and elastic-negative backbones. . . . .	68
	(a) Three hysteresis models for elastic-perfectly-plastic system, $a_h = 0$ , $T = 1s$ . . . . .	68

(b)	Three hysteresis models for elastic-negative, $a_c = -0.2$ , $T = 1s$ . . . . .	68
(c)	Kinematic hysteresis for elastic-negative system, $a_c = -0.2$ , $T = 1s$ for record #29 at intensity $R = 2.4$ . . . . .	68
(d)	Pinching hysteresis for elastic-negative system, $a_c = -0.2$ , $T = 1s$ for record #29 at intensity $R = 2.4$ ). . . . .	68
5.1	The 16%, 50%, 84% fractile IDAs and limit-state capacities. . . . .	73
5.2	The median IDA compared against the SPO generated by an inverted-triangle load pattern. . . . .	73
5.3	Four $\theta_{\text{roof}}$ SPOs produced by different load patterns. . . . .	75
5.4	The most-damaging of the four SPO curves, shown in both $\theta_{\text{roof}}$ and $\theta_{\text{max}}$ terms. . . . .	75
5.5	Approximating the most-damaging of the four $\theta_{\text{roof}}$ SPO with a trilinear model. . . . .	75
5.6	The fractile IDA curves for the SDOF with the trilinear backbone, as estimated by SPO2IDA. . . . .	75
5.7	Generating the fractile IDAs from nonlinear dynamic analyses versus the MDOF SPO2IDA approximation for the 9-story building. . . . .	78
(a)	Full IDA $\theta_{\text{roof}}$ fractile curves . . . . .	78
(b)	SPO2IDA estimated $\theta_{\text{roof}}$ fractile curves . . . . .	78
(c)	Full IDA $\theta_{\text{max}}$ fractile curves . . . . .	78
(d)	SPO2IDA estimated $\theta_{\text{max}}$ fractile curves . . . . .	78
5.8	The most-damaging SPO curve for the 5-story building, shown in both $\theta_{\text{roof}}$ and $\theta_{\text{max}}$ terms. . . . .	80
5.9	Approximating the 5-story $\theta_{\text{roof}}$ SPO with a trilinear model. . . . .	80
5.10	Generating the fractile IDAs from nonlinear dynamic analyses versus the MDOF SPO2IDA approximation for the 5-story building. . . . .	80
(a)	Full IDA $\theta_{\text{roof}}$ fractile curves . . . . .	80
(b)	SPO2IDA estimated $\theta_{\text{roof}}$ fractile curves . . . . .	80
(c)	Full IDA $\theta_{\text{max}}$ fractile curves . . . . .	80
(d)	SPO2IDA estimated $\theta_{\text{max}}$ fractile curves . . . . .	80
5.11	The most-damaging SPO curve for the 20-story building, shown in both $\theta_{\text{roof}}$ and $\theta_{\text{max}}$ terms. . . . .	81
5.12	Approximating the 20-story $\theta_{\text{roof}}$ SPO with a trilinear model. . . . .	81
5.13	Generating the fractile IDAs from nonlinear dynamic analyses versus the MDOF SPO2IDA approximation for the 20-story building. . . . .	82
(a)	Full IDA $\theta_{\text{roof}}$ fractile curves . . . . .	82
(b)	SPO2IDA estimated $\theta_{\text{roof}}$ fractile curves . . . . .	82
(c)	Full IDA $\theta_{\text{max}}$ fractile curves . . . . .	82
(d)	SPO2IDA estimated $\theta_{\text{max}}$ fractile curves . . . . .	82
6.1	The 5%-damped elastic acceleration spectra for thirty records, normalized to the first-mode period of the 20-story building. . . . .	88
6.2	Dispersion of the $S_a^c(\tau, 5\%)$ -values versus period $\tau$ for four different limit-states for the 5-story building. . . . .	90
(a)	Elastic region . . . . .	90
(b)	$\theta_{\text{max}} = 0.007$ . . . . .	90
(c)	$\theta_{\text{max}} = 0.01$ . . . . .	90
(d)	Global Instability . . . . .	90
6.3	The fractile IDA curves and capacities for four limit-states (Figure 6.2) of the 5-story building. . . . .	90
6.4	The optimal period $\tau$ as it evolves with $\theta_{\text{max}}$ for the 5-story building. . . . .	92

6.5	The dispersion for the optimal $S_a(\tau, 5\%)$ compared to $S_a(T_1, 5\%)$ and PGA, versus the limit-state definition, $\theta_{\max}$ , for the 5-story building. . . . .	92
6.6	Dispersion of the $S_a^c(\tau, 5\%)$ values versus period $\tau$ for four different limit-states for the 9-story building. . . . .	93
	(a) Elastic region . . . . .	93
	(b) $\theta_{\max} = 0.05$ . . . . .	93
	(c) $\theta_{\max} = 0.1$ . . . . .	93
	(d) Global Instability . . . . .	93
6.7	The fractile IDA curves and capacities for four limit-states (Figure 6.6) of the 9-story building. . . . .	93
6.8	The optimal period $\tau$ as it evolves with $\theta_{\max}$ for the 9-story building. . . . .	94
6.9	The dispersion for the optimal $S_a(\tau, 5\%)$ compared to $S_a(T_1, 5\%)$ and PGA, versus the limit-state definition, $\theta_{\max}$ , for the 9-story building. . . . .	94
6.10	Dispersion of the $S_a^c(\tau, 5\%)$ -values versus period $\tau$ for four limit-states of the 20-story building. . . . .	96
	(a) Elastic region . . . . .	96
	(b) $\theta_{\max} = 0.02$ . . . . .	96
	(c) $\theta_{\max} = 0.1$ . . . . .	96
	(d) Global Instability . . . . .	96
6.11	The fractile IDA curves and capacities for four limit-states (Figure 6.10) of the 20-story building. . . . .	96
6.12	The optimal period $\tau$ as it evolves with $\theta_{\max}$ for the 20-story building. . . . .	97
6.13	The dispersion for the optimal $S_a(\tau, 5\%)$ compared to $S_a(T_1, 5\%)$ and PGA, versus the limit-state definition, $\theta_{\max}$ , for the 20-story building. . . . .	97
6.14	The thirty IDA curves for the 5-story building in $S_a(T_1, 5\%)$ and $R_{sa}(1.5, T_1)$ coordinates. . . . .	98
6.15	The median IDA surface for the 5-story building in $S_a(T_1, 5\%)$ and $R_{sa}(1.5, T_1)$ coordinates. . . . .	98
6.16	Median contours for thirty IDA curves for the 5-story building in $S_a(T_1, 5\%)$ and $R_{sa}(1.5, T_1)$ coordinates. Their color indicates the level of $\theta_{\max}$ as shown in the color bar. . . . .	100
6.17	The 16%, 50% and 84% capacity lines at the limit-state of $\theta_{\max} = 0.016$ for the 5-story building. . . . .	100
6.18	Median contours for the 9-story building in $S_a(T_1, 5\%)$ and $R_{sa}(1.5, T_1)$ coordinates. Little has been gained by using a vector. . . . .	102
6.19	Median contours for the 20-story building in $S_a(T_1, 5\%)$ and $R_{sa}(1.5, T_1)$ coordinates. They are colored by the value of $\theta_{\max}$ . In this case, the use of a vector has only a small influence. . . . .	102
6.20	Median contours for the 20-story building in $S_a(T_1, 5\%)$ and $R_{sa}(0.5, T_1)$ coordinates. They are colored by the value of $\theta_{\max}$ . Some variability is explained but the contours are not simple. . . . .	103
6.21	Median contours for the 9-story building in $S_a(T_1, 5\%)$ and $R_{sa}(0.7, T_1)$ coordinates. They are colored by the value of $\theta_{\max}$ . The use of a vector is beneficial, and the contours have power-law shape. . . . .	104
6.22	Median contours for the 20-story building in $S_a(T_1, 5\%)$ and $R_{sa}(0.3, T_1)$ coordinates. They are colored by the value of $\theta_{\max}$ . The use of a vector is beneficial, and the contours have power-law shape. . . . .	104
6.23	The two optimal periods $\tau_a, \tau_b$ as they evolve with $\theta_{\max}$ for the 5-story building. . . . .	105
6.24	The dispersions for optimal $S_a(\tau_a, 5\%)^{1-\beta} S_a(\tau_b, 5\%)^\beta$ versus $S_a(T_1, 5\%)$ and PGA for the 5-story building. . . . .	105

6.25	The three optimal periods $\tau_a, \tau_b, \tau_c$ as they evolve with $\theta_{\max}$ for the 5-story building.	106
6.26	The dispersions for optimal $S_a(\tau_a, 5\%)^{1-\beta-\gamma} S_a(\tau_b, 5\%)^\beta S_a(\tau_c, 5\%)^\gamma$ versus the dispersions for PGA and $S_a(T_1, 5\%)$ for the 5-story building.	106
6.27	The 84% fractile of the suboptimal dispersion when using a single spectral value versus a power-law combination of two or three periods for the 5-story building. For comparison, the dispersion achieved by $S_a(T_1, 5\%)$ and the optimal three-periods power-law is also shown.	107
6.28	The two optimal periods $\tau_a, \tau_b$ as they evolve with $\theta_{\max}$ for the 9-story building.	109
6.29	The dispersions for optimal $S_a(\tau_a, 5\%)^{1-\beta} S_a(\tau_b, 5\%)^\beta$ versus $S_a(T_1, 5\%)$ and PGA for the 9-story building.	109
6.30	The three optimal periods $\tau_a, \tau_b, \tau_c$ as they evolve with $\theta_{\max}$ for the 9-story building.	110
6.31	The dispersions for optimal $S_a(\tau_a, 5\%)^{1-\beta-\gamma} S_a(\tau_b, 5\%)^\beta S_a(\tau_c, 5\%)^\gamma$ versus the dispersions for PGA and $S_a(T_1, 5\%)$ for the 9-story building.	110
6.32	The 84% fractile of the suboptimal dispersion when using a single spectral value versus a power-law combination of two or three periods for the 9-story building. For comparison, the dispersion achieved by $S_a(T_1, 5\%)$ and the optimal three-periods power-law is also shown.	111
6.33	The two optimal periods $\tau_a, \tau_b$ as they evolve with $\theta_{\max}$ for the 20-story building.	112
6.34	The dispersions for optimal $S_a(\tau_a, 5\%)^{1-\beta} S_a(\tau_b, 5\%)^\beta$ versus $S_a(T_1, 5\%)$ and PGA for the 20-story building.	112
6.35	The three optimal periods $\tau_a, \tau_b, \tau_c$ as they evolve with $\theta_{\max}$ for the 20-story building.	113
6.36	The dispersions for optimal $S_a(\tau_a, 5\%)^{1-\beta-\gamma} S_a(\tau_b, 5\%)^\beta S_a(\tau_c, 5\%)^\gamma$ versus the dispersions for PGA and $S_a(T_1, 5\%)$ for the 20-story building.	113
6.37	The 84% fractile of the suboptimal dispersion when using a single spectral value versus a power-law combination of two or three periods for the 20-story building. For comparison, the dispersion achieved by $S_a(T_1, 5\%)$ and the optimal three-periods power-law is also shown.	114
6.38	The regression coefficient function $\beta(\tau)$ at global dynamic instability for the 20-story building.	115

# Introduction

## 1.1 Motivation

Earthquake engineering has come a long way since its birth, and it still seems to grow rapidly as we gain experience. Each time an earthquake happens, we learn something new and the profession grows to accommodate it. Such is the case in the aftermath of the 1989 Loma Prieta and 1994 Northridge earthquakes, where we learned that sometimes a life-safe building is just not enough.

Both research and practice used to be mostly concerned with the design of structures that would be safe, in the sense of surviving a seismic event with a minimum number of casualties. Still, many building owners have realized the staggering costs incurred by a life-safe yet heavily damaged and non-operational building. Replacing or rehabilitating it, means stopping its operation, relocating the people and functions that it houses and finally dealing with an expensive construction market overwhelmed with competing projects after a major earthquake. Compare that to the slightly increased cost of having had a structure designed to higher standards, chosen to meet the specific needs of the (demanding) owner, and thus able to remain functional after a small but relatively frequent event, while still being safe if a rare destructive earthquake hits.

Thus was Performance-Based Earthquake Engineering (PBEE) born, a relatively new but rapidly growing idea that seems to be present in all guidelines that were recently published: Vision 2000 (SEAOC, 1995), ATC-40 (ATC, 1996), FEMA-273 (FEMA, 1997), and SAC/FEMA-350 (FEMA, 2000a). In loose terms, it requires that a building be designed to meet specific performance objectives under the action of the frequent or the rarer seismic events that it may experience in its lifetime. So, a building with a lifetime of 50 years may be required to sustain no damages under a frequent, “50% in 50 years” event, e.g., one that has a probability of 50% of being exceeded in the next 50 years. At the same time it should be able to remain repairable, despite sustaining some damage, during a “10% in 50 years” event and remain stable and life-safe for rare events of “2% in 50 years”, although, subsequently, it may have to be demolished. Obviously such performance objectives can be better tailored to a building’s function, e.g., being stricter for a hospital that needs to remain operational even after severe events, while being more relaxed for less critical facilities, flexible and able to suit each building owner’s needs (respecting a minimum of safety of course).

PBEE is quite a complicated subject and has created many new challenges that need to be overcome. We need methods to quantify structural damage (e.g., beams, columns, foundations) and non-structural damage (e.g., partitions, glass panels), ways to estimate the number of casualties, the loss of building contents, the building downtime, rehabilitation costs, even estimates of the price inflation after a major earthquake. But before we even get there, we have to start at the basis; we need a powerful analysis method that will accurately analyze structural models and estimate the (distribution of) demands that any level of shaking (frequent or not) may impose

and, specifically, determine the level of shaking that will cause a structure to exceed a specified limit-state, thus failing a given performance objective. In more accurate terms, we need a method that will allow us to predict the mean annual frequency of violating the prescribed limit-states.

Several methodologies have been proposed to fulfill this role, but arguably the most promising one is Incremental Dynamic Analysis (IDA). It takes the old concept of scaling ground motion records and develops it into a way to accurately describe the full range of structural behavior, from elasticity to collapse. Specifically, IDA involves subjecting a structural model to one (or more) ground motion record(s), each scaled to multiple levels of intensity, thus producing one (or more) curve(s) of response parameterized versus intensity level. By suitably summarizing such IDA curves, defining limit-states and combining the results with standard Probabilistic Seismic Hazard Analysis (PSHA), we can easily reach the goals we have set. But why stop there? IDA has great potential and can extend far beyond being just a solution for PBEE, to provide valuable intuition and help both researchers and professional engineers better understand the seismic behavior of structures.

## 1.2 Objectives and scope

The goal of this study is to unify the concept of Incremental Dynamic Analysis and place it in a concrete context of unambiguous definitions. Given that, this work aims to uncover the strengths of the methodology and show how it can be applied in a practical way to deal with the issues of PBEE. Furthermore, IDA is expanded and extended to cover larger ground. We will show its connection with old and established seismic analysis methods, like the response modification  $R$ -factor, or the Static Pushover Analysis (also known as the Nonlinear Static Procedure, [FEMA, 1997](#)). Additionally, we will use it as a tool to investigate the influence of elastic spectral shape in the seismic behavior of structures. The ultimate goal is to establish the use of nonlinear dynamic analyses under multiple ground motion records as the state of the art and try to encourage practice towards that direction, away from the current use of one to three accelerograms or just the Static Pushover.

## 1.3 Organization and outline

All chapters are designed to be autonomous, each being a self-contained, single paper that has either appeared in a professional journal or is being planned as a future publication. Still, it is suggested that one becomes acquainted with the concepts introduced by the next chapter before skipping ahead to other material that may be of interest:

**Chapter 2** establishes and defines the basic principles of Incremental Dynamic Analysis (IDA).

Despite being an altogether novel method, bits and pieces of it have appeared in the literature in several different forms. The goal is to establish a common frame of reference and unified terminology. First, the concept of the Intensity Measure ( $IM$ ) is introduced to better describe the scaling of a ground motion record, while the Damage Measure ( $DM$ ) is used to measure the structural response. Combined together they define the IDA curve that describes the response of a structure at several levels of intensity for a given ground motion record: from elasticity to nonlinearity and ultimately global dynamic instability. Suitable algorithms are presented to select the dynamic analyses and form the IDA curves, while properties of the IDA curve are looked into for both single-degree-of-freedom (SDOF) and multi-degree-of-freedom (MDOF) structures. In addition, we discuss methods for defining limit-states on the IDA curves and estimating their capacities. Appropriate summarization techniques for multi-record IDA studies and the association of the IDA study with the conventional Static Pushover (SPO) Analysis and the yield reduction  $R$ -factor are also discussed. Finally in

the framework of Performance-Based Earthquake Engineering (PBEE), the assessment of demand and capacity is viewed through the lens of an IDA study.

*Were this a car-dealership brochure, you would be looking at the shiny new Ferrari. This mythical beast has been around for a while, you may have heard about it or seen it in pictures, but may have felt intimidated. Now we are doing everything we can to describe it at length, give you complete understanding of the inner workings and offer it at a greatly reduced cost (of analysis).*

**Chapter 3** describes the practical use of IDA. Taking a realistic 9-story building as an example and using the theory and observations of the previous chapter, we will generate a complete application for PBEE assessment. We are going to take you through a step-by-step tutorial of performing IDA in this representative case-study: choosing suitable ground motion Intensity Measures (IMs) and representative Damage Measures (DMs), employing interpolation to generate continuous IDA curves, defining appropriate limit-states, estimating the corresponding capacities and summarizing the IDA demands and capacities. Finally, by combining such summarized results with PSHA in an appropriate probabilistic framework, the mean annual frequencies of exceeding each limit-state are calculated. At first, the reader is walked through the direct and efficient route to the final product. Then the acquired knowledge of the process is used to contemplate the choices that we have made along the way, highlighting the shortcuts we took and the pitfalls we have skillfully avoided.

*This is practically where we take you out, sitting at the wheel of the Ferrari, for a test-drive. See the beast, play with it and experience the thrill it delivers. Is there anything it cannot do?*

**Chapter 4** investigates the connection of the IDA with the Static Pushover (SPO) for SDOF systems. An established method for analyzing structures, the SPO is clearly superseded by the IDA, but still has a lot to offer in understanding the more complex analysis. Starting with the simplest of all systems, the SDOF, but allowing it to have a complex force-deformation backbone, we map the influence of the SPO, or the backbone, to the IDA. There is large tradition in the profession to provide equations for the mean peak displacement response of simple nonlinear oscillators, usually sporting the simplest (elastic-perfectly-plastic) backbones (SPOs). Here we tap into the power of IDA to take this concept one step further, in the hope of upgrading the SPO to become a light, inexpensive alternative to the IDA. The final product is SPO2IDA, an accurate, spreadsheet-level tool for Performance-Based Earthquake Engineering that is available on the internet. It offers effectively instantaneous estimation of nonlinear dynamic displacement demands and limit-state capacities, in addition to conventional strength reduction  $R$ -factors and inelastic displacement ratios, for any SDOF system whose Static Pushover curve can be approximated by a quadrilinear backbone.

*Even at a discount, not everybody can afford a Ferrari. So, how about using a good old reliable Toyota, but with a brand new Ferrari-like engine? We are only going to develop the engine now, creating a free, efficient and mass-producible replica called SPO2IDA, then let you see how it compares with the real thing.*

**Chapter 5** extends the connection between SPO and IDA to MDOF structures. Taking advantage of the tools generated in the previous chapter, we venture forth to apply them suitably to MDOF systems, in a manner similar to existing methodologies (e.g., FEMA, 1997). SPO2IDA allows the use of an SDOF system whose backbone closely matches the SPO of the MDOF structure even beyond its peak. The result is a fast and accurate method to estimate the seismic demand and capacity of first-mode-dominated MDOF systems. The summarized IDA curves of complex structures are effortlessly generated, enabling an engineer-

user to obtain accurate estimates of seismic demands and capacities for structural limit-states such as immediate occupancy or global dynamic instability. Testing the method against the full IDA for three MDOF systems shows the accuracy it can achieve, but also highlights its limitations.

*That is where we take our rejuvenated Toyota (SPO2IDA for MDOF systems) out to three different race tracks (buildings) and have a try-out versus the Ferrari (IDA). Conclusion: The Toyota cannot really win, but can hold its own, and performs much better than the original car we started with. We even come up with suggestions to the “Toyota manufacturers” (engineers who perform SPOs) on how to build their cars to better take advantage of our new engine.*

**Chapter 6** discusses the influence of the elastic spectral shape to the observed dispersion in the limit-state capacities extracted from IDA. Their record-to-record variability can be significant, but can be reduced with the introduction of efficient *IMs* that incorporate spectral information. While the use of inelastic spectral values can be advantageous, they need custom-made attenuation laws to be used in a PBEE framework. Thus we focus on elastic spectra, choosing to investigate an optimal single elastic spectral value, a vector of two, or a scalar combination of several optimal values. The resulting dispersions are calculated for each limit-state individually thus allowing us to observe the evolution of such optimal spectral values as the structural damage increases. Most importantly, we measure the sensitivity of such *IMs* to the suboptimal selection of the spectral values, shedding some light into the possibility of *a priori* selection of an efficient *IM*.

*That’s where we make some additions to our Ferrari only to realize we can make it more efficient (almost twice the miles per gallon) and turn it into a Batmobil. Still experimental, fresh off the works, but when we open up the throttle and unleash its power, it can take us to seismic outer-space!*

**Chapter 7** summarizes the virtues but also the limitations of our methods, describing directions for future work and improvements needed. Finally, it provides the overall conclusions and the summary of the thesis.

*Here, we praise the abilities and also put some dents to our Ferrari, Toyota and Batmobil. We acknowledge their weaknesses and suggest how to resolve them in the future.*

# Incremental Dynamic Analysis

Vamvatsikos, D. and Cornell, C. A. (2002a). *Earthquake Engineering and Structural Dynamics*, **31**(3): 491–514. © John Wiley & Sons Limited. Reproduced with permission.

## 2.1 Abstract

Incremental Dynamic Analysis (IDA) is a parametric analysis method that has recently emerged in several different forms to estimate more thoroughly structural performance under seismic loads. It involves subjecting a structural model to one (or more) ground motion record(s), each scaled to multiple levels of intensity, thus producing one (or more) curve(s) of response parameterized versus intensity level. To establish a common frame of reference, the fundamental concepts are analyzed, a unified terminology is proposed, suitable algorithms are presented, and properties of the IDA curve are looked into for both single-degree-of-freedom (SDOF) and multi-degree-of-freedom (MDOF) structures. In addition, summarization techniques for multi-record IDA studies and the association of the IDA study with the conventional Static Pushover Analysis and the yield reduction  $R$ -factor are discussed. Finally in the framework of Performance-Based Earthquake Engineering (PBEE), the assessment of demand and capacity is viewed through the lens of an IDA study.

## 2.2 Introduction

The growth in computer processing power has made possible a continuous drive towards increasingly accurate but at the same time more complex analysis methods. Thus the state of the art has progressively moved from elastic static analysis to dynamic elastic, nonlinear static and finally nonlinear dynamic analysis. In the last case the convention has been to run one to several different records, each once, producing one to several “single-point” analyses, mostly used for checking the designed structure. On the other hand methods like the nonlinear static pushover (SPO) (ATC, 1996) or the capacity spectrum method (ATC, 1996) offer, by suitable scaling of the static force pattern, a “continuous” picture as the complete range of structural behavior is investigated, from elasticity to yielding and finally collapse, thus greatly facilitating our understanding.

By analogy with passing from a single static analysis to the incremental static pushover, one arrives at the extension of a single time-history analysis into an incremental one, where the seismic “loading” is scaled. The concept has been mentioned as early as 1977 by Bertero (1977), and has been cast in several forms in the work of many researchers, including Luco and Cornell (1998, 2000), Bazzurro and Cornell (1994a,b), Yun et al. (2002), Mehanny and Deierlein (2000), Dubina et al. (2000), De Matteis et al. (2000), Nassar and Krawinkler (1991, pg.62–155) and Psycharis et al. (2000). Recently, it has also been adopted by the U.S. Federal Emergency Management

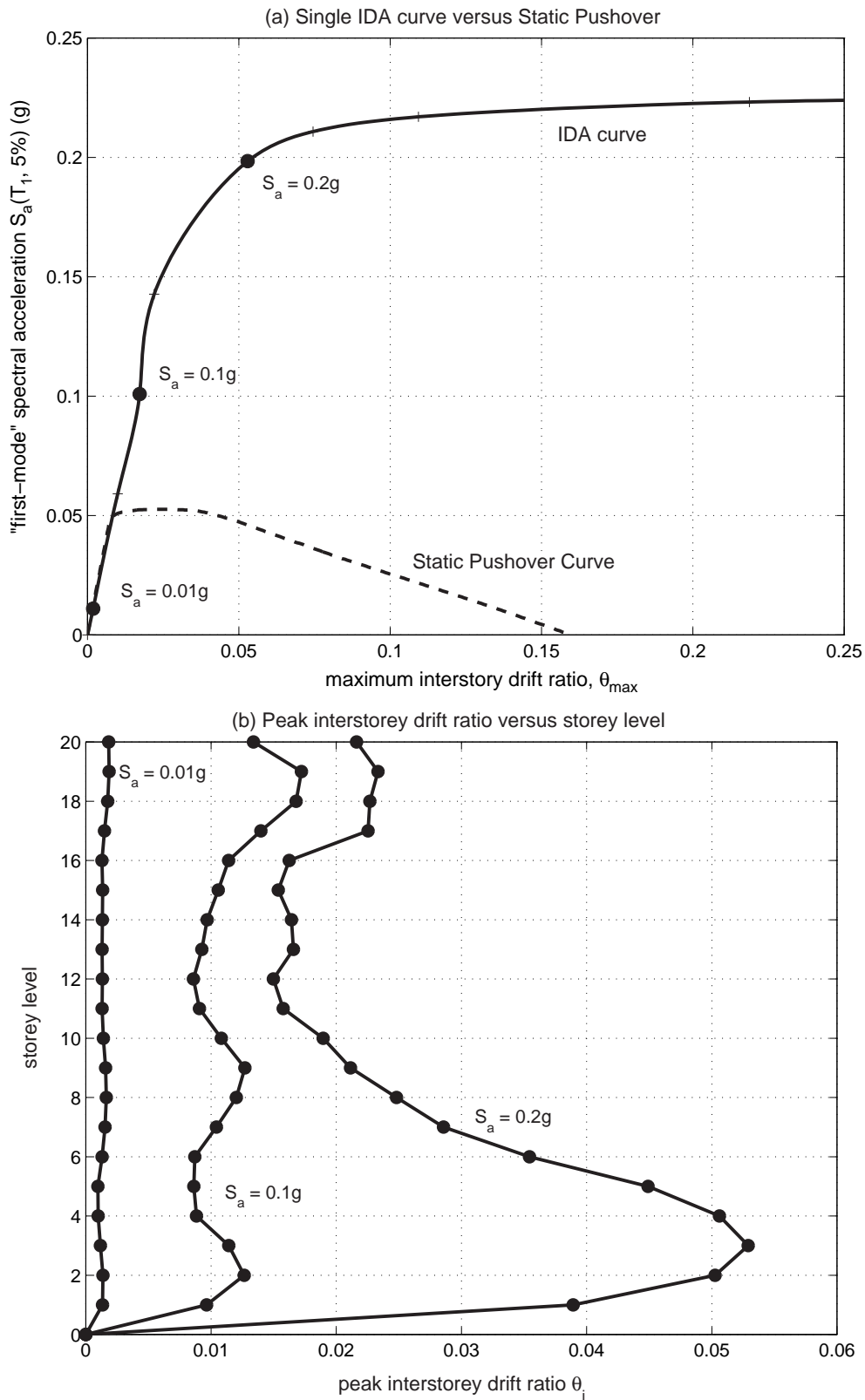


**Figure 2.1:** An example of information extracted from a single-record IDA study of a  $T_1 = 4$  sec, 20-story steel moment-resisting frame with ductile members and connections, including global geometric nonlinearities (P- $\Delta$ ) subjected to the El Centro, 1940 record (fault parallel component).

Agency (FEMA) guidelines (FEMA, 2000a,b) as the Incremental Dynamic Analysis (IDA) and established as the state-of-the-art method to determine global collapse capacity. The IDA study is now a multi-purpose and widely applicable method and its objectives, only some of which are evident in Figure 2.1(a,b), include

1. thorough understanding of the range of response or “demands” versus the range of potential levels of a ground motion record,
2. better understanding of the structural implications of rarer / more severe ground motion levels,
3. better understanding of the changes in the nature of the structural response as the intensity of ground motion increases (e.g., changes in peak deformation patterns with height, onset of stiffness and strength degradation and their patterns and magnitudes),
4. producing estimates of the dynamic capacity of the global structural system and
5. finally, given a multi-record IDA study, how stable (or variable) all these items are from one ground motion record to another.

Our goal is to provide a basis and terminology to unify the existing formats of the IDA study and set up the essential background to achieve the above-mentioned objectives.

### 2.3 Fundamentals of single-record IDAs

As a first step, let us clearly define all the terms that we need, and start building our methodology using as a fundamental block the concept of scaling an acceleration time history.

Assume we are given a single acceleration time-history, selected from a ground motion database, which will be referred to as the base, “as-recorded” (although it may have been pre-processed by seismologists, e.g., baseline corrected, filtered and rotated), unscaled accelerogram  $\mathbf{a}_I$ , a vector with elements  $a_1(t_i)$ ,  $t_i = 0, t_1, \dots, t_{n-1}$ . To account for more severe or milder ground motions, a simple transformation is introduced by uniformly scaling up or down the amplitudes by a scalar  $\lambda \in [0, +\infty)$ :  $\mathbf{a}_\lambda = \lambda \cdot \mathbf{a}_I$ . Such an operation can also be conveniently thought of as scaling the elastic acceleration spectrum by  $\lambda$  or equivalently, in the Fourier domain, as scaling by  $\lambda$  the amplitudes across all frequencies while keeping phase information intact.

**Definition 1.** *The SCALE FACTOR (SF) of a scaled accelerogram,  $\mathbf{a}_\lambda$ , is the non-negative scalar  $\lambda \in [0, +\infty)$  that produces  $\mathbf{a}_\lambda$  when multiplicatively applied to the unscaled (natural) acceleration time-history  $\mathbf{a}_I$ .*

Note how the SF constitutes a one-to-one mapping from the original accelerogram to all its scaled images. A value of  $\lambda = 1$  signifies the natural accelerogram,  $\lambda < 1$  is a scaled-down accelerogram, while  $\lambda > 1$  corresponds to a scaled-up one.

Although the SF is the simplest way to characterize the scaled images of an accelerogram it is by no means convenient for engineering purposes as it offers no information of the real “power” of the scaled record and its effect on a given structure. Of more practical use would be a measure that would map to the SF one-to-one, yet would be more informative, in the sense of better relating to its damaging potential.

**Definition 2.** *A MONOTONIC SCALABLE GROUND MOTION INTENSITY MEASURE (or simply intensity measure, IM) of a scaled accelerogram,  $\mathbf{a}_\lambda$ , is a non-negative scalar  $IM \in [0, +\infty)$  that constitutes a function,  $IM = f_{\mathbf{a}_I}(\lambda)$ , that depends on the unscaled accelerogram,  $\mathbf{a}_I$ , and is monotonically increasing with the scale factor,  $\lambda$ .*

While many quantities have been proposed to characterize the “intensity” of a ground motion record, it may not always be apparent how to scale them, e.g., Moment Magnitude, Duration, or Modified Mercalli Intensity; they must be designated as non-scalable. Common examples of scalable *IMs* are the Peak Ground Acceleration (*PGA*), Peak Ground Velocity, the  $\xi = 5\%$  damped Spectral Acceleration at the structure’s first-mode period ( $S_a(T_1, 5\%)$ ), and the normalized factor  $R = \lambda/\lambda_{\text{yield}}$  (where  $\lambda_{\text{yield}}$  signifies, for a given record and structural model, the lowest scaling needed to cause yielding) which is numerically equivalent to the yield reduction *R*-factor (e.g., Chopra, 1995) for, for example, bilinear SDOF systems (see later section). These *IMs* also have the property of being proportional to the *SF* as they satisfy the relation  $IM_{\text{prop}} = \lambda \cdot f_{a_1}$ . On the other hand the quantity  $S_{am}(T_1, \xi, b, c, d) = [S_a(T_1, \xi)]^b \cdot [S_a(cT_1, \xi)]^d$  proposed by Shome and Cornell (1999) and Mehanny and Deierlein (2000) is scalable and monotonic but non-proportional, unless  $b+d=1$ . Some non-monotonic *IMs* have been proposed, such as the inelastic displacement of a nonlinear oscillator by Luco and Cornell (2004), but will not be focused upon, so *IM* will implicitly mean monotonic and scalable hereafter unless otherwise stated.

Now that we have the desired input to subject a structure to, we also need some way to monitor its *state*, its response to the seismic load.

**Definition 3.** DAMAGE MEASURE (*DM*) or STRUCTURAL STATE VARIABLE is a non-negative scalar  $DM \in [0, +\infty]$  that characterizes the additional response of the structural model due to a prescribed seismic loading.

In other words a *DM* is an observable quantity that is part of, or can be deduced from, the output of the corresponding nonlinear dynamic analysis. Possible choices could be maximum base shear, node rotations, peak story ductilities, various proposed damage indices (e.g., a global cumulative hysteretic energy, a global Park–Ang index (Ang and De Leon, 1997) or the stability index proposed by Mehanny and Deierlein, 2000), peak roof drift  $\theta_{\text{roof}}$ , the floor peak interstory drift angles  $\theta_1, \dots, \theta_n$  of an  $n$ -story structure, or their maximum, the maximum peak interstory drift angle  $\theta_{\text{max}} = \max(\theta_1, \dots, \theta_n)$ . Selecting a suitable *DM* depends on the application and the structure itself; it may be desirable to use two or more *DMs* (all resulting from the same nonlinear analyses) to assess different response characteristics, limit-states or modes of failure of interest in a PBEE assessment. If the damage to non-structural contents in a multi-story frame needs to be assessed, the peak floor accelerations are the obvious choice. On the other hand, for structural damage of frame buildings,  $\theta_{\text{max}}$  relates well to joint rotations and both global and local story collapse, thus becoming a strong *DM* candidate. The latter, expressed in terms of the total drift, instead of the effective drift which would take into account the building tilt, (see Prakash et al., 1992, pg.88) will be our choice of *DM* for most illustrative cases here, where foundation rotation and column shortening are not severe.

The structural response is often a signed scalar; usually, either the absolute value is used or the magnitudes of the negative and the positive parts are separately considered. Now we are able to define the IDA.

**Definition 4.** A SINGLE-RECORD IDA STUDY is a dynamic analysis study of a given structural model parameterized by the scale factor of the given ground motion time history.

Also known simply as Incremental Dynamic Analysis (*IDA*) or Dynamic Pushover (*DPO*), it involves a series of dynamic nonlinear runs performed under scaled images of an accelerogram, whose *IMs* are, ideally, selected to cover the whole range from elastic to nonlinear and finally to collapse of the structure. The purpose is to record *DMs* of the structural model at each level *IM* of the scaled ground motion, the resulting response values often being plotted versus the intensity level as continuous curves.

**Definition 5.** An IDA CURVE is a plot of a state variable (*DM*) recorded in an IDA study versus one or more *IMs* that characterize the applied scaled accelerogram.

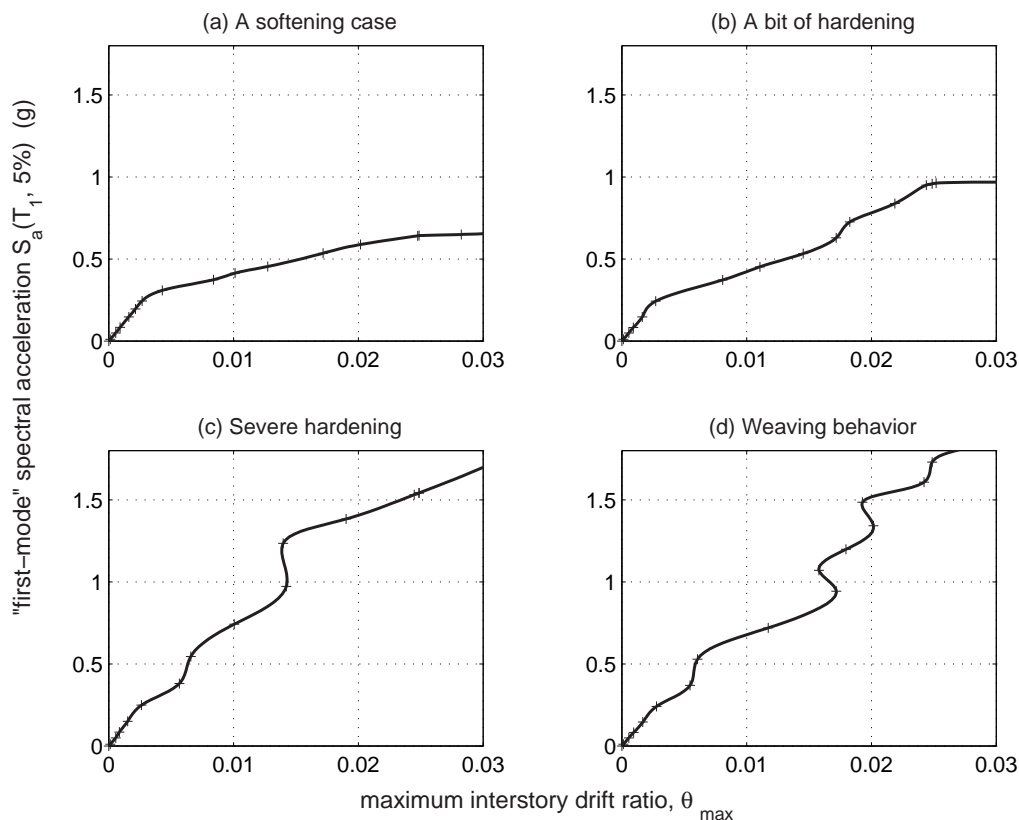


**Figure 2.2:** IDA curves of a  $T_1 = 1.8$  sec, 5-story steel braced frame subjected to 4 different records.

An IDA curve can be realized in two or more dimensions depending on the number of the *IMs*. Obviously at least one must be scalable and it is such an *IM* that is used in the conventional two-dimensional (2D) plots that we will focus on hereafter. As per standard engineering practice such plots often appear “upside-down” as the independent variable is the *IM* which is considered analogous to “force” and plotted on the vertical axis (Figure 2.1(a)) as in stress-strain, force-deformation or SPO graphs. As is evident, the results of an IDA study can be presented in a multitude of different IDA curves, depending on the choices of *IMs* and *DM*.

To illustrate the IDA concept we will use several MDOF and SDOF models as examples in the following sections. In particular the MDOFs used are a  $T_1 = 4$  sec 20-story steel-moment resisting frame (Luco and Cornell, 2000) with ductile members and connections, including a first-order treatment of global geometric nonlinearities (P- $\Delta$  effects), a  $T_1 = 2.2$  sec 9-story and a  $T_1 = 1.3$  sec 3-story steel-moment resisting frame (Luco and Cornell, 2000) with ductile members, fracturing connections and P- $\Delta$  effects, and a  $T_1 = 1.8$  sec 5-story steel chevron-braced frame with ductile members and connections and realistically buckling braces including P- $\Delta$  effects (Bazzurro and Cornell, 1994b).

## 2.4 Looking at an IDA curve: Some general properties

The IDA study is *accelerogram* and *structural model* specific; when subjected to different ground motions a model will often produce quite dissimilar responses that are difficult to predict a priori. Notice, for example, Figure 2.2(a–d) where a 5-story braced frame exhibits responses ranging from a gradual degradation towards collapse to a rapid, non-monotonic, back-and-forth twisting behavior. Each graph illustrates the *demands* imposed upon the structure by each ground motion record at different intensities, and they are quite intriguing in both their similarities and dissimilarities.

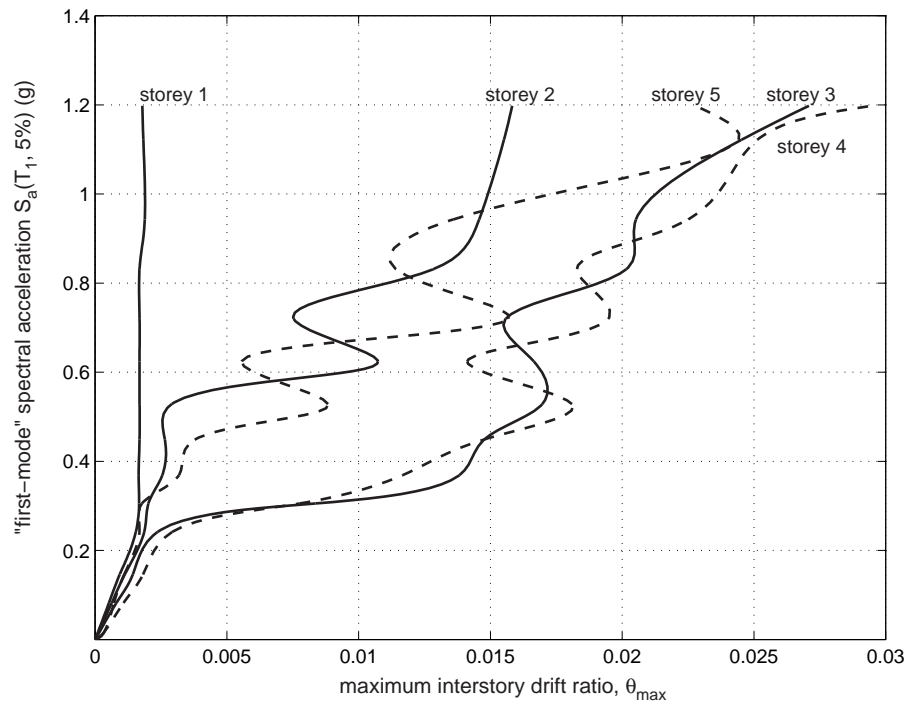


**Figure 2.3:** IDA curves of peak interstory drifts for each floor of a  $T_1 = 1.8$  sec 5-story steel braced frame. Notice the complex “weaving” interaction where extreme softening of floor 2 acts as a fuse to relieve those above (3,4,5).

All curves exhibit a distinct elastic linear region that ends at  $S_a^{\text{yield}}(T_1, 5\%) \approx 0.2g$  and  $\theta_{\text{max}}^{\text{yield}} \approx 0.2\%$  when the first brace-buckling occurs. Actually, any structural model with initially linearly elastic elements will display such a behavior, which terminates when the first nonlinearity comes into play, i.e., when any element reaches the end of its elasticity. The slope  $IM/DM$  of this segment on each IDA curve will be called its elastic “stiffness” for the given  $DM$ ,  $IM$ . It typically varies to some degree from record to record but it will be the same across records for SDOF systems and even for MDOF systems if the  $IM$  takes into account the higher mode effects (i.e., [Luco and Cornell, 2004](#)).

Focusing on the other end of the curves in Figure 2.2, notice how they terminate at different levels of  $IM$ . Curve (a) sharply “softens” after the initial buckling and accelerates towards large drifts and eventual collapse. On the other hand, curves (c) and (d) seem to weave around the elastic slope; they follow closely the familiar *equal displacement* rule, i.e., the empirical observation that for moderate period structures, inelastic global displacements are generally approximately equal to the displacements of the corresponding elastic model (e.g., [Veletsos and Newmark, 1960](#)). The twisting patterns that curves (c) and (d) display in doing so are successive segments of “softening” and “hardening”, regions where the local slope or “stiffness” decreases with higher  $IM$  and others where it increases. In engineering terms this means that at times the structure experiences acceleration of the rate of  $DM$  accumulation and at other times a deceleration occurs that can be powerful enough to momentarily stop the  $DM$  accumulation or even reverse it, thus locally pulling the IDA curve to relatively lower  $DM$ s and making it a non-monotonic function of the  $IM$  (Figure 2.2(d)). Eventually, assuming the model allows for some collapse mechanism and the  $DM$  used can track it, a final softening segment occurs when the structure accumulates  $DM$  at increasingly higher rates, signaling the onset of *dynamic instability*. This is defined analogously to static instability, as the point where deformations increase in an unlimited manner for vanishingly small increments in the  $IM$ . The curve then flattens out in a plateau of the maximum value in  $IM$  as it reaches the

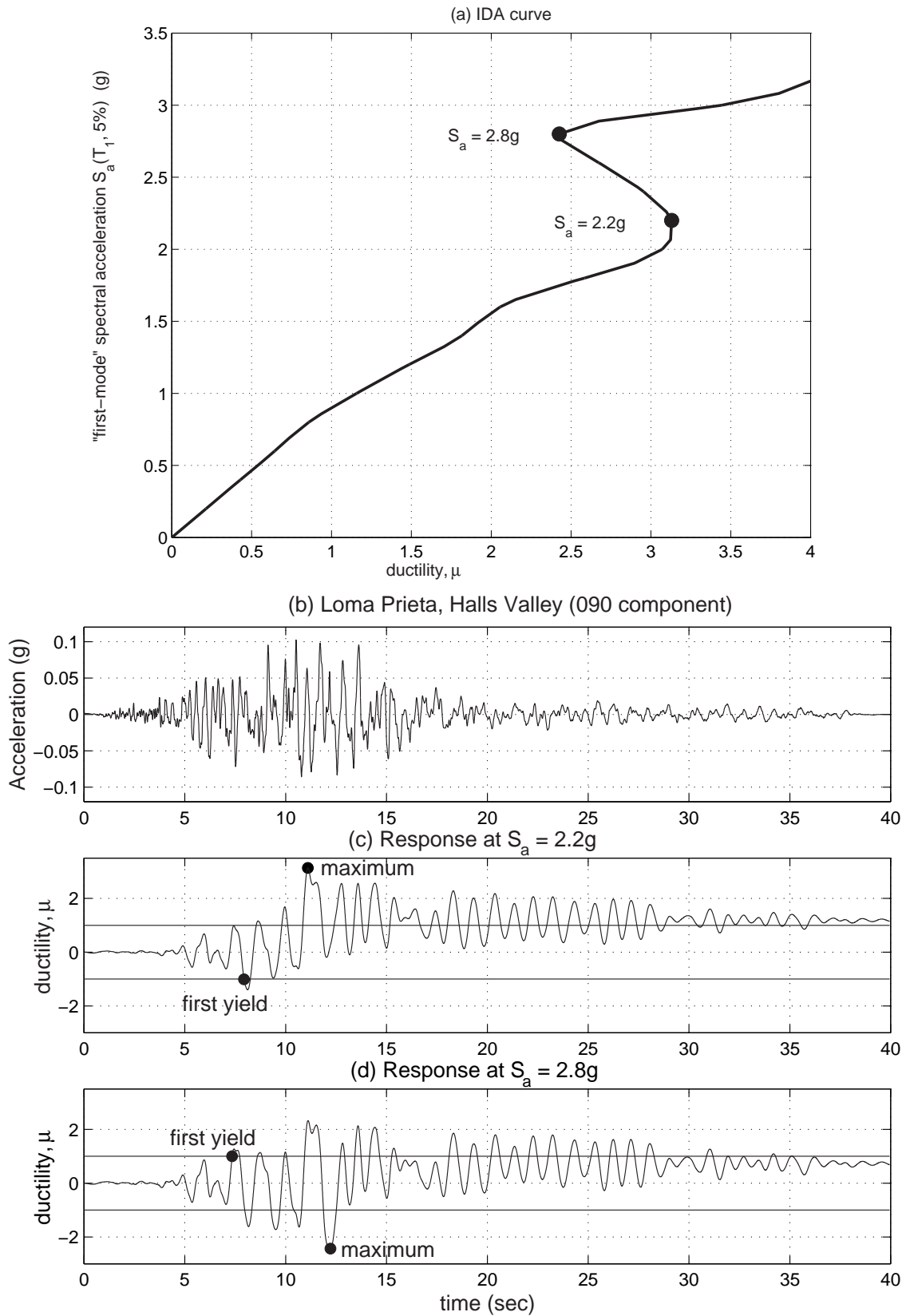


**Figure 2.4:** Ductility response of a  $T = 1$  sec, elasto-plastic oscillator at multiple levels of shaking. Earlier yielding in the stronger ground motion leads to a lower absolute peak response.

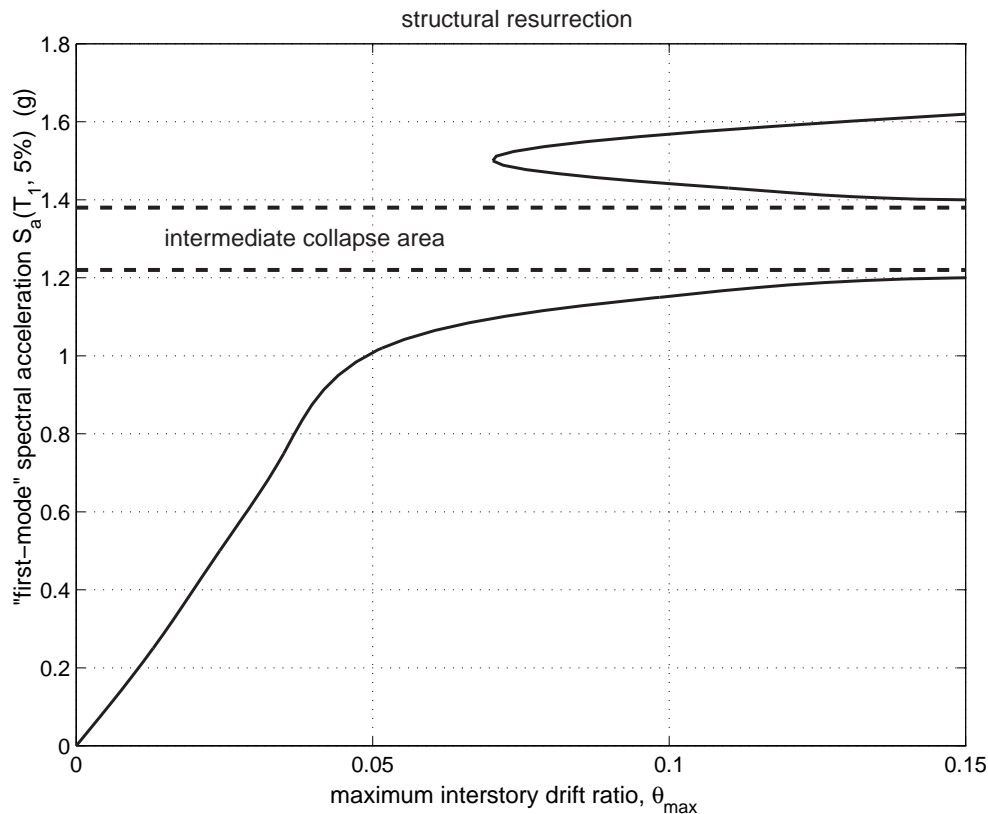


**Figure 2.5:** Structural resurrection on the IDA curve of a  $T_1 = 1.3$  sec, 3-story steel moment-resisting frame with fracturing connections.

*flatline* and *DM* moves towards “infinity” (Figure 2.2(a,b)). Although the examples shown are based on  $S_a(T_1, 5\%)$  and  $\theta_{\max}$ , these modes of behavior are observable for a wide choice of *DMs* and *IMs*.

Hardening in IDA curves is not a novel observation, having been reported before even for simple bilinear elastic-perfectly-plastic systems, e.g., by Chopra (1995, pg.257-259). Still it remains counter-intuitive that a system that showed high response at a given intensity level, may exhibit the same or even lower response when subjected to higher seismic intensities due to excessive hardening. But it is the *pattern* and the *timing* rather than just the intensity that make the difference. As the accelerogram is scaled up, weak response cycles in the early part of the response time-history become strong enough to inflict damage (yielding) thus altering the properties of the structure for the subsequent, stronger cycles. For multi-story buildings, a stronger ground motion may lead to earlier yielding of one floor which in turn acts as a fuse to relieve another (usually higher) one, as in Figure 2.3. Even simple oscillators when caused to yield in an earlier cycle, may be proven less responsive in later cycles that had previously caused higher *DM* values (Figure 2.4), perhaps due to “period elongation”. The same phenomena account for the *structural resurrection*, an extreme case of hardening, where a system is pushed all the way to global collapse (i.e., the analysis code cannot converge, producing “numerically infinite” *DMs*) at some *IM*, only to reappear as non-collapsing at a higher intensity level, displaying high response but still standing (e.g., Figure 2.5).

As the complexity of even the 2D IDA curve becomes apparent, it is only natural to examine the properties of the curve as a mathematical entity. Assuming a monotonic *IM* the IDA curve becomes a *function* ( $[0, +\infty) \rightarrow [0, +\infty)$ ), i.e., any value of *IM* produces a single value *DM*, while for any given *DM* value there is at least one or more (in non-monotonic IDA curves) *IMs* that generate it, since the mapping is not necessarily one-to-one. Also, the IDA curve is not necessar-

ily smooth as the  $DM$  is often defined as a maximum or contains absolute values of responses, making it non-differentiable by definition. Even more, it may contain a (hopefully finite) number of discontinuities, due to multiple excursions to collapse and subsequent resurrections.

## 2.5 Capacity and limit-states on single IDA curves

Performance levels or limit-states are important ingredients of Performance Based Earthquake Engineering (PBEE), and the IDA curve contains the necessary information to assess them. But we need to define them in a less abstract way that makes sense on an IDA curve, i.e., by a statement or a *rule* that when satisfied, signals reaching a limit-state. For example, Immediate Occupancy (FEMA, 2000a,b) is a structural performance level that has been associated with reaching a given  $DM$  value, usually in  $\theta_{\max}$  terms, while (in FEMA 350, FEMA, 2000a, at least) Global Collapse is related to the  $IM$  or  $DM$  value where dynamic instability is observed. A relevant issue that then appears is what to do when multiple points (Figure 2.6(a,b)) satisfy such a rule? Which one is to be selected?

The cause of multiple points that can satisfy a limit-state rule is mainly the hardening issue and, in its extreme form, structural resurrection. In general, one would want to be conservative and consider the lowest, in  $IM$  terms, point that will signal the limit-state. Generalizing this concept to the whole IDA curve means that we will discard its portion “above” the first (in  $IM$  terms) flatline and just consider only points up to this first sign of dynamic instability.

Note also that for most of the discussion we will be equating dynamic instability to numerical instability in the prediction of collapse. Clearly the non-convergence of the time-integration scheme is perhaps the safest and maybe the only numerical equivalent of the actual phenomenon of dynamic collapse. But, as in all models, this one can suffer from the quality of the numerical code, the stepping of the integration and even the round-off error. Therefore, we will assume that such matters are taken care of as well as possible to allow for accurate enough predictions. That being said, let us set forth the most basic rules used to define a limit-state.

First comes the *DM-based rule*, which is generated from a statement of the format: “If  $DM \geq C_{DM}$  then the limit-state is exceeded” (Figure 2.6(a)). The underlying concept is usually that  $DM$  is a damage indicator, hence, when it increases beyond a certain value the structural model is assumed to be in the limit-state. Such values of  $C_{DM}$  can be obtained through experiments, theory or engineering experience, and they may not be deterministic but have a probability distribution. An example is the  $\theta_{\max} = 2\%$  limit that signifies the Immediate Occupancy structural performance level for steel moment-resisting frames (SMRFs) with type-1 connections in the FEMA guidelines (FEMA, 2000b). Also the approach used by Mehanny and Deierlein (2000) is another case where a structure-specific damage index is used as  $DM$  and when its reciprocal is greater than unity, collapse is presumed to have occurred. Such limits may have randomness incorporated, for example, FEMA 350 (FEMA, 2000a) defines a local collapse limit-state by the value of  $\theta_{\max}$  that induces a connection rotation sufficient to destroy the gravity load carrying capacity of the connection. This is defined as a random variable based on tests, analysis and judgment for each connection type. Even a unique  $C_{DM}$  value may imply multiple limit-state points on an IDA curve (e.g., Figure 2.6(a)). This ambiguity can be handled by an ad hoc, specified procedure (e.g., by conservatively defining the limit-state point as the lowest  $IM$ ), or by explicitly recognizing the multiple regions conforming and non-conforming with the performance level. The  $DM$ -based rules have the advantage of simplicity and ease of implementation, especially for performance levels other than collapse. In the case of collapse capacity though, they may actually be a sign of model deficiency. If the model is realistic enough it ought to explicitly contain such information, i.e., show a collapse by non-convergence instead of by a finite  $DM$  output. Still, one has to recognize that such models can be quite complicated and resource-intensive, while numerics can often be unstable. Hence  $DM$ -based collapse limit-state rules can be quite useful. They also have the advantage of being

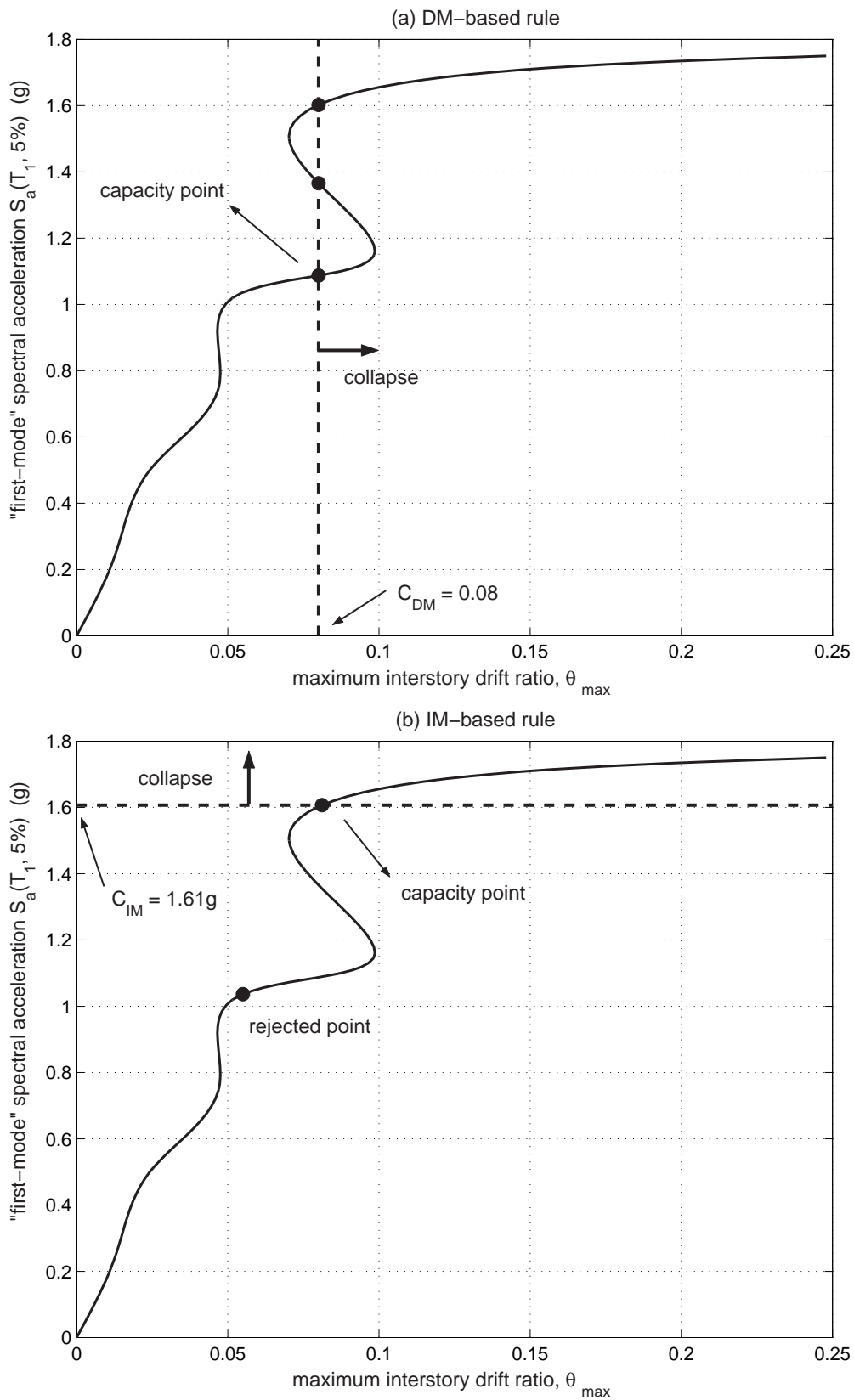


**Figure 2.6:** Two different rules producing multiple capacity points for a  $T_1 = 1.3$  sec, 3-story steel moment-resisting frame with fracturing connections. The *DM* rule, where the *DM* is  $\theta_{max}$ , is set at  $C_{DM} = 0.08$  and the *IM* rule uses the 20% slope criterion.

consistent with other less severe limit-states which are more naturally identified in  $DM$  terms, e.g.,  $\theta_{\max}$ .

The alternative *IM-based rule*, is primarily generated from the need to better assess collapse capacity, by having a single point on the IDA curve that clearly divides it to two regions, one of non-collapse (lower  $IM$ ) and one of collapse (higher  $IM$ ). For monotonic  $IM$ s, such a rule is generated by a statement of the form: “If  $IM \geq C_{IM}$  then the limit-state is exceeded” (Figure 2.6(b)). A major difference with the previous category is the difficulty in prescribing a  $C_{IM}$  value that signals collapse for all IDA curves, so it has to be done individually, curve by curve. Still, the advantage is that it clearly generates a single collapse region, and the disadvantage is the difficulty of defining such a point for each curve in a consistent fashion. In general, such a rule results in both  $IM$  and  $DM$  descriptions of capacity. A special (extreme) case is taking the “final” point of the curve as the capacity, i.e., by using the (lowest) flatline to define capacity (in  $IM$  terms), where all of the IDA curve up to the first appearance of dynamic instability is considered as non-collapse.

The FEMA (2000a) 20% tangent slope approach is, in effect, an  $IM$ -based rule; the *last* point on the curve with a tangent slope equal to 20% of the elastic slope is defined to be the capacity point. The idea is that the flattening of the curve is an indicator of dynamic instability (i.e., the  $DM$  increasing at ever higher rates and accelerating towards “infinity”). Since “infinity” is not a possible numerical result, we content ourselves with pulling back to a rate of  $\theta_{\max}$  increase equal to five times the initial or elastic rate, as the place where we mark the capacity point. Care needs to be exercised, as the possible “weaving” behavior of an IDA curve can provide several such points where the structure seems to head towards collapse, only to recover at a somewhat higher  $IM$  level, as in Figure 2.6(b); in principle, these lower points should thus be discarded as capacity candidates. Also the non-smoothness of the actual curve may prove to be a problem. As mentioned above, the IDA curve is at best piecewise smooth, but even so, approximate tangent slopes can be assigned to every point along it by employing a smooth interpolation. For sceptics this may also be thought of as a discrete derivative on a grid of points that is a good “engineering” approximation to the “rate-of-change”.

The above mentioned simple rules are the building blocks to construct composite rules, i.e., composite logical clauses of the above types, most often joined by logical OR operators. For example, when a structure has several collapse modes, not detectable by a single  $DM$ , it is advantageous to detect global collapse with an OR clause for each individual mode. An example is offshore platforms where pile or soil failure modes are evident in deck drift while failures of braces are more evident in maximum peak inter-tier drift. The first — in  $IM$  terms — event that occurs is the one that governs collapse capacity. Another case is Global Collapse capacity, which as defined by FEMA in FEMA (2000a,b) is in fact an OR conjunction of the 20% slope  $IM$ -based rule and a  $C_{DM} = 10\%$   $DM$ -based rule, where  $S_d(T_1, 5\%)$  and  $\theta_{\max}$  are the  $IM$  and  $DM$  of choice. If either of the two rules obtains, it defines capacity. This means that the 20% stiffness detects impending collapse, while the 10% cap guards against excessive values of  $\theta_{\max}$ , indicative of regions where the model may not be trustworthy. As a  $DM$  description of capacity is proposed, this definition may suffer from inaccuracies, since close to the flatline a wide range of  $DM$  values may correspond to only a small range of  $IM$ s, thus making the actual value of  $DM$  selected sensitive to the quality of IDA curve tracing and to the (ad hoc) 20% value. If, on the other hand, an  $IM$  description is used, the rule becomes more robust. This is a general observation for collapse capacity; it appears that it can be best expressed in  $IM$  terms.

## 2.6 Multi-record IDAs and their summary

As should be evident by now, a single-record IDA study cannot fully capture the behavior a building may display in a future event. The IDA can be highly dependent on the record chosen, so a sufficient number of records will be needed to cover the full range of responses. Hence, we have

to resort to subjecting the structural model to a suite of ground motion records.

**Definition 6.** A MULTI-RECORD IDA STUDY is a collection of single-record IDA studies of the same structural model, under different accelerograms.

Such a study, correspondingly produces sets of IDA curves, which by sharing a common selection of *IMs* and the same *DM*, can be plotted on the same graph, as in Figure 2.7(a) for a 5-story steel braced frame.

**Definition 7.** An IDA CURVE SET is a collection of IDA curves of the same structural model under different accelerograms, that are all parameterized on the same *IMs* and *DM*.

While each curve, given the structural model and the ground motion record, is a completely defined deterministic entity, if we wish to take into account the inherent randomness with respect to what record the building might experience, we have to bring a probabilistic characterization into play. The IDA given the structural model and a statistical population of records is no longer deterministic; it is a *random line*, or a random function  $DM = f(IM)$  (for a single, monotonic *IM*). Then, just as we are able to summarize a suite of records by having, for example, mean, median, and 16%, 84% response spectra, so we can define mean, median and 16%, 84% IDA curves (e.g., Figure 2.7(b)) to (marginally) summarize an IDA curve set. We, therefore, need methods for estimating statistics of a sample of 2D random lines (assuming a single *IM*), a topic of Functional Data Analysis (Ramsay and Silverman, 1996). They conveniently fall in two main categories.

First are the parametric methods. In this case a parametric model of the *DM* given the *IM* is assumed, each line is separately fit, providing a sample of parameter values, and then statistics of the parameters are obtained. Alternatively a parametric model of the median *DM* given the *IM* can be fit to all the lines simultaneously. As an example, consider the 2-parameter, power-law model  $\theta_{\max} = \alpha \cdot [S_a(T_1, 5\%)]^\beta$  introduced by Shome and Cornell (1999), which under the well-documented assumption of lognormality of the conditional distribution of  $\theta_{\max}$  given  $S_a(T_1, 5\%)$ , often provides a simple yet powerful description of the curves, allowing some important analytic results to be obtained (Jalayer and Cornell, 2002; Cornell et al., 2002). This is a general property of parametric methods; while they lack the flexibility to accurately capture each curve, they make up by allowing simple descriptions to be extracted.

On the other end of the spectrum are the non-parametric methods, which mainly involve the use of “scatterplot smoothers” like the running mean, running median, LOESS or the smoothing spline (Hastie and Tibshirani, 1990). Perhaps the simplest of them all, the running mean with a zero-length window (or cross-sectional mean), involves simply calculating values of the *DM* at each level of *IM* and then finding the average and standard deviation of *DM* given the *IM* level. This works well up to the point where the first IDA curve reaches capacity, when *DM* becomes infinite, and so does the mean IDA curve. Unfortunately most smoothers suffer from the same problem, but the cross-sectional median, or cross-sectional fractile is, in general, more robust. Instead of calculating means at each *IM* level, we now calculate sample medians, 16% and 84% fractiles, which become infinite only when collapse occurs in 50%, 84% and 16% of the records respectively. Another advantage is that under suitable assumptions (e.g., continuity and monotonicity of the curves), the line connecting the  $x\%$  fractiles of *DM* given *IM* is the same as the one connecting the  $(100 - x)\%$  fractiles of *IM* given *DM*. Furthermore, this scheme fits nicely with the well-supported assumption of lognormal distribution of  $\theta_{\max}$  given  $S_a(T_1, 5\%)$ , where the median is the natural “central value” and the 16%, 84% fractiles correspond to the median times  $e^{\pm \text{dispersion}}$ , where “dispersion” is the standard deviation of the logarithms of the values (Jalayer and Cornell, 2002).

Finally, a variant for treating collapses is proposed by Shome and Cornell (2000), where the conventional moments are used to characterize non-collapses, thus removing the problem of in-

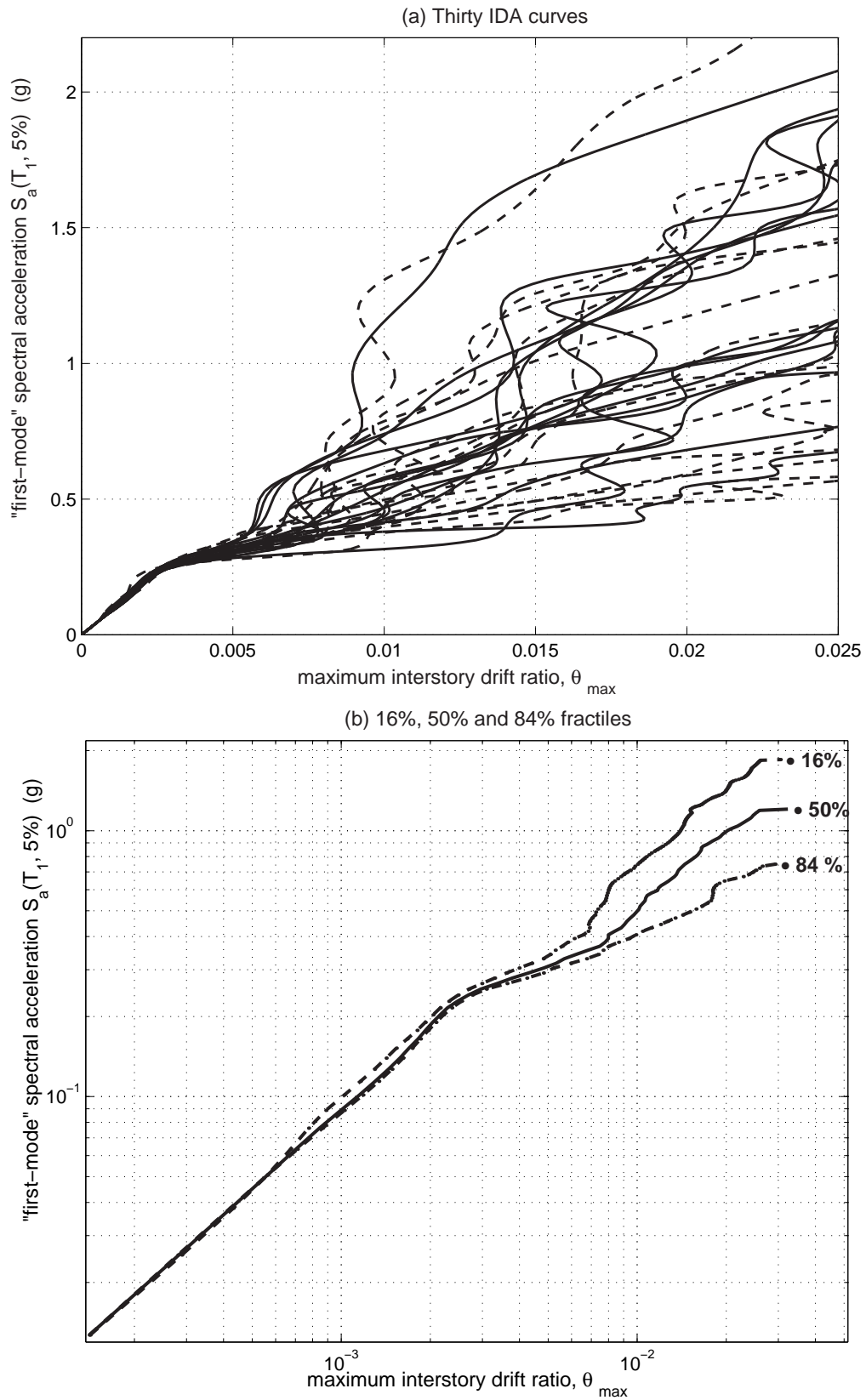


**Figure 2.7:** An IDA study for thirty records on a  $T_1 = 1.8$  sec, 5-story steel braced frame, showing (a) the thirty individual curves and (b) their summary (16%, 50% and 84%) fractile curves (in log-log scale).

finities, while the probability of collapse given the *IM* is summarized separately by a logistic regression.

A simpler, yet important problem is the summarizing of the capacities of a sample of  $N$  curves, expressed either in *DM* (e.g.,  $\{C_{\theta_{\max}}^i\}$ ,  $i = 1 \dots N$ ) or *IM* (e.g.,  $\{C_{S_a(T_1, 5\%)}^i\}$ ,  $i = 1 \dots N$ ) terms. Since there are neither random lines nor infinities involved, the problem reduces to conventional sample statistics, so we can get means, standard deviations or fractiles as usual. Still, the observed lognormality in the capacity data, often suggests the use of the median (e.g.,  $\hat{C}_{S_a(T_1, 5\%)}$  or  $\hat{C}_{\theta_{\max}}$ ), estimated either as the 50% fractile or as the antilog of the mean of the logarithms, and the standard deviation of the logarithms as dispersion. Finally, when considering limit-state probability computations (see section below), one needs to address potential dependence (e.g., correlation) between capacity and demand. Limited investigation to date has revealed little if any systematic correlation between *DM* capacity and *DM* demand (given *IM*).

## 2.7 The IDA in a PBEE framework

The power of the IDA as an analysis method is put to use well in a probabilistic framework, where we are concerned with the estimation of the annual likelihood of the event that the demand exceeds the limit-state or capacity  $C$ . This is the likelihood of exceeding a certain limit-state, or of failing a performance level (e.g., Immediate Occupancy or Collapse Prevention in FEMA, 2000a), within a given period of time. The calculation can be summarized in the framing equation adopted by the Pacific Earthquake Engineering Center (Cornell and Krawinkler, 2000)

$$\lambda(\mathbf{DV}) = \iint G(\mathbf{DV}|\mathbf{DM}) |dG(\mathbf{DM}|\mathbf{IM})| |d\lambda(\mathbf{IM})| \quad (2.1)$$

in which  $\mathbf{IM}$ ,  $\mathbf{DM}$  and  $\mathbf{DV}$  are vectors of intensity measures, damage measures and “decision variables” respectively. In this paper we have generally used scalar *IM* (e.g.,  $S_a(T_1, 5\%)$ ) and *DM* (e.g.,  $\theta_{\max}$ ) for the limit-state case of interest. The decision variable here is simply a scalar “indicator variable”:  $DV = 1$  if the limit-state is exceeded (and zero otherwise).  $\lambda(\mathbf{IM})$  is the conventional hazard curve, i.e., the mean annual frequency of *IM* exceeding, say,  $x$ . The quantity  $|d\lambda(x)| = |d\lambda(x)/dx| dx$  is its differential (i.e.,  $|d\lambda(x)/dx|$  is the mean rate density).  $|dG(\mathbf{DM}|\mathbf{IM})|$  is the differential of the (conditional) complementary cumulative distribution function (CCDF) of *DM* given *IM*, or  $f_{DM|IM}(y|x) dy$ . In the previous sections we discussed the statistical characterization of the random IDA lines. These distributions are precisely this characterization of  $|dG(\mathbf{DM}|\mathbf{IM})|$ . Finally in the limit-state case, when on the left-hand side of Equation (2.1) we seek  $\lambda(DV=1) = \lambda(0)$ ,  $G(0|\mathbf{DM})$  becomes simply the probability that the capacity  $C$  is less than some level of the *DM*, say,  $y$ ; so  $G(0|\mathbf{DM}) = F_C(y)$ , where  $F_C(y)$  is the cumulative distribution function of  $C$ , i.e., the statistical characterization of capacity, also discussed at the end of the previous section. In the global collapse case, capacity estimates also come from IDA analyses. In short, save for the seismicity characterization,  $\lambda(\mathbf{IM})$ , given an intelligent selection of *IM*, *DM* and structural model, the IDA produces, in arguably the most comprehensive way, precisely the information needed both for PBEE demand characterization and for global collapse capacity characterization.

## 2.8 Scaling legitimacy and *IM* selection

As discussed above, we believe there is useful engineering insight to be gained by conducting individual and sets of IDA studies. However, concern is often expressed about the “validity” of *DM* results obtained from records that have been scaled (up or down), an operation that is not uncommon both in research and in practice. While not always well expressed, the concern usually has something to do with “weaker” records not being “representative” of “stronger” ones. The

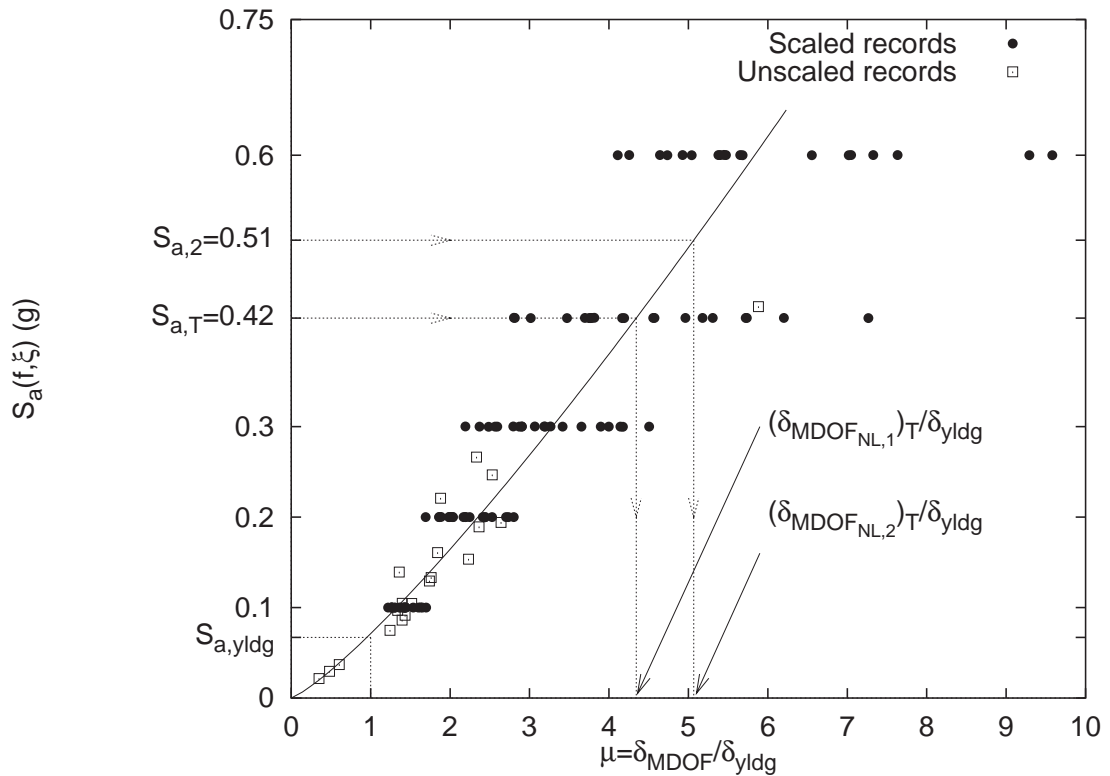


**Figure 2.8:** Roof ductility response of a  $T_1 = 1$  sec, MDOF steel frame subjected to 20 records, scaled to 5 levels of  $S_a(T_1, 5\%)$ . The unscaled record response and the power-law fit are also shown for comparison (from Bazzurro et al., 1998).

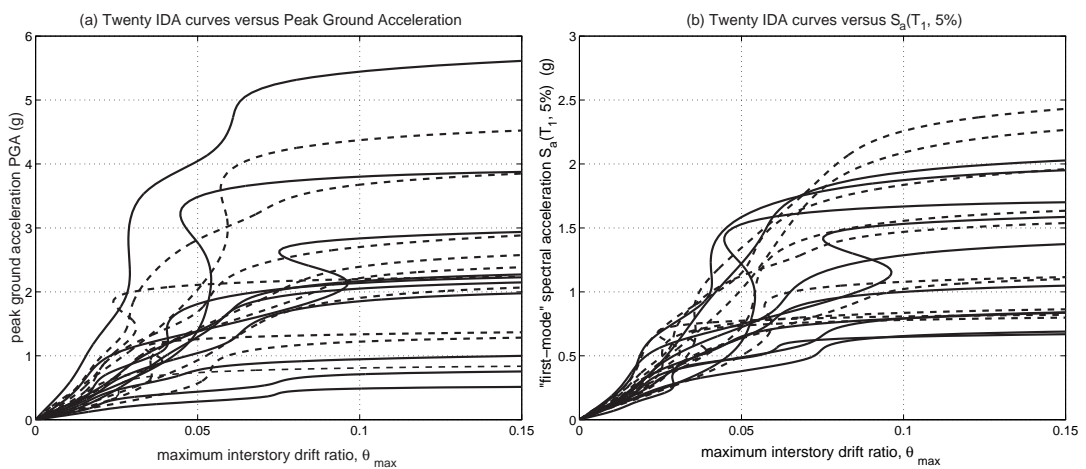


**Figure 2.9:** IDA curves for a  $T_1 = 2.2$  sec, 9-story steel moment-resisting frame with fracturing connections plotted against (a)  $PGA$  and (b)  $S_a(T_1, 5\%)$ .

issue can be more precisely stated in the context of the last two sections as: will the median (or any other statistic of)  $DM$  obtained from records that have been scaled to some level of  $IM$  estimate accurately the median  $DM$  of a population of unscaled records all with that same level of  $IM$ . Because of current record catalog limitations, where few records of any single given  $IM$  level can be found, and because we have interest usually in a range of  $IM$  levels (e.g., in integrations such as Equation (2.1)), it is both more practical and more complete to ask: will the (regression-like) function median  $DM$  versus  $IM$  obtained from scaled records (whether via IDAs or otherwise) estimate well that same function obtained from unscaled records? There is a growing body of literature related to such questions that is too long to summarize here (e.g., [Shome and Cornell, 1998, 1999](#)). An example of such a comparison is given in Figure 2.8 from [Bazzurro et al. \(1998\)](#), where the two regressions are so close to one another that only one was plotted by the authors. Suffice it to say that, in general, the answer to the question depends on the structure, the  $DM$ , the  $IM$  and the population in mind. For example, the answer is “yes” for the case pictured in Figure 2.8, i.e., for a moderate period (1 sec) steel frame, for which  $DM$  is maximum interstory drift and  $IM$  is first-mode-period spectral acceleration, and for a fairly general class of records (moderate to large magnitudes,  $M$ , all but directivity-influenced distances,  $R$ , etc.). On the other hand, for all else equal except  $IM$  defined now as  $PGA$ , the answer would be “no” for this same case. Why? Because such a (first-mode dominated) structure is sensitive to the strength of the frequency content near its first-mode frequency, which is well characterized by the  $S_a(1 \text{ sec}, 5\%)$  but not by  $PGA$ , and as magnitude changes, spectral shape changes implying that the average ratio of  $S_a(1 \text{ sec}, 5\%)$  to  $PGA$  changes with magnitude. Therefore the scaled-record median drift versus  $PGA$  curve will depend on the fractions of magnitudes of different sizes present in the sample, and may or may not represent well such a curve for any (other) specified population of magnitudes. On the other hand, the  $IM$  first-mode spectral acceleration will no longer work well for a tall, long-period building that is sensitive to shorter periods, again because of spectral shape dependence on magnitude.

There are a variety of questions of efficiency, accuracy and practicality associated with the wise choice of the  $IM$  for any particular application (e.g., [Luco and Cornell, 2004](#)), but it can generally be said here that if the  $IM$  has been chosen such that the regression of  $DM$  jointly on  $IM$ ,  $M$  and  $R$  is found to be effectively independent of  $M$  and  $R$  (in the range of interest), then, yes, scaling of records will provide good estimates of the distribution of  $DM$  given  $IM$ . Hence we can conclude that scaling is indeed (in this sense) “legitimate”, and finally that IDAs provide accurate estimates of  $DM$  given  $IM$  statistics (as required, for example, for PBEE use; see [Bazzurro et al. \(1998\)](#), [Shome and Cornell \(1999\)](#)).

IDA studies may also bring a fresh perspective to the larger question of the effective  $IM$  choice. For example, smaller dispersion of  $DM$  given  $IM$  implies that a smaller sample of records and fewer nonlinear runs are necessary to estimate median  $DM$  versus  $IM$ . Therefore, a desirable property of a candidate  $IM$  is small dispersion. Figure 2.9 shows IDAs from a 9-story steel moment-resisting frame in which the  $DM$  is  $\theta_{\max}$  and the  $IM$  is either (a)  $PGA$  or (b)  $S_a(T_1, 5\%)$ . The latter produces a lower dispersion over the full range of  $DM$  values, as the IDA-based results clearly display. Furthermore, the IDA can be used to study how well (with what dispersion) particular  $IM$ s predict collapse capacity; again  $S_a(T_1, 5\%)$  appears preferable to  $PGA$  for this structure as the dispersion of  $IM$  values associated with the “flatlines” is less in the former case.

## 2.9 The IDA versus the $R$ -factor

A popular form of incremental seismic analysis, especially for SDOF oscillators, has been that leading to the yield reduction  $R$ -factor (e.g., [Chopra, 1995](#)). In this case the record is left unscaled, avoiding record scaling concerns; instead, the yield force (or yield deformation, or, in the multi-member MDOF case, the yield stress) of the model is scaled down from that level that

coincides with the onset of inelastic behavior. If both are similarly normalized (e.g., ductility = deformation/yield-deformation and  $R = S_a(T_1, 5\%) / S_a^{\text{yield}}(T_1, 5\%)$ ), the results of this scaling and those of an IDA will be identical for those classes of systems for which such simple structural scaling is appropriate, e.g., most SDOF models, and certain MDOF models without axial-force–moment interaction, without second-or-higher-order geometric nonlinearities, etc. One might argue that these cases of common results are another justification for the legitimacy of scaling records in the IDA. It can be said that the difference between the  $R$ -factor and IDA perspectives is one of design versus assessment. For design one has an allowable ductility in mind and seeks the design yield force that will achieve this; for assessment one has a fixed design (or existing structure) in hand and seeks to understand its behavior under a range of potential future ground motion intensities.

## 2.10 The IDA versus the Nonlinear Static Pushover

The common incremental loading nature of the IDA study and the SPO suggests an investigation of the connection between their results. As they are both intended to describe the same structure, we should expect some correlation between the SPO curve and any IDA curve of the building (Figure 2.1), and even more so between the SPO and the summarized (median) IDA curve, as the latter is less variable and less record dependent. Still, to plot both on the same graph, we should preferably express the SPO in the  $IM$ ,  $DM$  coordinates chosen for the summarized IDA. While some  $DM$ s (e.g.,  $\theta_{\max}$ ) can easily be obtained from both the static and the dynamic analysis, it may not be so natural to convert the  $IM$ s, e.g., base shear to  $S_a(T_1, 5\%)$ . The proposed approach is to adjust the “elastic stiffness” of the SPO to be the same as that of the IDA, i.e., by matching their elastic segments. This can be achieved in the aforementioned example by dividing the base shear by the building mass, which is all that is needed for SDOF systems, times an appropriate factor for MDOF systems.

The results of such a procedure are shown in Figures 2.10(a,b) where we plot the SPO curve, obtained using a first-mode force pattern, versus the median IDA for a 20-story steel moment-resisting frame with ductile connections and for a 5-story steel braced frame using  $S_a(T_1, 5\%)$  and  $\theta_{\max}$  coordinates. Clearly both the IDA and the SPO curves display similar ranges of  $DM$  values. The IDA always rises much higher than the SPO in  $IM$  terms, however. While a quantitative relation between the two curves may be difficult, deserving further study (e.g., [Seneviratna and Krawinkler, 1997](#)), qualitatively we can make some, apparently, quite general observations that permit inference of the approximate *shape* of the median IDA simply by looking at the SPO.

1. By construction, the elastic region of the SPO matches well the IDA, including the first sign of nonlinearity appearing at the same values of  $IM$  and  $DM$  for both.
2. A subsequent reduced, but still non-negative stiffness region of the SPO correlates on the IDA with the approximate “equal-displacement” rule (for moderate-period structures) ([Veletsos and Newmark, 1960](#)), i.e., a near continuation of the elastic regime slope; in fact this near-elastic part of the IDA is often preceded by a *hardening* portion (Figure 2.10(a)). Shorter-period structures will instead display some softening.
3. A negative slope on the SPO translates to a (softening) region of the IDA, which can lead to collapse, i.e., IDA flat-lining (Figure 2.10(a)), unless it is arrested by a non-negative segment of the SPO before it reaches zero in  $IM$  terms (Figure 2.10(b)).
4. A non-negative region of the SPO that follows after a negative slope that has caused a significant  $IM$  drop, apparently presents itself in the IDA as a new, modified “equal-displacement” rule (i.e., an near-linear segment that lies on a secant) that has lower “stiffness” than the elastic (Figure 2.10(b)).

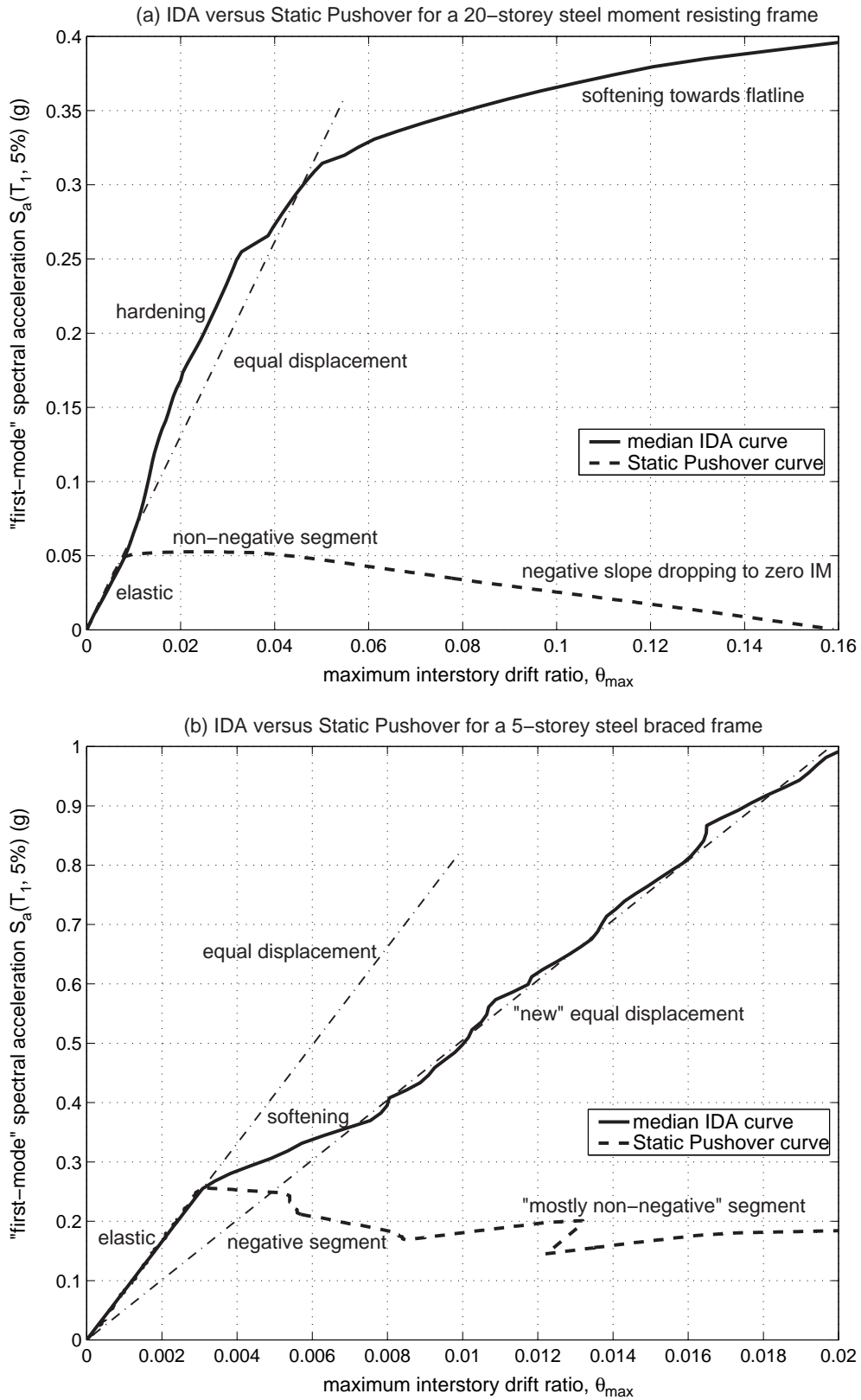


**Figure 2.10:** The median IDA versus the Static Pushover curve for (a) a  $T_1 = 4$  sec, 20-story steel moment-resisting frame with ductile connections and (b) a  $T_1 = 1.8$  sec, 5-story steel braced frame.

## 2.11 IDA Algorithms

Despite the theoretical simplicity of an IDA study, actually performing one can potentially be resource intensive. Although we would like to have an almost continuous representation of IDA curves, for most structural models the sheer cost of each dynamic nonlinear run forces us to think of algorithms designed to select an optimal grid of discrete  $IM$  values that will provide the desired coverage. The density of a grid on the curve is best quantified in terms of the  $IM$  values used, the objectives being: a high *demand resolution*, achieved by evenly *spreading* the points and thus having no gap in our  $IM$  values larger than some tolerance, and a high *capacity resolution*, which calls for a *concentration* of points around the flatline to bracket it appropriately, e.g., by having a distance between the highest (in terms of  $IM$ ) “non-collapsing” run and the lowest “collapsing” run less than some tolerance. Here, by collapsing run we mean a dynamic analysis performed at some  $IM$  level that is determined to have caused collapse, either by satisfying some collapse-rule ( $IM$  or  $DM$  based, or more complex) or simply by failing to converge to a solution. Obviously, if we allow only a fixed number of runs for a given record, these two objectives compete with one another.

In a multi-record IDA study, there are some advantages to be gained by using information from the results of one record to adapt the grid of points to be used on the next. Even without exploiting these opportunities, we can still design efficient methods to tackle each record separately that are simpler and more amenable to parallelization on multiple processors. Therefore we will focus on the *tracing* of single IDA curves.

Probably the simplest solution is a *stepping* algorithm, where the  $IM$  is increased by a constant step from zero to collapse, a version of which is also described in Yun et al. (2002). The end result is a uniformly-spaced (in  $IM$ ) grid of points on the curve. The algorithm needs only a pre-defined step value and a rule to determine when to stop, i.e., when a run is collapsing.

**repeat**

increase  $IM$  by the step

scale record, run analysis and extract  $DM$  (s)

**until** collapse is reached

Although it is an easily programmable routine it may not be cost-efficient as its quality is largely dependent on the choice of the  $IM$  step. Even if information from previously processed ground motion records is used, the step size may easily be too large or too small for this record. Even then, the variability in the “height” (in  $IM$  terms) of the flatline, which is both accelerogram and  $IM$  dependent, tends to unbalance the distribution of runs; IDA curves that reach the flatline at a low  $IM$  level receive fewer runs, while those that collapse at higher  $IM$  levels get more points. The effect can be reduced by selecting a good  $IM$ , e.g.,  $S_a(T_1, 5\%)$  instead of  $PGA$ , as  $IM$ s with higher  $DM$  variability tend to produce more widely dispersed flatlines (Figure 2.9). Another disadvantage is the implicit coupling of the capacity and demand estimation, as the demand and the capacity resolutions are effectively the same and equal to the step size.

Trying to improve upon the basis of the stepping algorithm, one can use the ideas on searching techniques available in the literature (e.g., Press et al., 1986). A simple enhancement that increases the speed of convergence to the flatline is to allow the steps to increase, for example by a factor, resulting in a geometric series of  $IM$ s, or by a constant, which produces a quadratic series. This is the *hunting phase* of the code where the flatline is bracketed without expending more than a few runs.

**repeat**

increase  $IM$  by the step

scale record, run analysis and extract  $DM$  (s)

increase the step  
**until** collapse is reached

Furthermore, to improve upon the capacity resolution, a simple enhancement is to add a step-reducing routine, for example bisection, when collapse (e.g., non-convergence) is detected, so as to tighten the bracketing of the flatline. This will enable a prescribed accuracy for the capacity to be reached regardless of the demand resolution.

**repeat**  
 select an *IM* in the gap between the highest non-collapsing and lowest non-collapsing *IM*s  
 scale record, run analysis and extract *DM* (s)  
**until** highest collapsing and lowest non-collapsing *IM*-gap < tolerance

Even up to this point, this method is a logical replacement for the algorithm proposed in Yun et al. (2002) and in the FEMA guidelines (FEMA, 2000a) as this algorithm is focused on optimally locating the capacity, which is the only use made of the IDA in those two references. If we also wish to use the algorithm for demand estimation, coming back to fill in the gaps created by the enlarged steps is desirable to improve upon the demand resolution there.

**repeat**  
 select an *IM* that halves the largest gap between the *IM* levels run  
 scale record, run analysis and extract *DM* (s)  
**until** largest non-collapsing *IM*-gap < tolerance

When all three pieces are run sequentially, they make for a more efficient procedure, a *hunt & fill* tracing algorithm, described in detail by Vamvatsikos and Cornell (2002b), that performs increasingly larger leaps, attempting to bound the *IM* parameter space, and then fills in the gaps, both capacity and demand-wise. It needs an initial step and a stopping rule, just like the stepping algorithm, plus a step increasing function, a capacity and a demand resolution. The latter two can be selected so that a prescribed number of runs is performed on each record, thus tracing each curve with the same load of resources.

A subtle issue here is the summarization of the IDA curves produced by the algorithm. Obviously, if the same step is used for all records and if there is no need to use another *IM*, the stepping algorithm immediately provides us with stripes of *DM* at given values of *IM* (e.g., Figure 2.8). So a “cross-sectional median” scheme could be implemented immediately on the output, without any post-processing. On the other hand, a hunt & fill algorithm would produce *DM* values at non-matching levels of *IM* across the set of records, which necessitates the interpolation of the resulting IDA curve to calculate intermediate values. Naturally, the same idea can be applied to the output of any IDA tracing algorithm, even a stepping one, to increase the density of discrete points without the need for additional dynamic analyses. Ideally, a flexible, highly non-parametric scheme should be used. Coordinate-transformed natural splines, as presented in Vamvatsikos and Cornell (2002b), are a good candidate. Actually all the IDA curves in the figures of the paper are results of such an interpolation of discrete points. However, before implementing any interpolation scheme, one should provide a dense enough grid of *IM* values to obtain a high confidence of detecting any structural resurrections that might occur before the final flatline.

## 2.12 Conclusions

The results of Incremental Dynamic Analyses of structures suggest that the method can become a valuable additional tool of seismic engineering. IDA addresses both demand and capacity of structures. This paper has presented a number of examples of such analyses (from simple oscillators to 20-story frames), and it has used these examples to call attention to various interesting

properties of individual IDAs and sets of IDAs. In addition to the peculiarities of non-monotonic behavior, discontinuities, “flatlining” and even “resurrection” behavior within individual IDAs, one predominate impression left is that of the extraordinary variability from record to record of the forms and amplitudes of the IDA curves for a single building (e.g., Figure 2.7(a)). The (deterministic) vagaries of a nonlinear structural system under irregular input present a challenge to researchers to understand, categorize and possibly predict. This variability also leads to the need for statistical treatment of multi-record IDA output in order to summarize the results and in order to use them effectively in a predictive mode, as for example in a PBEE context. The paper has proposed some definitions and examples of a variety of issues such as these IDA properties, the scaling variables (*IMs*), limit-state forms, and collapse definitions. Further we have addressed the question of “legitimacy” of scaling records and the relationships between IDAs and *R*-factors as well as between IDAs and the Static Pushover Analysis. Finally, while the computational resources necessary to conduct IDAs may appear to limit them currently to the research domain, computation is an ever-cheaper resource, the operations lend themselves naturally to parallel computation, IDAs have already been used to develop information for practical guidelines (FEMA, 2000a,b), and algorithms presented here can reduce the number of nonlinear runs per record to a handful, especially when the results of interest are not the curious details of an individual IDA curve, but smooth statistical summaries of demands and capacities.

# Applied Incremental Dynamic Analysis

Vamvatsikos, D. and Cornell, C. A. (2003a). *Earthquake Spectra*, (in preparation).

## 3.1 Abstract

Presenting a practical and detailed example of how to perform Incremental Dynamic Analysis (IDA), interpret the results and apply them to Performance-Based Earthquake Engineering. IDA is an emerging analysis method that offers thorough seismic demand and capacity prediction capability by using a series of nonlinear dynamic analyses under a multiply scaled suite of ground motion records. Realization of its opportunities requires several steps and the use of innovative techniques at each one of them. Using a 9-story steel moment-resisting frame with fracturing connections as a testbed, the reader is guided through each step of IDA: (1) Choosing suitable ground motion Intensity Measures and representative Damage Measures, (2) using appropriate algorithms to select the record scaling, (3) employing proper interpolation and (4) summarization techniques for multiple records to estimate the probability distribution of the structural demand given the seismic intensity and (5) defining limit-states, such as the dynamic global system instability, to calculate the corresponding capacities. Finally, (6) the results can be used to gain intuition for the structural behavior, highlighting the connection between the Static Pushover (SPO) and the dynamic response, or (7) they can be integrated with conventional Probabilistic Seismic Hazard Analysis (PSHA) to estimate mean annual frequencies of limit-state exceedance. Building upon this detailed example based on the 9-story, a complete commentary is provided, discussing the choices that are available to the user, and showing their implications for each step of the IDA.

## 3.2 Introduction

An important issue in Performance-Based Earthquake Engineering (PBEE) is the estimation of structural performance under seismic loads, in particular the estimation of the mean annual frequency (MAF) of exceeding a specified level of structural demand (e.g., the maximum, over all stories, peak interstory drift ratio  $\theta_{\max}$ ) or a certain limit-state capacity (e.g., global dynamic instability). A promising method that has recently risen to meet these needs is Incremental Dynamic Analysis (IDA), which involves performing nonlinear dynamic analyses of the structural model under a suite of ground motion records, each scaled to several intensity levels designed to force the structure all the way from elasticity to final global dynamic instability (Vamvatsikos and Cornell, 2002a).

Applying IDA to determine the performance of a structure requires several steps. First, a proper nonlinear structural model needs to be formed, and a suite of records must be compiled. Then, for each record, the scaling levels must be selected, the dynamic analyses run and the

**Table 3.1:** The set of twenty ground motion records used.

No	Event	Station	$\phi^\circ$ <sup>1</sup>	Soil <sup>2</sup>	M <sup>3</sup>	R <sup>4</sup> (km)	PGA (g)
1	Loma Prieta, 1989	Agnews State Hospital	090	C,D	6.9	28.2	0.159
2	Imperial Valley, 1979	Plaster City	135	C,D	6.5	31.7	0.057
3	Loma Prieta, 1989	Hollister Diff. Array	255	-,D	6.9	25.8	0.279
4	Loma Prieta, 1989	Anderson Dam Downstream	270	B,D	6.9	21.4	0.244
5	Loma Prieta, 1989	Coyote Lake Dam Downstream	285	B,D	6.9	22.3	0.179
6	Imperial Valley, 1979	Cucapah	085	C,D	6.5	23.6	0.309
7	Loma Prieta, 1989	Sunnyvale Colton Ave	270	C,D	6.9	28.8	0.207
8	Imperial Valley, 1979	El Centro Array #13	140	C,D	6.5	21.9	0.117
9	Imperial Valley, 1979	Westmoreland Fire Station	090	C,D	6.5	15.1	0.074
10	Loma Prieta, 1989	Hollister South & Pine	000	-,D	6.9	28.8	0.371
11	Loma Prieta, 1989	Sunnyvale Colton Ave	360	C,D	6.9	28.8	0.209
12	Superstition Hills, 1987	Wildlife Liquefaction Array	090	C,D	6.7	24.4	0.180
13	Imperial Valley, 1979	Chihuahua	282	C,D	6.5	28.7	0.254
14	Imperial Valley, 1979	El Centro Array #13	230	C,D	6.5	21.9	0.139
15	Imperial Valley, 1979	Westmoreland Fire Station	180	C,D	6.5	15.1	0.110
16	Loma Prieta, 1989	WAHO	000	-,D	6.9	16.9	0.370
17	Superstition Hills, 1987	Wildlife Liquefaction Array	360	C,D	6.7	24.4	0.200
18	Imperial Valley, 1979	Plaster City	045	C,D	6.5	31.7	0.042
19	Loma Prieta, 1989	Hollister Diff. Array	165	-,D	6.9	25.8	0.269
20	Loma Prieta, 1989	WAHO	090	-,D	6.9	16.9	0.638

<sup>1</sup> Component    <sup>2</sup> USGS, Geomatrix soil class    <sup>3</sup> Moment magnitude    <sup>4</sup> Closest distance to fault rupture

results postprocessed. Thus, we can generate IDA curves of the structural response, as measured by a Damage Measure (*DM*, e.g., peak roof drift ratio  $\theta_{\text{roof}}$  or  $\theta_{\text{max}}$ ), versus the ground motion intensity level, measured by an Intensity Measure (*IM*, e.g., peak ground acceleration, PGA, or the 5%-damped first-mode spectral acceleration  $S_a(T_1, 5\%)$ ). In turn these are interpolated for each record and summarized over all records to estimate the distribution of demand *DM* given intensity *IM*. Subsequently, limit-states (e.g., Immediate Occupancy or Collapse Prevention in FEMA, 2000a,b) can be defined on each IDA curve and summarized to produce the probability of exceeding a specified limit-state given the *IM* level. The final results are in a suitable format to be conveniently integrated with a conventional PSHA hazard curve in order to calculate MAFs of exceeding a certain limit-state capacity, or a certain demand.

Building upon this foundation, we will discuss several topics of practical interest, showing in detail the reasons behind the choices made in our example and the advantages or disadvantages of each. In particular, subjects like the number of runs, the algorithms used for scaling-level selection, and possible approximations used for the probabilistic calculations are going to be presented showing their impact upon the accuracy of PBEE calculations.

### 3.3 Model and ground motion records

To illustrate our methodology, we will use a centerline model of a 9-story steel moment-resisting frame designed for Los Angeles according to the 1997 NEHRP provisions (Lee and Foutch, 2002). The model has a first-mode period of  $T_1 = 2.37$  sec and it incorporates ductile members, shear panels and realistically fracturing Reduced Beam Section connections, while it includes the influence of interior gravity columns and a first-order treatment of global geometric nonlinearities (P- $\Delta$  effects).

In addition we need a suite of ground motion records. Previous studies (Shome and Cornell, 1999) have shown that for mid-rise buildings, ten to twenty records are usually enough to provide sufficient accuracy in the estimation of seismic demands, assuming a relatively efficient *IM*, like  $S_a(T_1, 5\%)$ , is used. Consequently, we have selected a set of twenty ground motion records, listed in Table 3.1, that belong to a bin of relatively large magnitudes of 6.5 – 6.9 and moderate distances,

all recorded on firm soil and bearing no marks of directivity; effectively they represent a scenario earthquake.

### 3.4 Performing the Analysis

Once the model has been formed and the ground motion records have been selected, we need a fast and automated way to perform the actual dynamic analyses required for IDA. This entails appropriately scaling each record to cover the entire range of structural response, from elasticity, to yielding, and finally global dynamic instability. Our task is made significantly easier by using an advanced algorithm, like *hunt & fill* (Vamvatsikos and Cornell, 2002a). This ensures that the record scaling levels are appropriately selected to minimize the number of required runs: Analyses are performed at rapidly increasing levels of  $IM$  until numerical non-convergence is encountered (signaling global dynamic instability), while additional analyses are run at intermediate  $IM$ -levels to sufficiently bracket the global collapse and increase the accuracy at lower  $IM$ s. The user only needs to specify the desired accuracy for demand and capacity, select the maximum tolerable number of dynamic analyses, and then wait for a few hours to get the results. Since the algorithm has been implemented in software (Vamvatsikos and Cornell, 2002b) able to wrap around most existing analysis programs (e.g., DRAIN-2DX, Prakash et al., 1992) it renders IDA almost effortless, needing no human supervision.

As an example, we will show in detail the computations resulting to the  $IM$ -levels selected by *hunt & fill* when tracing record #14 from Table 3.1. To express the scaling level we need an initial, temporary choice of  $IM$ , and we have chosen  $S_a(T_1, 5\%)$ , a decision that need not restrict us in any way: scaling can be re-expressed in any other scalable  $IM$  (Vamvatsikos and Cornell, 2002a) that we wish after the runs are performed. Hence, in  $S_a(T_1, 5\%)$  terms, the algorithm was configured to use an initial step of 0.1g, a step increment of 0.05g and a designated first elastic run at 0.005g, while a maximum of 12 runs was allowed for each record. Additionally, we specified a resolution of 10% on the global collapse capacity, i.e., we expect the model to develop numerical non-convergence and show practically infinite  $\theta_{max}$  at some high intensity level, and we wish this level to be known within 10% of its  $IM$ -value. Finally, we allowed the demand resolution, i.e., the maximum difference between successive  $IM$ -values, to run to its best attainable value by expending all the 12 runs. Alternatively we could have designated some minimum satisfactory  $IM$ -gap below which we do not wish to proceed, thus saving some runs.

**Table 3.2:** Sequence of runs generated by the *hunt & fill* tracing algorithm for record #14.

No.	calculations	$S_a(T_1, 5\%)$ (g)	$\theta_{max}$
1		0.005	0.05%
2	0.005 + 0.10	0.105	0.79%
3	0.105 + 0.10 + 1 × 0.05	0.255	2.02%
4	0.255 + 0.10 + 2 × 0.05	0.455	3.01%
5	0.455 + 0.10 + 3 × 0.05	0.705	5.85%
6	0.705 + 0.10 + 4 × 0.05	1.005	+∞
7	0.705 + (1.005 − 0.705)/3	0.805	18.83%
8	0.805 + (1.005 − 0.805)/3	0.872	+∞
9	(0.805 + 0.705)/2	0.755	9.18%
10	(0.705 + 0.455)/2	0.580	3.27%
11	(0.455 + 0.255)/2	0.355	2.96%
12	(0.255 + 0.105)/2	0.180	1.34%

Using the above settings we get the sequence of runs shown in Table 3.2. The first run is meant to be in the elastic region. In the subsequent five runs, 2–6, we are hunting upwards till

the first numerical non-convergence appears in the form of “infinite”  $\theta_{\max}$ . Then, the dynamic analysis algorithm does not converge thus either failing to complete the dynamic run (as happened for this record) or producing extreme values of  $\theta_{\max}$ , say 200%. The next two runs, 7–8, are used to better bracket the first appearance of non-convergence, closing within 10% of its  $IM$ -value  $((0.872 - 0.805)/0.805 = 8.32\% < 10\%)$  so that the gap between highest converging and lowest non-converging run is less than 10% of the former. Notice, that instead of placing each new run in the middle of the gap, the algorithm places it closer to the converging run, only one third of the way to the non-converging one. This ensures that the search will be somewhat biased towards converging runs, which are more informative than non-converging ones (which are essentially discarded). The rest of the runs, up to the maximum of 12, are used to fill in the IDA at lower levels, being sequentially placed in the middle of the largest  $IM$ -gaps. Thus, the large gaps left by the initial increasing steps to the flatline (runs 2–6), are filled in; this step increases the demand resolution and, given enough runs, it ensures that the algorithm has not missed an earlier collapse. Although it is a rare phenomenon in multi-degree-of-freedom structural models, certain records may cause them to collapse for a range of  $IM$ -values, but not for some higher  $IM$ , an event we call *structural resurrection* (Vamvatsikos and Cornell, 2002a). By reducing the  $IM$ -gaps with runs 9–12, we are making sure that we have not missed such an earlier (in  $IM$  terms) global collapse and the flatline we have found is the first one to occur.

Notice that the maximum  $IM$ -gap, i.e., the demand resolution, is about 0.13g (but less than half on average), while the  $IM$ -difference between the highest converging and lowest non-converging run (the capacity resolution) is much less than 10% of the highest converging  $IM$ , about 0.06g. Naturally, if we knew a priori the approximate  $IM$ -height of the flatline, we could use a stepping algorithm with 12 runs and constant step of 0.1g to achieve similar results with a homogeneous distribution of the accuracy, but this scheme would fail with the next records, producing either too few or too many runs, due to the large record-to-record variability.

Assuming that the computational cost for each run is the same, then, the more the analyses per record, the longer for IDA to complete but the better the accuracy. Still, with the use of such an advanced algorithm no runs are wasted, thus 12 runs per record will suffice to strike a good compromise between speed and accuracy. Nevertheless, it may be pointed out that performing 240 dynamic runs for a model with thousands of degrees-of-freedom is a daunting task. Yet, even for such a complicated model, it took less than 12 hours on two 1999-era Pentium-class processors running independently. The process is completely automated and so easily performed overnight that actually setting up the structural model can now be expected to take substantially more (human) time than doing the analysis, while computer time is becoming an ever-cheaper commodity.

### 3.5 Postprocessing

Equally important to the analysis is the postprocessing of the resulting data and perhaps the most important issue is selecting a suitable  $IM$  and  $DM$ . There are several issues of efficiency and sufficiency associated with the  $IM$  selection (Luco and Cornell, 2004). Since there are no directivity-influenced records in our suite and the building is of medium height (hence first-mode-dominated), the 5%-damped first-mode spectral acceleration  $S_a(T_1, 5\%)$  will be our choice; it has been proven to be both efficient, by minimizing the scatter in the results, requiring only a few ground motion records to provide good demand and capacity estimates, and sufficient, as it provides a complete characterization of the response without the need for magnitude or source-to-site distance information (Shome and Cornell, 1999). Similarly, selecting a  $DM$  can be application-specific; for example, the peak floor accelerations are correlated with contents’ damage and many types of non-structural elements’ damage, while the maximum peak interstory drift ratio  $\theta_{\max}$  (the maximum over time and over all stories of the interstory drift ratios recorded during the timehistory analysis)

is known to relate well (FEMA, 2000a) to global dynamic instability and several structural performance limit-states upon which we intend to focus. Therefore,  $\theta_{\max}$  will be our *DM*-choice. Still, it must be emphasized that these *IM* and *DM* choices are by no means limiting. Assuming that additional *DM*s have been recorded from the analyses, they can be substituted instead of  $\theta_{\max}$ , and by employing the postprocessing techniques presented, the IDA data can be expressed in a different scalable *IM*, without any need to rerun the dynamic analyses.

Having selected our *IM* and *DM*, we are still faced with an abundance of IDA-generated data that need to be sorted out and presented in meaningful ways. It is a time-consuming and challenging task that we are going to step our way through, but it can be rendered totally effortless with the proper software. Actually, most of what follows is a direct description of the inner workings of an automated postprocessing program (Vamvatsikos and Cornell, 2002b), whose graphical output appears in the accompanying figures.

### 3.5.1 Generating the IDA curves by Interpolation

Once the desired *IM* and *DM* values (in our case  $S_a(T_1, 5\%)$  and  $\theta_{\max}$ ) are extracted from each of the dynamic analyses, we are left with a set of discrete points for each record that reside in the *IM-DM* plane and lie on its IDA curve, as in Figure 3.1. By interpolating them, the entire IDA curve can be approximated without performing additional analyses. To do so, we may use a basic piecewise linear approximation, or the superior spline interpolation. Based on the concept of natural, coordinate-transformed, parametric splines with a centripetal scheme for knot-selection (Lee, 1989; Farin, 1990), a realistic interpolation can be generated that accurately represents the real IDA curve, as shown in Figure 3.1 for our example of record #14 in Table 3.2. Having the complete curve available, it is now possible to calculate *DM* values at arbitrary levels of *IM*, allowing the extraction of more (*IM*, *DM*) points with a minimum of computation.

The spline comes in  $n$  cubic polynomial pieces and is parameterized on a single non-negative parameter,  $t \in [0, t_1] \cup \dots \cup [t_{n-1}, t_n]$ , where  $n$  is the number of convergent runs/points including the default (0,0) point, i.e.,  $n = 10 + 1 = 11$  for record #14, Table 3.2. For each value of the parameter  $t$ , and depending on the interval  $[t_{i-1}, t_i]$  where it lies, we get two polynomials, one for the *IM* (the  $x$ -variable) and one for the *DM* (the  $y$ -variable):

$$\begin{cases} x_i(t) = a_{xi}t^3 + b_{xi}t^2 + c_{xi}t + d_{xi} \\ y_i(t) = a_{yi}t^3 + b_{yi}t^2 + c_{yi}t + d_{yi} \end{cases} \quad t \in [t_{i-1}, t_i], \quad i = 1, \dots, n \quad (3.1)$$

With the help of Equation (3.1) we can approximate the *DM*-value at arbitrary levels of *IM* and vice versa. All we need is to solve the appropriate  $x_i(t)$  polynomial piece given the value of  $x$  to get the parameter  $t$  and then replace at the corresponding  $y_i(t)$  piece to get the appropriate  $y$ -value (*DM*), i.e.,

$$DM = y(x^{-1}(IM)), \quad (3.2)$$

$$IM = x(y^{-1}(DM)), \quad (3.3)$$

where the  $-1$  superscript denotes the inverse of a function. All these operations only involve polynomials, hence they are trivial to perform, especially if properly coded in a program.

The smooth IDA curve provided by the interpolation scheme offers much to observe. Even for the single record depicted in Figure 3.1 the IDA curve is not at all simple. It starts as a straight line in the elastic range but then shows the effect of yielding and slightly “softens” at 0.3g by displaying a tangent slope less than the elastic. Subsequently, it “hardens”, having a local slope higher than the elastic, and the building apparently responds with almost the same  $\theta_{\max} \approx 3\%$  for  $S_a(T_1, 5\%)$  in the range of 0.35g – 0.55g. Finally, the IDA curve starts softening again, showing ever decreasing slopes, i.e., greater rates of *DM* accumulation as *IM* increases, reaching

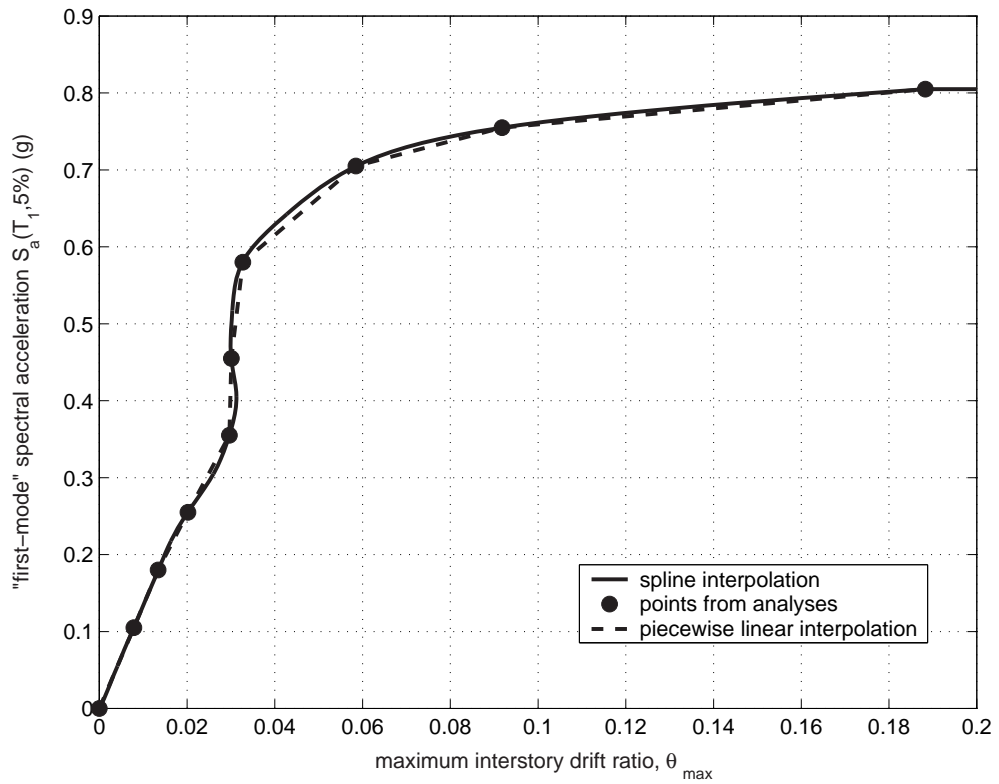


**Figure 3.1:** The numerically-converging dynamic analysis points for record #14, Table 3.2, are interpolated, using both a spline and a piecewise linear approximation.

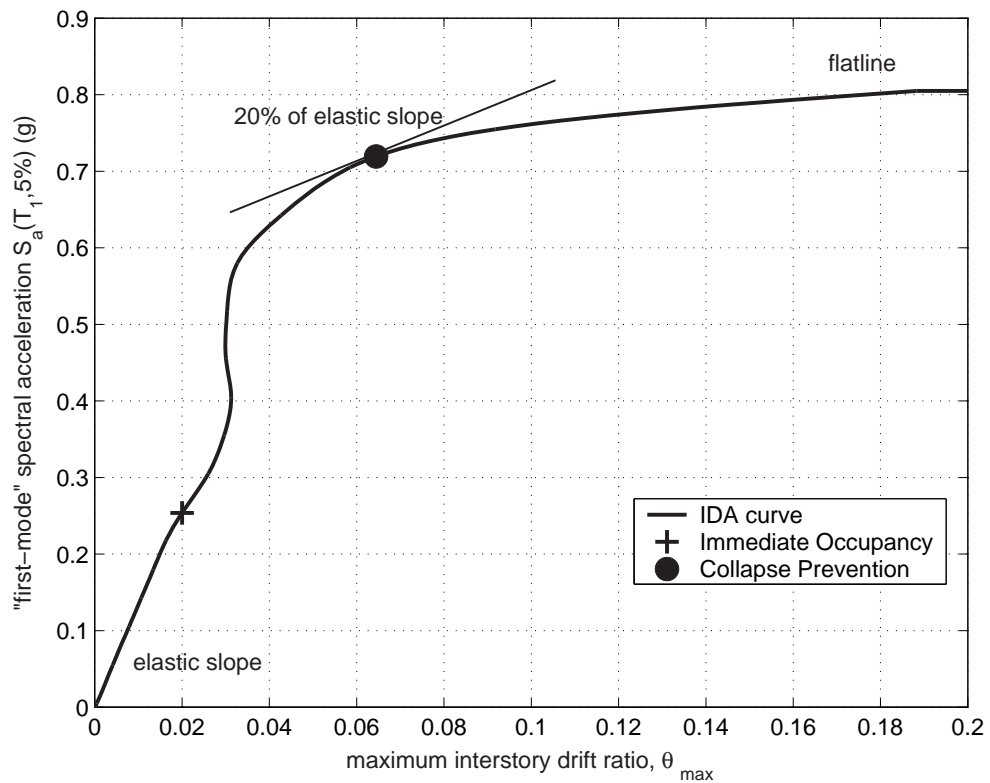


**Figure 3.2:** The limit-states, as defined on the IDA curve of record #14.

the “flatline” at  $S_a(T_1, 5\%) \approx 0.81\text{g}$ , where the structure responds with practically “infinite”  $\theta_{\max}$  values and numerical non-convergence has been encountered during the analysis. That is when the building has reached global dynamic instability, when a small increment in the *IM*-level results in unlimited increase of the *DM*-response.

Observing Figure 3.1, it becomes apparent that the relation of *IM* (or  $x$ ) and  $t$  in Equation 3.1 should always be monotonically increasing. The formulation presented does not strictly enforce this property, but a properly fitted spline will always observe this restriction. Consequently, Equation (3.2) will always return only one *DM* for a given *IM*. On the other hand, the relation of *DM* and  $t$  is often non-monotonic, due to the occasional hardening of IDA curves, hence Equation (3.3) may generate more than one *IM* solutions that produce a given *DM*.

### 3.5.2 Defining Limit-States on an IDA curve

In order to be able to do the performance calculations needed for PBEE, we need to define limit-states on the IDA curves. For our case study, we chose to demonstrate three: Immediate Occupancy (IO), Collapse Prevention (CP), both defined in FEMA (2000a,b), and global dynamic instability (GI). For a steel moment-resisting frame with Reduced Beam Section connections, IO is violated at  $\theta_{\max} = 2\%$  according to FEMA (2000a). On the other hand, CP is not exceeded on the IDA curve until the final point where the local tangent reaches 20% of the elastic slope (Figure 3.2) or  $\theta_{\max} = 10\%$ , whichever occurs first in *IM* terms (FEMA, 2000a). The main idea is to place the CP limit-state at a point where the IDA curve is softening towards the flatline but at low enough values of  $\theta_{\max}$  so that we still trust the structural model. Finally, GI happens when the flatline is reached and any increase in the *IM* results in practically infinite *DM* response.

Calculating the *IM*-value of the flatline capacity is trivial, as our best estimate is actually somewhere between the highest numerically-converging run and the lowest non-converging one, as produced by the hunt & fill algorithm. We choose to use the *IM*-value of the highest numerically-converging run as the estimate, e.g.,  $S_a(T_1, 5\%) = 0.81\text{g}$  for record #14. We could have used, for example, the average of the highest converging and lowest non-converging run,  $(0.81 + 0.87)/2 = 0.84\text{g}$ , but the difference is negligible and gets smaller and smaller as we increase our capacity resolution in the hunt & fill tracing algorithm.

It is equally easy to calculate the *IM*-values for the IO limit-state; all we need to do is use Equation (3.3) for  $DM \equiv \theta_{\max} = 2\%$ , calculate all the *IM*-values that produce  $\theta_{\max} = 2\%$  and, if more than one, select the lowest. This is the one that signals the very first exceedance of the limit-state for the given record. For our example of record #14 in Figure 3.2, IO is violated for  $S_a(T_1, 5\%) \geq 0.26\text{g}$  or  $\theta_{\max} \geq 2\%$ .

On the other hand, the CP points are harder to generate, as we need the tangent slope (i.e., the first-order derivative) of the IDA curve to find points where the local stiffness is 20% of the elastic. We also need the curvature of the IDA curve, to discard candidate points that lie on a hardening part of the curve, rather than the desired softening. The cubic spline interpolation is by definition twice differentiable everywhere, so if we use the prime to denote differentiation by the interpolation-parameter  $t$  and apply the chain-rule, we can generate the first two derivatives of *IM* (or  $x$ ) given *DM* (or  $y$ ):

$$\frac{dx}{dy} = \frac{x'}{y'} \quad (3.4)$$

$$\frac{d^2x}{dy^2} = \frac{x''y' - y''x'}{(y')^3} \quad (3.5)$$

According to the CP limit-state concept, we need to find the highest (in *IM*-value) point where the IDA slope is equal to 20% of the elastic while the point also belongs to a softening branch. Additionally, another candidate point is at  $\theta_{\max} = 10\%$ ; therefore whichever comes first (in *IM*),

the slope or the  $\theta_{\max}$  limit, decides capacity. Hence, we specify:

$$\left. \frac{dx}{dy} \right|_t = 0.20 \left. \frac{dx}{dy} \right|_{t=0} \quad (3.6)$$

$$\left. \frac{d^2x}{dy^2} \right|_t < 0 \quad (3.7)$$

$$t = y^{-1}(10\%), \quad (3.8)$$

All we need to do is solve for all  $t$  satisfying Equation (3.6) and select the maximum such  $t$  (corresponding to the maximum  $IM$ ) that still satisfies Equation (3.7). Then, we compare against the minimum  $t$  that satisfies (3.8). Whichever is the smallest is the  $t$  that defines the CP point. Following this procedure with record #14 we get:  $S_a(T_1, 5\%) = 0.72g$ ,  $\theta_{\max} = 6.4\%$  from Equations (3.6)–(3.7), and  $S_a(T_1, 5\%) = 0.76g$ ,  $\theta_{\max} = 10\%$  from (3.8). By choosing the smallest  $t$ , or equivalently the smallest  $IM$ , we end up with the first of the two points, i.e., in this case the slope limit defines CP (Figure 3.2).

### 3.5.3 Summarizing the IDAs

By generating the IDA curve for each record and subsequently defining the limit-state capacities, a large amount of data can be gathered, only part of which is seen in Figure 3.3. There, the IDA curves display a wide range of behavior, showing large record-to-record variability, thus making it essential to summarize such data and quantify the randomness introduced by the records. We need to employ appropriate summarization techniques that will reduce this data to the distribution of  $DM$  given  $IM$  and to the probability of exceeding any specific limit-state given the  $IM$  level.

The limit-state capacities can be easily summarized into some central value (e.g., the mean or the median) and a measure of dispersion (e.g., the standard deviation, or the difference between two fractiles). Consequently, we have chosen to calculate the 16%, 50% and 84% fractile values of  $DM$  ( $DM_{16\%}^c$ ,  $DM_{50\%}^c$  and  $DM_{84\%}^c$  respectively) and  $IM$  ( $IM_{16\%}^c$ ,  $IM_{50\%}^c$  and  $IM_{84\%}^c$  respectively) for each limit-state, as shown in Table 3.3, and also graphically depicted in Figure 3.4. For example, reading off Table 3.3, at  $S_a(T_1, 5\%) = 0.83g$  or equivalently at  $\theta_{\max} = 0.10$ , 50% of the ground motion records have forced the 9-story structure to violate CP.

**Table 3.3:** Summarized capacities for each limit-state.

	$S_a(T_1, 5\%)$ (g)			$\theta_{\max}$		
	$IM_{16\%}^c$	$IM_{50\%}^c$	$IM_{84\%}^c$	$DM_{16\%}^c$	$DM_{50\%}^c$	$DM_{84\%}^c$
IO	0.18	0.27	0.33	0.02	0.02	0.02
CP	0.57	0.83	1.29	0.07	0.10	0.10
GI	0.74	0.91	1.35	$+\infty$	$+\infty$	$+\infty$

There are several methods to summarize the IDA curves, but the cross-sectional fractiles are arguably the most flexible and robust with respect to the infinite  $DM$ s introduced by the flatlines (Vamvatsikos and Cornell, 2002a). Using the spline interpolation we can generate stripes of  $DM$ -values at arbitrary levels of the  $IM$ ; each stripe contains twenty  $DM$ -values, one for each record, that may be finite or even infinite when a record has already reached its flatline at a lower  $IM$ -level. By summarizing the  $DM$ -values for each stripe into their 16%, 50% and 84% percentiles, we get fractile values of  $DM$  given  $IM$  that are in turn interpolated for each fractile to generate the 16%, 50% and 84% fractile IDA curves, shown in Figure 3.4. For example, given  $S_a(T_1, 5\%) = 0.4g$ , 16% of the records produce  $\theta_{\max} \leq 2.3\%$ , 50% of the records  $\theta_{\max} \leq 2.5\%$  and 84%  $\theta_{\max} \leq 6.5\%$ . Under suitable assumptions of continuity and monotonicity of the IDA curves (as shown at a later section), the fractiles can also be used in the inverse way, e.g., in order to generate demand

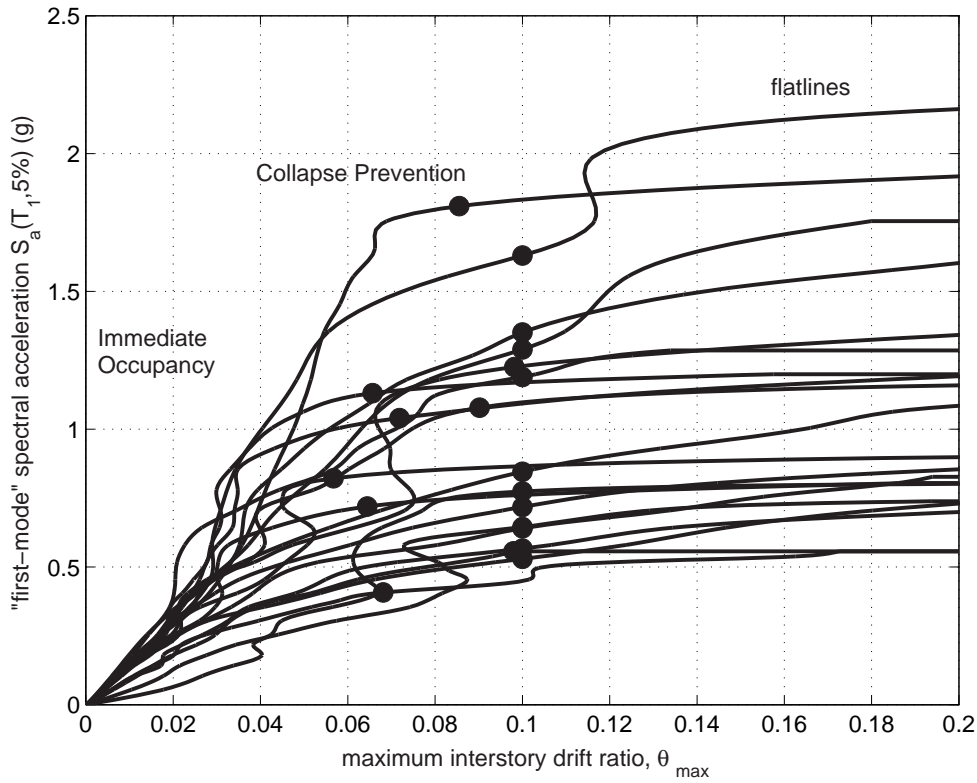


**Figure 3.3:** All twenty IDA curves and the associated limit-state capacities. The IO limit is at the intersection of each IDA with the  $\theta_{max} = 2\%$  line, the CP limit is represented by the dots, while GI occurs at the flatlines.

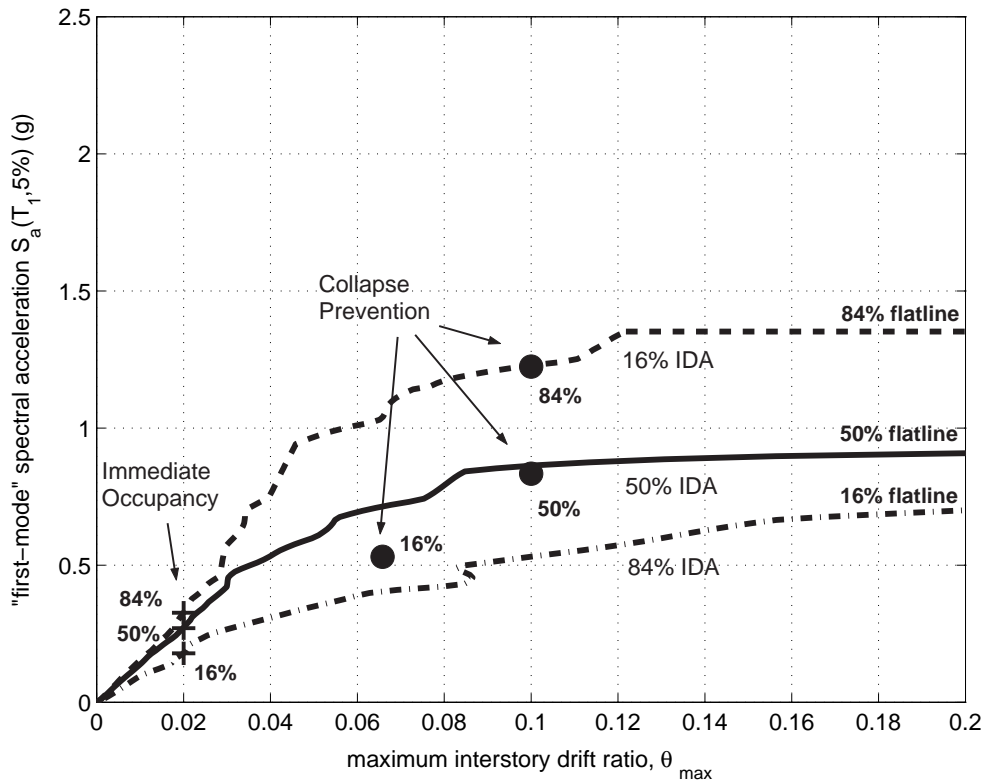


**Figure 3.4:** The summary of the IDA curves and corresponding limit-state capacities into their 16%, 50% and 84% fractiles.

$\theta_{\max} = 4\%$ , 84% of the records need to be scaled at levels  $S_a(T_1, 5\%) \geq 0.31g$ , 50% of the records at  $S_a(T_1, 5\%) \geq 0.52g$  and 16% at  $S_a(T_1, 5\%) \geq 0.76g$ . Consequently, the 16%, 50% and 84% IO points and GI flatlines actually reside on the 84%, 50% and 16% IDA curves respectively, a direct result of the definition of these limit-states. On the other hand, no such general property exists for the CP points, but experience has shown that they usually lie quite close and often on top of their corresponding fractile IDAs, just like the other limit-state points.

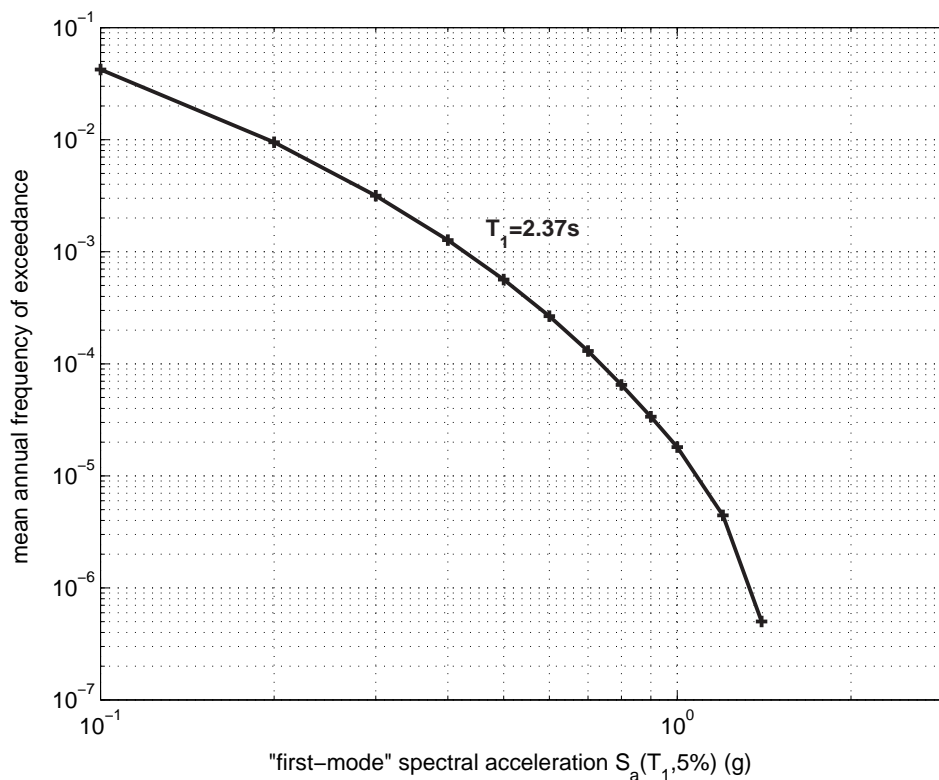


**Figure 3.5:** Hazard curve for the Van Nuys Los Angeles site, for  $S_a(2.37s, 5\%)$ .

### 3.5.4 PBEE calculations

One of the goals of PBEE is producing MAFs of exceedance for the limit-states. This can be easily accomplished with the summarized results that have been calculated so far, especially if one considers the formats proposed by SAC/FEMA (FEMA, 2000a,b) or by the Pacific Earthquake Engineering Research Center (Cornell and Krawinkler, 2000). The process invariably involves calculating the MAF of exceeding values of the chosen  $IM$ , readily available for  $S_a(T_1, 5\%)$  from conventional PSHA, and appropriately integrating with the conditional probabilities of exceeding each limit-state (given the  $IM$  or  $DM$  level) to produce the desired MAFs of limit-state exceedance. It is a relatively straightforward method that has been described in extent, for example, by Cornell et al. (2002).

Here we will perform such calculations using a form of the framing equation adopted by the Pacific Earthquake Engineering Research Center (Cornell and Krawinkler, 2000; Vamvatsikos and Cornell, 2002a),

$$\lambda(DV) = \iint G(DV|DM) |dG(DM|IM)| |d\lambda(IM)| \quad (3.9)$$

To simplify the above equation and the ones to follow, we will loosely use  $\lambda(X)$ ,  $F(X)$  and  $G(X)$  to denote the MAF function, cumulative distribution function (CDF) and the complementary CDF

(CCDF), respectively, of their arguments. For example,  $\lambda(X)$  actually means  $\lambda_X(x)$  and is a different function from  $\lambda(Y) \equiv \lambda_Y(y)$ .

In this paper we have generally used  $S_a(T_1, 5\%)$  for the  $IM$  and  $\theta_{\max}$  as  $DM$  for the limit-states of interest. The decision variable,  $DV$ , here is simply a scalar ‘‘indicator variable’’:  $DV = 1$  if the limit-state is exceeded (and zero otherwise).  $\lambda(IM) \equiv \lambda_{IM}(x)$  is the conventional hazard curve, i.e., the MAF of  $IM$  exceeding, say,  $x$ .  $|dG(DM|IM)|$  is the differential of the (conditional) CCDF of  $DM$  given  $IM$ , or  $\int_{DM|IM}(y|x) dy$ , i.e., it is the probabilistic characterization of the distribution of  $DM$  given  $IM$ , offered by the fractile IDAs. Finally in the limit-state (LS) case, when on the left-hand side of Equation (3.9) we seek the MAF of exceeding the limit-state,  $\lambda(DV=1) = \lambda(0) = \lambda_{LS}$  and  $G(0|DM)$  becomes simply the probability that the capacity  $DM^c$  is less than some level of the  $DM$ ; so  $G(0|DM) = F(DM^c|DM)$ , where  $F(DM^c|DM)$  is the CDF of  $DM^c$ , i.e., the statistical characterization of the  $DM$ -value of capacity, as offered, e.g., by the fractiles of  $DM$ -capacity.

Thus, for our purposes, we can modify Equation (3.9) to become:

$$\begin{aligned} \lambda_{LS} &= \iint G(0|DM) |dG(DM|IM)| |d\lambda(IM)| \\ &= \int_{DM=0}^{DM=+\infty} F(DM^c|DM) \left\{ \int_{IM=0}^{IM=+\infty} \left| \frac{dG(DM|IM)}{dDM} \right| \left| \frac{d\lambda(IM)}{dIM} \right| dIM \right\} dDM \\ &= \int_{DM=0}^{DM=+\infty} F(DM^c|DM) \left| \frac{d\lambda(DM)}{dDM} \right| dDM \end{aligned} \quad (3.10)$$

where the integration over  $IM$  in the braces needs to be carried out either numerically or by an appropriate analytic approximation (Cornell et al., 2002) to produce the absolute value of the  $DM$  hazard gradient  $|d\lambda(DM)/dDM|$ . Then we can proceed to integrate over  $DM$  and estimate  $\lambda_{LS}$ . If, on the other hand, we first integrate-out the  $DM$ , then we can rewrite the above equation to use the  $IM$ -value of capacity:

$$\begin{aligned} \lambda_{LS} &= \int G(0|IM) |d\lambda(IM)| \\ &= \int_{IM=0}^{IM=+\infty} F(IM^c|IM) \left| \frac{d\lambda(IM)}{dIM} \right| dIM \end{aligned} \quad (3.11)$$

where the quantity in the absolute value is the  $IM$  hazard gradient and  $F(IM^c|IM)$  is the CDF of the  $IM$ -value of limit-state capacity. In this case, all quantities in Equation (3.11) are known, and only one integration is needed to calculate  $\lambda_{LS}$ .

We can proceed to the MAF calculations using either the  $DM$ -form (Equation 3.10) or the pure  $IM$ -form (Equation 3.11). There are several issues of compatibility with current guidelines (e.g., FEMA, 2000a) that may dictate the use of the  $DM$ -approach, otherwise the  $IM$ -form is more attractive, as it needs only one integration rather than two; hence, it will be our method of choice. Still, it must be emphasized that either of the two approaches should provide the exact same results if the integrations are performed with sufficient accuracy (see also Jalayer and Cornell, 2002). These are just two ways to the same goal, and the choice lies with the user.

The MAF calculations for any of the two approaches can be carried out either numerically or with an analytical approximation. If a high degree of accuracy is desired, a trapezoidal rule can be employed to directly integrate Equation (3.11). All we need to do is assign 1/20 probability to each of the 20 records, then derive the empirical CDF of the  $IM$ -value of capacity and numerically integrate with values of the hazard curve slope, calculated either by differentiating a smooth interpolation or by simply reading them off Figure 3.5. On the other hand, if we make some reasonable approximations, Equation (3.11) can be analytically integrated (Shome and Cornell, 1999; Cornell et al., 2002). We only need to assume that the  $IM$ -values of capacity are lognormally distributed and then approximate the  $IM$ -hazard curve by fitting a straight line in the log-log space,

$\lambda(IM) = k_0 IM^{-k}$ , either by a global regression, same for all limit-states, or by a local fit at the median  $IM$ -capacity for each limit-state. Then we arrive at the equation

$$\lambda_{LS} = \lambda(IM_{50\%}^c) \cdot \exp\left(\frac{1}{2}(k \cdot S_{\ln IM^c})^2\right) \quad (3.12)$$

where  $S_{\ln IM^c} = (\ln IM_{50\%}^c - \ln IM_{16\%}^c)$  is (approximately) the standard deviation of the natural logarithm of the  $IM$ -capacity.

**Table 3.4:** MAFs of exceedance for each limit-state, calculated both numerically from Equation (3.11) and with the approximate analytical form (3.12), using either a global or a local fit to the  $IM$ -hazard curve.

	IO	CP	GI
numerical	0.019	0.0004	0.00010
analytical (global fit)	0.017	0.0002	0.00003
analytical (local fit)	0.008	0.0005	0.00040

As an example, the MAFs of exceeding each of the three limit-states (IO, CP and GI) were calculated using both the approximate analytic approach (with either the global or the local fit to the hazard curve) and the “exact” numerical integration (Table 3.4). In general, it seems that by approximating the hazard curve with a global fit, the MAFs are consistently underestimated. On the other hand, the local fit seems to cause overestimation for all limit-states but IO. The approximations may sometimes miss the MAFs by a factor of three or get as close as 10%. Still, the large record-to-record variability coupled with the limited size of our suite of twenty records may generate considerable standard errors around these estimates, possibly making the approximate results statistically indistinguishable from the exact MAF for some limit-states. This is an issue that is going to be investigated in a later section.

### 3.5.5 Taking advantage of the data: SPO versus IDA

Beyond the essential calculations needed for PBEE, there is much more information that we could easily glean out of the IDA by taking a closer look at the results and plotting them in new ways. For example, Figure 3.6 displays a story-to-story profile of the median peak interstory drift ratios at several  $S_a(T_1, 5\%)$ -levels. As the intensity increases, then, in a median sense across all records, the fifth floor seems to accumulate most of the deformation. On the other hand, in Figure 3.7 the individual story drift IDA curves are plotted for record #1, showing a record-specific picture of the odd-numbered stories. Most interesting for this record is the sudden change of behavior that occurs around  $S_a(T_1, 5\%) = 0.82g$ , when the top floors suddenly start accumulating more and more deformation as  $IM$  increases, while the previously leading lower floors are held back, displaying almost constant peak interstory drifts.

It is also very informative to visually compare on the same figure the Static Pushover (SPO) curve (also known as the Nonlinear Static Procedure curve, e.g., FEMA, 1997) versus the median (50%-fractile) IDA. Since the SPO curve usually comes in base shear versus  $\theta_{\text{roof}}$  (peak roof drift ratio) coordinates, it needs to be transformed into  $IM$  and  $DM$  axes. In our case, the  $\theta_{\text{max}}$  response can be easily extracted from the SPO analysis results, while the base shear can be converted to acceleration units by dividing with the building mass times some (ad hoc) factor chosen to make the curves match in their elastic range. This can be achieved for our structure by dividing the base shear with 85% of the total building mass (which is very close to the ratio of the first modal over the total mass). By thus plotting the two curves together, as pictured in Figure 3.8, we see that they correspond to each other. The elastic region of the IDA matches the SPO by construction, and the post-yield non-negative SPO segment corresponds to a continuation of the elastic region in the IDA, where the IDA is following the familiar “equal displacement” rule for moderate period

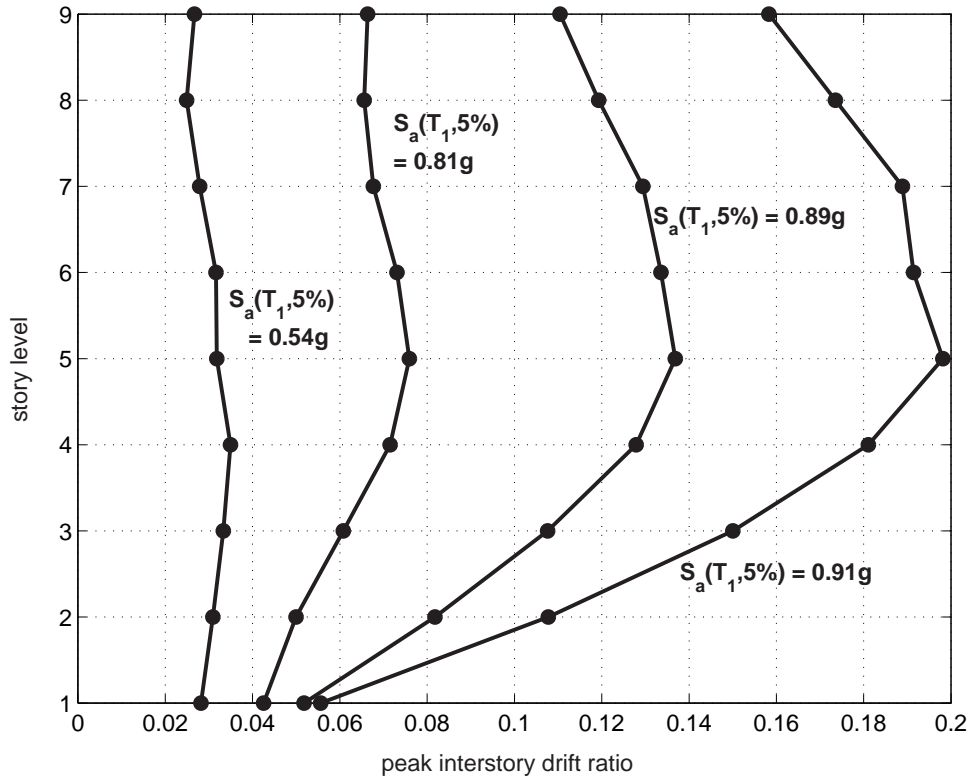


Figure 3.6: The median peak interstory drift ratios for all stories at several specified  $S_a(T_1, 5\%)$  levels.

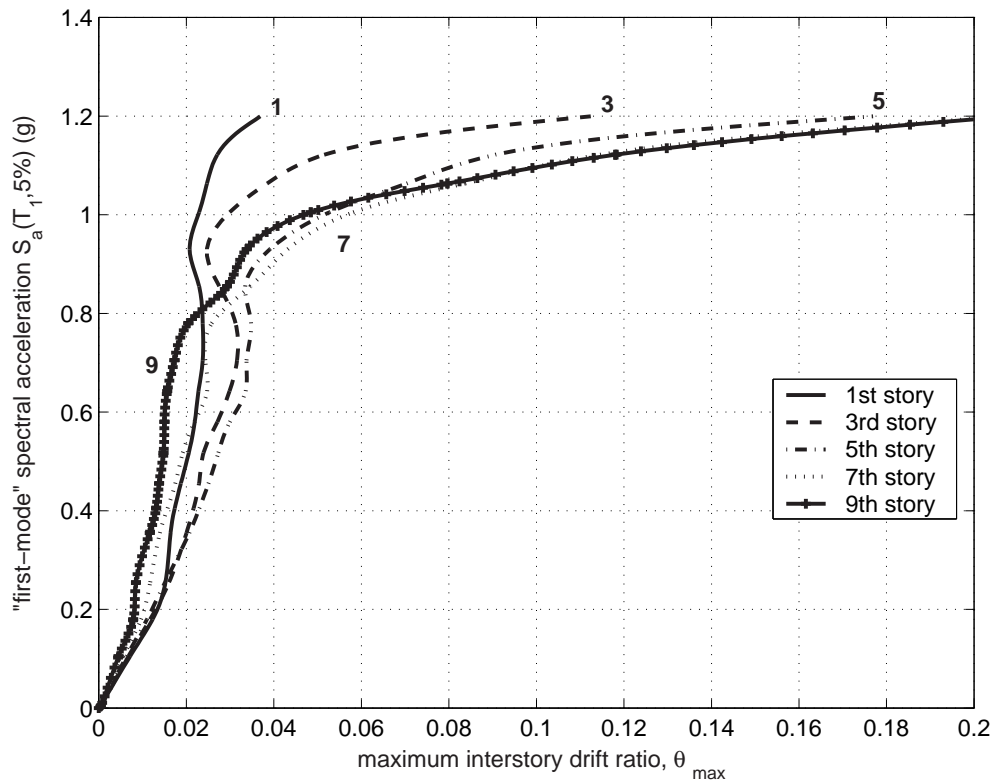
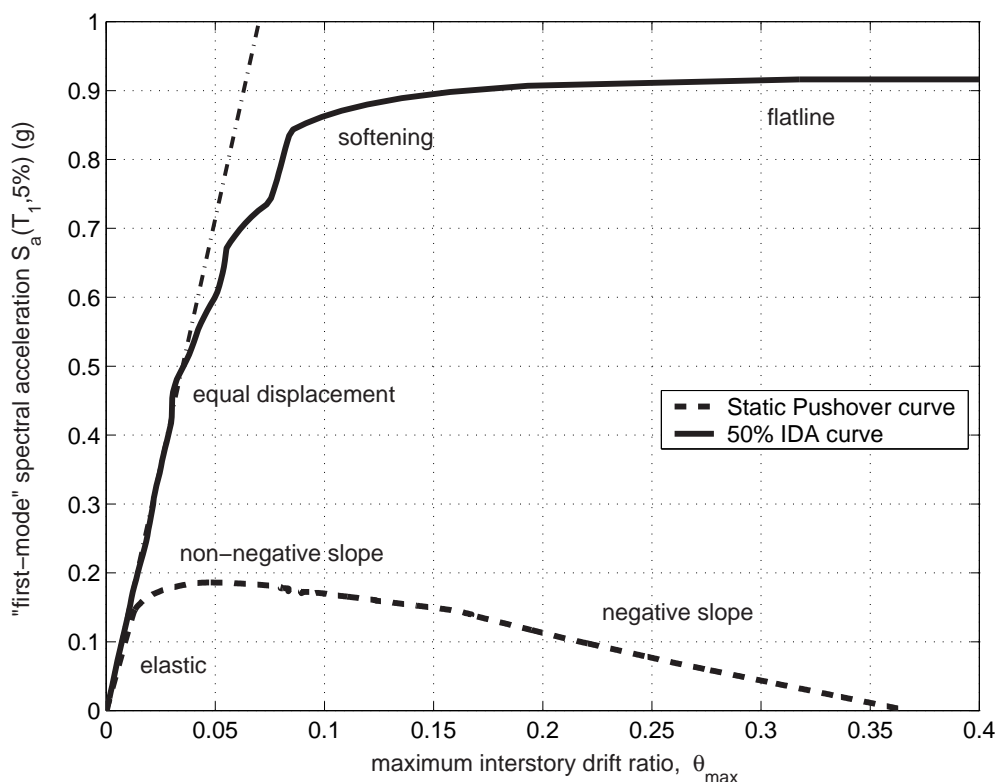


Figure 3.7: The IDA curves of the odd stories for record #1.



**Figure 3.8:** The SPO curve generated from an inverse-triangle (maximum force at roof) load pattern versus the median IDA.

structures (Veletsos and Newmark, 1960). When the SPO turns into a negative slope, the IDA softens and acquires a local slope less than the initial elastic, that gradually decreases till the IDA becomes flat. Essentially, the ending of the SPO at zero strength signals the end of the IDA by the flatline.

The question then arises as to why this relationship exists. Some light can be shed on this issue if we simplify the problem and think in terms of a single-degree-of-freedom system with a force-deformation backbone that has the shape of the building's SPO curve. Then we need to realize that in terms of dynamics, where the IDA is concerned, an ascending part of the "backbone" generally means a "dynamically stable" part while a descending branch corresponds to a "dynamically unstable" part (e.g., Macrae and Kawashima, 1997). For each dynamic run the  $\theta_{\max}$  value serves as an indicator of whether the building has remained completely in the ascending parts (approximately  $\theta_{\max} < 5\%$  in Figure 3.8) or it has ventured into the descending branch as well. So, for lower *IMs*, approximately  $S_a(T_1, 5\%) < 0.6$  g in Figure 3.8, the building (in a median sense, i.e., for at least 50% of the records) oscillates along the ascending part of its "SPO backbone" thus the increase in  $\theta_{\max}$  is controlled and stable in the median. But for higher *IMs* the building (in a median sense again) also sustains more and more cycles in the descending part of the "SPO backbone", thus the median  $\theta_{\max}$  increases uncontrollably towards infinity. This can help us understand why the behavior of the median IDA changes so drastically when the median  $\theta_{\max}$  is higher than 5%, as it shifts from an ascending to a descending branch. On the contrary, the median IDA remains virtually indifferent when this moderate period structure passes from the elastic part to the non-negative post-yield segment of the SPO, since both are ascending branches.

Observing these facts, one could stipulate that some more direct, perhaps quantitative rules may be devised to connect the two curves. Actually, one such attempt has been tried out both for single (Vamvatsikos and Cornell, 2004c) and multi-degree-of-freedom systems (Vamvatsikos and Cornell, 2004b) with encouraging results.

### 3.6 Discussion of choices and their influence on IDA

We took the reader through a direct, hands-on example of how to perform IDA and apply it for the purposes of PBEE. At each step we had to make some choices, e.g., how to set up the dynamic analysis algorithm, what tracing algorithm and interpolation scheme to use, how to summarize the IDAs (using stripes given the *IM* instead of stripes given the *DM*) or how many records and how many runs per record to allow. Still, we chose not to focus on such details; instead we proceeded by making seemingly ad hoc choices. Now, armed with the knowledge of the complete IDA process, we can discuss such choices, explain the reasons behind them and understand their influence to the final results.

#### 3.6.1 Numerical convergence

The details of the analysis and the structural model play an important role in generating accurate IDA curves. Especially in the region of global dynamic instability, the very existence of the flatline and the associated numerical non-convergence may often generate several accuracy problems. Ideally, the structural model would be composed of (numerically) robust and well-tested elements, while the dynamic analysis algorithm should be able to accurately track the structural response through, e.g., yielding events, sharp strength drops, load redistribution and geometric nonlinearities; it would fail to converge only when the structure has exhausted its reserves to become dynamically unstable, thus correctly matching global dynamic instability with numerical non-convergence. Unfortunately, most algorithms and element models have not really been designed or tested to operate in such extreme ranges of behavior. As a result, some records may cause a premature non-convergence, creating a characteristic halting of the IDA curve which does not resemble a flatline.

All the flatlines in our model normally occur beyond  $\theta_{\max} = 12\%$  (Figure 3.3), meaning that the model can remain stable at least up to such  $\theta_{\max}$ -values. Still, in our initial attempt to trace the IDA curves, two of the twenty records failed prematurely, at  $\theta_{\max} \approx 2\%$ , barely past the end-of-elasticity value of  $\theta_{\max} \approx 1\%$ . The main reason is the use of a large, complex model with many degrees of freedom, plus the adoption of the fracturing connection model (Shi and Foutch, 1997) with sharp strength drops that probably tend to destabilize the solution algorithm of DRAIN-2DX (Prakash et al., 1992). Further confirmation is provided by the SPO-to-IDA connection, as  $\theta_{\max}$  values in the order of 2% are still on the ascending branch of the SPO in Figure 3.8, thus deemed unable to cause collapse. Actually, each IDA curve should be able to behave stably at least up to the start of the SPO's negative slope, at about  $\theta_{\max} = 7\%$ . Still, this comparison should not be carried too far; while the SPO ends at  $\theta_{\max} = 37\%$ , the post-peak part of the SPO is often very load-pattern dependent, and an arbitrary load pattern may result in very optimistic  $\theta_{\max}$  values that do not reflect the dynamic behavior (Vamvatsikos and Cornell, 2004b).

Such illegitimate and premature collapses are thus relatively easily identified, either by looking at the SPO or at the IDAs of other records, but how are they to be fixed? Of course, if the model or the elements or the algorithm are deficient in the first place, the situation is hopeless. Experience has shown that this is not the case with the well-tested DRAIN-2DX; it is more a problem of correctly setting up the analysis parameters, rather than anything else. The best strategy is to tweak the analysis knobs, e.g., reduce the integration time-step, adopt a variable-step solution or experiment with the parameters of the event-to-event solver. In our case-study, the dynamic analyses of the two problematic records had to be repeated at a reduced time-step, one-fourth instead of one-half of the acceleration timehistory time-step, thus easily resolving convergence issues. Note that after such false, premature collapses are dealt with, then further (reasonable) changes in the parameters of the solution algorithm will make only small arbitrary changes to the IDA results. For example, it has been found empirically that changing the integration time-step can incur arbitrary changes of up to 10% to the flatline heights, where, surprisingly, smaller steps

do not necessarily mean more stability (i.e., higher flatline heights). This is simply the effect of small errors piling up on each step of the time-integration that may affect convergence when the structure is close to the flatline, sometimes causing it to collapse a bit earlier and sometimes not. This is the reason why when tracing each record we specified a capacity resolution of only 10%; a better accuracy does not have much meaning in the presence of these analysis uncertainties.

Such inaccuracies remain relatively insignificant when good analysis software is used. Actually, we cannot stress enough the need for reliable, bug-free algorithms and well-tested, robust element models. Such tools are exactly what makes the difference in such analyses, especially for the limit-states close to global dynamic instability, and when available, with only a little attention to the analysis details allow us to easily obtain accurate IDA curves.

### 3.6.2 Choice of Tracing Algorithm

When tracing the IDA curve for each record, the choice of the *IM*-level for each run is a decision left to the automated tracing algorithm that we use. We have theoretically argued about the superiority of the hunt & fill algorithm versus the use of a constant *IM*-step (i.e., the stepping algorithm) in [Vamvatsikos and Cornell \(2002a\)](#), so it is time to see in detail what the true differences really are when both are applied to the 9-story structure.

Before we proceed, keep in mind that given the same structural model, analysis program and computing platform, still not all runs are equal in computational cost. In general, the closer the run is to the flatline (either at a lower or a higher *IM*) the longer it takes to complete the analysis. On the other hand, both converging and non-converging runs that are far away from the flatline will be significantly faster, as convergence or non-convergence will be achieved within a minimum of iterations. Still, when comparing the tracing algorithms, we will assume that the intent is to trace the whole IDA curve and a similar amount of runs will be spent both high and low in the curve (in *IM* terms). Thus, looking at each record as a whole, the total amount of runs (converging and non-converging alike) spent for it provide a very accurate idea of the computational time needed, while the number of converging runs accurately describes the accuracy achieved.

**Table 3.5:** Comparing the sensitivity to parameters of the stepping versus the hunt & fill algorithm.

Algorithm	Parameter (g)	Total C+NC <sup>1</sup>	min C <sup>2</sup>	max C <sup>2</sup>	average C <sup>2</sup>
stepping (step-size sensitivity)	0.05	475	11	45	22.8
	0.075	318	7	30	14.9
	0.1	244	5	22	11.2
	0.2	128	2	11	5.4
	0.3	87	1	7	3.4
hunt & fill (initial-step sensitivity)	0.05	280	12	13	12.2
	0.1	280	12	13	12.2
	0.2	280	11	13	12.0
	0.3	280	11	12	11.8
hunt & fill (step-increment sensitivity)	0.025	280	11	13	12.4
	0.05	280	12	13	12.2
	0.1	280	11	13	12.0
	0.2	280	11	13	11.9

<sup>1</sup> Converging and non-converging runs for all records

<sup>2</sup> Converging runs per record

The most important task that a user faces when applying either of the two algorithms is setting up their parameters correctly. For the stepping algorithm, the only parameter is the step size, while for the hunt & fill the most important ones are the initial step, the step increment and the allowed number of runs per record. Both algorithms were used to trace the IDAs of the 9-story structure for the suite of 20 records, using various settings for their parameters, the results shown in [Table 3.5](#).

Obviously, changing the step size of the stepping algorithm generates huge differences in the total number of runs. Still, if we let the minimum number of converging runs generated for any of the 20 records be our standard for accuracy, we need at least a step size of 0.05g, or 475 runs to get at least 11 runs per record and reach the standards of hunt & fill. Also, if we do not set the stepping size correctly, we either get too few or too many runs, the resolution easily dropping to 1 or 2 runs in the worst case, if we happen to set a step size of 0.2g or 0.3g. On the other hand, we can change the initial step or the step increment for the hunt & fill within a wide range, increasing them or reducing them by 2 or 4 times, and the hunting algorithm remains practically unchanged, constantly providing at least 11 converging runs per record. In essence, it has the right knobs to be tuned to the tolerance limits that we wish and allows us to do the runs the way we want, not the way nature decides through the records.

Still, one may notice that if we over-increase the initial step or the step increment, then the accuracy starts to slowly drop, as the algorithm overshoots the flatline by a lot and spends many non-converging runs to find its way down. But still the effect is minor, not overwhelming. Notice also that keeping both parameters relatively small seems to improve accuracy both on average and in the minimum. Still, we should not decrease them too much because as the steps become smaller we are risking expending all the allotted runs before reaching the flatline.

Coming back to our example, in Table 3.2, we used  $S_a(T_1, 5\%)$  to measure the *IM*-value for our runs. Why not another *IM*? We could have used pretty much any monotonic and scalable *IM* (Vamvatsikos and Cornell, 2002a) that we might want, but the less efficient it is, the further dispersed the IDA flatlines would be, and we would start having some resolution discrepancies within tracing, i.e., a greater difference between the observed number of minimum and maximum convergent runs per record in our suite. By using at least  $S_a(T_1, 5\%)$ , we are assured that our algorithm, be it hunt & fill or stepping, will be efficient for a wide range of conditions. If another, more efficient *IM* appears that can drastically reduce the record-to-record flatline variability, then the hunt & fill would only marginally benefit, but the stepping algorithm would significantly improve. In conclusion, the hunt & fill procedure desensitizes IDA from the *IM* selection and the setting of the algorithm's parameters, easily achieving the desired resolution, in contrast to the very sensitive stepping algorithm. Additionally, it fixes the number of total runs performed, so we can plan ahead and assign enough computers to run in parallel so the IDA is computed in time.

### 3.6.3 Interpolation issues

By interpolating the discrete points to generate each record's IDA curve we are gaining one enormous advantage: we do not need to have our runs in stripes of the same *IM*-level. The consequences are very important. First, this allows us to use the hunt & fill algorithm instead of the stepping one, thus gaining in all the aspects described previously. Second, it allows us to express the IDA results in any *IM*. All we need is to calculate the new *IM* for each run, re-plot the IDA curves and re-interpolate versus the new *IM*. In this way, IDA becomes truly independent of the *IM* used for tracing, allowing us to reuse the same data again and again, without needing to run any more analyses.

But why use complex spline schemes instead of the simpler linear interpolation? In Figures 3.9 and 3.10, we present a comparison of the linear and the spline interpolation scheme, pitted against each other for a given number of converging runs. We have tweaked the hunt & fill tracing so that in all cases the flatline is accurately reached with the same number of runs, and then the algorithm is allowed to fill in the gaps using up to a total of 4, 6, 8 or 18 runs. Unless we are only interested in the flatline, 4 converging runs are just too few to capture the IDA adequately, regardless of the interpolation scheme used. Clever postprocessing cannot make up for gross data gaps. On the other hand, if we allow only 2 more runs, for a total of 6, the results are markedly better, but only if we are using a spline scheme. Had we used 6 linearly interpolated runs we would be grossly underestimating the CP limit-state capacity, finding a capacity point at only  $S_a(T_1, 5\%) = 0.63g$ ,

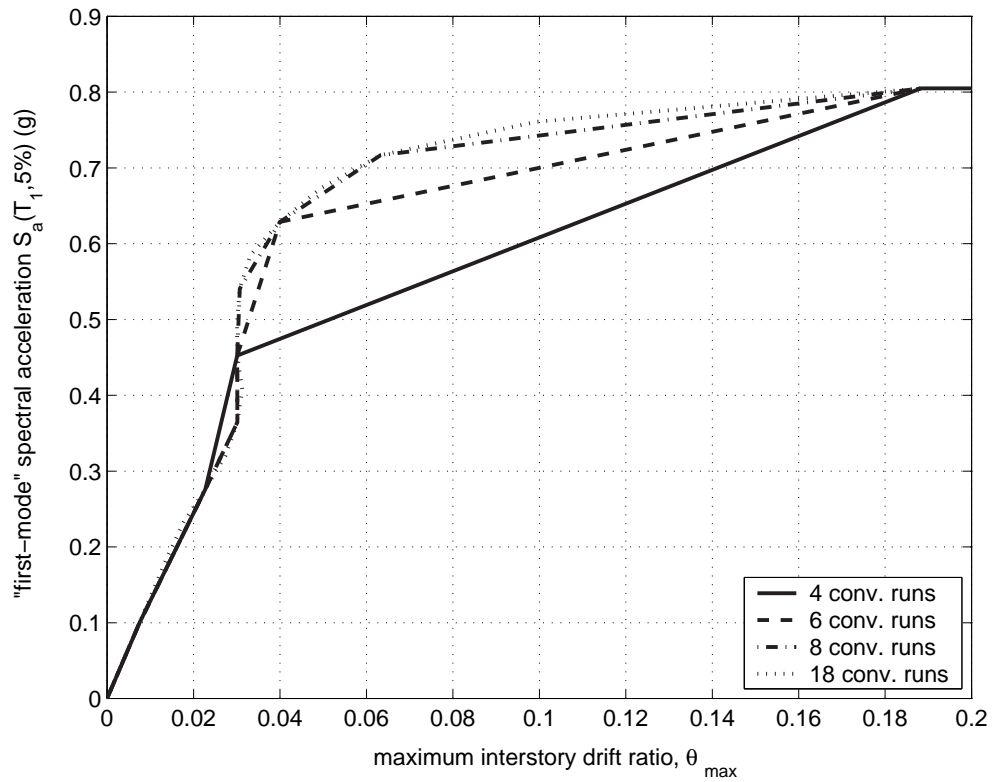


**Figure 3.9:** Linearly interpolated IDA curve for record #14, traced with a different total number of converging runs.

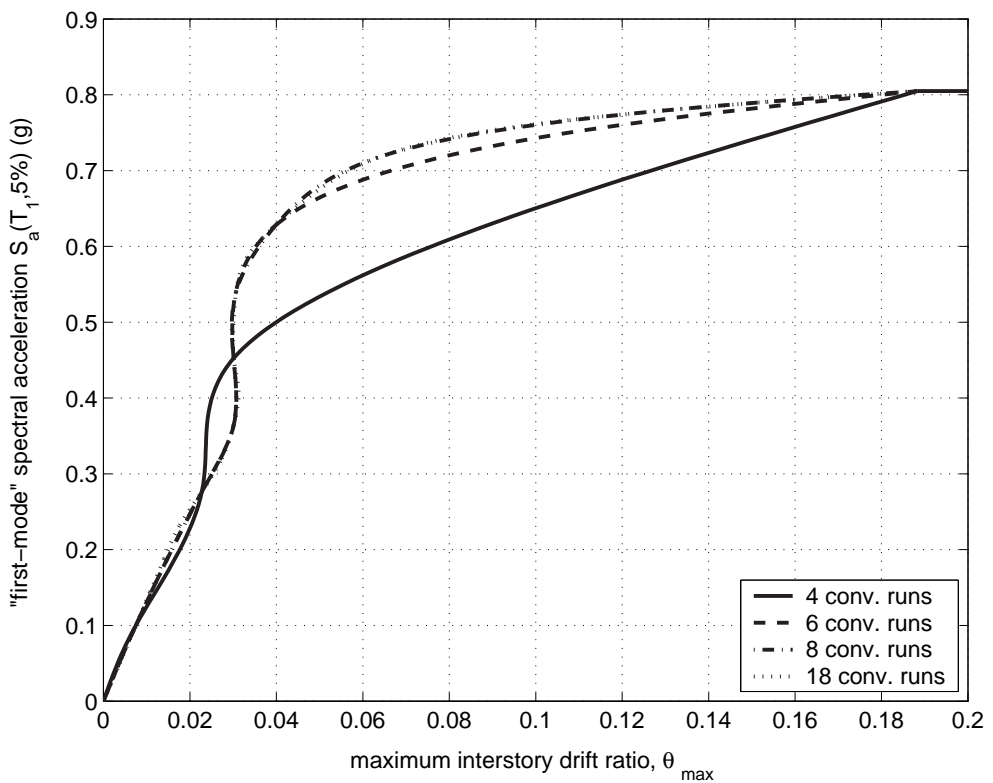


**Figure 3.10:** Spline-interpolated IDA curve for record #14, traced with a different total number of converging runs.

$\theta_{\max} = 4\%$  instead of the correct 0.72g and 6.4%. At 8 and 18 runs, the spline interpolations are practically indistinguishable, while the linear ones are close enough but still can be told apart. In conclusion, if we allow enough runs, the interpolation scheme doesn't really matter, both schemes will provide good results. On the other hand, if we use too few runs, it doesn't really matter again because both schemes are going to give us bad results. But there is a gray area in between, where using a better and smarter interpolation can make the difference to increase the accuracy in our final IDA curve. In retrospect, this is precisely what gives us confidence to reduce the allotted number of runs and save on computational resources.

### 3.6.4 Sensitivity of the limit-state capacities to their definition

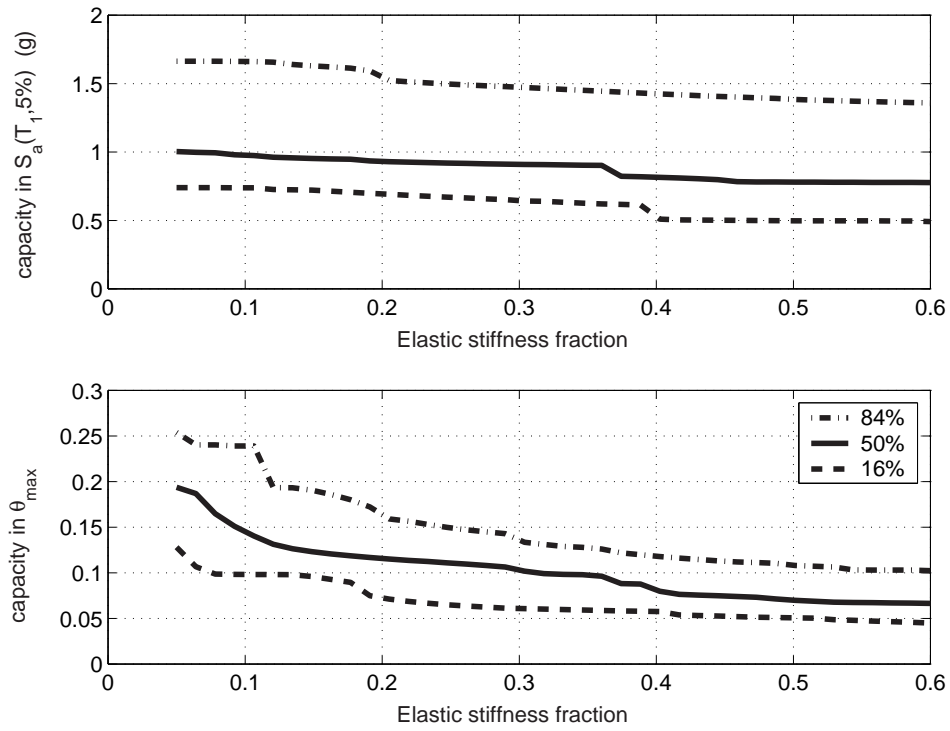
Several limit-states were defined on the IDA curves, often through the use of ad hoc rules. For example, the IO limit-state was defined at  $\theta_{\max} = 2\%$ , while the CP limit-state was based on the arbitrary 20% fraction of the elastic slope (or stiffness) and the additional  $\theta_{\max} = 10\%$  limit (FEMA, 2000a). On the other hand, the GI limit-state was unambiguously defined to be on the flatline of the IDA, being subject to no such arbitrary rules. Therefore, it is of interest to investigate the sensitivity of the summarized *IM*, *DM* capacities to these choices, both for the IO and the CP limit-state.

For the IO limit-state, the simplicity of the definition makes it easy to understand what is happening. If we look at Figure 3.4, it is obvious that IO is occurring in the "equal displacement" region of the fractile IDAs, i.e., the fractiles are almost straight lines resembling a continuation of the elastic segment. In turn, this means that moderate changes to the defining value for IO, i.e., from  $\theta_{\max} = 2\%$  to 1% or 3% will proportionately increase or decrease the *IM* and *DM* values of capacity.

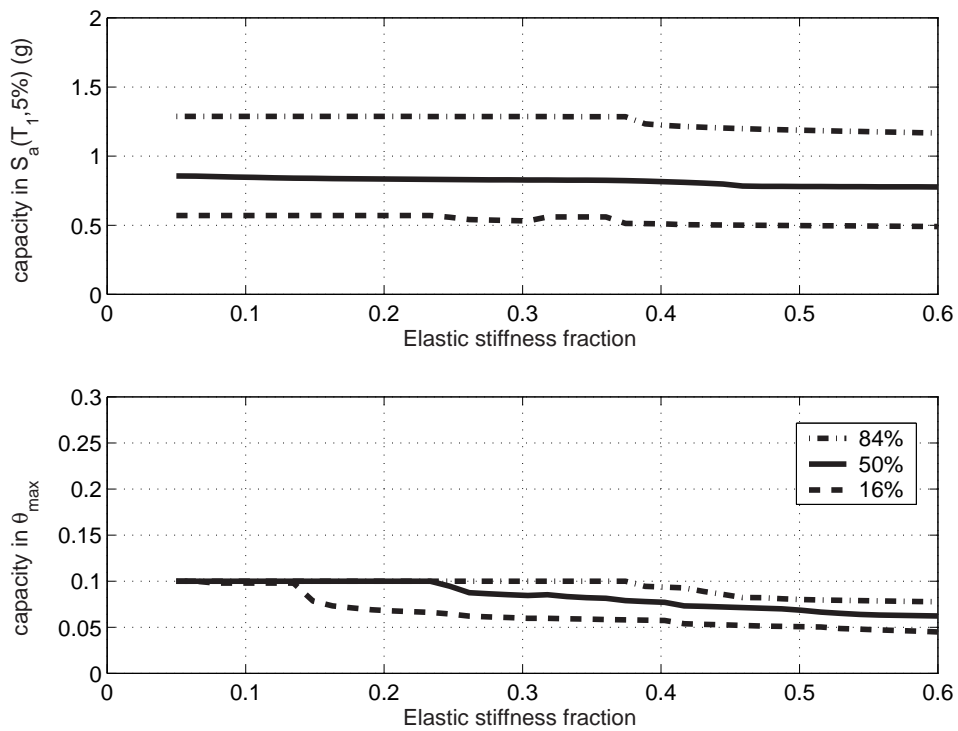
On the other hand, the definition of the CP limit-state is quite more complicated. The elastic stiffness fraction controls how much the IDA has to soften, i.e., how close to the flatline it can come, before CP is reached. Hence, increasing this fraction will force the CP points (e.g., Figure 3.3) to move to lower *IM*s and *DM*s. The influence of the  $\theta_{\max} = 10\%$  limit is more straightforward. It enforces a rigid limit on the capacity points, restricting the  $\theta_{\max}$  value they can reach, i.e., it is another way to restrict the CP points from coming close to the flatline. Actually, in our case of the 9-story building, Figure 3.3, it becomes obvious that by changing the  $\theta_{\max} = 10\%$  limit to, say, 8% or 12%, the *IM*-value of capacity will only slightly change, but the *DM*-value will be highly influenced, the 50% and 84%  $\theta_{\max}$  capacities actually becoming 8% or 12% respectively.

To show the combined influence of the two rules on the CP limit-state, the fraction of the elastic stiffness has been varied from 10% to 60% and the resulting fractile  $S_a(T_1, 5\%)$ ,  $\theta_{\max}$  capacities have been plotted, both when the  $\theta_{\max} = 10\%$  rule is imposed (Figure 3.11(b)) and when it is not (Figure 3.11(a)). In the latter case, the *IM* capacity becomes relatively sensitive, almost linearly, to the elastic stiffness fraction. The *DM* capacity is even more sensitive, decreasing in a geometric fashion as the fraction increases. This makes absolute sense given the shape of the IDAs (Figure 3.3); close to global collapse, each IDA softens towards the flatline, hence, as the slope-fraction decreases, the CP *IM* capacity approaches the flatline *IM*-height. On the other hand, the *DM* capacity is destabilized by the same flattening, since by definition, in the vicinity of the flatline, small changes in the elastic stiffness fraction result to large changes of the *DM*-value.

If we include the  $\theta_{\max} = 10\%$  limit, as in Figure 3.11(b), both the *IM* and especially the *DM* capacity are stabilized, as this hard upper limit simply cuts off all higher values. Furthermore, this limit seems to drastically reduce the *DM*-capacity dispersion, at all levels of the elastic stiffness fraction. Obviously, several records now have the same CP limit-state *DM* capacity, namely  $\theta_{\max} = 10\%$ . Therefore, the 10% limit makes the CP capacity more stable, but no less arbitrary, as the  $\theta_{\max} = 10\%$  limit is often the governing rule. Actually, looking at the tables in FEMA (2000a,b) it becomes obvious that 10% is often the quoted median  $\theta_{\max}$ -capacity for all



(a) Resulting  $S_a(T_1, 5\%)$  and  $\theta_{max}$  capacities when the  $\theta_{max} = 10\%$  limit is not imposed.



(b) Resulting  $S_a(T_1, 5\%)$  and  $\theta_{max}$  capacities when the  $\theta_{max} = 10\%$  limit is imposed.

**Figure 3.11:** The sensitivity of the fractile (16%, 50% and 84%)  $S_a(T_1, 5\%)$  and  $\theta_{max}$  capacities for the CP limit-state to the elastic stiffness fraction used (20% is the standard by FEMA, 2000a). The results are less sensitive if the  $\theta_{max} = 10\%$  limit is used.

but the tallest buildings. Is, then, this arbitrarily imposed  $\theta_{\max} = 10\%$  a problem? From an MAF-sensitivity point-of-view, the answer is negative. In Equation 3.11 it becomes apparent that it is only the *IM*-value of capacity that truly matters. As we have observed, at least for this structure, the *IM*-value of CP-capacity is only mildly sensitive to the definition of the rules, thus yielding similarly mildly sensitive MAFs. Even if the calculation is done using the *DM*-form in Equation (3.10), assuming that the integrations are accurately performed, the conclusions will still be the same.

There are also several other details and corresponding sensitivity issues in the implementation of the CP limit-state definition, that may or may not make a difference. For example, in Yun et al. (2002) the 20% fraction is applied to the median elastic stiffness of all records and the resulting reduced stiffness is used for the capacity point estimation. On the other hand, we have used the 20% fraction on the elastic stiffness of each individual record to define its CP capacity. In this case, the summarized capacities show negligible difference between the two approaches. On the other hand, in Yun et al. (2002) CP is defined to occur at the first point where the IDA curve softens to 20% of the (median) elastic slope, while we use the last point where it reaches the reduced stiffness. This may make a large difference for some records that alternatively harden and soften before global collapse, and may be interpreted as another sign of sensitivity to the CP definition. Still, for reasons explained in Vamvatsikos and Cornell (2002a), we believe it is more consistent with the CP limit-state concept to use the last rather than the first such point, thus resolving this problem.

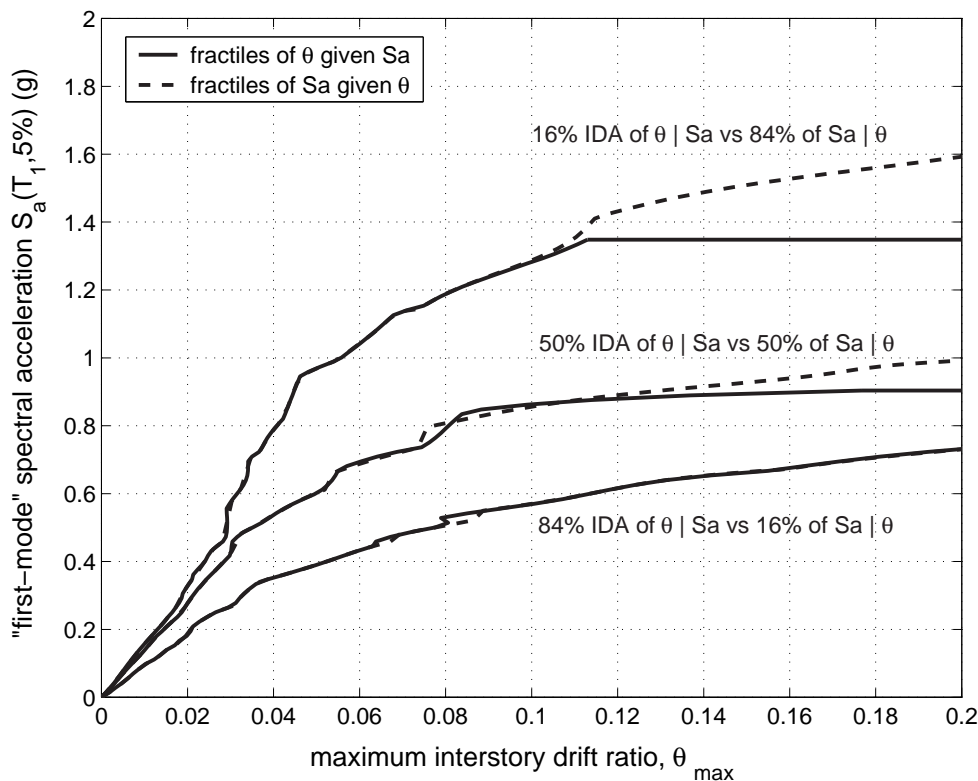
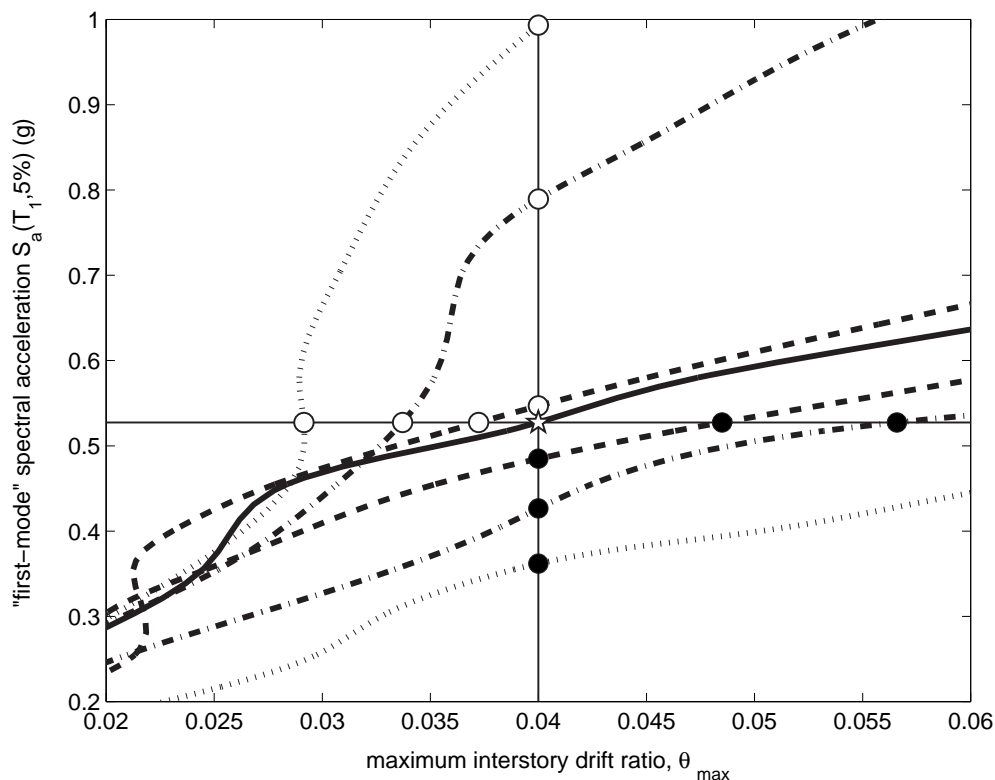


Figure 3.12: Summarization into fractiles of *IM* given *DM* versus fractiles of *DM* given *IM*.

### 3.6.5 Summarization given *IM* or *DM*

When summarizing the IDA curves, we decided to use stripes of *DM* given levels of *IM*, instead of stripes of *IM* given *DM*. It often becomes an issue in the literature (e.g., Miranda, 2001), whether one should summarize given *IM* or *DM*. The first approach can be thought of providing



**Figure 3.13:** Two stripes, one given *DM* and one given *IM*, converging on the same median (the star). The records are No.18,5,19,6,9,10,13 from the highest to the lowest *IM* at  $\theta_{\max} = 4\%$ .

the distribution of demand *DM* that a given level of intensity *IM* can generate in the structure, while the latter is the distribution of intensities *IM* that are required to produce a given level of damage *DM*. Clearly, if we use the mean and standard deviation to summarize such stripes, the results will be very different between the two approaches (e.g., Miranda, 2001). When fractiles are employed, though, this is not so; as shown in Figure 3.12, the 16%, 50% and 84% fractiles given *IM* ( $S_a(T_1, 5\%)$ ) almost perfectly match the 84%, 50% and 16% fractiles respectively, given *DM* ( $\theta_{\max}$ ).

The reasons behind this surprising fact become apparent in Figure 3.13. There, we have selected a subset of only seven records and have generated a (vertical) stripe of *IM*s given  $DM \equiv \theta_{\max} = 4\%$ . The median falls on the fourth, the middle of the seven curves, and is estimated to be  $S_a(T_1, 5\%) = 0.53g$  (represented by a star). A (horizontal) stripe given *IM* is generated at this precise level and, remarkably, the median *DM* given  $S_a(T_1, 5\%) = 0.53g$  is found to lie on the same IDA curve, right at the star, at  $\theta_{\max} = 4\%$ . To better illustrate this, we use white dots for IDA crossings on the left of the horizontal stripe and on the top of the vertical, but black dots at the bottom of the vertical or to the right of the horizontal. Local continuity and monotonicity assure that any IDA curve can only have two dots of the same color, i.e., each IDA curve will remain on the same side of the median curve.

Of course, it often happens that IDA curves are neither continuous, nor monotonic as due to hardening increased *IM*s may sometimes produce lower or the same *DM*-response (Figure 3.1). But even then, significant discrepancies (e.g., serious hardening in several curves at the same time) must occur to influence the robust fractiles, thus only slightly disturbing the matching of the fractiles given *DM* and given *IM*, and only in isolated places.

Why then are the 50% and 84% flatlines in Figure 3.12 not exactly matching? In the case of the seven curves in Figure 3.13, the median is conveniently falling right on the fourth of the seven curves. Since in Figure 3.12 a sample of 20 records is used, none of the three fractiles

matches one of 20 curves. In that case, there are several ways to approximate the fractiles, and the one that we use involves linear interpolation between the closest two curves. For example, for 20 records, the median is calculated as the average of the 10th and the 11th record, as ordered on the relevant stripe. Obviously such interpolation generates different results given *IM* or *DM*. This problem becomes more apparent close to the flatline, where for summarization given *DM* we always have finite values of *IM* to interpolate, while for the summarization given *IM*, one of the closest two records produces infinite *DM* (which cannot be used for interpolation). If we use a larger sample, such discrepancies are reduced and eventually eliminated. Similarly, we could use another method to approximate the fractiles, e.g., select the lower of the two points that we use for the interpolation and similarly eliminate the problem. In any case, given the record-to-record variability, the fractiles are close enough and increasing the sample size they will actually converge to the same curves, no matter what method we use to estimate them.

### 3.6.6 Sensitivity to the record suite size

The IDA curves display significant record-to-record variability, as becomes obvious in Figure 3.3. It is only natural to investigate the accuracy of the results given the limited sample size of twenty records. Traditional analytical forms are difficult to implement for the fractiles or the MAFs, hence we turn to the bootstrap method (Efron and Tibshirani, 1993) to fill this gap. Application of the bootstrap involves sampling with replacement from the twenty records to generate an arbitrary number of alternate record suites and a corresponding number of summarized capacities or MAF estimates. From such samples of estimates, one can easily calculate the standard error or confidence intervals of the desired coverage (e.g., percentile bootstrap confidence intervals) for both fractile *IM*, *DM* capacities and MAFs.

**Table 3.6:** Median *IM* and *DM* capacities for each limit-state, shown versus the bootstrapped standard error and the 90% confidence interval on the median estimate.

	$S_a(T_1, 5\%)$ (g)			$\theta_{\max}$		
	$IM_{50\%}^c$	SE <sup>1</sup>	90% CI <sup>2</sup>	$DM_{50\%}^c$	SE <sup>1</sup>	90% CI <sup>2</sup>
IO	0.27	0.02	[0.24, 0.30]	0.02	-	-
CP	0.83	0.14	[0.72, 1.13]	0.10	0.004	[0.09, 0.10]
GI	0.91	0.17	[0.75, 1.20]	$+\infty$	-	-

<sup>1</sup> Standard Error      <sup>2</sup> Confidence Interval

The bootstrap estimate of the standard error, plus a 90% bootstrap confidence interval on the median *IM* and *DM* limit-state capacities appear on Table 3.6. It becomes obvious that using only 20 records provides a relatively accurate estimate of the capacity values for this structure; the median *IM* capacities show very small dispersion that predictably increases for limit-states closer to global dynamic instability. We should expect comparable, albeit higher, standard errors (and wider confidence intervals) for the 16% and 84% fractiles, as they are closer to the edges of the sample and thus relatively more variable. On the other hand, the fractile *DM* capacities have practically negligible standard error. In the case of IO and GI, this is a direct result of their definition, as they both lie at fixed values of  $\theta_{\max}$  (2% and  $+\infty$  respectively). Similarly, the median *DM* capacity for CP is almost always dominated by the  $\theta_{\max} = 10\%$  rule, drastically reducing its dispersion. Again, this difference in the standard errors does not imply that using the *DM*-based form (Equation 3.10) instead of the *IM*-based (Equation 3.11), will result in higher confidence (less dispersion) in the MAFs estimate. The results should be identical even in this aspect when using any of the two approaches.

The influence of the number of records becomes more apparent if we realize that the standard error of the mean estimate (and approximately of the median as well) tends to fall of with a rate of

**Table 3.7:** MAFs for each limit-state, calculated both numerically and with the approximate analytical form (global or local fit). The bootstrapped standard error and 90% confidence interval on the MAF estimate are also presented. Additionally, we test the hypothesis that the approximate  $\lambda_{LS}$  is equal to the exact at the 95% confidence level.

limit-state	method	$\lambda_{LS}$	SE <sup>1</sup>	90% CI <sup>2</sup>	“equal” to exact?
IO	exact	0.019	0.011	[0.007, 0.04]	
	global	0.017	> 1000	[0.005, 0.33]	yes
	local	0.008	2.5	[0.004, 0.04]	yes
CP	exact	0.0004	0.0002	[0.0002, 0.0009]	
	global	0.0002	0.0008	[0.0001, 0.0004]	yes
	local	0.0005	> 1000	[0.0001, 0.7]	yes
GI	exact	0.0001	0.00007	[0.0001, 0.0003]	
	global	0.00003	0.00006	[0.00001, 0.00002]	yes
	local	0.0004	> 1000	[0.00003, 160]	yes

<sup>1</sup> Standard Error      <sup>2</sup> Confidence Interval

$1/\sqrt{n}$  where  $n$  is the number of records (e.g., Benjamin and Cornell, 1970). Hence, quadrupling the number of records to use a total of  $n = 80$ , results in only half the dispersion, while decreasing it by a factor of four, to use only  $n = 5$ , will (approximately) double the dispersion.

How do the standard errors in the fractile capacities translate to the estimates of the MAFs? By applying the bootstrap to both the “exact” numerical (Equation 3.11) and the approximate analytic form (Equation 3.12) with either a local or a global fit to the hazard curve, we get the results shown in Table 3.7. As seen from the “exact” results, the limited sample of 20 records causes standard errors in the order of 50% in the estimates of the  $\lambda_{LS}$  for all limit-states. On the other hand, the approximation through Equation (3.12) considerably increases the standard error; in some cases it is in the order of 200% but sometimes the approximation totally fails and considerably overestimates the MAF. For the IO limit-state, it is the approximation with a global fit that may be destabilized, while at the CP and GI limit-state, it is the local fit that may become highly inaccurate. What happens is that individual bootstrap samples violate the assumptions needed to derive Equation (3.12); in some cases the *IM*-capacities are not nearly lognormally distributed and in other cases either the global or the local fit fail to capture the shape of the hazard curve.

The bootstrap also offers us a way to investigate the accuracy of the approximate versus the “exact” calculation of the MAFs, given that we have only used 20 records. By bootstrapping the difference of the “exact” minus the approximate MAFs, a 95% confidence interval can be generated for each limit-state. If the interval contains zero, then, at the 95% confidence level, we cannot reject the hypothesis that the analytical and the numerical method produce the same results. As seen in Table 3.7, given the record-to-record variability and the limited sample size, the approximate results cannot be distinguished from the exact ones for any limit-state. In general, as long as we take care not to violate the stated assumptions, Equation (3.12) will provide good estimates.

### 3.7 Conclusions

The step-by-step practical application of Incremental Dynamic Analysis has been demonstrated for a 9-story steel moment-resisting frame. By using publicly available software it has become almost trivial to perform the analysis, interpolate the IDA curves, estimate limit-state capacities and summarize the results into a format that can be easily integrated with modern PBEE frameworks. IDA offers a complete methodology to handle the abundant data from numerous analyses and extract useful conclusions. Still, the attention to detail is important: How many records, how

many runs per record, how well interpolated, the use of approximations, are just some of the issues that can make a difference in the accuracy of the final IDA results. The methods that have been presented are designed to strike a favorable compromise between speed and accuracy and thus resolve such issues. Perhaps, the single most important thing to remember is the wealth of information that can be found in IDA if only we take advantage of ever-cheaper computing power and automated methods to investigate the structure's behavior.

### **3.8 Acknowledgements**

Financial support for this research was provided by the sponsors of the Reliability of Marine Structures Affiliates Program of Stanford University.

# Direct Estimation of the Seismic Demand and Capacity of Oscillators with Multi-Linear Static Pushovers through Incremental Dynamic Analysis

Vamvatsikos, D. and Cornell, C. A. (2003b). *Earthquake Engineering and Structural Dynamics*, (in preparation).

## 4.1 Abstract

SPO2IDA is introduced, a new software tool that is capable of practically instantaneously recreating the seismic behavior of oscillators with complex multi-linear backbones at almost any period. Essentially, it provides a direct connection between the Static Pushover (SPO) curve and the results of Incremental Dynamic Analysis (IDA), a computer-intensive procedure that offers thorough (demand and capacity) prediction capability by using a series of nonlinear dynamic analyses under a suitably scaled suite of ground motion records. To achieve this, the seismic behavior of numerous single-degree-of-freedom (SDOF) systems is investigated through IDA. The oscillators are of moderate period with pinching hysteresis and feature backbones ranging from simple bilinear to complex quadrilinear with an elastic, a hardening and a negative-stiffness segment plus a final residual plateau that terminates with a drop to zero strength. The results of the analysis are summarized into their 16%, 50% and 84% fractile IDA curves. By appropriately reducing the fractile IDAs down to a few parameters and finding the simplest backbones that can mimic the seismic performance of more complex ones, we introduce a unique and efficient way to treat the backbone shape. The vast economies that are realized in the number of backbones to be investigated allow us an easy extension to the all-periods pinching model, opening the way to similar extensions designed to cover other aspects of SDOF systems. The final product is SPO2IDA, an accurate, spreadsheet-level tool for Performance-Based Earthquake Engineering that is freely available on the internet. It offers effectively instantaneous estimation of demands and limit-state capacities, in addition to conventional strength reduction  $R$ -factors and inelastic displacement ratios, for any SDOF system whose SPO curve can be approximated by such a quadrilinear backbone.

## 4.2 Introduction

Of great interest in Performance-Based Earthquake Engineering (PBEE) is the accurate estimation of the seismic demand and capacity of structures. To accomplish the task several important meth-

ods have emerged, a promising one being Incremental Dynamic Analysis (IDA), a parametric analysis method that estimates seismic demand and capacity by subjecting the structural model to several ground motion records, each scaled to multiple levels of intensity (Vamvatsikos and Cornell, 2002a). Still, the need for simplified methods for professional practice remains, and the rational choice has often been the use of results stemming from the dynamic analysis of single-degree-of-freedom (SDOF) approximations to the multi-degree-of-freedom (MDOF) structural model. Such methods often use an oscillator with a backbone curve that mimics the Static Pushover (SPO, also known as Nonlinear Static Procedure) curve of the MDOF structure (e.g., FEMA, 1997). However, most systematic demand research efforts have not progressed further than using an oscillator with a bilinear backbone, allowing only for either positive (Nassar and Krawinkler, 1991; Lee et al., 1999) or negative (Al-Sulaimani and Roessett, 1985) post-yield stiffness or, still more simply, elastic perfectly-plastic behavior (Riddell and Newmark, 1979; Newmark and Hall, 1982; Vidic et al., 1994; Miranda, 2000), while few, if any, attempts have been made to quantify its dynamic, global-instability collapse capacity (e.g., FEMA, 2000a). As an extension to existing procedures, it is only natural to apply the IDA method to SDOF systems featuring a variety of backbones and to attempt to quantify the resulting demands and capacities in a handful of comparatively simple empirical equations.

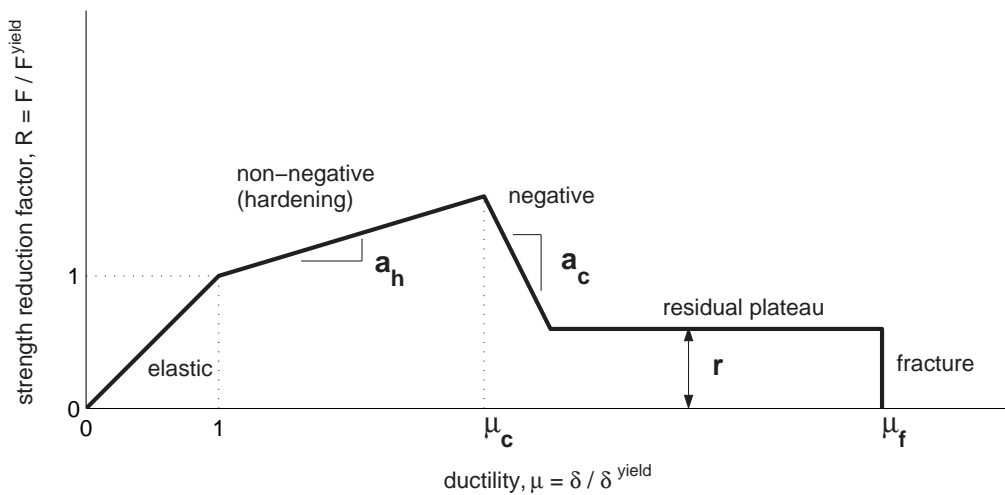


**Figure 4.1:** The backbone to be investigated and its five controlling parameters.

### 4.3 Methodology

To study the influence of the SPO curve on the dynamic behavior, we have chosen a piecewise linear backbone that is composed of up to four segments (Figure 4.1). A full quadrilinear backbone starts elastically, yields at ductility  $\mu = 1$  and hardens at a slope  $a_h \in [0, 1)$ , then at ductility  $\mu_c \in (1, +\infty)$  turns negative at a slope  $a_c \in [-\infty, 0)$ , but is revived at  $\mu_r = \mu_c + (1 - r + (\mu_c - 1)a_h)/|a_c|$  by a residual plateau of height  $r \in [0, 1]$ , only to fracture and drop to zero strength at  $\mu_f \in [1, +\infty)$ . By suitably varying the five parameters,  $a_h$ ,  $\mu_c$ ,  $a_c$ ,  $r$  and  $\mu_f$ , almost any (bilinear, trilinear or quadrilinear) shape of the SPO curve may easily be matched.

To fully investigate the dynamic behavior of a single SDOF model, we will use IDA for a suite of thirty ground motion records (Table 4.1) that have been selected to represent a scenario earthquake; the moment magnitude is within the range of 6.5 – 6.9, they have all been recorded on firm soil (USGS type C or B) and show no directivity effects. IDA involves performing a series of nonlinear dynamic analyses for each record by scaling it to several levels of intensity that are suitably selected to uncover the full range of the model's behavior: elastic, yielding, non-linear

**Table 4.1:** The suite of thirty ground motion records used.

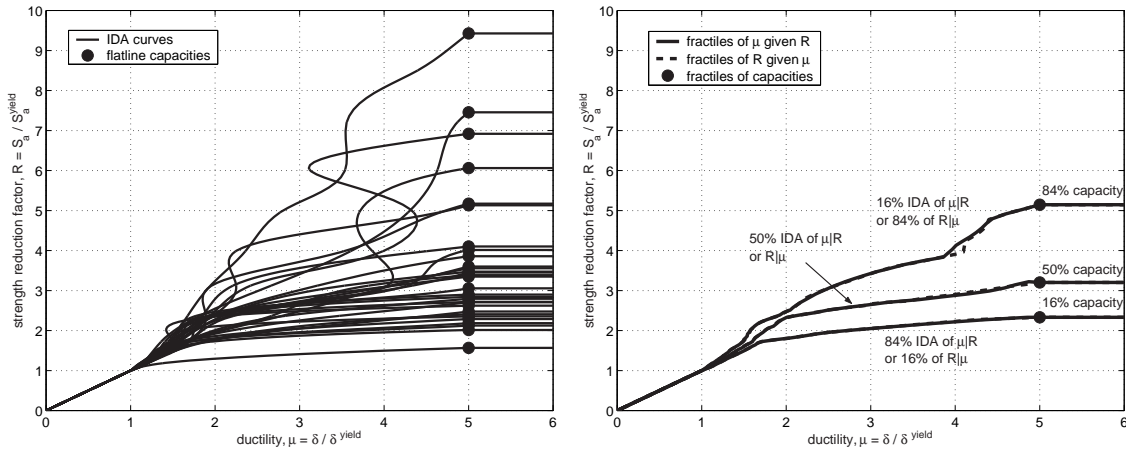
No	Event	Station	$\phi^{\circ}$ <sup>1</sup>	Soil <sup>2</sup>	M <sup>3</sup>	R <sup>4</sup> (km)	PGA (g)
1	Loma Prieta, 1989	Agnews State Hospital	090	C,D	6.9	28.2	0.159
2	Northridge, 1994	LA, Baldwin Hills	090	B,B	6.7	31.3	0.239
3	Imperial Valley, 1979	Compuertas	285	C,D	6.5	32.6	0.147
4	Imperial Valley, 1979	Plaster City	135	C,D	6.5	31.7	0.057
5	Loma Prieta, 1989	Hollister Diff. Array	255	-,D	6.9	25.8	0.279
6	San Fernando, 1971	LA, Hollywood Stor. Lot	180	C,D	6.6	21.2	0.174
7	Loma Prieta, 1989	Anderson Dam Downstream	270	B,D	6.9	21.4	0.244
8	Loma Prieta, 1989	Coyote Lake Dam Downstream	285	B,D	6.9	22.3	0.179
9	Imperial Valley, 1979	El Centro Array #12	140	C,D	6.5	18.2	0.143
10	Imperial Valley, 1979	Cucapah	085	C,D	6.5	23.6	0.309
11	Northridge, 1994	LA, Hollywood Storage FF	360	C,D	6.7	25.5	0.358
12	Loma Prieta, 1989	Sunnyvale Colton Ave	270	C,D	6.9	28.8	0.207
13	Loma Prieta, 1989	Anderson Dam Downstream	360	B,D	6.9	21.4	0.24
14	Imperial Valley, 1979	Chihuahua	012	C,D	6.5	28.7	0.27
15	Imperial Valley, 1979	El Centro Array #13	140	C,D	6.5	21.9	0.117
16	Imperial Valley, 1979	Westmoreland Fire Station	090	C,D	6.5	15.1	0.074
17	Loma Prieta, 1989	Hollister South & Pine	000	-,D	6.9	28.8	0.371
18	Loma Prieta, 1989	Sunnyvale Colton Ave	360	C,D	6.9	28.8	0.209
19	Superstition Hills, 1987	Wildlife Liquefaction Array	090	C,D	6.7	24.4	0.18
20	Imperial Valley, 1979	Chihuahua	282	C,D	6.5	28.7	0.254
21	Imperial Valley, 1979	El Centro Array #13	230	C,D	6.5	21.9	0.139
22	Imperial Valley, 1979	Westmoreland Fire Station	180	C,D	6.5	15.1	0.11
23	Loma Prieta, 1989	Halls Valley	090	C,C	6.9	31.6	0.103
24	Loma Prieta, 1989	WAHO	000	-,D	6.9	16.9	0.37
25	Superstition Hills, 1987	Wildlife Liquefaction Array	360	C,D	6.7	24.4	0.2
26	Imperial Valley, 1979	Compuertas	015	C,D	6.5	32.6	0.186
27	Imperial Valley, 1979	Plaster City	045	C,D	6.5	31.7	0.042
28	Loma Prieta, 1989	Hollister Diff. Array	165	-,D	6.9	25.8	0.269
29	San Fernando, 1971	LA, Hollywood Stor. Lot	090	C,D	6.6	21.2	0.21
30	Loma Prieta, 1989	WAHO	090	-,D	6.9	16.9	0.638

<sup>1</sup> Component    <sup>2</sup> USGS, Geomatrix soil class    <sup>3</sup> moment magnitude    <sup>4</sup>closest distance to fault rupture

inelastic and finally global dynamic instability. Each dynamic analysis can be represented by at least two scalars, an Intensity Measure (*IM*), which corresponds to the scaling factor of the record (e.g., the strength reduction factor  $R = S_a(T_1, 5\%) / S_a^y(T_1, 5\%)$ , which is equal to the 5%-damped first-mode spectral acceleration  $S_a(T_1, 5\%)$  normalized by its value that causes first yield) and a Damage Measure (*DM*), which monitors the structural response of the model (e.g., peak ductility  $\mu$ ).

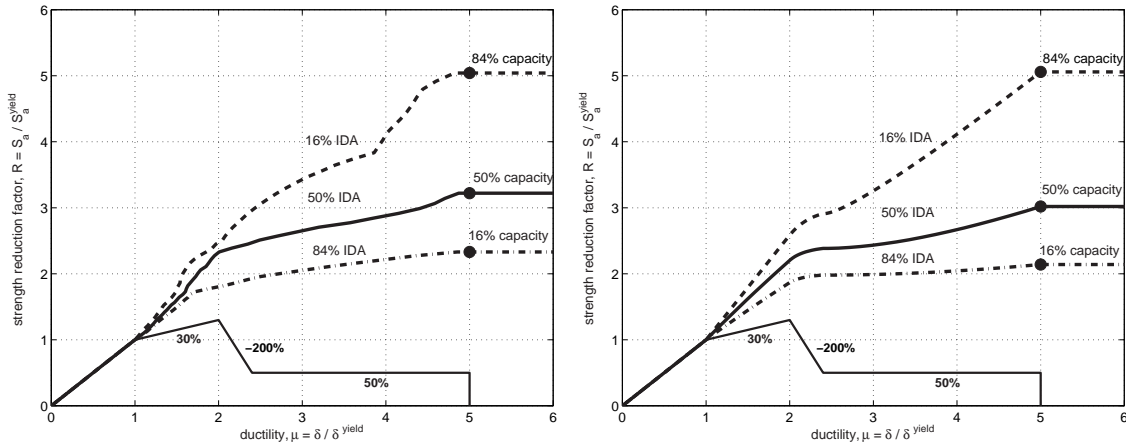
By suitably interpolating between the runs that were performed for a given record, we can plot on the *DM-IM* axes an IDA curve for each record, e.g., Figure 4.2(a). Each curve ends with a characteristic “flatline” which indicates that the *DM* rapidly increases towards “infinite” values for small changes in the *IM*, thus signalling global dynamic instability and defining the global-collapse capacity at the *IM* where the IDA curve effectively becomes flat. Such “capacity points” are visible as black dots in Figure 4.2(a). A set of IDA curves can be summarized into 16%, 50% and 84% cross-sectional fractile IDAs of response  $\mu$  given the intensity  $R$  or  $R$  given  $\mu$ , depending on how the cross-sections of the curves are taken, e.g., at specified levels of  $R$  or  $\mu$  (Vamvatsikos and Cornell, 2002a). Fortunately, under suitable assumptions of continuity and monotonicity, the  $x\%$ -fractile IDA  $\mu_{x\%}(R)$  ( $x \in \{16, 50, 84\}$ ) of  $\mu$  given  $R$ , will be identical (or nearly identical if the assumptions are slightly violated, Vamvatsikos and Cornell, 2004a) to the  $(100 - x\%)$ -fractile IDA  $R_{(100-x\%)}(\mu)$  of  $R$  given  $\mu$  as shown in Figure 4.2(b). As a direct result, if we similarly summarize the capacity points, the  $(100 - x\%)$  global-instability collapse capacity will always appear on the flatline of the  $x\%$ -fractile IDA of  $\mu$  given  $R$  (Figure 4.2(c)).

By thus summarizing the fractile IDA curves, we get both a characterization of the distri-



(a) Thirty IDA curves and flatline capacities

(b) Summarization into fractile IDAs, given  $R$  or  $\mu$



(c) The fractile IDAs from (b) versus the SPO curve

(d) The fractile IDAs, as estimated by SPO2IDA

**Figure 4.2:** Generating the fractile IDA curves and capacities from dynamic analyses versus estimating them by SPO2IDA for an SPO with  $a_h = 0.3$ ,  $\mu_c = 2$ ,  $a_c = -2$ ,  $r = 0.5$ ,  $\mu_f = 5$ .

bution of  $R$  given  $\mu$  and  $\mu$  given  $R$ . While the individual IDAs are highly variable and often non-monotonic, i.e., higher values of  $R$  do not necessarily correspond to higher values of  $\mu$  (Vamvatsikos and Cornell, 2002a), the fractiles are much smoother and empirically are found to be almost always monotonic. They are thus suitable to be modeled with relatively simple functions.

If we choose to plot the SPO of the SDOF system on  $\mu$  versus  $R = F/F^y$  axes (where  $F$  is the total base shear and  $F^y$  its value that causes first yield) we can make it appear versus the summarized IDA curves on the same graph (Vamvatsikos and Cornell, 2002a), as in Figure 4.2(c). Such a comparison shows that the SPO and the fractiles are composed of the same number of corresponding and distinguishable segments. Moreover, each segment has its own nature. The elastic segment of the SPO naturally coincides with the elastic IDA region for all three fractiles, while the yielding and hardening of the SPO forces the 16%, 84% IDAs to branch uniformly around the median which approximately follows the familiar “equal displacement” rule ( $\mu \approx R$ ) for moderate (and long) periods (Veletsos and Newmark, 1960). The SPO’s negative stiffness appears as a characteristic flattening of all three IDAs that stops when the residual plateau is activated, causing

the “revival” of the IDA curves towards higher  $R$ -values. Ultimately, all IDA curves submit to the SPO fracturing, thus signaling collapse by producing a flatline (and the corresponding fractile capacity point).

This consistent behavior makes it is possible to approximate each separate segment of the IDA by its prominent features, e.g., the height of the flatline or the slope and intercept of a fitted line. By examining a large enough population of SDOF systems with different shapes of the backbone, we can track the evolution of the features of each segment, and subsequently model them as a function of the SPO parameters. Thus, we are able to generate almost the same fractile IDAs and capacities (within some acceptable tolerance) without needing to repeat the multiple dynamic analyses. This set of rules and equations will be collectively called the SPO2IDA tool, a typical example of its accuracy visible in Figure 4.2(d).

However, the complexity of the backbone has forced us to initially limit the scope of our investigation by choosing SDOF systems that share an identical moderately pinching hysteresis model with no cyclic deterioration (Nassar and Krawinkler, 1991), having viscous damping of  $\xi = 5\%$  and a moderate period of  $T_1 = 0.92\text{sec}$ . The results will thus be a good approximation for the moderate period range, and will provide a good basis for an extension to shorter and longer periods. Still, the full investigation of a five-dimensional space of parameters requires a staggering amount of dynamic analyses, especially since the parameters do not influence the IDAs independently of each other. Nevertheless, there are several facts that allow us to reduce the size of the problem. First, since we are measuring the *peak* ductility, at any given value of  $\mu$  the IDA will only be influenced by the segments of the SPO backbone that appear at lesser or equal ductilities. This would not be true if we were monitoring, say, permanent deformation. So, in fitting the hardening branch, the negative stiffness is of no consequence, while in fitting the negative branch, the plateau plays no part. Therefore, we can cut the problem into smaller pieces, as we only need to investigate a bilinear elastic-hardening, a trilinear elastic-hardening-negative but still, a full quadrilinear for the plateau. Even then, we may not have to go all the way, even for the plateau. The idea is that some of the SPO parameters may be redundant, so their influence can be summarized in only one or two new parameters which combine them. In effect this means that (for the same damping and period) we are going to search for “equivalent backbones”, in the sense that such oscillators would share very similar dynamic behavior in the region of interest, as manifested by their displaying the same fractile IDAs.

When modeling the IDA features we will use least-squares fits of polynomials, either in the linear or in the log-domain. To simplify the expressions to follow, we will represent linear combinations of functions  $p(y_1, \dots, y_k)$  of given variables  $y_1, \dots, y_k$ , as a sum  $\sum_i b_{x\%,i} p_i(y_1, \dots, y_k)$ , where the appropriate functions  $p_i$  and coefficients  $b_{x\%,i}$  (corresponding to the  $x\%$ -fractile) will be provided in tables.

As a general principle, note that the relatively small number of records, the record-to-record variability and the fitting error, combine to introduce some noise which tends to become larger as the ductility response itself increases. So we will generally fit elaborate models but only as complex as the noise in the IDA results allows. Still, as we try to interpolate as closely as possible given the noise, we are risking eliciting criticism for “overfitting” (in the sense that a simpler model would do only a little worse). The idea is to provide as a complete and objective model as the record-to-record noise allows, and in retrospect observe it and simplify it enough to satisfy the arithmo-phobic users.

## 4.4 Moderate period pinching model

### 4.4.1 Fitting the hardening branch of the IDA

Fitting the hardening part is the easiest task, and actually several attempts have been done in the past (Nassar and Krawinkler, 1991; Lee et al., 1999; Miranda, 2000), sometimes for a wider

variety of parameters (e.g., site conditions, cyclic strength deterioration etc.) than what we will use here. Since this fit only involves a single parameter,  $a_h$ , it is relatively straightforward; we will assume a second-order polynomial model in the log-space to fit the fractile ductilities given  $R$ , and subsequently calculate and fit the resulting coefficients for several values of the hardening slope  $a_h$ . This procedure produces for each of the three fractile IDAs the following model

$$\ln \mu_{x\%} = \beta_{x\%} \ln R + \gamma_{x\%} \ln^2 R, \quad R \in (1, R_{(100-x)\%}(\mu_c)] \quad (4.1)$$

$$\text{where } \beta_{x\%}, \gamma_{x\%} = \sum_i b_{x\%,i} P_i(a_h), \quad \text{for any } a_h \in [0, 0.9]$$

where the coefficients and functions can be conveniently found in Table 4.2. An example of its application is found in Figure 4.2(d) for  $1 < \mu \leq 2$ .

**Table 4.2:** Coefficients and functions needed for the IDA hardening part in Equation (4.1).

$x\% =$	$b_{x\%,i}$ for $\beta_{x\%}$			$b_{x\%,i}$ for $\gamma_{x\%}$		
	16%	50%	84%	16%	50%	84%
1	0.6164	0.7132	1.0024	0.1454	0.2928	0.4003
$a_h$	-0.1697	-0.0415	1.5907	-0.1394	-0.6415	-3.0742
$a_h^2$	1.3103	1.5158	-7.1722	-0.2576	0.0347	9.7763
$a_h^3$	-1.9551	-2.5525	10.3472	0.6156	0.9604	-12.8813
$a_h^4$	1.2201	1.3921	-4.8024	-0.3707	-0.6620	5.8376

The results are actually only mildly dependant on  $a_h$ , especially for low ductilities. So we can roughly approximate the median IDA by the “equal displacement rule”, under which  $\mu_{50\%}(R) \approx R$ , and generate the 16%, 84% fractiles as the edges of a 60%-wide band centered on the median (in the log-space), i.e.,  $\mu_{(50\pm 34)\%}(R) \approx \mu_{50\%}(R)^{1\pm 0.3} \approx R^{1\pm 0.3}$ .

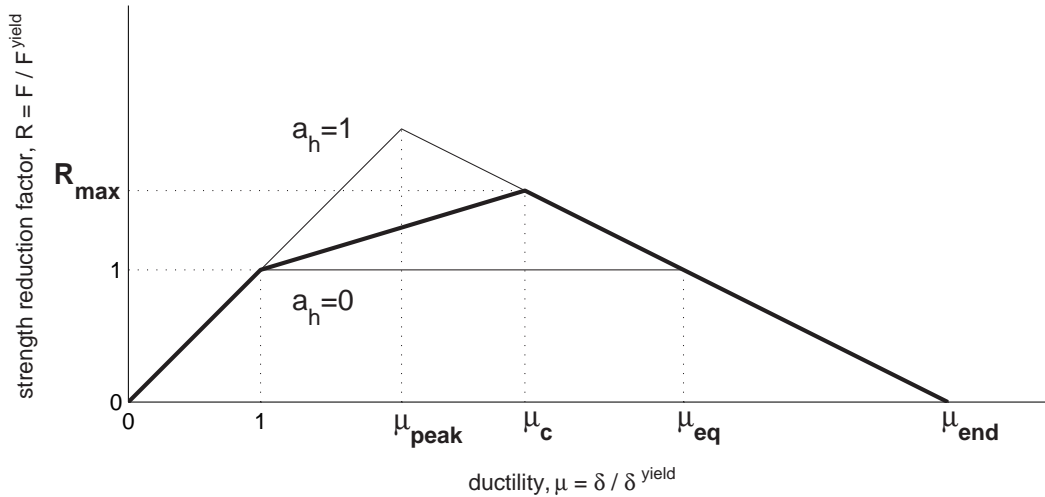


**Figure 4.3:** An elastic-hardening-negative backbone and the two extremes of its “equivalent” set.

#### 4.4.2 Fitting the negative branch of the IDA

Negative stiffness is found in SPOs of structures such as non-ductile reinforced-concrete frames, braced steel frames, moment-resisting steel frames with fracturing connections and P- $\Delta$  sensitive systems. The most prominent feature of the negative branch is the characteristic flattening of the summarized IDAs which results in a flatline unless it is arrested by the residual plateau, as seen in Figure 4.2(c), for  $2 < \mu \leq 2.4$ . By accurately capturing this feature, the entire branch

could be modeled as a continuous convex curve that smoothly departs from the hardening segment at ductility  $\mu_c$  to blend into the flatline at  $\mu_{\text{end}} = \mu_c + (1 + a_h \mu_c - a_h)/|a_c|$ . Still, appropriately modeling the negative branch flatline requires a trilinear (elastic-hardening-negative) backbone that involves three independent parameters ( $a_c$ ,  $a_h$  and  $\mu_c$ ). Conveniently enough, it was found empirically that this flatline height and, even more, the complete negative part of the IDA are very similar for the set of backbones that have coincident negative branches, like those in Figure 4.3. Actually, the flatline height among such an equivalent set varies only a little and always in a consistent linearly increasing fashion between the two extremes, i.e., the  $a_h = 0$  and the  $a_h = 1$  cases where the negative branch starts at  $\mu_{\text{eq}} = \mu_c + a_h(\mu_c - 1)/|a_c|$ , and  $\mu_{\text{peak}} = (\mu_c |a_c| + 1 + a_h(\mu_c - 1))/(1 + |a_c|)$  respectively. So we only need to model the capacities for the extreme values of  $a_h$  and linearly interpolate in-between. The final recommended model becomes:

$$R_{(100-x)\%}(\mu_{\text{end}}) = R_{(100-x)\%}(\mu_c) + \left(e^{\beta_{x\%}} - 1\right) \left[ l_{(100-x)\%}^{\text{eq}} + a_h \left( \mu_{\text{peak}} - l_{(100-x)\%}^{\text{eq}} \right) \right], \quad (4.2)$$

$$l_{(100-x)\%}^{\text{eq}} = (\mu_{\text{eq}})^{\gamma_{x\%}}, \quad \text{for any } a_c \in [-4, -0.01], a_h \in [0, 1), \mu_c \in [1, 9] \quad (4.3)$$

$$\text{where } \beta_{x\%}, \gamma_{x\%} = \sum_i b_{x\%,i} p_i(a_c)$$

where the coefficients are found in Table 4.3.

**Table 4.3:** Coefficients and functions needed for the flatline of the IDA softening part in Equation (4.2).

$x\% =$	$b_{x\%,i}$ for $\beta_{x\%}$ ( $y = \ln  a_c $ )			$b_{x\%,i}$ for $\gamma_{x\%}$ ( $y =  a_c $ )		
	16%	50%	84%	16%	50%	84%
$y^{-1}$	0	0	0	-0.5111	-0.3817	-0.4118
1	0.2252	0.3720	0.6130	-0.6194	-0.3599	-0.2610
$y$	-0.1850	-0.3023	-0.4392	0.0928	-0.0019	-0.0070
$y^2$	0.1039	0.1056	0.0847	0.0163	0.0186	0.0158

As a first, simpler approximation for moderate values of the negative slope  $a_c$ , one may assume that in log-space the 16% and 84% flatlines are roughly 30%-lower and 30%-higher than the median, i.e.,  $R_{(50\pm 34)\%}(\mu_{\text{end}}) = R_{50\%}(\mu_{\text{end}})^{1\pm 0.3}$ .

#### 4.4.3 Fitting the residual part of the IDA

The residual plateau in the SPO is encountered, for example, in braced frames or fracturing moment-resisting frames. Only limited inspection of such models has appeared in the literature (e.g., Stear and Bea, 1999). The effect of the SPO residual plateau is to “revive” the IDA, allow it to escape the flatline and move on to higher  $R$ -values, in an almost linear-system-like fashion, e.g., Figure 4.2(c) for  $3 < \mu < 5$ . We can model this prominent feature by a linear model in the log-space and capture this entire IDA region by a continuous convex curve that smoothly rises from the flatline. This would have been a difficult model, depending on all five backbone parameters, but for the empirical finding that in this region of the IDA, the full quadrilinear model displays virtually the same behavior as an equivalent trilinear (elastic-negative-plateau) model that has the same negative slope  $a_c$ , but sports a reduced plateau height of  $r_{\text{eq}} = r/(1 + a_h(\mu_c - 1))$ . Actually,  $r_{\text{eq}}$  is the residual plateau height of the full model but measured relative to the peak  $R$ -value,  $R_{\text{max}} = 1 + a_h(\mu_c - 1)$ , reached by the SPO (Figure 4.3), instead of relative to the yield strength.

This revelation leaves us with only two influential parameters,  $a_c$  and  $r_{eq}$ , resulting in the model:

$$\begin{aligned} \ln \mu_{x\%} &= \beta_{x\%} + \gamma_{x\%} \ln R, & R \in (R_{(100-x)\%}(\mu_r), R_{(100-x)\%}(\mu_f)] & \quad (4.4) \\ \text{where } \beta_{x\%}, \gamma_{x\%} &= \sum_i b_{x\%,i} p_i(a_c, r_{eq}), \\ &\text{for any } a_c \in [-4, -0.01], \quad r_{eq} \in [0.05, 0.90] \end{aligned}$$

where the coefficients can be found in Table 4.4. An example of this model's application can be seen in Figure 4.2(d) for  $3 < \mu \leq 5$ .

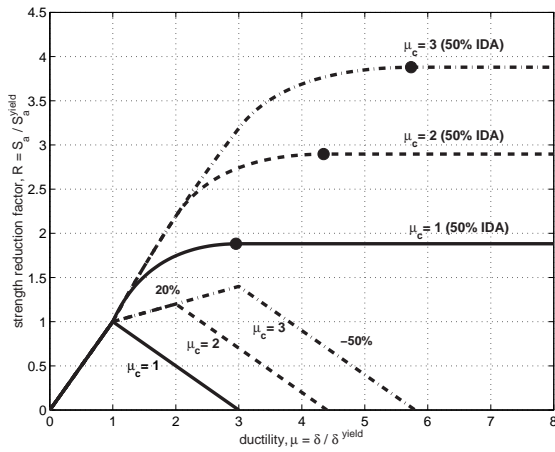
**Table 4.4:** Coefficients and functions needed for fitting the IDA residual part in Equation (4.4).

$x\% =$	$b_{x\%,i}$ for $\beta_{x\%}$			$b_{x\%,i}$ for $\gamma_{x\%}$		
	16%	50%	84%	16%	50%	84%
1	-0.3615	0.2391	0.9557	1.1022	1.0846	1.0176
$\ln  a_c $	-0.0729	-0.0297	-0.0696	0.0180	0.0081	0.0203
$\ln r_{eq}$	-0.4557	-0.4907	-0.4759	0.1111	0.1218	0.1086
$\ln r_{eq} \cdot \ln  a_c $	-0.0372	-0.0272	-0.0308	0.0136	0.0086	0.0061

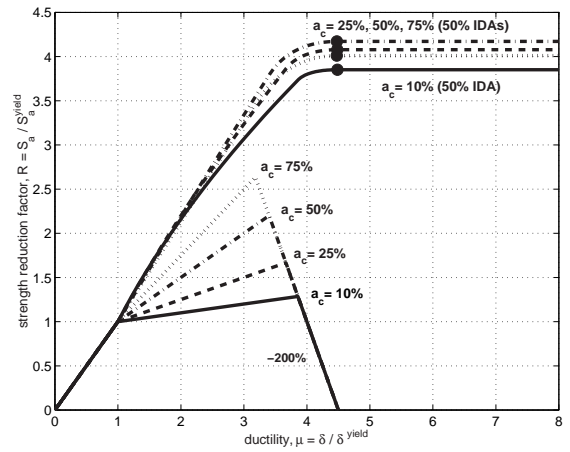
By observing the results, one can derive that the median IDA does behave much like a secant linear segment that takes on smaller slopes as  $r_{eq}$  decreases, eventually becoming one with the flatline induced by the negative branch of the SPO. So, by restricting ourselves to (quite practical) ductilities of 10 or less, the modeling could be further simplified if one decides to model the residual branch of the median IDA as a secant by assuming  $\gamma_{50\%} = 1$ , while generating the 16%, 84% fractiles as a 100%-wide band centered on the median (in the log-space), i.e.,  $\mu_{(50\pm 34)\%}(R) \approx \mu_{50\%}(R)^{1\pm 0.5} \approx \beta_{50\%} \cdot R^{1\pm 0.5}$ . The existing table of  $\beta_{50\%}$  coefficients, although not optimal, can still be used for this approximation, since the difference is negligible.

#### 4.4.4 Joining the pieces: The SPO2IDA tool

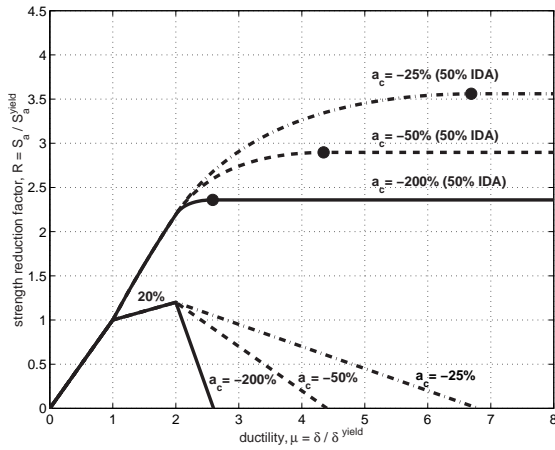
We have separately modeled the three segments but we have chosen to keep track of only the flattening caused by the negative SPO and the ‘‘secant’’ caused by the residual. To join them into smooth and continuous curves that accurately resemble the fractile IDAs we need two ‘‘filleting curves’’ that will connect the negative branch flatline to the hardening and the ‘‘secant’’. We can choose to neglect such details and linearly extend all three pieces to a point of mutual interception, which is usually accurate enough. Alternatively, we can generate splines through a knot-insertion algorithm (Farin, 1990), which provides a smooth transition from segment to segment, while at the same time offering computational simplicity and robustness, as it preserves convexity and can be made to be monotonic (as the fractile IDAs are empirically known to be). Once this step has been completed, we have an almost complete description of the IDA for any ductility, modeled as an invertible one-to-one function of either  $\mu$  or  $R$ , a choice left to the user as an advantage of the equivalency of the fractiles given  $R$  or  $\mu$ . We are only missing the final flatline, caused by the SPO's ending at ductility  $\mu_f$ . This can be accurately and easily modeled in the IDAs by adding a flatline at height  $R_{(100-x)\%}(\mu_f)$ , simultaneously producing the  $(100-x)\%$ -fractile of global-collapse capacity. By implementing in software the modeling and joining of the IDA segments we have generated the SPO2IDA tool, available in a spreadsheet or as an online internet application (Vamvatsikos, 2001), and it does a remarkable job of reproducing the real behavior of oscillators, as demonstrated in Figure 4.2(d).



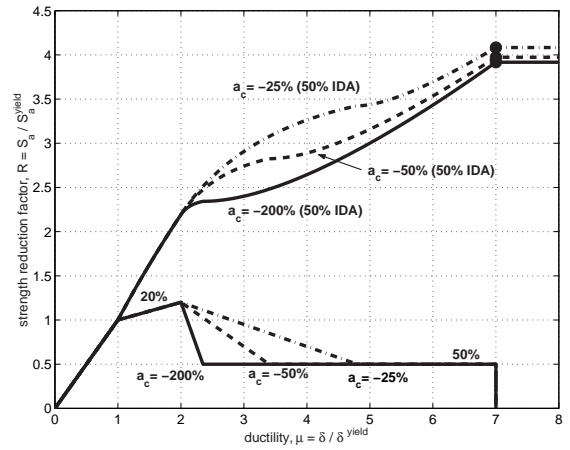
(a) Increasing  $\mu_c$  helps performance



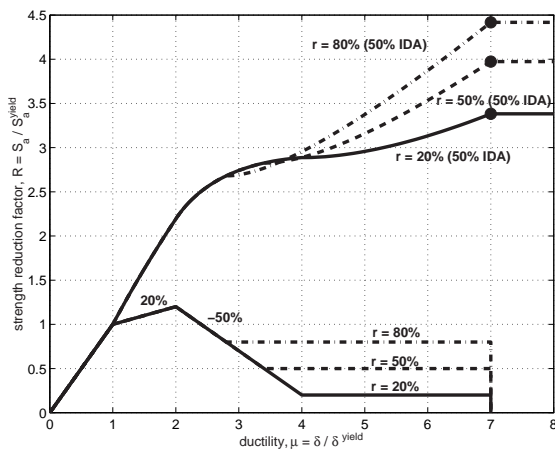
(b) Increasing  $a_h$  has negligible effects if same  $\mu_{eq}$



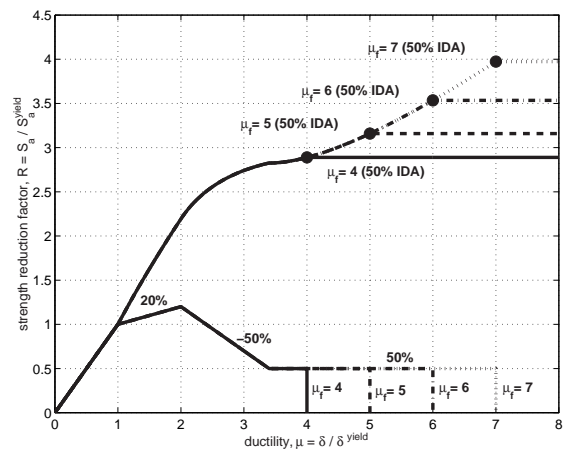
(c) The milder the negative slope,  $a_c$ , the better



(d)  $a_c$  is changing, but constant  $r_{eq}$  anchors capacity



(e) Higher plateau  $r$  benefits demand and capacity



(f) Increasing the fracturing ductility  $\mu_f$  helps

**Figure 4.4:** Demonstrating SPO2IDA: the median demand and collapse capacity as the SPO changes.

#### 4.4.5 Illustrative Results and Observations

The ease of computation provided by such a tool, plus the unique perspective offered by the IDA-versus-SPO picture, can offer remarkable intuition into the seismic behavior of systems. As a demonstration of the SPO2IDA tool, we present Figure 4.4, an array of cases to briefly study the influence of the backbone on the seismic demand and capacity. In each figure we select a basic backbone, vary one or two of its parameters and then generate the median IDA responses and the corresponding global instability collapse-capacities for each case. Figure 4.4(a) shows the benefit of delaying the negative branch of the SPO and allowing hardening to reach higher ductilities. Each increase in  $\mu_c$  allows the median to stay on “equal displacement” longer, proportionally increasing the capacity. On the other hand, in Figure 4.4(b), radically changing the hardening slope  $a_h$  but keeping an identical negative branch generates an equivalent set of trilinear SPOs, whose capacities only slightly increase with  $a_h$ . Actually, the difference in the capacity is small enough to be within the noise in the fitted data, so the resulting capacities are not strictly increasing with  $a_h$ . Decreasing the negative slope  $a_c$  in Figure 4.4(c) has a beneficial effect when no residual plateau is present, as the milder slopes allow higher capacities. Still, if we include an extensive enough residual plateau (Figure 4.4(d)), the benefits of the milder slope are restricted to the somewhat lower  $\mu$ -demands that may influence some earlier limit-states; the global instability collapse capacity is almost the same for all cases, as the backbones have the same  $r_{eq}$ , therefore the milder  $a_c$ 's are providing only a small advantage. Figure 4.4(e) shows the benefits of increasing the residual plateau that consequently increases the slope of the “secant” that the IDA follows, thus improving capacities and decreasing the demands. And finally, Figure 4.4(f) shows the obvious advantage of allowing higher fracturing ductilities  $\mu_f$ . The value of  $\mu_f$  literally decides where to terminate the IDA, at times fully negating the effect of the plateau if it becomes too small; at  $\mu_f = 4$  the IDA hardly receives any benefit from the plateau. As intuitive or surprising as some of the pictures in Figure 4.4 may be, they are only a glimpse of what our new tool can really do.

#### 4.4.6 SPO2IDA error estimates for moderate periods

Since the SPO2IDA tool is based on fitting over only a small subset of the SDOF backbones it can simulate, just showing the fitting error over the sample of oscillators that we have used would greatly underestimate the true prediction error. In order to be objective we have generated a large separate test sample of randomly chosen bilinear, trilinear and quadrilinear backbones, that were analyzed both through full IDA and SPO2IDA. Thus, for each backbone and each of the three  $x\%$ -fractiles we are presented with two IDA curves, the “real” curve  $R_{(100-x)\%}(\mu)$  and the approximate  $\hat{R}_{(100-x)\%}(\mu)$ , or equivalently expressed in  $\mu$  given  $R$  coordinates,  $\mu_{x\%}(R)$  versus  $\hat{\mu}_{x\%}(R)$ .

We are interested in knowing the error in two different settings: error in estimating a demand  $\mu$  given a certain level on intensity  $R$  and error in estimating a capacity  $R$  given a certain level of demand  $\mu$ . In both cases, the *absolute* difference between exact and approximate results tends to increase rapidly when we progress further into the nonlinear range, making this measure unsuitable. We choose instead to quantify the errors by integrating the *relative absolute* difference of each approximate  $x\%$ -fractile IDA curve versus the real one over their length, either in  $\mu$  or  $R$  coordinates accordingly, a concept similar to the one used by Lee et al. (1999):

$$(\varepsilon_R)_{x\%} = \int_0^{\mu_f} \frac{|R_{(100-x)\%}(\mu) - \hat{R}_{(100-x)\%}(\mu)|}{R_{(100-x)\%}(\mu)} d\mu \quad (4.5)$$

$$(\varepsilon_\mu)_{x\%} = \int_0^{R_f} \frac{|\mu_{x\%}(R) - \hat{\mu}_{x\%}(R)|}{\mu_{x\%}(R)} dR \quad (4.6)$$

In each case, the fractile-capacity error  $(\varepsilon_R)_{x\%}$  is calculated over the full demand spectrum from zero to  $\mu_f$ , and the fractile-demand error  $(\varepsilon_\mu)_{x\%}$  is similarly calculated up to  $R_f$ , where either of

the two curves compared flatlines first.

**Table 4.5:** Average fractile-demand and fractile-capacity errors for moderate periods and a variety of backbone shapes, as caused by the fitting in SPO2IDA and by the record-to-record variability in IDA.

$x\% =$	SPO2IDA			10 records			30 records		
	16%	50%	84%	16%	50%	84%	16%	50%	84%
elastic-hardening									
$\varepsilon_R$	0.02	0.01	0.02	0.11	0.07	0.07	0.06	0.04	0.04
$\varepsilon_\mu$	0.01	0.01	0.02	0.06	0.06	0.09	0.04	0.03	0.05
elastic-hardening-negative									
$\varepsilon_R$	0.02	0.03	0.03	0.09	0.06	0.06	0.05	0.03	0.03
$\varepsilon_\mu$	0.02	0.03	0.03	0.07	0.05	0.06	0.04	0.03	0.04
elastic-hardening-negative-plateau									
$\varepsilon_R$	0.16	0.14	0.18	0.20	0.12	0.13	0.12	0.08	0.07
$\varepsilon_\mu$	0.09	0.11	0.18	0.20	0.18	0.23	0.11	0.11	0.14

What is more important to the user than just an error measure is an assessment of how large is SPO2IDA’s estimation error, caused by imperfect fitting, as compared to the full IDA estimation error caused by the record-to-record variability when using a limited sample of records. To provide such a standard for comparison, we will use the bootstrap method (Efron and Tibshirani, 1993) to estimate the equivalent  $(\varepsilon_R)_{x\%}$  and  $(\varepsilon_\mu)_{x\%}$  error that one would expect to encounter when using only 10 or 30 randomly chosen records from the same scenario earthquake. According to the bootstrap principle, the original 30 records are sampled with replacement to generate numerous alternate samples of 10 and 30 records, which are then applied to each of the randomly-chosen backbones, thus resulting to a large number of alternate estimates of the fractile IDAs for each test-case. Then, using the original 30-record suite results as “exact”, the average (over all bootstrap samples)  $(\varepsilon_R)_{x\%}$  and  $(\varepsilon_\mu)_{x\%}$  are calculated, as shown in Table 4.5.

Before we interpret these results, it is important to understand that SPO2IDA was based on the 30-record IDA, thus its error, as calculated in the table, comes *in addition* to the error induced by record-variability in the 30-record fractile IDAs, i.e., SPO2IDA cannot be more accurate than a 30-record IDA. Still, if the additional (fitting induced) error it incurs is small enough, it will disappear (as when taking the square root of sum of squares of the two errors) under the considerable (record-variability induced) error in estimating the fractiles with a 30-record IDA. Thus, by comparing the  $(\varepsilon_R)_{x\%}$  and  $(\varepsilon_\mu)_{x\%}$  of SPO2IDA versus the average such errors due to the record-to-record variability, we observe that SPO2IDA can estimate the fractile demands or capacities with an error comparable to the record-to-record noise around the 10-record full IDA results. This means that statistically, the difference between the full IDA and SPO2IDA results is on average insignificant when only 10 records are used. If 30 records are employed for IDA, SPO2IDA again performs very well for all backbones except the complex quadrilaterals where it has, on average, an error somewhat more significant, but still comparable to the record-to-record induced noise. All in all, SPO2IDA is proven to be remarkably accurate, able to outperform the 10-record full IDA and in many cases match the 30-record IDA.

Naturally, the values in Table 4.5 do not tell the whole story, as they describe the performance of SPO2IDA averaged over numerous backbone shapes and over the length (either in  $R$  or  $\mu$  terms) of the fractile curves. Some individual backbone shapes may be captured better than others and within the curves themselves some segments may be more accurately matched. As evident from Table 4.5, the error tends to increase for more complex backbones. This is caused by the cascading of the models, i.e., as more segments are added to the backbone, each additional segment relies on the accuracy achieved in the previous ones. Thus, the more complex our backbone, the more

error we should expect in the later segments (e.g., the residual plateau). But even within the same segment of the curve, the distribution of the error is not homogeneous, neither for the full IDA, nor for the SPO2IDA. In the IDA results, as the ductility increases beyond yielding, the record-to-record variability and the error it induces increase as well. This, in turn, introduces higher noise in the fitted data, thus making the fitted equations less accurate at higher ductilities. So, in general, one should expect errors lower than average at low ductilities and higher than average at high ductilities for both methods. Finally, since we have relied on regression to fit the IDA curves, just like all fits these equations will perform better in the middle of the fitted dataset and worse at the edges (Weisberg, 1985). So, one should generally expect higher errors closer to the edges where some fits are least accurate, e.g., at  $a_c = -0.01$  for Equation 4.2 or at  $r_{eq} = 0.9$  and  $a_c = -0.01$  in Equation 4.4. All such observations taken into consideration, there are some combinations of backbone parameters that may cause SPO2IDA to produce a mediocre estimate for some segment of the IDA, but in our experience even these cases are rare.

## 4.5 Extension to all-periods pinching model

Up to now we have described a procedure used to obtain the fractile IDA curves of a fairly limited model. Still, this can be easily extended to other periods, dampings, or hysteretic models. What we have really introduced above is a methodology that permits the accurate modeling of the SDOF fractile IDA curves for complex backbones by investigating only a small number of them. If one wishes to capture the behavior of a different SDOF system, or use a different suite of ground motion records, all that is needed is repeating the above three fits for the hardening, negative and residual part to include the new parameters. As an example, we are going to extend SPO2IDA to both short and long periods, still using the same suite of 30 records, moderately pinching hysteresis and viscous damping of  $\xi = 5\%$ . The overall concept will be precisely the same as for the moderate periods, simply the necessary coefficients will be given by more complicated equations that, in addition to the backbone parameters, will now include the oscillator period  $T$ .

Unfortunately, the oscillator period influences each of the backbone regions in a complex, coupled way, that makes it impossible to assume independence. So, where we had mostly one or two dimensional fits, now we will have two and three dimensional ones. This fact increases the number of oscillators that we have to investigate by an order of magnitude, and unfortunately no fancy methods can help us further reduce the dimensionality of the problem. Still, the same fundamental results that we employed previously to reduce the number of backbones investigated are not period dependent, i.e., the equivalency of the backbones is found to be valid for the short and long periods as well.

### 4.5.1 Fitting the hardening branch of the IDA

Several researchers have provided similar fits for wide period ranges but most have focused on just the elastic-perfectly-plastic model (Newmark and Hall, 1982; Miranda, 2000), while even those who have gone beyond that have only a limited coverage of the hardening slope  $a_h$  (Nassar and Krawinkler, 1991), or consider the effect of  $a_h$  to be independent of period  $T$  (Lee et al., 1999). On the other hand, we will make no such simplifications. Using Equation (4.1), which accurately captures the shape of the hardening part of the IDA, all we need to do is provide fits for the coefficients  $\beta_{x\%}$  and  $\gamma_{x\%}$  that depend both on  $T$  and  $a_h$ .

$$\ln \beta_{x\%} = \sum_i b_{x\%,i} p_{x\%,i}(a_h, T), \quad \ln(\gamma_{x\%} + 1) = \max \left( \sum_i b_{x\%,i} p_i(a_h, T), 0 \right), \quad (4.7)$$

for any  $a_h \in [0, 0.9], T \in [0.2s, 4s]$

where the coefficients  $b_{x\%,i}$  and corresponding functions can be conveniently found in Table 4.6.

**Table 4.6:** Coefficients needed for the IDA hardening part in Equation (4.7).

$x\% =$	$b_{x\%,i}$ for $\beta_{x\%}$			$b_{x\%,i}$ for $\gamma_{x\%}$		
	16%	50%	84%	16%	50%	84%
$\ln^{-1}(T+1)$	-0.1520	-0.1985	-0.6344	0.1925	0.3689	0.9434
1	-0.5027	-0.0955	0.2649	0.1246	0.0480	0.0277
$\ln T$	-0.0542	-0.0316	0.0818	-0.1045	-0.1747	-0.4226
$\ln^2 T$	0.0181	0.0291	-0.1250	0.0605	0.1364	0.3241
$a_h \ln^{-1}(T+1)$	-0.1520	-0.1985	-0.6344	0.1925	0.3689	0.9434
$a_h$	0.8058	0.3737	-0.0954	-0.1989	-0.2105	-0.0297
$a_h \ln T$	0.2037	0.2334	0.5720	-0.0822	-0.1916	-0.5081
$a_h \ln^2 T$	-0.2572	-0.3683	-0.5508	0.1711	0.3816	0.5662
$a_h^{0.5} \ln^{-1}(T+1)$	-0.1520	-0.1985	-0.6344	0.1925	0.3689	0.9434
$a_h^{0.5}$	-0.3675	-0.3041	-0.1600	0.0713	0.1533	-0.0010
$a_h^{0.5} \ln T$	-0.1520	-0.1985	-0.6344	0.1925	0.3689	0.9434
$a_h^{0.5} \ln^2 T$	0.2258	0.3128	0.6418	-0.2237	-0.4964	-0.8851

As expected, the results are similar in the moderate and long period range, the median following the “equal displacement” rule, but the situation is much different in the short period domain. In that region there is significant dependence on both  $a_h$  and  $T$ , making any simplifications of the above equations quite difficult.

#### 4.5.2 Fitting the negative branch of the IDA

Again, using Equations (4.2) and (4.3) we only need to fit and redefine the coefficients  $\beta_{x\%}$  and  $\gamma_{x\%}$  so that they depend both on  $T$  and  $a_c$ :

$$\beta_{x\%} = \sum_i b_{x\%,i} p_i(a_c, T), \quad \gamma_{x\%} = \min \left( \sum_i b_{x\%,i} p_i(a_c, T), 1 \right) \quad (4.8)$$

for any  $a_c \in [-4, -0.02]$ ,  $T \in [0.2s, 4s]$

where the coefficients and relevant functions are found in Table 4.7.

**Table 4.7:** Coefficients needed for the flatline of the IDA softening part in Equation (4.8).

$x\% =$	$b_{x\%,i}$ for $\beta_{x\%}$				$b_{x\%,i}$ for $\gamma_{x\%}$		
	16%	50%	84%		16%	50%	84%
1	0.2391	0.3846	0.5834	1	-0.2508	-0.2762	-0.2928
$\ln T$	0.0517	0.0887	0.1351	$ a_c $	-0.5517	-0.1992	-0.4394
$\ln  a_c $	-1.2399	-1.3531	-1.4585	$a_c^2$	0.0941	-0.0031	0.0683
$\ln  a_c  \ln T$	-0.0976	-0.1158	-0.1317	$ a_c ^{-1}$	0.0059	0.0101	0.0131
$\ln^2  a_c $	0.0971	0.1124	0.1100	$\ln T$	0.1681	0.2451	0.1850
$\ln^2  a_c  \ln T$	0.0641	0.0501	0.0422	$ a_c  \ln T$	0.1357	-0.0199	0.1783
$\ln^3  a_c $	-0.0009	0.0041	0.0056	$a_c^2 \ln T$	-0.0127	0.0091	-0.0305
$\ln^3  a_c  \ln T$	0.0072	0.0067	0.0074	$ a_c ^{-1} \ln T$	0.0010	-0.0075	-0.0066
				$\ln^2 T$	-0.1579	-0.0135	0.0027
				$ a_c  \ln^2 T$	0.2551	-0.0841	0.0447
				$a_c^2 \ln^2 T$	-0.0602	0.0222	-0.0151
				$ a_c ^{-1} \ln^2 T$	0.0087	-0.0003	-0.0025

### 4.5.3 Fitting the residual part of the IDA

Similarly, by using the equivalent residual concept, only three influential parameters exist,  $a_c$ ,  $r_{eq}$  and  $T$ , resulting in the same model as in Equation (4.4), only now we will define new coefficients:

$$\beta_{x\%}, \gamma_{x\%} = \sum_i b_{x\%,i} p_i(a_c, r_{eq}, T), \quad (4.9)$$

for any  $a_c \in [-4, -0.05]$ ,  $r_{eq} \in [0.05, 0.90]$ ,  $T \in [0.2s, 4s]$

where the coefficients can be found in Table 4.8.

**Table 4.8:** Coefficients needed for fitting the IDA residual part in Equation (4.9).

$x\% =$	$b_{x\%,i}$ for $\beta_{x\%}$			$b_{x\%,i}$ for $\gamma_{x\%}$		
	16%	50%	84%	16%	50%	84%
1	-0.2226	0.1401	0.7604	1.0595	1.0635	1.0005
$\ln  a_c $	-0.0992	-0.0817	-0.1035	0.0236	0.0177	0.0283
$\ln r_{eq}$	-0.4537	-0.5091	-0.5235	0.1237	0.1466	0.1607
$\ln r_{eq} \cdot \ln  a_c $	-0.0398	-0.0236	-0.0287	0.0111	0.0048	-0.0004
$\ln r_{eq}^{-1}$	0.0829	-0.0364	-0.0174	-0.0023	0.0102	0.0021
$\ln r_{eq}^{-1} \cdot \ln  a_c $	0.0193	-0.0126	-0.0118	0.0008	0.0019	0.0035
$\ln T$	-0.1831	-0.2732	-0.5651	-0.0881	-0.1044	-0.1276
$\ln T \cdot \ln  a_c $	-0.0319	0.0015	0.0437	-0.0077	-0.0137	-0.0413
$\ln T \cdot \ln r_{eq}$	0.1461	0.1101	0.0841	-0.0239	-0.0090	-0.0085
$\ln T \cdot \ln r_{eq} \cdot \ln  a_c $	-0.0227	-0.0045	0.0159	0.0025	-0.0014	-0.0198
$\ln T \cdot \ln r_{eq}^{-1}$	-0.0108	0.0333	0.0033	0.0082	-0.0003	0.0037
$\ln T \cdot \ln r_{eq}^{-1} \cdot \ln  a_c $	-0.0081	-0.0000	0.0033	0.0007	-0.0013	-0.0043
$\ln^2 T$	0.1660	0.1967	0.0929	0.0317	0.0038	0.0673
$\ln^2 T \cdot \ln  a_c $	-0.0124	-0.0304	0.0130	0.0006	0.0065	0.0074
$\ln^2 T \cdot \ln r_{eq}$	0.0273	0.0396	0.0580	-0.0173	-0.0484	-0.0737
$\ln^2 T \cdot \ln r_{eq} \cdot \ln  a_c $	-0.0167	-0.0209	-0.0144	0.0056	0.0068	0.0255
$\ln^2 T \cdot \ln r_{eq}^{-1}$	-0.0182	0.0311	0.0221	0.0007	-0.0112	-0.0073
$\ln^2 T \cdot \ln r_{eq}^{-1} \cdot \ln  a_c $	-0.0097	-0.0047	0.0007	0.0004	0.0008	0.0005

### 4.5.4 Illustrative Results and Observations

Using splines to connect the above presented three fits and to integrate them into SPO2IDA, we have generated a tool that can accurately capture the behavior of a complex quadrilinear backbone for a wide range of periods, from 0.2s to 4s (Vamvatsikos, 2002). An example of its application is presented in Figure 4.5. Therein the median IDA curve of an elastic-hardening-negative-plateau backbone is recreated for several oscillator periods. Starting from at a moderate period of  $T = 1s$ , the flatline happens at  $R \approx 4.1$ , but if we decrease the period down to  $T = 0.3s$ , we observe that the IDA becomes more aggressive; softening commences at very low values of  $R$  and the flatline is reached very quickly, at  $R \approx 2.7$  for  $T = 0.3s$ . On the other end, when the period is increased, the median IDA is “milder”, it rises and straightens out, staying longer on the “equal displacement” rule, i.e., on the  $\mu = R$  line. Thus, the flatline is greatly delayed, occurring at  $R \approx 5.5$  at  $T = 4s$ . Obviously, the oscillator period has a significant effect on the flatline but also on all the features of the fractile IDAs. The only exception appears for moderate and long periods in the region where the backbone is still hardening. There the median IDA follows the equal displacement rule and thus becomes insensitive to the (moderate or long) period. As observed at least for the median in Figure 4.5, SPO2IDA is now able to capture all such period-dependent effects.

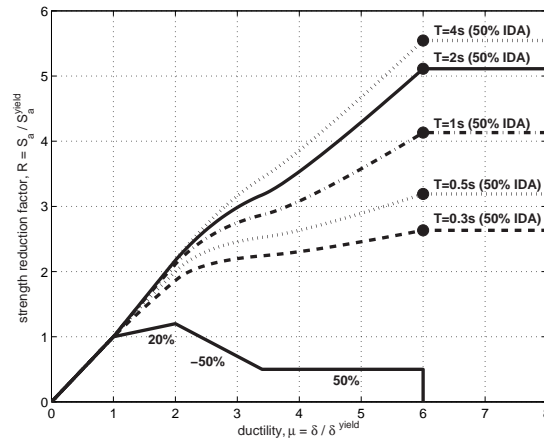


**Figure 4.5:** Median IDAs for a backbone with  $a_h = 0.2$ ,  $\mu_c = 2$ ,  $a_c = -0.5$ ,  $r = 0.5$ ,  $\mu_f = 6$  but varying periods.

#### 4.5.5 SPO2IDA error estimates for all periods

Similarly to the moderate period model, we have generated a separate test-sample of various oscillators with randomly generated backbones and periods. Then we performed a calculation of the fractile demand and capacity errors  $(\epsilon_\mu)_{x\%}$  and  $(\epsilon_R)_{x\%}$  according to Equations (4.5)–(4.6) both shown in Table 4.9. Therein we have also included the bootstrapped  $(\epsilon_\mu)_{x\%}$  and  $(\epsilon_R)_{x\%}$  values for a full IDA with 10 and 30 records.

Once again, the SPO2IDA error is, practically speaking, comparable to the error induced by the record-to-record variability in a full 30-record IDA for all cases, except the last, the quadrilinear one. Again, the most complex of the backbones is harder to capture, but still, the SPO2IDA error remains within reasonable limits.

**Table 4.9:** Average fractile-demand and fractile-capacity errors for short, moderate and long periods and a variety of backbone shapes, as caused by the fitting in SPO2IDA and by the record-to-record variability in IDA.

$x\% =$	SPO2IDA			10 records			30 records		
	16%	50%	84%	16%	50%	84%	16%	50%	84%
elastic-hardening									
$\epsilon_R$	0.04	0.04	0.05	0.09	0.07	0.09	0.06	0.04	0.05
$\epsilon_\mu$	0.02	0.03	0.04	0.06	0.06	0.09	0.04	0.04	0.06
elastic-hardening-negative									
$\epsilon_R$	0.05	0.04	0.05	0.08	0.06	0.09	0.05	0.04	0.04
$\epsilon_\mu$	0.05	0.03	0.04	0.07	0.07	0.10	0.04	0.04	0.04
elastic-hardening-negative-plateau									
$\epsilon_R$	0.20	0.18	0.20	0.21	0.16	0.18	0.14	0.10	0.12
$\epsilon_\mu$	0.19	0.24	0.26	0.20	0.17	0.24	0.12	0.12	0.15

The same observations apply here as in the moderate period range; the errors in Table 4.9 are averaged over numerous backbones, periods and along each individual fractile curve. Therefore, individual cases may perform better or worse than the posted values. The only difference from the moderate period case is the additional consideration of period. Generally, in the short period range, the record-to-record variability is higher thus degrading the accuracy of both IDA and SPO2IDA. Still, barring some isolated below-average-accuracy estimates, the results are very reliable.

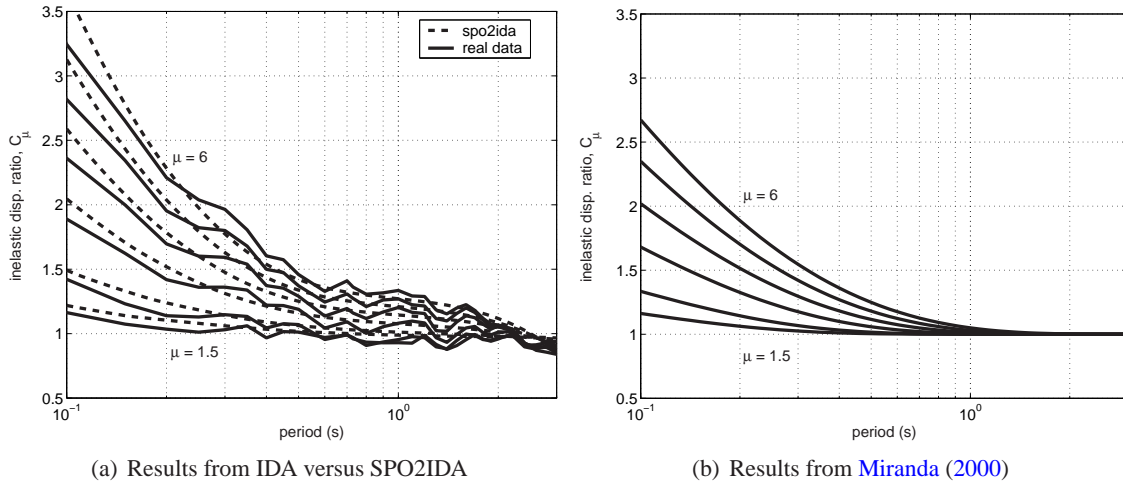


**Figure 4.6:** Comparing estimates of mean  $C_\mu$  ratios generated by SPO2IDA for the special elastic-perfectly-plastic case versus the real data and results from [Miranda \(2000\)](#) for  $\mu = 1.5, 2, 3, 4, 5, 6$ .

#### 4.6 From the IDA to the inelastic displacement ratios

On a more practical aspect, SPO2IDA can directly produce  $R$ -factors and inelastic displacement ratios, often used in seismic guidelines (e.g., [FEMA, 1997](#)). The direct mapping of the  $\mu$ -given- $R$  to the  $R$ -given- $\mu$  fractiles effortlessly provides fractile  $R$ -factors. Similarly, one can easily generate  $(C_\mu)_{x\%}$ , the  $x\%$ -fractile of inelastic to elastic displacement ratio given  $\mu$ , and  $(C_R)_{x\%}$ , the  $x\%$ -fractile of inelastic to elastic displacement ratio given  $R$ , as defined in [Miranda \(2001\)](#). Actually the fractiles of the two ratios are equivalent as  $(C_\mu)_{x\%} = (C_R)_{x\%} = \mu_{x\%}(R)/R = \mu/R_{(100-x)\%}(\mu)$ . By modeling the fractiles in SPO2IDA we can use the same fits to generate the  $R$ -factors and both the inelastic displacement ratios; had we chosen to model the mean response, we would need a separate fit for each of the three quantities ([Miranda, 2001](#)).

On the other hand, instead of the fractiles, the mean  $R$ -factors or mean inelastic displacement ratios may be of interest. If  $E[\cdot]$  is the expectation operator, then we want to estimate  $E[R]$ ,  $E[C_\mu] = \mu E[1/R]$  for a given value of  $\mu$  and  $E[C_R] = E[\mu]/R$  for a given value of  $R$ . Actually, for values of  $R$  higher than any of the flatlines,  $E[\mu]$  and correspondingly  $E[C_R]$  become infinite. At lower  $R$ -values the distribution of  $\mu$  given  $R$  is approximately lognormal ([Shome and Cornell, 1999](#)) and so is the distribution of  $R$  given  $\mu$  for *any*  $\mu$ -value. In those ranges we can use the properties of the lognormal distribution (e.g., [Benjamin and Cornell, 1970](#)) to show that

$$E[R] = R_{50\%}(\mu) \cdot \exp\left(\frac{1}{2}\sigma_{\ln R}^2\right), \quad \sigma_{\ln R} = \frac{1}{2}(\ln R_{84\%}(\mu) - \ln R_{16\%}(\mu)) \quad (4.10)$$

$$E[C_R] = \frac{E[\mu]}{R} = \frac{\mu_{50\%}(R)}{R} \cdot \exp\left(\frac{1}{2}\sigma_{\ln \mu}^2\right), \quad \sigma_{\ln \mu} = \frac{1}{2}(\ln \mu_{84\%}(R) - \ln \mu_{16\%}(R)) \quad (4.11)$$

$$E[C_\mu] = \mu E\left[\frac{1}{R}\right] = \frac{\mu}{R_{50\%}(\mu)} \cdot \exp\left(\frac{1}{2}\sigma_{-\ln R}^2\right), \quad \sigma_{-\ln R} = \sigma_{\ln R} \quad (4.12)$$

In Figure 4.6(a) we have used Equation (4.12) to calculate average  $C_\mu$  ratios using SPO2IDA for an elastic-perfectly-plastic system over a range of periods from 0.1s to 3s using SPO2IDA. On the same figure we also plot the average  $C_\mu$  calculated directly from the 30 record suite through IDA, without the use of any approximation or fit. Clearly, the SPO2IDA results closely match the exact ones, except perhaps for the shortest of periods. As a further comparison, we have recreated in Figure 4.6(b) the  $C_\mu$  results from the proposed equation in [Miranda \(2000\)](#), generated for an elastic-perfectly-plastic model with kinematic hardening, using over 200 records that have

a wide magnitude and source-to-site distance range, and that were all recorded on firm soil. As expected, the results are comparable everywhere but in the short period range, where the record-to-record variability is maximum. Of course, such a specialized fit should be expected to outperform SPO2IDA, having much less error, especially in the short periods. Still, our tool is proven to be suited to many applications, even beyond estimating the fractile IDAs that it was originally designed for.

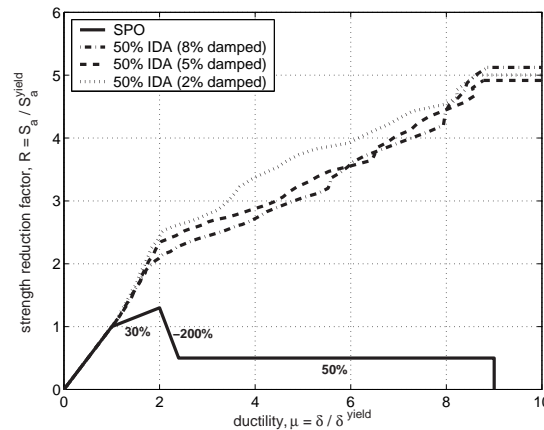


**Figure 4.7:** Viscous damping has negligible influence, as shown for moderate periods for a backbone with  $a_h = 0.3$ ,  $\mu_c = 2$ ,  $a_c = -2$ ,  $r = 0.5$ ,  $\mu_f = 5$ .

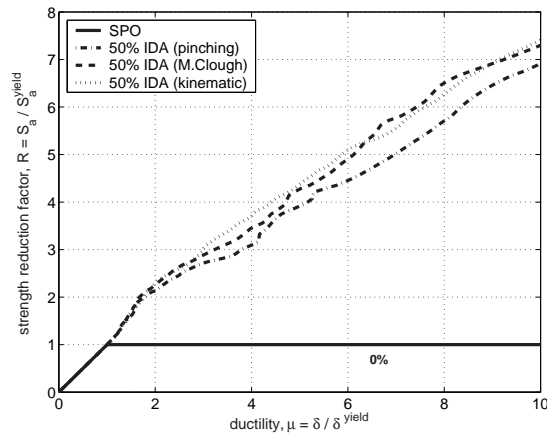
#### 4.7 Influence of other SDOF parameters

By mostly focusing on the oscillator backbone we have restricted our modeling effort in several other aspects; ground motion records were selected from a narrow magnitude and distance bin and correspond to firm soil only, while hysteresis-wise, we have only considered a 5% damped, moderately pinching model. Do these choices seriously restrict SPO2IDA, or can the results be applied in cases beyond what we have considered?

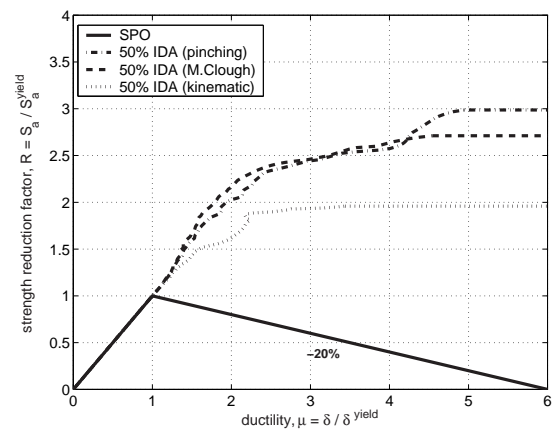
Regarding the selection of the records, the issue of magnitude, source-to-site distance and soil site appear. It has been well documented in the literature that the elastic-perfectly-plastic and the elastic-hardening system results (mean  $R$ -factor,  $C_\mu$  and  $C_R$ ) are not significantly influenced by magnitude, except maybe in the shortest of periods (Ruiz-Garcia and Miranda, 2003), or distance, unless near-fault directivity is an issue (e.g., Miranda, 2000; Nassar and Krawinkler, 1991). Actually, several researchers have found evidence of significant difference between forward-directivity and non-directivity influenced records (Cuesta and Aschheim, 2001; Baez and Miranda, 2000), while a recent study by Chopra and Chintanapakdee (2001), proposes modifying  $R$ - $\mu$ - $T$  relationships to account for such effects. In that case, SPO2IDA needs to be upgraded before being applied when directivity matters. On the other hand, regarding soil-site issues Miranda (2000) has found little dependence within different firm soil sites. But Miranda (1993) and Rahnema and Krawinkler (1993) confirm that soft soil sites can be significantly different and their effect needs to be taken into account when applicable. Obviously, this effect has not been taken into consideration for SPO2IDA.

As for the details of the oscillator itself, at least viscous damping does not seem to be an important issue. As shown in Figure 4.7, at least for moderate and long periods, there is, practically speaking, little or no difference in the actual normalized response  $R$ ,  $\mu$  of systems that have the same backbone, but damping ratios as low as 2% or as high as 8%.

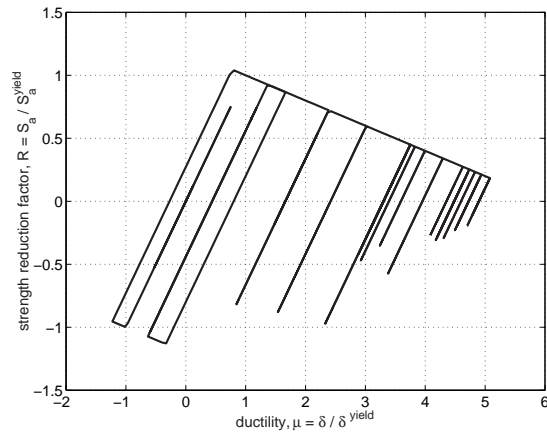
The oscillator hysteresis is another problem, and we have only used a moderately pinching model; we have not considered the influence of the degree of pinching nor the use of other models that otherwise account for pinching, e.g., modified Clough, or models that totally dismiss pinching



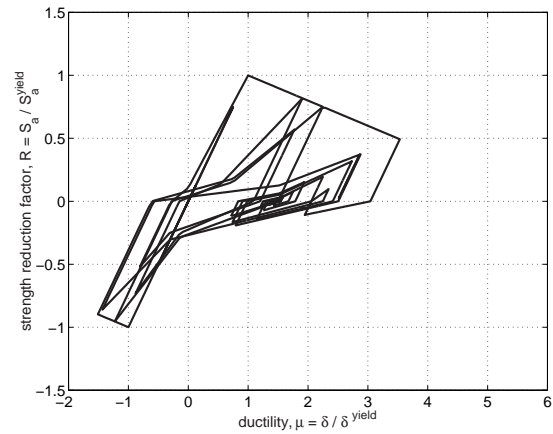
(a) Three hysteresis models for elastic-perfectly-plastic system,  $a_h = 0$ ,  $T = 1s$ .



(b) Three hysteresis models for elastic-negative,  $a_c = -0.2$ ,  $T = 1s$ .



(c) Kinematic hysteresis for elastic-negative system,  $a_c = -0.2$ ,  $T = 1s$  for record #29 at intensity  $R = 2.4$ .



(d) Pinching hysteresis for elastic-negative system,  $a_c = -0.2$ ,  $T = 1s$  for record #29 at intensity  $R = 2.4$ .

**Figure 4.8:** The different effect of the hysteresis model on oscillators with elastic-perfectly-plastic and elastic-negative backbones.

and stiffness degradation, e.g., the kinematic model used with the standard elastic-perfectly-plastic system (for the details of the models see, e.g., [Rahnama and Krawinkler, 1993](#)). For an elastic-perfectly-plastic backbone (Figure 4.8(a)) the effect is practically negligible, as the three models generate the same median (and similarly all fractile) IDA curves. This is not the case for the elastic-negative backbone, as seen in Figure 4.8(b). The median IDA (and actually any individual IDA curve) of the kinematic shows consistently higher  $\mu$ -demands and lower  $R$ -capacities versus the two peak-oriented models, which are almost the same. The reason is that the kinematic model cannot maintain full loops when on the descending branch of the backbone, as seen in Figure 4.8(c); when the oscillator unloads and subsequently reloads it remains on the same elastic slope that leads it quickly back to the negative backbone, not allowing any hysteretic energy absorption, an effect also observed by [Mahin and Lin \(1983\)](#), [Rahnama and Krawinkler \(1993\)](#), [Krawinkler and Seneviratna \(1998\)](#). On the other hand, the pinching model is able to display the more realistic full loops of Figure 4.8(d), a behavior that is similarly matched by the modified Clough model, thus both having quite similar median (and also all fractile) IDAs in Figure 4.8(b).

In general, once we go past the peak of the backbone, the hysteretic model may indeed become an important parameter, and previous sensitivity studies on just elastic-perfectly-plastic backbones will not be adequate.

Another issue that may influence SPO2IDA is that the hysteretic model used has no cyclic deterioration features, i.e., if subjected to cycles of the same deformation amplitude the hysteretic loops will not change or deteriorate in any way. In [Rahnema and Krawinkler \(1993\)](#) there appears some evidence that cyclic deterioration may play a significant role, i.e., severe cyclic strength deterioration seems to be increasing the demands. On the other hand, [\(Gupta and Kunnath, 1998\)](#) have qualitatively investigated such effects and found them to be more pronounced at the lower periods (less than 0.5s), where the numerous high frequency cycles can emphasize the details of the hysteretic model, causing enough large loading-unloading cycles to induce significant strength deterioration.

In conclusion, the degree of pinching, the cyclic deterioration and other such hysteretic details may or may not be important but they are mostly confined to the level of the SDOF system. When the ultimate goal of a tool like SPO2IDA is actually approximating the response of a first-mode-dominated MDOF building ([Vamvatsikos and Cornell, 2004b](#)), in a manner similar to [FEMA \(1997\)](#), then it becomes questionable whether focusing on such details makes sense. While the oscillator backbone can be modeled after the MDOF SPO curve, it is hard to capture other hysteretic characteristics of the MDOF in the equivalent SDOF. And even when a methodology is devised that allows such assessments, a study by [Foutch and Shi \(1998\)](#) has found small effect of such details of the hysteretic modeling of connections in steel moment resisting frames to the response of MDOF systems. In our opinion, it seems a greater priority to investigate directivity and soft soils rather than focus on the smaller details of hysteresis.

## 4.8 Conclusions

A complete methodology has been presented that accurately accounts for the effect of the backbone on the seismic behavior of an oscillator with arbitrary period. The investigated backbone shapes range from simple bilinear to complex quadrilinear with an elastic, a hardening and a negative-stiffness segment plus a final residual plateau that terminates with a drop to zero strength. Long hardening segments are found to significantly improve performance, while their slope has only a small effect. On the other hand, the steeper the slope of the negative-stiffness segment, the higher the demands and the lower the capacities past the peak of the backbone. Residual plateaus that are higher in terms of strength or longer in terms of ductility, both benefit the post-peak performance. Finally, the oscillator period significantly influences the effect of all segments except the hardening one in the moderate or long period ranges. Several different backbone shapes were found to produce similar dynamic behavior. Thus, the required number of backbone shapes to be investigated is drastically reduced, allowing the effect of a complete quadrilinear backbone to be captured with only a handful of regressions. In accordance, a number of equations have been proposed, defining a flexible, publicly available, software tool for performing fast assessments of the (median and dispersion of) demand and capacity of virtually any oscillator. Thus, an engineer-user is able to effortlessly get an accurate, spreadsheet-level estimate of the performance of the oscillator without having to perform the costly analyses, providing ready insights into the relative advantages and disadvantages of possible design or retrofit alternatives.

## 4.9 Acknowledgments

Financial support for this research was provided by the sponsors of the Reliability of Marine Structures Affiliates Program of Stanford University. We would also like to thank L. Ibarra and Professors H. Krawinkler, A. Ayoub for providing the SDOF analysis program.

#### 4.10 Appendix: The SPO2IDA algorithm

Here we provide the exact details of the algorithm that actually constructs the fractile curves in SPO2IDA from the three fitted segments. The only user input is the five parameters of the backbone  $a_h, \mu_c, a_c, r, \mu_f$  and the period  $T$  (if applicable). Before we start, we need to determine which of the three parts (hardening, negative, residual) are going to be needed for the backbone. For example, if  $\mu_f$  is equal to  $\mu_c$  then no negative or residual part need to be plotted, similarly, if  $r = 0$  the residual does not exist. Once that is decided we can proceed to generate each individual part.

First, we generate the elastic part for each line. This is really straightforward and actually the same for all fractiles. Then, we append the hardening part. The only twist to this is calculating the  $R$ -value where the hardening stops, but this can be easily done by solving for each fractile the second-order Equation (4.1) for  $R$ , given  $\mu = \mu_c$ , to get

$$\ln R_{(100-x)\%}(\mu_c) = \begin{cases} \frac{-\beta_{x\%} + \sqrt{\beta_{x\%}^2 + 4\gamma_{x\%} \ln \mu_c}}{2\gamma_{x\%}} & \text{if } \gamma_{x\%} \neq 0 \\ \frac{\ln \mu_c}{\beta_{x\%}} & \text{if } \gamma_{x\%} = 0 \end{cases} \quad (4.13)$$

Then it is trivial to calculate the hardening part directly from Equation (4.1). Additionally, to facilitate the smooth fit with the negative part, it is also useful to calculate the slope of the IDA (in the log-log domain) at the end of the hardening,  $s_{x\%}(\mu_c) = \beta_{x\%} + \gamma_{x\%} \ln R_{(100-x)\%}(\mu_c)$ .

##### for each $x\%$ -fractile IDA

generate the elastic part as a straight line  $(\mu, R) = (0, 0) \dots (1, 1)$

get the  $\beta_{x\%}, \gamma_{x\%}$  coefficients for the hardening branch

calculate  $\ln R_{(100-x)\%}(\mu_c)$

select  $N$  equidistant points  $R_i \in (1, R_{(100-x)\%}(\mu_c)]$ ,  $i = 1 \dots N$

calculate the corresponding  $\mu_i = \exp(\beta_{x\%} \ln R_i + \gamma_{x\%} \ln^2 R_i)$ ,  $i = 1 \dots N$

calculate slope-at-end  $s_{x\%}(\mu_c)$

**end**

To generate the negative part we need some way for a smooth transition from the hardening to the flatline that will be induced by the negative if the residual does not exist. True to our cascading-models principle, we will note that indeed, up to ductility  $\mu_r$  the IDA will behave as if the residual did not exist, so it makes sense to ignore it in this part. As discussed previously we will use the repeated-midpoint insertion spline for this purpose (Farin, 1990). All we need is to supply a *control polygon* and the algorithm will generate a smooth curve that tangentially touches the midpoint of each segment of the polygon. So if we let

$$\ln \mu_{x\%}^{\text{int}} = [\ln R_{(100-x)\%}(\mu_{\text{end}}) - \ln R_{(100-x)\%}(\mu_c)] s_{x\%}(\mu_c) + \ln \mu_c, \quad (4.14)$$

then the points

$$(\mu, R) = \begin{pmatrix} 2 \ln \mu_c - \ln \mu_{x\%}^{\text{int}} & 2 \ln R_{(100-x)\%}(\mu_c) - \ln R_{(100-x)\%}(\mu_{\text{end}}) \\ \ln \mu_{x\%}^{\text{int}} & \ln R_{(100-x)\%}(\mu_{\text{end}}) \\ 2 \ln \mu_{\text{end}} - \ln \mu_{x\%}^{\text{int}} & \ln R_{(100-x)\%}(\mu_{\text{end}}) \end{pmatrix} \quad (4.15)$$

define the appropriate control polygon. All we need is to fit the spline to this polygon and it will blend the hardening segment nicely into the flatline at  $\mu_{\text{end}}$ . Since we may have a residual segment following, we would want to truncate this spline at  $\mu_r$  and also calculate the slope at that point (e.g., through finite differences) to fit the next segment.

**for each  $x\%$ -fractile IDA**

estimate  $R_{(100-x)\%}(\mu_{\text{end}})$  from Equation (4.2)  
 define the control polygon  
 fit a spline to the polygon in the log-log domain  
 calculate  $N$  points  $(\ln \mu, \ln R)$  on the fitted spline, spanning the range from  $\mu_c$  to  $\mu_r$   
 transform them to the linear domain  
 calculate the slope-at-end of the segment  $s_{x\%}(\mu_r)$

**end**

Finally we are left with the residual plateau part. The fits provide us only with the linear behavior (in log-log) at ductilities beyond  $\mu_r$ , so we need again a smooth transition from the relatively flat segment caused by the negative part. If we calculate the  $\beta_{x\%}$ ,  $\gamma_{x\%}$  coefficients from Equation (4.4), then we can calculate the ductility at the intersection of the tangent at the end of the negative-branch with the residual-plateau ‘‘secant’’ line:

$$\ln R_{(100-x)\%}^{\text{mid}} = \frac{\ln \mu_r - s_{x\%}(\mu_r) \ln R_{(100-x)\%}(\mu_r) - \beta_{x\%}}{\gamma_{x\%} - s_{x\%}(\mu_r)} \quad (4.16)$$

$$\ln \mu_{x\%}^{\text{mid}} = \beta_{x\%} + \gamma_{x\%} \ln R_{(100-x)\%}^{\text{mid}} \quad (4.17)$$

Then the tangent and the secant provide the following control polygon that allows a smooth spline fit in the log-log domain:

$$(\mu, R) = \begin{pmatrix} 2 \ln \mu_r - \ln \mu_{x\%}^{\text{mid}} & 2 \ln R_{(100-x)\%}(\mu_r) - \ln R_{(100-x)\%}^{\text{mid}} \\ \ln \mu_{x\%}^{\text{int}} & \ln R_{(100-x)\%}^{\text{mid}} \\ 3 \ln \mu_{x\%}^{\text{mid}} & 3 \ln \mu_{x\%}^{\text{mid}} - \beta_{x\%} / \gamma_{x\%} \end{pmatrix} \quad (4.18)$$

All we need to do is calculate this transition part with the spline and then add as many points as we need along the linear (in log-log) segment provided by the residual-plateau fit to reach the fracturing at ductility  $\mu_f$ . The final touch is adding a flatline at  $\mu_f$ :

**for each  $x\%$ -fractile IDA**

estimate  $\beta_{x\%}$ ,  $\gamma_{x\%}$  from Equation (4.4) or Equation (4.9)  
 define the control polygon  
 fit a spline to the polygon in the log-log domain  
 calculate  $N$  points  $(\ln \mu, \ln R)$  on the fitted spline, spanning the range from  $\mu_r$  to  $\mu_f$   
 transform them to the linear domain  
 append a flatline, as a linear segment  $(\mu, R) = (\mu_f, R_{(100-x)\%}(\mu_f)) \dots (+\infty, R_{(100-x)\%}(\mu_f))$

**end**

If we plot the points that we have calculated, we will get graphs of the fractile IDAs, just like the figures presented earlier.

# Direct estimation of the seismic demand and capacity of MDOF systems through Incremental Dynamic Analysis of an SDOF approximation

Vamvatsikos, D. and Cornell, C. A. (2003c). *ASCE Journal of Structural Engineering*, (in preparation).

## 5.1 Abstract

Introducing a fast and accurate method to estimate the seismic demand and capacity of first-mode-dominated multi-degree-of-freedom systems in regions ranging from near-elastic to global collapse. This is made possible by exploiting the connection between the Static Pushover (SPO) and the Incremental Dynamic Analysis (IDA). While the computer-intensive IDA would require several nonlinear dynamic analyses under multiple suitably-scaled ground motion records, the simpler SPO helps approximate the multi-degree-of-freedom system with a single-degree-of-freedom oscillator whose backbone matches the structure's SPO curve far beyond its peak. Similar methodologies exist but they usually employ oscillators with a bilinear backbone. In contrast, the empirical equations implemented in the SPO2IDA software allow the use of a complex quadrilinear backbone shape. Thus, the entire summarized IDA curves of the resulting system are effortlessly generated, enabling an engineer-user to obtain accurate estimates of seismic demands and capacities for limit-states such as immediate occupancy or global dynamic instability. Using three multi-story buildings as case studies, the methodology is favorably compared to the full IDA.

## 5.2 Introduction

At the core of Performance-Based Earthquake Engineering (PBEE) lies the accurate estimation of the seismic demand and capacity of structures, a task that several methods are being proposed to tackle. One of the promising candidates is IDA (Vamvatsikos and Cornell, 2002a), a computer-intensive procedure that has been incorporated in modern seismic codes (e.g., FEMA, 2000a) and offers thorough demand and capacity prediction capability, in regions ranging from elasticity to global dynamic instability, by using a series of nonlinear dynamic analyses under suitably multiply-scaled ground motion records. Still, professional practice favors simplified methods, mostly using single-degree-of-freedom (SDOF) models that approximate the multi-degree-of-freedom (MDOF) system's behavior by matching its SPO curve, coupled with empirical equations

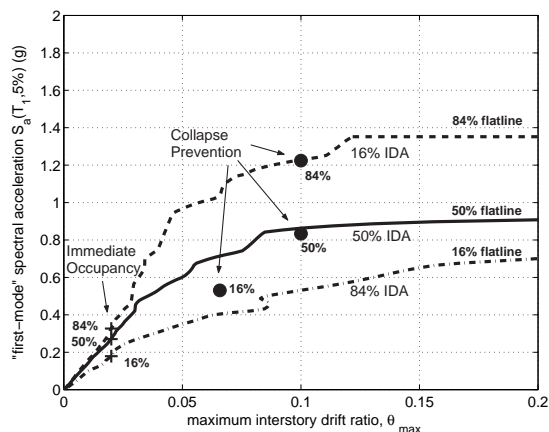


**Figure 5.1:** The 16%, 50%, 84% fractile IDAs and limit-state capacities.

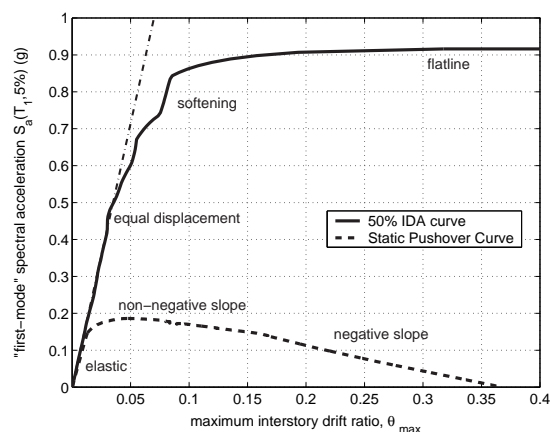


**Figure 5.2:** The median IDA compared against the SPO generated by an inverted-triangle load pattern.

derived for such oscillators to rapidly obtain a measure of the seismic demand (e.g., Fajfar and Fischinger, 1988; Fajfar and Gaspersic, 1996; FEMA, 1997). Such procedures could be extended to reach far into the nonlinear range and approximate the results of IDA, but they use oscillators with bilinear backbones that only allow for elastic perfectly-plastic behavior, and occasionally positive or negative post-yield stiffness (e.g., Miranda, 2000; Nassar and Krawinkler, 1991; Al-Sulaimani and Roessett, 1985). With the emergence of the SPO2IDA software (Vamvatsikos and Cornell, 2004d), empirical relations for full quadrilinear backbones are readily available, which, when suitably applied to the MDOF SPO, allow us to accurately approximate the full IDA and investigate the connection between the structure's SPO curve and its seismic behavior.

### 5.3 IDA fundamentals

To illustrate our methodology, we will perform IDA for a centerline model of a 9-story steel-moment resisting frame designed for Los Angeles according to the 1997 NEHRP provisions (Lee and Foutch, 2002). The model incorporates ductile members, shear panels and realistically fracturing Reduced Beam Section connections, while it includes the influence of interior gravity columns and a first-order treatment of global geometric nonlinearities (P- $\Delta$  effects). Essentially, it is a first-mode-dominated structure that has its fundamental mode at a period of  $T_1 = 2.3$  sec, accounting for 84.3% of the total mass, hence allowing for some significant sensitivity to higher modes.

We have also compiled a suite of twenty ground motion records that have been selected to represent a scenario earthquake (Vamvatsikos and Cornell, 2004a); the moment magnitude is within the range of 6.5 – 6.9, they have all been recorded on firm soil and show no directivity effects. IDA involves performing a series of nonlinear dynamic analyses for each record by scaling it to several levels of intensity that are suitably selected to uncover the full range of the model's behavior: from elastic to yielding and nonlinear inelastic, finally leading to global dynamic instability. Each dynamic analysis can be characterized by at least two scalars, an Intensity Measure (*IM*), which represents the scaling factor of the record (e.g., the 5%-damped first-mode spectral acceleration  $S_a(T_1, 5\%)$ ) and a Damage Measure (*DM*), which monitors the structural response of the model (e.g., maximum, over all stories, peak interstory drift ratio  $\theta_{\max}$  or peak roof drift ratio  $\theta_{\text{roof}}$ ).

By suitably interpolating between the results of the dynamic analyses, we can plot on the *DM-IM* axes an IDA curve for each record. The twenty IDA curves that are thus produced can then be summarized into the 16%, 50% and 84% fractiles, as presented in Figure 5.1 and explained in detail by Vamvatsikos and Cornell (2004a). Additionally, limit-states such as Immediate Occupancy (IO) and Collapse Prevention (CP) (FEMA, 2000a), or the global dynamic instability (GI, evident by the characteristic flattening, termed the *flatline*, on each IDA) can be easily defined on

the curves. Finally, by combining the results of IDA with Probabilistic Seismic Hazard Analysis within a proper framework (e.g., [Cornell et al., 2002](#); [Vamvatsikos and Cornell, 2002a](#)), we can estimate the mean annual frequencies (MAFs) of exceeding each limit-state, one of the ultimate goals of PBEE. Still, the calculation of the full, twenty-record IDA for this model requires about 24 hours of computing on a single 1999-era processor, something that may be beyond the practicing engineer.

A path to a simpler solution appears if we choose to plot the SPO of the MDOF system on  $\theta_{\max}$  versus  $S_a(T_1, 5\%)$  axes, where the total base shear is divided by the total mass and scaled to match the elastic part of the IDA by an appropriate factor (that is equal to one for SDOF systems). By thus plotting the SPO curve versus the median IDA curve on the same graph (Figure 5.2), we observe that both curves are composed of the same number of corresponding and distinguishable segments ([Vamvatsikos and Cornell, 2002a](#)). The elastic segment of the SPO coincides by design with the elastic IDA region, having the same *elastic stiffness*, while the yielding and hardening of the SPO (evident by its non-negative slope up to the peak) forces the median IDA to approximately follow the familiar *equal displacement* rule for moderate period structures ([Veletsos and Newmark, 1960](#)) by maintaining the same slope as in the elastic region. Past the peak, the SPO's negative stiffness appears as a characteristic flattening of the IDA, the flatline, that eventually signals global collapse when the SPO curve reaches zero strength. This apparent qualitative connection of the SPO and the IDA drives our research effort to provide a simple procedure that will use the (relatively easy-to-obtain) SPO plus some empirical quantitative rules to estimate the fractile IDAs for a given structure, providing the IDA curves at a fraction of the IDA computations.

#### 5.4 SPO2IDA for SDOF systems

Based on the established principle of using SDOF oscillators to approximate MDOF systems, we have investigated the SPO-to-IDA connection for simple oscillators. The SDOF systems studied were of short, moderate and long periods with moderately pinching hysteresis and 5% viscous damping, while they featured backbones ranging from simple bilinear to complex quadrilinear with an elastic, a hardening and a negative-stiffness segment plus a final residual plateau that terminated with a drop to zero strength. The oscillators were analyzed through IDA and the resulting curves were summarized into their 16%, 50% and 84% fractile IDA curves which were in turn fitted by flexible parametric equations ([Vamvatsikos and Cornell, 2004d](#)). Having compiled the results into the SPO2IDA tool, available online ([Vamvatsikos, 2002](#)), an engineer-user is able to effortlessly get an accurate estimate of the performance of virtually any oscillator without having to perform the costly analyses, almost instantaneously recreating the fractile IDAs in normalized coordinates of  $R = S_a(T_1, 5\%) / S_a^y(T_1, 5\%)$  (where  $S_a^y(T_1, 5\%)$  is the  $S_a(T_1, 5\%)$ -value to cause first yield) versus ductility  $\mu$ .

#### 5.5 SPO2IDA for MDOF Systems

Adopting an approach similar to FEMA 273 ([FEMA, 1997](#)) we can use the SDOF IDA results generated by SPO2IDA to approximate the seismic behavior of the first-mode-dominated MDOF system. This entails using an SDOF oscillator having the structure's fundamental period, whose backbone closely matches the SPO of the MDOF building. The resulting fractile IDA curves for the SDOF system only need to be properly rescaled from their  $R, \mu$  coordinates to predict the fractile  $\theta_{\text{roof}}$  IDAs and additionally, using the SPO, can be transformed to estimate the fractile  $\theta_{\max}$  IDAs. While the methodology may seem straightforward, the ability of SPO2IDA to extend the results well into the SPO's post-peak region pushes the method to its limits and poses several challenges that have to be overcome.

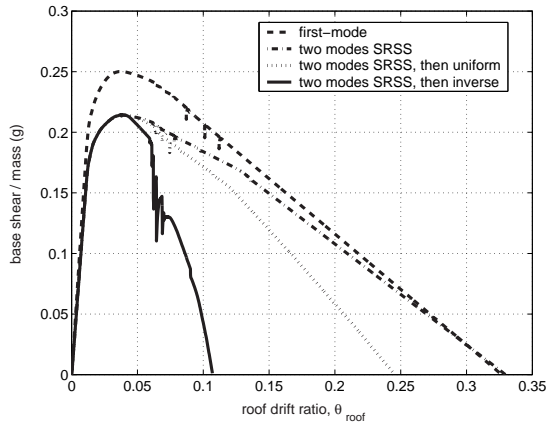


**Figure 5.3:** Four  $\theta_{\text{roof}}$  SPOs produced by different load patterns.

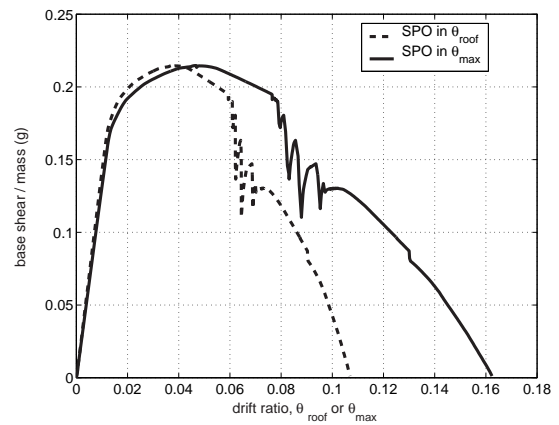


**Figure 5.4:** The most-damaging of the four SPO curves, shown in both  $\theta_{\text{roof}}$  and  $\theta_{\text{max}}$  terms.

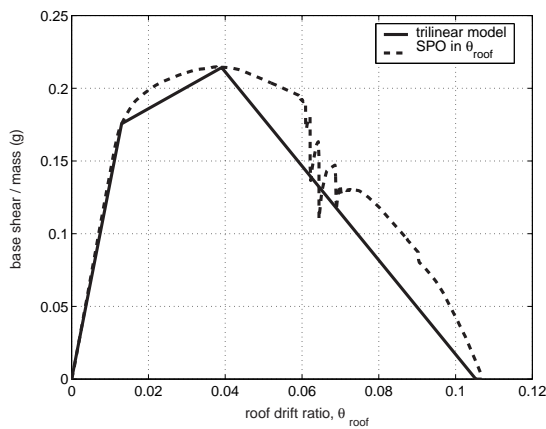


**Figure 5.5:** Approximating the most-damaging of the four  $\theta_{\text{roof}}$  SPO with a trilinear model.

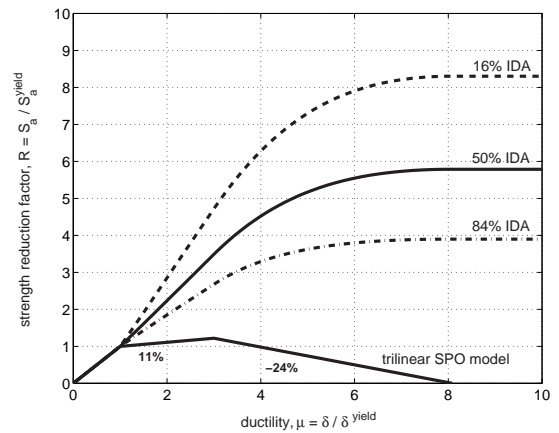


**Figure 5.6:** The fractile IDA curves for the SDOF with the trilinear backbone, as estimated by SPO2IDA.

### 5.5.1 Defining the SPO

While for an SDOF system the SPO is uniquely defined, this is not the case for the MDOF; depending on the load pattern selection, one may generate several different SPO curves, as evident in Figure 5.3. Therein we have plotted the  $\theta_{\text{roof}}$  SPOs for the 9-story building subjected to four different load patterns, producing four quite different SPOs. Beginning from the outermost SPO to the innermost, we observe the following:

1. A load pattern that is proportional to the first-mode shape times the story masses is the most optimistic of the four, as it predicts the highest strength and roof drift ratio,  $\theta_{\text{roof}} \approx 0.32$ , before system collapse occurs.
2. If instead of just the first mode we use a Square-Root-Sum-of-Squares (SRSS) combination of the first two mode shapes we get the second most optimistic curve, where the maximum strength has dropped significantly, but the roof drift ratio at collapse remains  $\theta_{\text{roof}} \approx 0.32$ .
3. By changing the load pattern at the peak of the previous SPO to a uniform one, i.e., a shape that is directly proportional to the story masses and resembles an SRSS of the first two mode shapes of the damaged structure at the peak of the SPO, we uncover a severer drop towards collapse, with zero-strength occurring at  $\theta_{\text{roof}} \approx 0.24$ .
4. If instead of the uniform we impose in the post-peak region the inverse of the pre-peak SRSS pattern (the minimum force now being at the roof-level), it surprisingly produces the

severest SPO of all, with global collapse happening at  $\theta_{\text{roof}} \approx 0.11$ , almost one third of the prediction generated by the pure first-mode load pattern.

In essence, the choice of the load pattern has a significant effect on the calculated SPO curve for large levels of deformation and, evidently, each of the four possible realizations pictured in Figure 5.3 will produce a different estimate for the seismic demands and capacities. As shown for simple oscillators by Vamvatsikos and Cornell (2004d), if we progress from the outermost SPO to the innermost one, the estimates of *DM*-demands past the SPO peak will monotonically increase, and correspondingly the estimated *IM*-capacity for any limit-state that lies beyond the peak will decrease.

So, how is one to choose among the four SPOs? Since we have the full IDA results, we can compare the deformed shapes of the structure produced by the various SPOs versus the IDA. While the median IDA deformed shape shows that in the post-peak region most of the deformations are concentrated on the upper floors, only the innermost (most-damaging) of the four SPOs manages to produce a similar deformation pattern. The other three load patterns seem to concentrate deformations mostly at the lower floors, thus not forcing the structure through the same path to collapse as the dynamic analysis does. We should expect that this most-damaging, worst-case SPO will provide a good approximation to the behavior of the 9-story structure during a nonlinear dynamic analysis.

Such a conclusion can be generalized to structures other than the particular 9-story; it makes sense to assume that a structure under seismic excitation will collapse following the weakest-link, most-damaging, least-energy path. On the other hand, the use of a rigid load pattern will, in general, constrain the deformed shape of the structure, allowing it to withstand higher lateral loads and carry them to higher ductilities. Hence, we suggest that the SDOF oscillator whose backbone mimics the worst-case SPO will most accurately approximate the dynamic behavior of the true MDOF model. Specifically, we should expect that in the post-peak region, the further an SPO lies from the worst-case one, the more unconservative results it will produce; i.e., SPOs that envelop the worst-case one, when they are used as basis for the calculations of our method, they will generate upper-bound estimates of limit-state capacities and lower-bound estimates of demands. Hence, we choose to focus on the most-damaging of the four SPOs for all the calculations that follow.

Unfortunately, there is no obvious recipe to help us arrive at the worst-case SPO. It is hard to predict in advance what load pattern will be the most appropriate, especially if one does not have a priori the dynamic analysis results to confirm that the dynamic and static deformed shapes match. Fully adaptive schemes may prove to be able to find the least-energy path to collapse, several candidates having been proposed at least by Krawinkler and Seneviratna (1998), Gupta and Kunnath (2000) and Antoniou et al. (2002), but none of the proposed schemes has been sufficiently tested and verified in the post-peak region, where good accuracy matters the most for all limit-states that lie close to global dynamic instability (e.g., CP and GI). A simpler, viable solution for regular structures involves using a pattern proportional to the SRSS of several mode shapes times the story masses or a code-supplied pattern, at most up to the peak of the SPO (i.e.,  $\theta_{\text{roof}} \approx 0.02$  or  $\theta_{\text{max}} \approx 0.04$  in Figure 5.4), and consequently testing at least three configurations in the post-peak region: Continuing the pre-peak pattern (i.e., maximum force is at the roof), changing to a uniform or using the inverse of the pre-peak pattern (maximum force at the first story). By performing these three basic pushovers we get sufficiently broad coverage and can pick a load pattern that will provide a good enough approximation to the overall most damaging, worst-case SPO.

Once we have an acceptable estimate of the worst-case  $\theta_{\text{roof}}$  SPO, it is a simple matter to approximate it with a piecewise-linear backbone, in this case a trilinear elastic-hardening-negative model (Figure 5.5), and process it through SPO2IDA. Instantaneously we will get estimates of the fractile IDAs (normalized to  $R$  and  $\mu$ ) for the SDOF with the matching trilinear backbone, as

shown in Figure 5.6.

### 5.5.2 Estimating the IDA elastic stiffness

SPO2IDA will provide us with accurate estimates of the SDOF system fractile IDAs, but the results will be in dimensionless  $R$  versus  $\mu$  coordinates and need to be properly scaled to  $S_a(T_1, 5\%)$  versus  $\theta_{\text{roof}}$  or  $\theta_{\text{max}}$  axes. Therefore, we need to determine for each  $x\%$ -fractile,  $x \in \{16, 50, 84\}$ , the values of  $S_a(T_1, 5\%)$ ,  $\theta_{\text{roof}}$  and  $\theta_{\text{max}}$  that correspond to its yield point, namely  $S_{a,x\%}^y(T_1, 5\%)$ ,  $\theta_{\text{roof},x\%}^y$  and  $\theta_{\text{max},x\%}^y$ . Obviously, for an SDOF system, this task is trivial; the backbone directly provides the yield displacement (same for all fractiles), while it also offers the yield base shear, which when divided by the total mass will result to the value of  $S_a^y(T_1, 5\%)$  (again, common for all fractiles). This is much harder for an MDOF system, mainly due to the effect of the higher modes; some records will force the structure to yield earlier and some later, at varying levels of  $IM$  and  $DM$ . The problem can be simplified if we assume that the SPO accurately captures at least the median value  $\theta_{\text{roof},50\%}^y$  and that all fractiles IDAs yield at about the same value of  $S_{a,x\%}^y(T_1, 5\%)$ . This assumption is not strictly true for MDOF systems and it becomes highly accurate only if the first mode is dominant but, in general, it is more than enough for our purposes. In this case, we only need to estimate the elastic stiffness ( $IM/DM$ ) of the median  $\theta_{\text{roof}}$  and  $\theta_{\text{max}}$  IDA, or, even better, the elastic stiffness of all three fractile  $\theta_{\text{roof}}$  and  $\theta_{\text{max}}$  IDAs,  $k_{\text{roof},x\%}$  and  $k_{\text{max},x\%}$  respectively.

Since such a task involves dynamic linear elastic analysis, it can be easily performed with a minimum of computations. The direct way is to select a suitable suite of records and perform elastic response spectrum or timehistory analysis for each record to determine the  $\theta_{\text{roof}}$  and  $\theta_{\text{max}}$  response. Then, we can estimate the 16%, 50% and 84% fractiles of the sample of elastic stiffnesses,  $S_a(T_1, 5\%)/\theta_{\text{roof}}$  and  $S_a(T_1, 5\%)/\theta_{\text{max}}$ , calculated for each ground motion.

A simpler method appears if we approximate the median  $\theta_{\text{roof}}$  and  $\theta_{\text{max}}$  elastic stiffness by dividing any elastic SPO level of base shear by the total building mass times the corresponding elastic  $\theta_{\text{roof}}$  or  $\theta_{\text{max}}$  value respectively. This is the same operation one would perform for an SDOF system, hence we cannot recover information about the variability in the elastic stiffnesses. Therefore, we are forced to assume that  $k_{\text{roof},x\%} = k_{\text{roof},50\%}$  and  $k_{\text{max},x\%} = k_{\text{max},50\%}$ , which is accurate only when higher modes are negligible. This is the same assumption adopted for the standard Nonlinear Static Procedure, e.g., [Fajfar and Fischinger \(1988\)](#), [Fajfar and Gaspersic \(1996\)](#), [FEMA \(1997\)](#), although, in that case, normalization is done by the first mode mass rather than the total, something that usually makes very little difference.

Obviously, only the first method is an exact calculation of the elastic IDA stiffnesses, and hence is the method of choice for the calculations to follow. The simpler method reduces the computational load, but in a manner similar to [FEMA \(1997\)](#), it neglects the variability in the elastic stiffness. This reduces its accuracy and restricts its usefulness to shorter buildings with insignificant higher mode effects. Ultimately, the selection of the estimating procedure is a trade-off between speed and accuracy, and depends solely on each user's needs.

### 5.5.3 Putting it all together

Having determined the appropriate elastic stiffnesses for the fractile IDAs, all that remains is to properly de-normalize and scale the SPO2IDA results, from  $R$  versus  $\mu$  coordinates, into  $S_a(T_1, 5\%)$  versus  $\theta_{\text{roof}}$  and  $\theta_{\text{max}}$  axes. Since the SPO has been approximated with a trilinear elastic-hardening-negative model (Figure 5.5), its yield-point values of base shear,  $\theta_{\text{roof}}$  and  $\theta_{\text{max}}$ , namely  $F^y$ ,  $\theta_{\text{roof},\text{spo}}^y$  and  $\theta_{\text{max},\text{spo}}^y$ , are readily available. As explained previously, we will assume that each  $x\%$ -fractile IDA,  $x \in \{16, 50, 84\}$ , yields at the same value of  $S_{a,x\%}^y(T_1, 5\%)$ , but at dif-

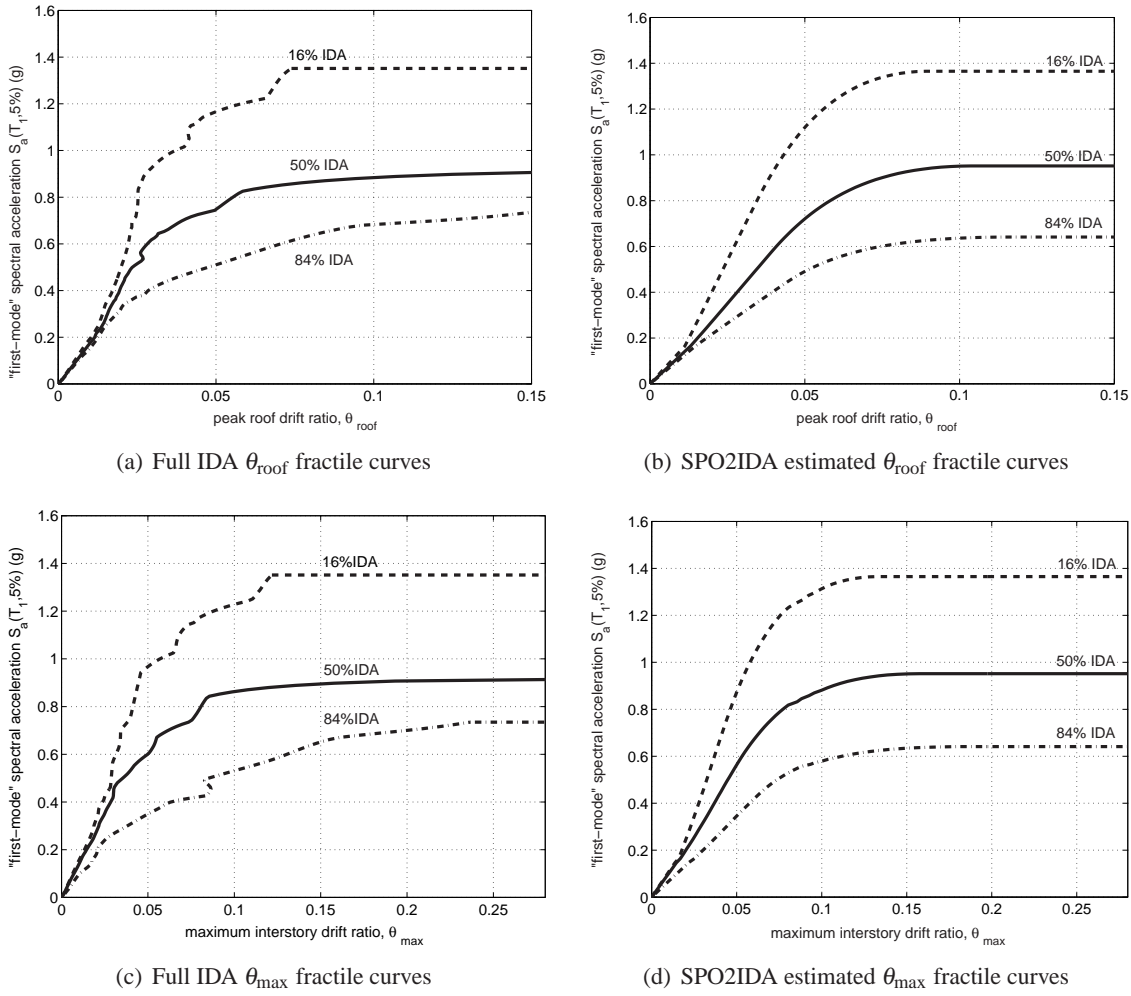


**Figure 5.7:** Generating the fractile IDAs from nonlinear dynamic analyses versus the MDOF SPO2IDA approximation for the 9-story building.

ferent  $\theta_{\text{roof},x\%}^y$  and  $\theta_{\text{max},x\%}^y$ , hence, for all  $x \in \{16, 50, 84\}$  we get:

$$S_{a,x\%}^y(T_1, 5\%) = \theta_{\text{roof},\text{spo}}^y \cdot k_{\text{roof},50\%}, \quad (5.1)$$

$$\theta_{\text{roof},x\%}^y = S_{a,x\%}^y(T_1, 5\%) / k_{\text{roof},x\%} \quad (5.2)$$

$$\theta_{\text{max},x\%}^y = S_{a,x\%}^y(T_1, 5\%) / k_{\text{max},x\%} \quad (5.3)$$

Using Equations (5.1–5.3), we can easily rescale the results of SPO2IDA and bring them into proper  $S_a(T_1, 5\%)$  versus  $\theta_{\text{roof}}$  axes to generate the  $\theta_{\text{roof}}$  fractile IDAs, as seen in Figure 5.7(b), which clearly compare very well against the real IDAs in Figure 5.7(a).

If all that we want is an estimate of the *IM*-capacity for global dynamic instability of the structure, we need not proceed further. On the other hand, to estimate other limit-state capacities (e.g., IO or CP), we need the IDAs expressed in other *DMs*, usually  $\theta_{\text{max}}$ . The SPO curve actually provides the means for such a transformation thanks to the direct  $\theta_{\text{roof}}$ -to- $\theta_{\text{max}}$  mapping it establishes when expressed in  $\theta_{\text{roof}}$  and  $\theta_{\text{max}}$  coordinates (Figure 5.4), a concept that has been used at least in FEMA 273 (FEMA, 1997). The variation that we propose involves shifting the *DM* axes of the SPO for each  $x\%$ -fractile, scaling the elastic  $\theta_{\text{roof}}$  values of the SPO by  $\theta_{\text{roof},x\%}^y / \theta_{\text{roof},\text{spo}}^y$  and shifting the inelastic  $\theta_{\text{roof}}$  values by  $\theta_{\text{roof},x\%}^y - \theta_{\text{roof},\text{spo}}^y$ . By performing the equivalent operation to the  $\theta_{\text{max}}$  SPO values, i.e., scaling the elastic  $\theta_{\text{max}}$  by  $\theta_{\text{max},x\%}^y / \theta_{\text{max},\text{spo}}^y$  and shifting the inelastic

values by  $\theta_{\max,x\%}^y - \theta_{\max,\text{spo}}^y$ , we provide a custom  $\theta_{\text{roof-to-}\theta_{\max}}$  mapping that will correctly transform demands for each fractile, recognizing the variability in elastic stiffness. Of course, were it possible to get the equivalent of a “fractile SPO”, by tracing in some way the force-deformation path that the structure would follow for 16%, 50% and 84% of the ground motion records, such transformations would not be needed. In the absence of such data, we use this method to roughly approximate such fractile SPOs, at least in the elastic range.

The results are visible in Figure 5.7(d) and compare favorably with the real IDA estimates in Figure 5.7(c). Indeed, the estimated IDAs seem to slightly overestimate capacities and underestimate demands, mostly an effect of higher modes plus having just an approximation rather than the real worst-case SPO. For example, the post-peak load pattern cannot take advantage of the sharp drops due to connection fracturing that clearly appear (Figure 5.4), but instead allows the structure to recover. A more adaptive pattern would probably do better. Still, even this rough approximation is good enough considering the roughly  $\pm 20\%$  standard error (estimated by bootstrapping, Efron and Tibshirani, 1993) that exists in estimating the fractiles from the twenty-record full IDA.

On the other hand, regarding ease-of-computation, if we assume that a single 1999-era processor is used, the analysis time is reduced from 24 hours for the MDOF IDA, to only several minutes for the SPO and the elastic response spectrum analyses, not to mention the practically instantaneous SPO2IDA procedure. Thus, we have achieved a fast and inexpensive estimate of the MDOF dynamic behavior at only a small cost in accuracy, the results, at least for this structure, lying within the statistical error (caused by the record-to-record variability) of estimating the fractile IDAs from MDOF nonlinear dynamic analyses with twenty ground motion records.

## 5.6 Application to a 5-story braced frame

Let us now test the proposed procedure on a different structure, using a centerline model of a  $T_1 = 1.8$  sec 5-story steel chevron-braced frame with ductile members and connections but realistically buckling braces including P- $\Delta$  effects (Bazzurro and Cornell, 1994b). For this building, the higher modes are practically insignificant, thus there is little or no ambiguity about the shape of the backbone. It suffices to use a load pattern that is proportional to the first mode shape times the story masses, thus getting the SPO curve shown in Figure 5.8 in  $\theta_{\text{roof}}$  and  $\theta_{\max}$  coordinates.

Taking advantage of the SPO2IDA tool, the  $\theta_{\text{roof}}$  SPO curve is closely matched with a trilinear elastic-negative-plateau model (Figure 5.9). Finally, by combining the results from SPO2IDA with the fractile elastic stiffnesses, we generate the approximate  $\theta_{\text{roof}}$  and  $\theta_{\max}$  fractile IDAs. Using the same suite of records as for the 9-story, the IDA curves are calculated and summarized in their 16%, 50% and 84% fractiles. By comparing the true  $\theta_{\text{roof}}$  fractile IDAs in Figure 5.10(a) versus the approximate results in Figure 5.10(b), it becomes apparent that they are in excellent agreement. Similarly, the  $\theta_{\max}$  fractile IDAs in Figure 5.10(c) are accurately captured by the approximate results, shown in Figure 5.10(d). Clearly, as we should expect for such a building with insignificant higher modes, the proposed procedure is a very cost-effective way to approximate the IDA results. But what happens at the other end, for a tall structure with significant higher mode effects?

## 5.7 Application to a 20-story moment frame

In order to test the limits of our method, we decided to use it on a tall structure, heavily influenced by higher modes. Our choice was a centerline model of a 20-story steel moment-resisting frame (Luco and Cornell, 2000) with ductile members and connections that includes the influence of the interior gravity columns plus a first-order treatment of global geometric nonlinearities (P- $\Delta$  effects). Its first mode has a period of  $T_1 = 4$  sec and accounts for 80.2% of the total mass, placing this structure beyond the realm of first-mode-dominated buildings. Once more, the structure is

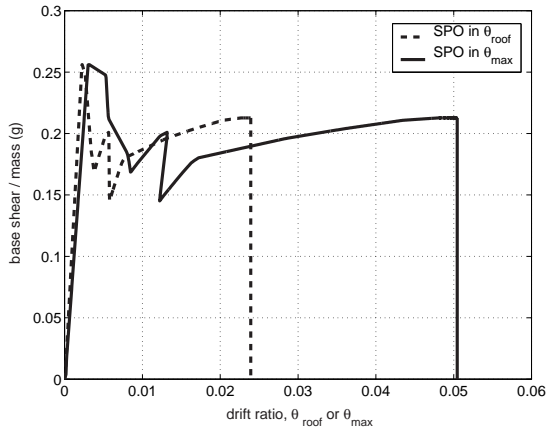


**Figure 5.8:** The most-damaging SPO curve for the 5-story building, shown in both  $\theta_{\text{roof}}$  and  $\theta_{\text{max}}$  terms.

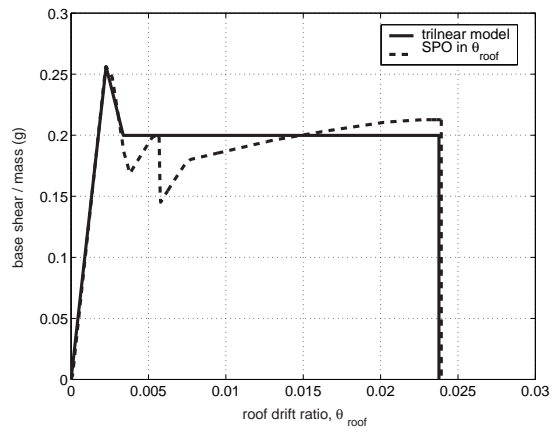
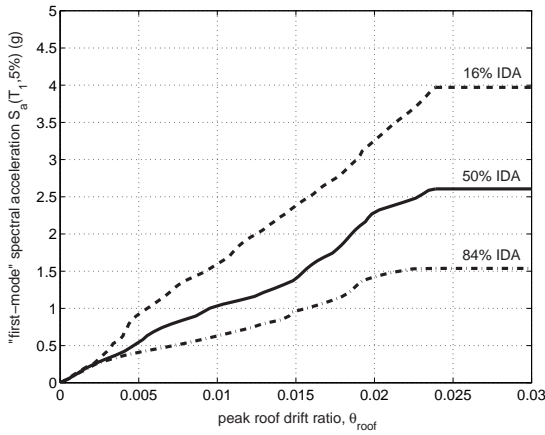
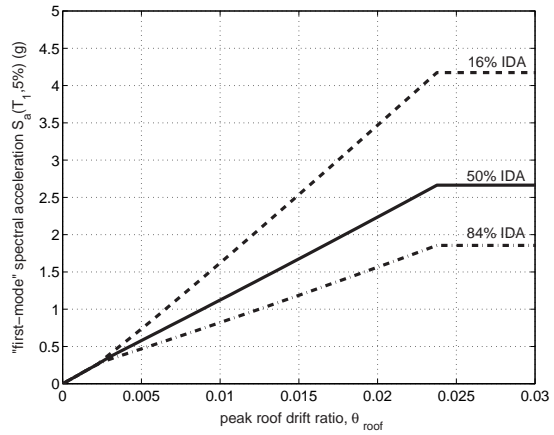


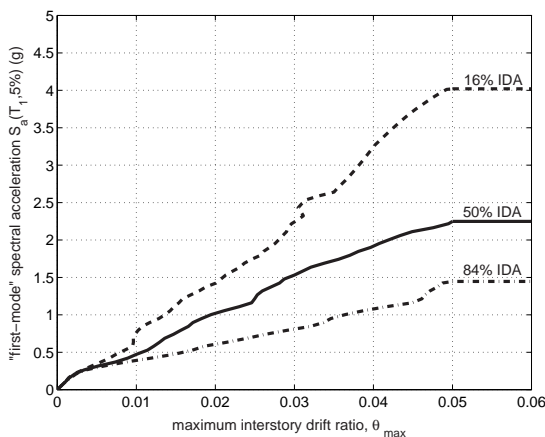
**Figure 5.9:** Approximating the 5-story  $\theta_{\text{roof}}$  SPO with a trilinear model.



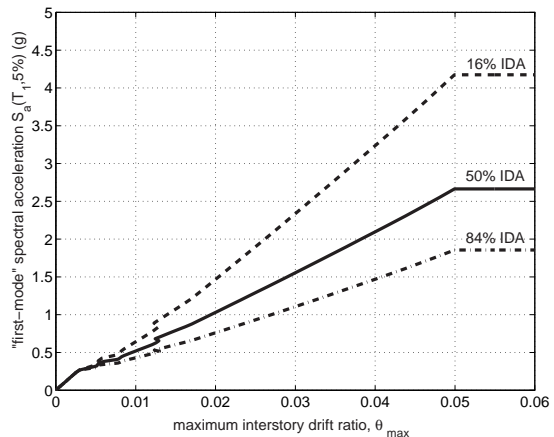
(a) Full IDA  $\theta_{\text{roof}}$  fragility curves



(b) SPO2IDA estimated  $\theta_{\text{roof}}$  fragility curves



(c) Full IDA  $\theta_{\text{max}}$  fragility curves



(d) SPO2IDA estimated  $\theta_{\text{max}}$  fragility curves

**Figure 5.10:** Generating the fragility IDAs from nonlinear dynamic analyses versus the MDOF SPO2IDA approximation for the 5-story building.

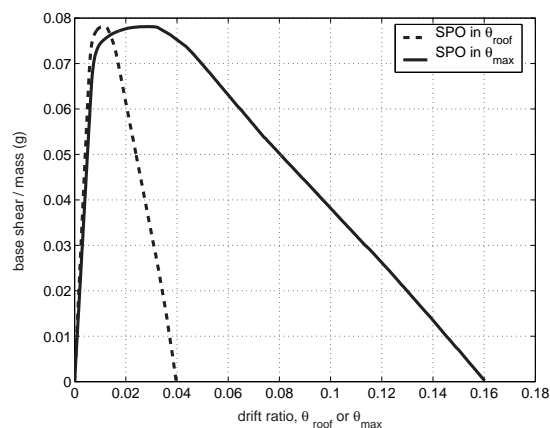


**Figure 5.11:** The most-damaging SPO curve for the 20-story building, shown in both  $\theta_{\text{roof}}$  and  $\theta_{\text{max}}$  terms.

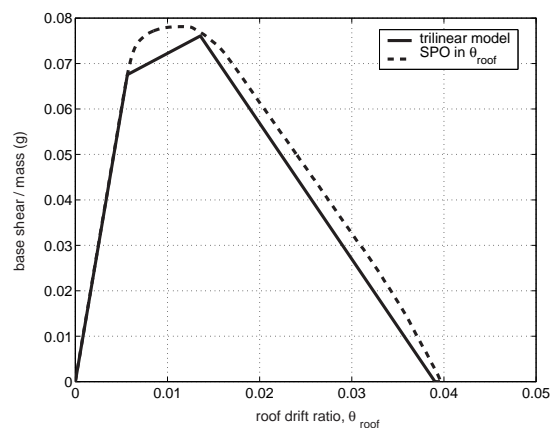


**Figure 5.12:** Approximating the 20-story  $\theta_{\text{roof}}$  SPO with a trilinear model.

analyzed through IDA for the same suite of records used previously, the resulting fractile IDA curves to be used as the standard for comparison.

First of all, the worst-case SPO needs to be determined. Surprisingly, this is an easy task, compared with the previously examined 9-story building. Because of the height of the structure, the massive P- $\Delta$  effects are dominating and quickly push the structure towards global collapse. There is only one path to collapse, and almost all reasonable load patterns will force the structure to take it. Hence, a simple load pattern proportional to the first modal shape times the story masses is adequate to capture the worst-case SPO, even beyond its peak, the resulting curve shown in Figure 5.11 in  $\theta_{\text{roof}}$  and  $\theta_{\text{max}}$  coordinates. Comparing versus the IDA, we can confirm again that the worst-case SPO and the IDA produce similar deformation patterns, concentrating most deformation at the lower stories of this building.

Using a trilinear elastic-hardening-negative backbone, we can accurately capture the  $\theta_{\text{roof}}$  SPO (Figure 5.12), then use SPO2IDA and the fractile elastic stiffnesses to reach the results shown in Figures 5.13(b) and 5.13(d). By comparing them versus the real fractile IDA curves, in Figures 5.13(a) and 5.13(c), one notices several striking differences and similarities. The  $\theta_{\text{roof}}$  IDAs are relatively well estimated. There is some overestimation of  $\theta_{\text{roof}}$  demands in the near-elastic region, as the MDOF system is capable of high hardening that the SDOF system cannot reproduce, still, in the region near collapse, the  $\theta_{\text{roof}}$  IDAs are almost perfectly matched. On the other hand, the proposed method largely overestimates the  $\theta_{\text{max}}$  IDA demands and correspondingly underestimates the  $S_a(T_1, 5\%)$ -values of capacities, especially for limit-states in the near-elastic domain, but maintains good accuracy close to global collapse. It seems that the higher modes are influencing the accuracy of the approximation, reducing it in the near-elastic range but not close to global collapse.

It is well known that it is very difficult to capture the higher mode effects with just the SPO (Krawinkler and Seneviratna, 1998). The  $\theta_{\text{roof}}$  response is somewhat insensitive to them because of its global nature, but local damage measures, like  $\theta_{\text{max}}$ , are not, thus making it very difficult to capture the correct  $\theta_{\text{roof}}$ -to- $\theta_{\text{max}}$  mapping with just the SPO. For example, even in the elastic range, the ratio of the elastic stiffnesses of the median  $\theta_{\text{roof}}$  to the median  $\theta_{\text{max}}$  IDA is about 1.5. This means that at any level of  $S_a(T_1, 5\%)$ , the median  $\theta_{\text{max}}$  is about 50% higher than the median  $\theta_{\text{roof}}$ , i.e., a high degree of deformation localization exists even in the elastic region. On the other hand, the equivalent ratio for the SPO produced with the first-mode load pattern is only 1.3; much less localization is predicted by the static analysis than the dynamic. Even more so, this ratio for the 84%  $\theta_{\text{roof}}$  and  $\theta_{\text{max}}$  IDAs is almost 2, which explains why the estimation seems to suffer away from the median in the near-elastic region. Such differences are a direct manifestation of higher

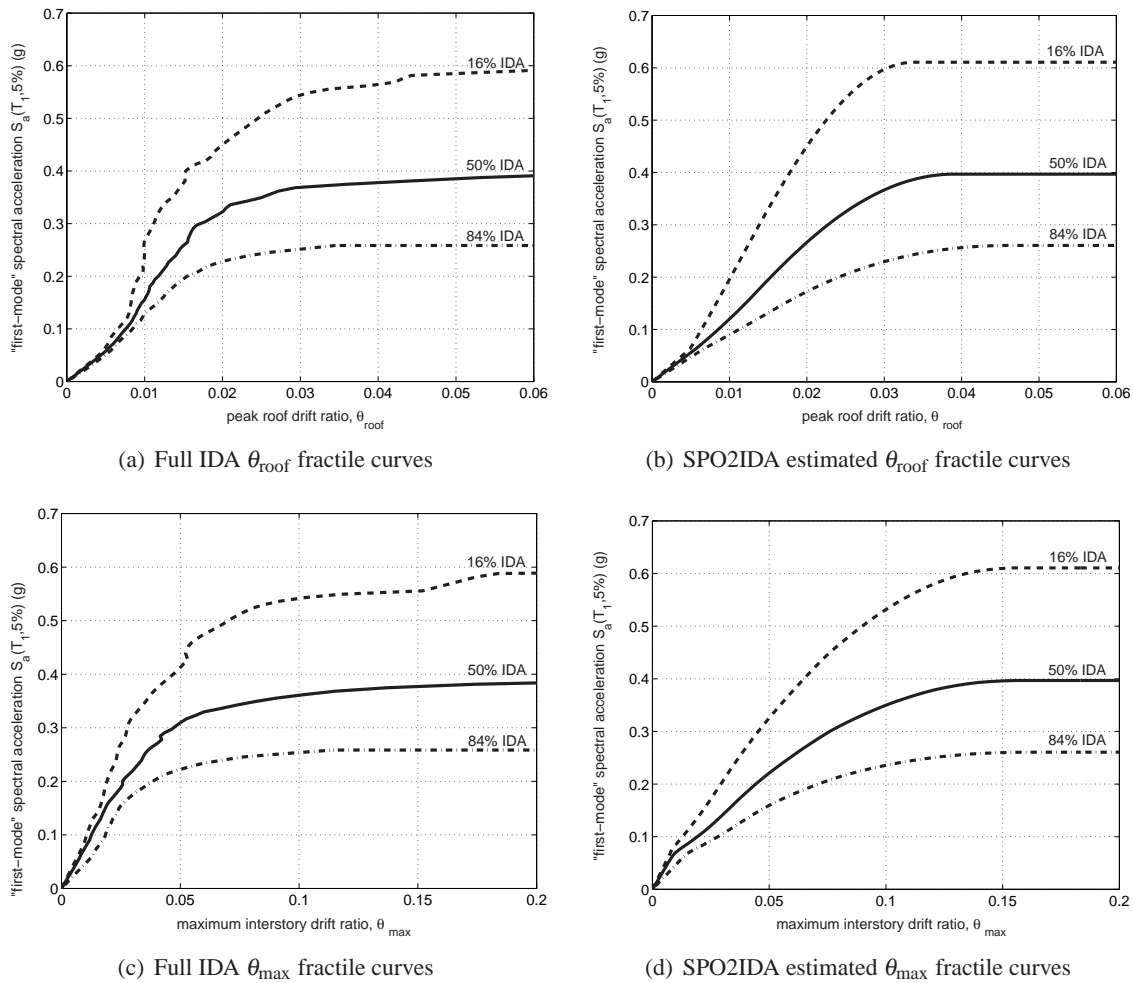


**Figure 5.13:** Generating the fractile IDAs from nonlinear dynamic analyses versus the MDOF SPO2IDA approximation for the 20-story building.

modes and cannot be possibly captured by the SPO. This fundamental deficiency of the SPO is precisely the reason why our prediction of the  $\theta_{\text{max}}$  fractile IDAs, especially in the near-elastic domain, is not as good for this building. Still, adaptive SPO procedures may better capture the  $\theta_{\text{roof}}$ -to- $\theta_{\text{max}}$  connection, maybe even the variability, and if indeed they are proven to do so, the method described here will highly benefit from their use.

Despite such limitations of the SPO, when nearing global dynamic instability even the elusive  $\theta_{\text{max}}$  fractile IDAs are almost perfectly captured. It seems that even such a complex structure can be accurately modeled by an SDOF system close to collapse. While in the elastic or near-elastic region all the modes are interacting to create a complex behavior, as damage accumulates, some of the dominant frequencies seem to be “silenced” and the structure becomes more predictable, more first-“mode” dominated. Some evidence appears if we calculate the eigenvalues from the tangent stiffness matrix at several points along the SPO curve. Then, we observe that the first-eigenvalue mass steadily increases, from 80.4% of the total mass in elasticity to more than 90.2% at the peak of the SPO. The most probable cause is that the element yielding, buckling or fracturing generates preferred paths of structural deformation, providing locations where most of the deformation concentrates. Thus, the building becomes somewhat less complex, preferring to vibrate in a mode defined by the combination of those damaged elements. We can only assume that such damage can simplify our structure’s behavior and an SDOF system with the proper backbone seems to be able to capture that.

## 5.8 Limit-state capacity estimation using the MDOF SPO2IDA

Apparently, the SPO2IDA approximation provides reasonable estimates, within the limitations of the SPO, for the fractile IDA curves of all three buildings that we have examined. Having these results at our disposal we can follow the same steps as we did for the full IDA to perform PBEE calculations; the only difference is that we have to calculate the summarized  $IM$ -capacities for the defined limit-states (IO, CP and GI) directly on the fractile IDAs instead of estimating them individually on each record's IDA curve and then summarize them (Vamvatsikos and Cornell, 2004a).

This is straightforward for the IO and GI limit-states (Vamvatsikos and Cornell, 2004a); their fractile capacities reside on the fractile IDAs (e.g., Figure 5.1), so we only need to calculate the values of  $S_{a,x\%}^c(T_1, 5\%)$  where each  $x\%$ -fractile IDA,  $x \in \{16, 50, 84\}$ , reaches  $\theta_{\max} = 0.02$  to violate the IO limit-state, or reaches the flatline for GI. On the other hand, the CP limit-state points do not necessarily lie on the fractile IDAs, e.g., Figure 5.1, but, in most cases, they are quite close (Vamvatsikos and Cornell, 2004a). Therefore, we propose to apply the SAC/FEMA definition of the CP limit-state point (FEMA, 2000a) directly to the fractile IDAs and thus estimate the fractile CP capacity points. The final results are shown for all three buildings on Table 5.1.

**Table 5.1:** Comparing the real and estimated 16%, 50% and 84%  $S_a^c(T_1, 5\%)$  capacities over three limit-states for each of the studied structures. Note that the 5-story reaches global collapse quite early, so the GI and CP limit-states coincide.

		16% (g)		50% (g)		84% (g)	
		Real	Est	Real	Est	Real	Est
5-story	IO	0.61	0.75	1.02	1.05	1.43	1.55
	CP&GI	1.43	1.84	2.23	2.72	4.04	4.26
9-story	IO	0.18	0.14	0.27	0.20	0.33	0.24
	CP	0.57	0.58	0.83	0.88	1.29	1.31
	GI	0.74	0.64	0.91	0.95	1.35	1.37
20-story	IO	0.12	0.08	0.16	0.10	0.21	0.15
	CP	0.23	0.22	0.34	0.35	0.53	0.57
	GI	0.26	0.26	0.39	0.40	0.63	0.61

**Table 5.2:** Comparing the real and estimated 16%, 50% and 84%  $\theta_{\max}$ -value of capacity for the CP limit-state for each of the studied structures.

		16%		50%		84%	
		Real	Est	Real	Est	Real	Est
5-story	CP	0.05	0.05	0.05	0.05	0.05	0.05
9-story	CP	0.07	0.10	0.10	0.10	0.10	0.10
20-story	CP	0.05	0.10	0.06	0.10	0.07	0.10

By comparing the full IDA versus the approximate results in Table 5.1, it becomes obvious that the proposed method manages to perform very well for a variety of buildings and for each of the three limit-states. Even for the 20-story building, only the IO limit-state is seriously hampered by the approximation, simply an effect of IO happening at the near-elastic region of the IDA where the structure is toughest to predict, as explained earlier. As presented in Vamvatsikos and Cornell (2004a), these  $IM$ -values are actually all that we need, coupled with conventional Probabilistic Seismic Hazard Analysis, to get estimates for the MAF of limit-state exceedance. Hence, from the results of Table 5.1, we should expect that the MDOF SPO2IDA method can provide quite accurate MAF predictions.

If we want to use an alternative format similar to FEMA 350 (FEMA, 2000a), we need instead

the  $DM$ -values of the capacity points. For IO the appropriate  $DM$ -value is 0.02, by definition, while for GI it is  $+\infty$ . For the CP limit-state the results are listed in Table 5.2, where it becomes obvious that the SPO2IDA estimates are quite accurate, except perhaps for the 20-story building. Still, the actual estimate of the MAF of the CP limit-state exceedance will not be as bad as indicated by these results; assuming that the appropriate  $DM$ -based integrations are accurately carried through, they should provide the same result with the  $IM$ -based ones (Jalayer and Cornell, 2002; Vamvatsikos and Cornell, 2004a). These somewhat higher estimates of  $DM$  capacity for the 20-story are tempered by equally high estimates of  $DM$  demand, in the end producing accurate estimates of MAFs. Using either  $DM$  or  $IM$ -based frameworks, the MDOF SPO2IDA procedure can be used to easily calculate the MAF of exceeding a limit-state, even for higher mode influenced buildings in the case that we restrict ourselves to the near-collapse region.

## 5.9 Sensitivity to user choices

The SPO2IDA method for MDOF structures has proven to be quite accurate. Still, several questions may be raised, regarding the sensitivity of the capacities displayed in Tables 5.1 and 5.2 to the average user's choices when applying the proposed methodology.

Obviously, the largest effect comes from finding or missing the right SPO. When the structure fails due to a global failure mode, e.g., due to P- $\Delta$  like the 20-story building, or it has insignificant higher mode effects, e.g., like the 5-story building, then the right SPO should be easy to calculate. Almost any reasonable load pattern, e.g., one proportional to the first mode shape times the story masses, will suffice. If, on the other hand, there are significant higher mode effects and the structure fails mainly due to a succession of local events, e.g., connections fractured or braces buckling, then it is much tougher to find the worst-case SPO. One needs only use the SPO2IDA tool to understand the large influence of the backbone on the IDA (Vamvatsikos and Cornell, 2004d), and realize that no estimation beyond the SPO peak will be accurate without the right SPO. In such cases, it is important to use several, preferably adaptive, load patterns and, in the absence of a proven automated method, use trial and error to select the best of the tried patterns.

Assuming we have found the right  $\theta_{\text{roof}}$ ,  $\theta_{\text{max}}$  SPO, like in our examples, we now have to fit the first with a multilinear model. Obviously, there are many trilinear models that we could use instead of the ones in Figures 5.4, 5.8 and 5.11. Would using them change the final results? It is recommended that one becomes familiar with the SPO2IDA tool and understand the influence of the backbone to the SDOF fragility IDAs (Vamvatsikos and Cornell, 2004d). This greatly helps realize the implications of how to best fit the  $\theta_{\text{roof}}$  SPO. For example, the backbone's hardening slope is not as important, while the negative slope greatly influences global collapse. Therefore, care should be exercised to always fit the  $\theta_{\text{roof}}$  SPO closer where it matters most to achieve the most accurate results. Even so, the quadrilinear model offered by SPO2IDA allows much flexibility, and as was the case with all our examples, the shape of the  $\theta_{\text{roof}}$  SPO can be reasonably captured. In that case, no major differences should be expected in the final results.

Another important issue is the estimation of the elastic stiffness. Up to now we have relied on the direct estimation from elastic timehistory analysis for each record. How much accuracy will one sacrifice by using a simpler method, and what are the implications for the estimates of capacities?

Since the normalized SPO2IDA results for the SDOF fragilities are scaled exclusively by the median elastic  $\theta_{\text{roof}}$  stiffness,  $k_{\text{roof},50\%}$ , its value directly influences the  $IM$ -estimates of capacity for all limit-states. As a direct effect of Equations (5.1)-(5.3), if all the other  $k_{\text{roof},x\%}$ ,  $k_{\text{max},x\%}$  were accurately predicted but  $k_{\text{roof},50\%}$  was overestimated or underestimated by  $\alpha\%$ , we will see a proportional  $\alpha\%$  overestimation or underestimation of all limit-state capacities. Intuitively, this can be understood if we realize that the value of  $k_{\text{roof},50\%}$  determines the scaling of the vertical  $IM$ -axis for the fragility IDAs. Similarly, the five other elastic stiffnesses control the scaling of the

horizontal  $DM$ -axis. Therefore, errors in calculating them have an effect only on limit-states other than  $GI$ , as they cannot influence the height of the flatlines. What they do influence is the  $\theta_{\text{roof}}$  and  $\theta_{\text{max}}$  values of the IDAs, thus causing limit-states like  $IO$  and  $CP$  to appear earlier or later (in  $IM$ -terms) than normal. Thus, it makes sense to be accurate in our estimates of all  $k_{\text{roof},x\%}$  and  $k_{\text{max},x\%}$  values.

Keeping these observations in mind, let us investigate the accuracy of the proposed methods. Obviously, if higher modes cannot be neglected, then the direct method is the only one that can be used. It is by far the best way to estimate the variability in the elastic stiffnesses, caused by the higher modes. If, though, higher modes are deemed unimportant or we are only interested in the median capacities, we can use the simpler method to get rapid estimates with little computational effort. The estimates  $k_{\text{roof},50\%}$  and  $k_{\text{max},50\%}$ , as obtained by the two methods, are compared in Table 5.3, where it becomes obvious that the simpler method performs remarkably well, even for the 20-story building. At most, it overestimates  $k_{\text{roof},50\%}$  by 15%, but in the tall structures it misses  $k_{\text{max},50\%}$  by almost 30%, something that should be expected as  $\theta_{\text{roof}}$  is a local  $DM$ , more influenced by the (neglected) higher modes.

**Table 5.3:** Comparing the median IDA elastic  $\theta_{\text{roof}}$  and  $\theta_{\text{max}}$  stiffnesses, as estimated by several different methods for the three structures.

	5-story (g)		9-story (g)		20-story (g)	
	$k_{\text{roof},50\%}$	$k_{\text{max},50\%}$	$k_{\text{roof},50\%}$	$k_{\text{max},50\%}$	$k_{\text{roof},50\%}$	$k_{\text{max},50\%}$
direct	118.2	90.0	12.6	9.7	11.2	7.4
base shear / mass	114.5	84.6	14.2	13.0	12.0	9.9
50% spectrum	118.2	90.0	18.3	3.0	5.6	0.3
“scaled” 50% spectrum	118.2	90.0	18.7	3.0	6.2	0.3

Looking for an intermediate alternative to the above suggested procedures, the estimates for  $k_{\text{roof},50\%}$  and  $k_{\text{max},50\%}$  are presented for a seemingly reasonable method; elastic spectrum response analysis is performed using the median spectrum of the unscaled suite of records used for IDA. As shown in Table 5.3, this is not worth the extra calculations as it badly misses the correct values for all but the most first-mode-dominated building. This is to be expected, as the median spectrum does not necessarily provide the median response for true MDOF structures. Even more so, the 16% or 84% spectra will not provide the 16% or 84% response.

To further prove this point, an “improvement” of the above method is used, where all spectra are first scaled to the same  $S_a(T_1, 5\%)$ -value and then the median spectrum is generated. Again, the results are less than satisfactory for all but the 5-story building, but even then, the base shear over mass approach is much simpler and almost as accurate.

## 5.10 Conclusions

A new method has been presented that can approximate the seismic demands and capacities of first-mode-dominated MDOF structures for their entire range of behavior, from elasticity to global dynamic instability. Based on the Static Pushover (SPO) and building upon software able to accurately predict the Incremental Dynamic Analysis (IDA) curves for SDOF systems, it can estimate, with reasonable accuracy, the fractile IDA curves of first-mode-dominated MDOF systems. Several novel concepts are derived in the process, perhaps the most important being the worst-case, most-damaging SPO. It often needs carefully selected load patterns to emerge, yet it is the worst-case SPO that best captures the path that leads to global collapse, thus allowing accurate prediction of the IDA results. Equally interesting is the apparent “simplification” that occurs in MDOF systems near global collapse. This permits SDOF systems with appropriate backbones to capture the onset of global dynamic instability even for higher-mode-influenced structures. Combining all

these observations, we can conclude that simply by using the appropriate SPO curve plus, perhaps, a few elastic response spectrum analyses, the engineer-user is able to generate accurate predictions of the seismic behavior of complex MDOF structures within a fraction of the time needed for a full IDA.

### **5.11 Acknowledgements**

Financial support for this research was provided by the sponsors of the Reliability of Marine Structures Affiliates Program of Stanford University.

# Investigating the influence of elastic spectral shape on limit-state capacities through IDA

## 6.1 Introduction

The IDA curves and, correspondingly, the limit-state capacities display large record-to-record variability, even for the simplest of structures, as evident in the previous chapters. This observed dispersion is closely connected to the *IM* used; some *IM*s are more *efficient* than others, better capturing and explaining the differences from record to record, thus bringing the results from all records closer together. Compare, for example, Figures 2.9(a) and 2.9(b) (Chapter 2), where PGA is proven to be deficient relative to  $S_a(T_1, 5\%)$  in expressing limit-state capacities, as it increases their dispersion, practically everywhere on the IDAs. On the other hand, even the improvement achieved by  $S_a(T_1, 5\%)$  still leaves something to be desired, as dispersions are in the order of 30% or more.

Why should we search for such a better *IM*? There is a clear computational advantage if we can select it *a priori*, before the IDA is performed. By reducing the variability in the IDA curves, we need fewer records to achieve a given level of confidence in estimating the fractile *IM*-values of limit-state capacities. Typically, a reduction to the *IM*-capacity dispersion by a factor of two means that we need four times fewer records to achieve the same confidence in the results, as explained in Chapter 3. Obviously, the computational savings can be enormous.

Additionally, it is speculated that increasing the efficiency of the *IM*, may also lead to improved *sufficiency* as well. A sufficient *IM* produces the same distribution of demands and capacities independently of the record selection, e.g., there is no bias in the fractile *IM*-capacities if we select records with low rather than high magnitudes or if the records do or do not contain directivity pulses (Luco and Cornell, 2004). The goals of efficiency and sufficiency are not necessarily tied together as the former aims at reducing the variability in the IDA results while the latter at reducing (or eliminating) their dependance on record characteristics other than the *IM*. Still, using a more efficient *IM* will bring the results from all records closer, and similarly bring close the IDA curves of records coming from different magnitudes or containing different directivity pulses, thus reducing the importance of any magnitude or directivity dependance.

While  $S_a(T_1, 5\%)$  is found to be sufficient for first-mode-dominated, moderate period structures when directivity is not present (Shome and Cornell, 1999), it is not necessarily so for other cases (Luco and Cornell, 2004). Therefore, it is important to try and improve our *IM*s beyond the capabilities of  $S_a(T_1, 5\%)$ . Figure 6.1 may provide some clues; therein we have plotted the 5%-damped acceleration spectra of the 30 records in Table 4.1, normalized by  $S_a(3.98s, 5\%)$ , i.e.,

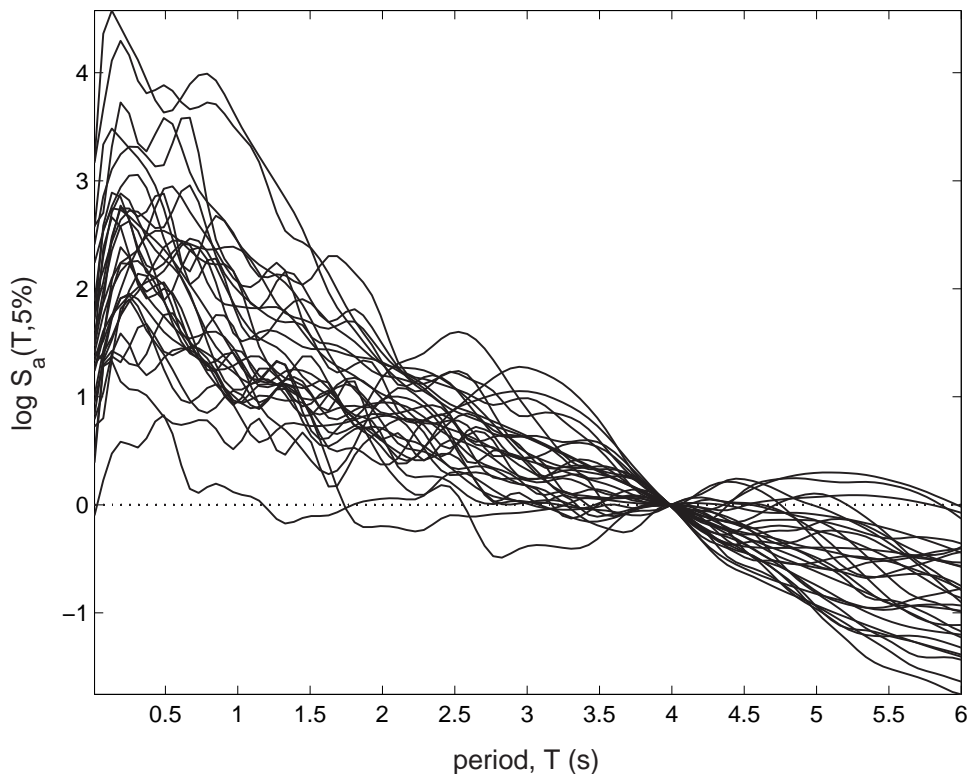


**Figure 6.1:** The 5%-damped elastic acceleration spectra for thirty records, normalized to the first-mode period of the 20-story building.

the value of  $S_a(T_1, 5\%)$  at the first period of the 20-story building used in Chapter 5. There is obviously much variability in the individual spectra that cannot be captured by just  $S_a(T_1, 5\%)$ . A structure is not always dominated by a single frequency, and even then, when the structure sustains damage its properties change. Thus, spectral regions away from the elastic first-mode period,  $T_1$ , may become more influential. By taking the differences in the individual spectral shapes into account, we may be able to reduce the variability in the IDA curves and come up with an overall better *IM*.

Such information may be incorporated into the *IM* by using appropriate inelastic spectral values (Luco and Cornell, 2004). This seems to be a promising method, as it directly incorporates the influence of the record on an oscillator that can yield and experience damage in a way similar to the structure. Still, in the context of PBEE, the use of inelastic spectral values requires new, custom-made attenuation relationships. On the other hand, using the elastic spectral values allows the use of the attenuation laws available in the literature. Therefore, there is still much to be gained from the use of *IMs* based on elastic spectra.

Actually, studies by Shome and Cornell (1999), Carballo and Cornell (2000), Mehanny and Deierlein (2000) and Cordova et al. (2000) have shown that the elastic spectral shape can be a useful tool in determining an improved *IM*. Shome and Cornell (1999) found that the inclusion of spectral values at the second-mode period ( $T_2$ ) and at the third-mode ( $T_3$ ), namely  $S_a(T_2, 5\%)$  and  $S_a(T_3, 5\%)$ , significantly improved the efficiency of  $S_a(T_1, 5\%)$  for tall buildings. Carballo and Cornell (2000) observed greatly reduced variability in the *DM* demands when spectral shape information was included by compatibilizing a suite of records to their median elastic spectrum. In addition, Mehanny and Deierlein (2000) and Cordova et al. (2000) observed an improvement in the efficiency of  $S_a(T_1, 5\%)$  when an extra period, longer than the first-mode was included by employing an *IM* of the form  $S_a(T_1, 5\%)^{1-\beta} S_a(c \cdot T_1, 5\%)^\beta$  (with suggested values  $\beta = 0.5$ ,  $c = 2$ ). Additionally, they presented some evidence suggesting that sufficiency may be improved as well,

since the new *IM* made the IDA curves of several near-fault records practically indistinguishable, regardless of the directivity-pulse period. Motivated by such encouraging results, we are going to use the methodology and tools developed in Chapters 2 and 3 to better investigate the potential of incorporating elastic spectral shape information to *IMs* to reduce the dispersion in IDA results.

## 6.2 Methodology

We will employ three different structures for our investigation into the potential use of the elastic acceleration spectrum. These will be the  $T_1 = 1.8$ s 5-story steel braced-frame, the  $T_1 = 2.4$ s 9-story steel moment-resisting frame and the  $T_1 = 4$ s 20-story steel moment-resisting frame, all introduced in Chapter 5. For each one we will use the suite of 30 records introduced in Chapter 4, Table 4.1 to perform IDA and we will proceed to define numerous limit-states, each at a given  $\theta_{\max}$  value, to represent the capacity of the structure at successive damaged states. Finally, the appropriate  $S_a^c(T_1, 5\%)$ -values will be calculated, i.e., the values of  $S_a(T_1, 5\%)$ -capacity for each record and each limit-state. The ultimate goal is to minimize the dispersion in the *IM*-capacities for each limit-state *individually* by selecting appropriate spectral values or functions of spectral values to be the *IM*. As a measure of the dispersion we will use the standard deviation of the logarithm of the *IM*-capacities, which is a natural choice for values that are approximately lognormally distributed (e.g., Shome and Cornell, 1999).

Fortunately, no further dynamic analyses are needed to perform this dispersion-minimization; all we need to do is to transform each limit-state's  $S_a^c(T_1, 5\%)$ -values in the coordinates of the trial *IMs* and calculate their new dispersion. For example, if we want the dispersion of the capacities in PGA terms, then for each unscaled record (or at a scale factor of one) we know both the PGA and  $S_a(T_1, 5\%)$ -values and the former can be appropriately scaled by the same factor that the value of  $S_a^c(T_1, 5\%)$  implies; e.g., for the 20-story building, the unscaled record #1 of Table 4.1 has  $S_a(T_1, 5\%) = 0.044$ g and  $\text{PGA} = 0.159$ g, while global instability occurs at  $S_a^c(T_1, 5\%) = 0.40$ g, representing a scale factor of  $0.40/0.044 \approx 9.1$ . Hence, the *IM*-capacity at the global instability limit-state in PGA terms is  $\text{PGA}^c = 9.1 \cdot 0.159 = 1.45$ g. Similarly we can accomplish such transformations for any *IM* based on elastic spectral values. Thus, we are taking full advantage of the observations in Chapter 3, by appropriately postprocessing the existing dynamic runs instead of performing new ones.

The adopted approach in evaluating the candidate *IMs* is very different from the one used by Shome and Cornell (1999), Mehanny and Deierlein (2000), Cordova et al. (2000) and Luco and Cornell (2004). There, the focus is on demands, i.e., *DM*-values, all four studies looking for a single “broad-range” *IM* that will improve efficiency for all damage levels of a given structure. On the other hand, our search will be more focused, zeroing on each limit-state separately to develop a “narrow-range” *IM* that will better explain the given limit-state rather than all of them. Thus, we are able to follow the evolution of such *IMs* as damage increases in the structure, hopefully gaining valuable intuition in the process. Still, since we use only  $\theta_{\max}$  to define the structural limit-states, our observations may or may not be applicable when limit-states are defined on other structural response measures (e.g., peak floor accelerations).

Regarding the choice of *IMs* to use, we will start by investigating single spectral coordinates. This does not constitute an investigation of spectral *shape* per se as it focuses on the use of just one value at one period. Still, it will provide a useful basis as we expand our trial *IMs* to include vectors and scalar combinations of several spectral values. In all cases the focus will be on the efficiency gained by incorporating elastic spectrum information in each of the above ways. Another issue of interest is the robustness offered by each *IM*, i.e., how much efficiency it retains when the user selects spectral values other than those chosen by the dispersion-minimization process. This is an important question when trying to identify *a priori* an appropriate *IM* in order to take advantage of its efficiency and use fewer records in the analysis. We are not aiming to provide the final answer

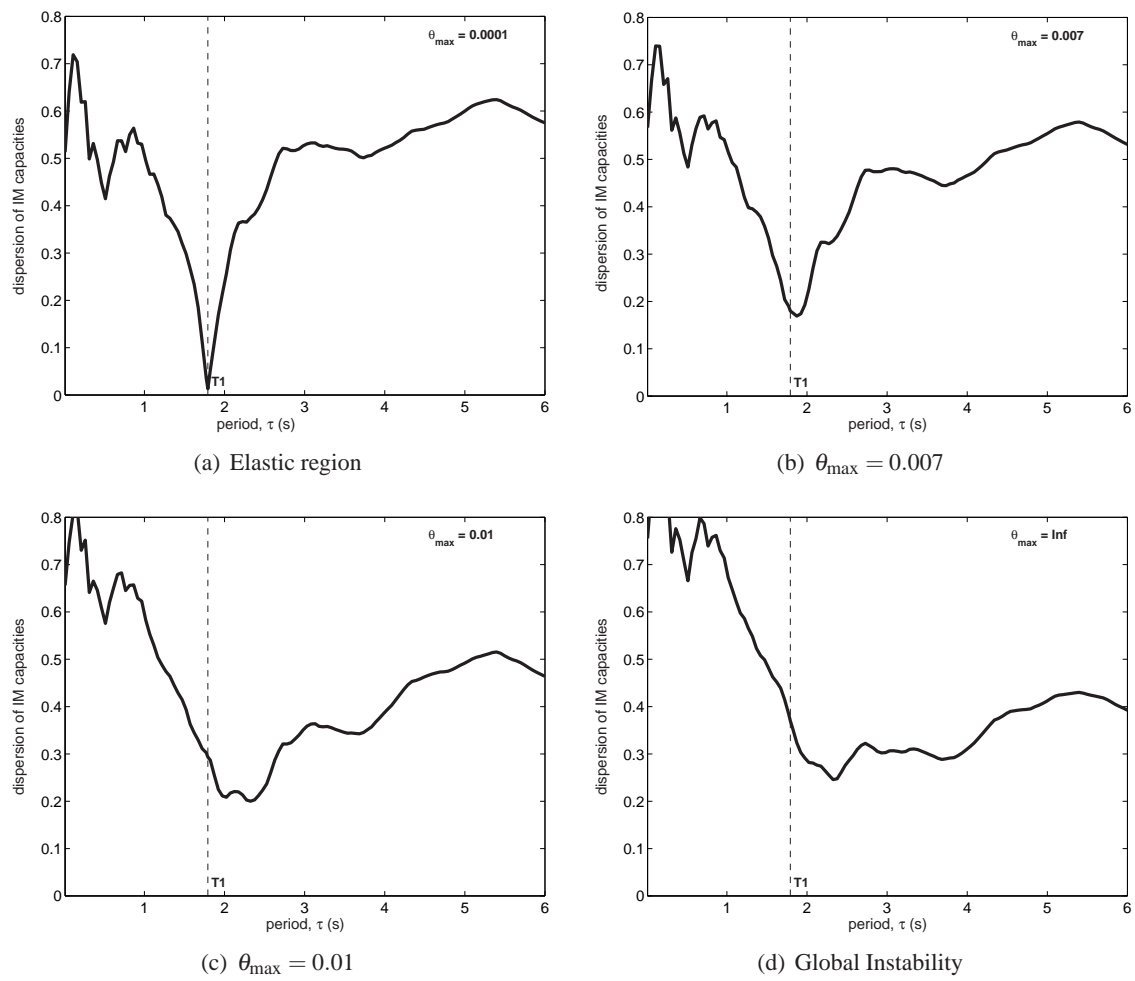


**Figure 6.2:** Dispersion of the  $S_a^c(\tau, 5\%)$ -values versus period  $\tau$  for four different limit-states for the 5-story building.

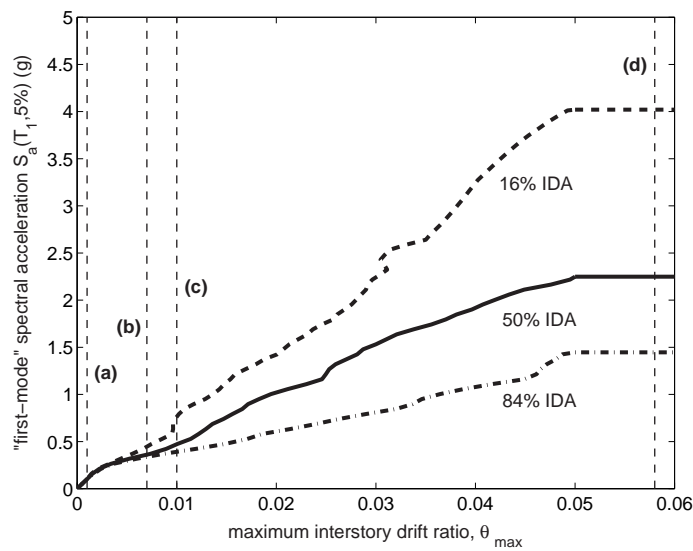


**Figure 6.3:** The fractile IDA curves and capacities for four limit-states (Figure 6.2) of the 5-story building.

for the best *a priori* *IM*, but rather to investigate the efficiency and the potential for practical implementation offered by several promising candidates.

### 6.3 Using a single spectral value

The use of a single spectral value, usually at the first-mode of the structure, i.e.,  $S_a(T_1, 5\%)$ , has seen widespread use for IDAs, having been incorporated into the FEMA (2000a,b) guidelines and used throughout most of our research. Obviously, it is an accurate measure for SDOF systems or first-mode-dominated structures in the elastic range. But when higher modes are important or the structure deforms into the nonlinear range, it may not be optimal. There seems to be a consensus that when structures are damaged and move into the nonlinear region, period lengthening will occur (e.g., Cordova et al., 2000). In that sense, there may be some merit in looking for elastic spectral values at longer, or in general different, periods than the first-mode. Therefore we will conduct a search, across all periods in the spectrum, to determine the one that most reduces the variability in the *IM*-values of limit-state capacities.

Some representative results are shown in Figure 6.2 for the 5-story building, for limit-states at four levels of  $\theta_{\max}$  (Figure 6.3), namely 0.01% (elastic), 0.7% (early inelastic), 1% (highly nonlinear) and  $+\infty$  (global instability). The structure has obviously insignificant higher modes, since  $S_a(T_1, 5\%)$  produces practically zero dispersion for the capacities in the elastic region. As the structure becomes progressively more damaged, the optimal period moves away from  $T_1$ , lengthening to higher values as expected. Initially, only a narrow band of periods around the optimal  $\tau$  display low dispersions. When close to global collapse, this band around the optimal period increases so that any period from 2s to 4s will achieve low dispersion, at most 30% compared to about 40% when using  $S_a(T_1, 5\%)$ . A summary of the results is shown in Figure 6.4, where the optimal period is shown versus the  $\theta_{\max}$ -value of all the limit-states considered, while the best achieved dispersion is presented in Figure 6.5, compared against the dispersion when using PGA and  $S_a(T_1, 5\%)$ . As observed before, the optimal period increases after yielding, from  $\tau = T_1$  to  $\tau = 2.4$ s. Similarly, the dispersion increases for all three *IM*s in Figure 6.5, but with the use of the optimal period, the efficiency is improved, at least by 40% compared to  $S_a(T_1, 5\%)$ .

Similar results for the 9-story building are presented in Figure 6.6, for the limit-states appearing in Figure 6.7 at  $\theta_{\max}$  equal to 0.5% (elastic), 5% (inelastic), 10% (close to global collapse) and  $+\infty$  (global instability). The building has significant higher modes, as evident in Figure 6.6(a), since the first mode is not optimal even in the elastic region. While all three modes,  $T_1$ ,  $T_2$  and  $T_3$ , seem to locally produce some dispersion reduction, the overall best single period is somewhere between the  $T_1$  and  $T_2$ , at  $\tau \approx 1.2$ s. As damage increases, the optimal period lengthens to higher values, to finally settle close to  $T_1$  when global instability occurs. In Figure 6.8, the results are summarized for all limit-states, showing the gradual lengthening of the optimal period. Similarly, in Figure 6.9 the optimal dispersion thus achieved is compared versus the results when using PGA and  $S_a(T_1, 5\%)$ . Remarkably, only in the elastic and near-elastic region does this single optimal spectral value provide some improvement, in the order of 10%. Close to global collapse, no gains are realized over  $S_a(T_1, 5\%)$ .

For the 20-story structure, the results for four limit-states are shown in Figure 6.10, for  $\theta_{\max}$  equal to 0.5% (elastic), 2% (near-elastic), 10% (close to global collapse) and  $+\infty$  (global instability); each limit-state is shown versus the fractile IDAs in Figure 6.11. This is a building where higher modes are even more important, and by looking at Figure 6.10(a), it seems that, at least initially, the second-mode period,  $T_2$ , manages to explain more than  $T_1$  in the dispersion of the *IM* capacity values. The limit-states are defined on  $\theta_{\max}$ , the maximum of the story drifts, which often appears in the upper stories at low ductilities and is thus quite sensitive to the higher frequencies. As damage increases, the optimal period moves away from  $T_2$  and at global collapse reaches a value somewhere in the middle of  $T_1$  and  $T_2$ , at about  $\tau \approx 2.5$ s. In Figure 6.12 the summarized

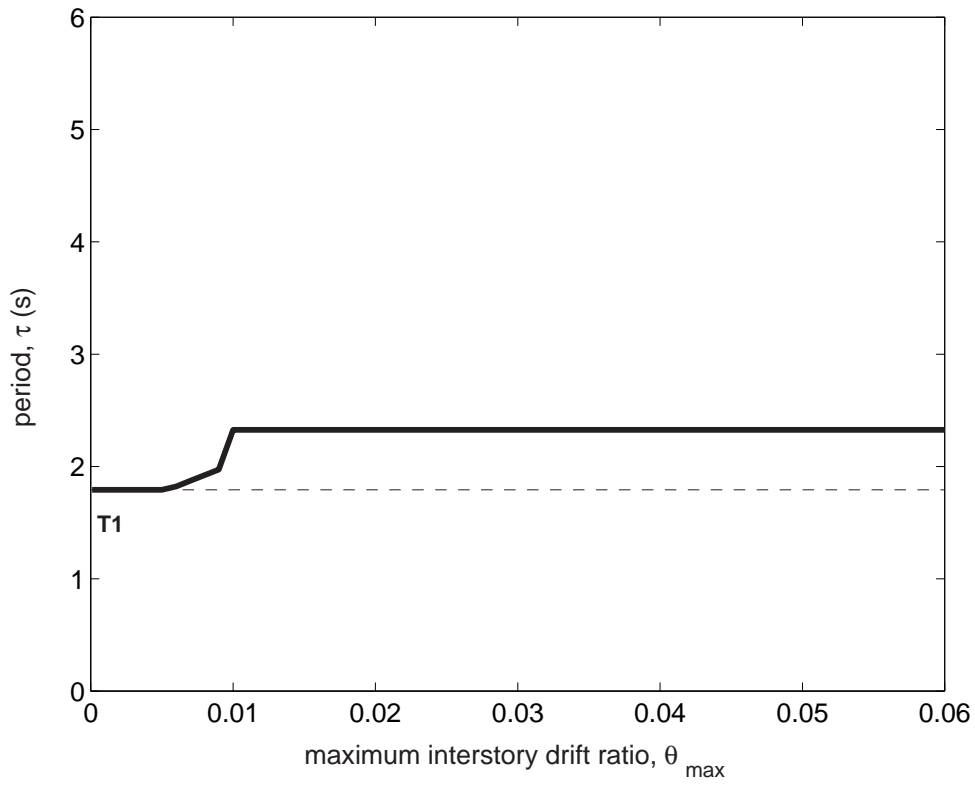


Figure 6.4: The optimal period  $\tau$  as it evolves with  $\theta_{\max}$  for the 5-story building.

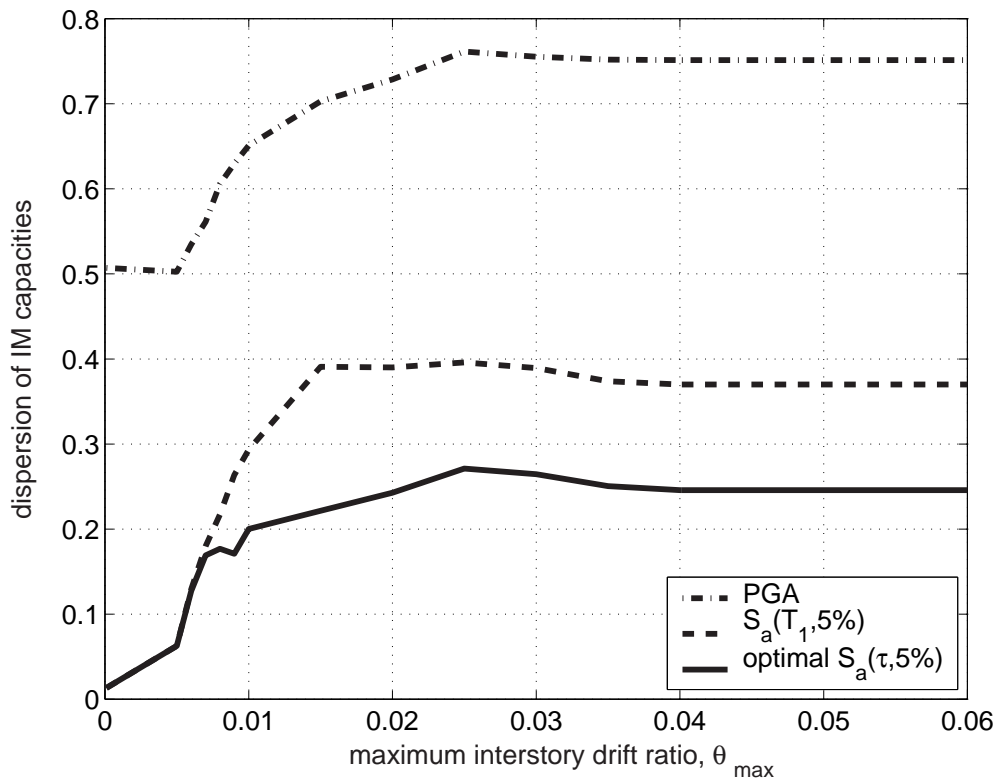
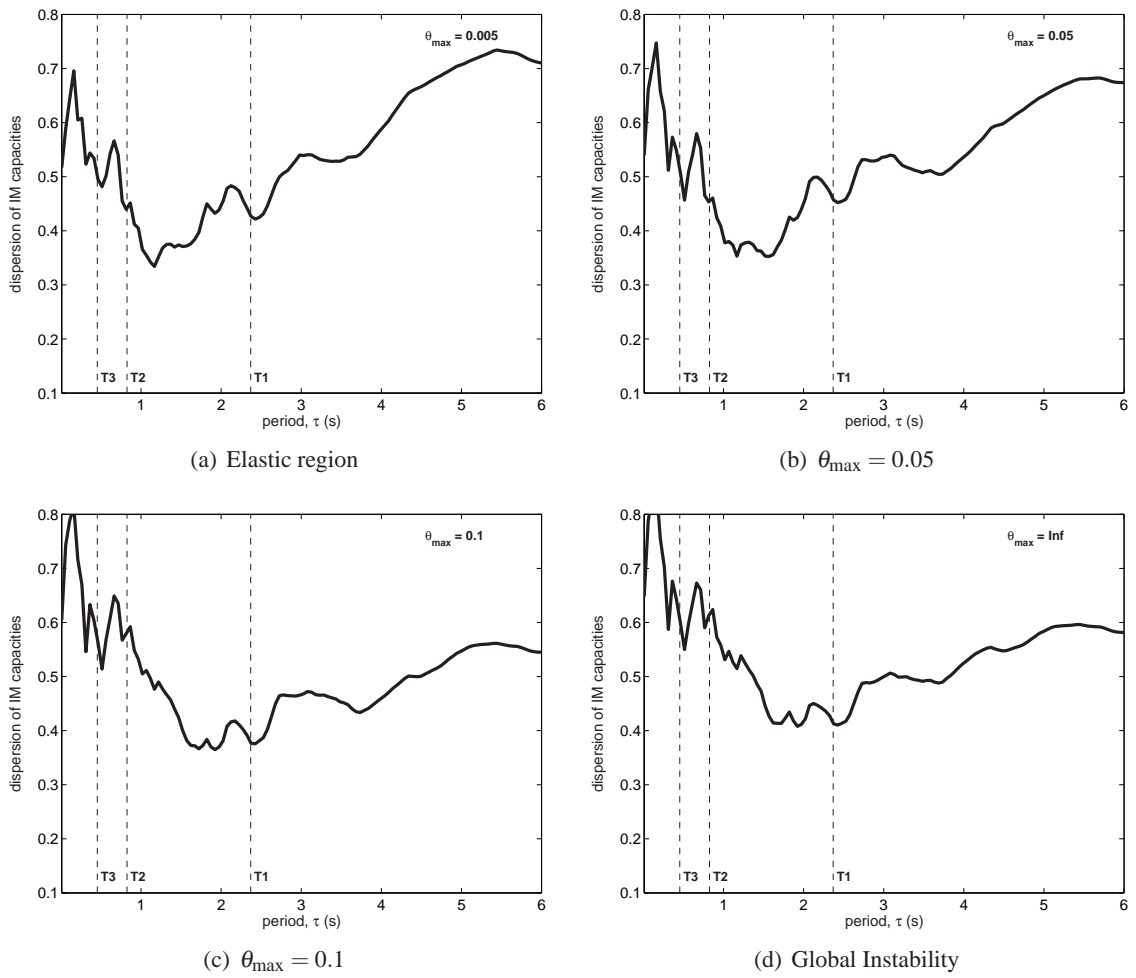
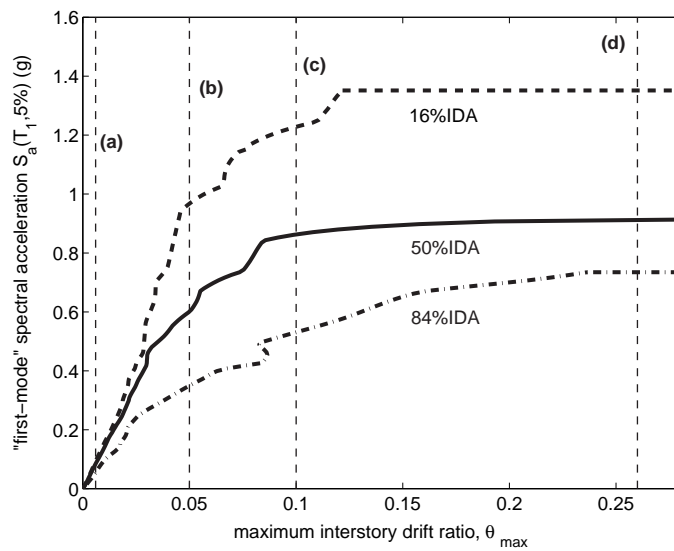


Figure 6.5: The dispersion for the optimal  $S_a(\tau, 5\%)$  compared to  $S_a(T_1, 5\%)$  and PGA, versus the limit-state definition,  $\theta_{\max}$ , for the 5-story building.



**Figure 6.6:** Dispersion of the  $S_a^c(\tau, 5\%)$  values versus period  $\tau$  for four different limit-states for the 9-story building.



**Figure 6.7:** The fractile IDA curves and capacities for four limit-states (Figure 6.6) of the 9-story building.

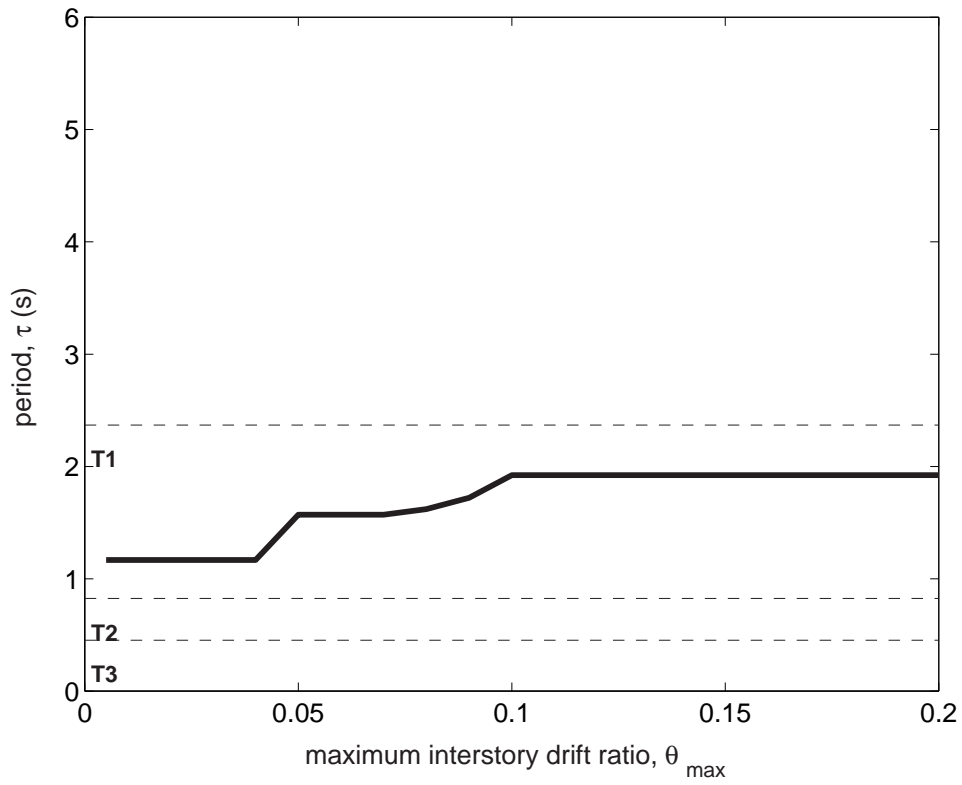


Figure 6.8: The optimal period  $\tau$  as it evolves with  $\theta_{\max}$  for the 9-story building.

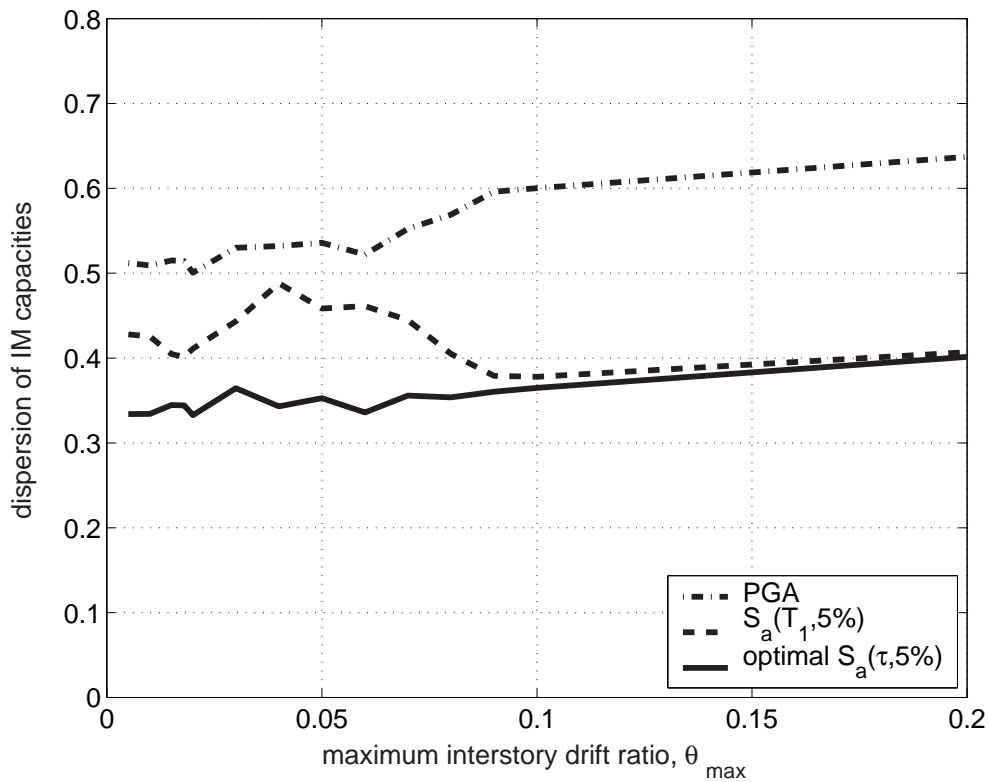


Figure 6.9: The dispersion for the optimal  $S_a(\tau,5\%)$  compared to  $S_a(T_1,5\%)$  and PGA, versus the limit-state definition,  $\theta_{\max}$ , for the 9-story building.

results confirm the above observations for the limit-states defined on all values of  $\theta_{\max}$  and, similarly to the 9-story, only small reductions in dispersion are realized with the use of one spectral coordinate, as seen in Figure 6.13. At least, in this case, using a single optimal period seems to achieve somewhat better performance than  $S_a(T_1, 5\%)$  close to global collapse.

Summarizing our observations, the use of a single spectral value seems to offer some benefits, but mostly to structures with insignificant higher modes. For such structures, it seems relatively easy to identify the optimal period, as it is invariably an appropriately lengthened value of the first-mode period  $T_1$ . One could almost say that practically any (reasonably) lengthened first-mode period will work well. On the other hand, when higher modes are present, one spectral value is probably not enough. There do exist specific periods that one can use to reduce the variability, but they appear in a very narrow range and are difficult to pinpoint as damage increases. It would be difficult to pick *a priori* a single period for such structures as a slight miss will probably penalize the dispersion considerably.

Most probably, the reason behind this apparent difficulty is that even into the nonlinear range the structure is sensitive to more than one frequency. Thus, our attempt to capture this effect with just one period results in the selection of some arbitrary spectral coordinate that happens to provide the right “mix” of spectral values at the significant frequencies. Looking at all the previous figures, it becomes obvious that missing by a little bit will again, in most cases, pump up the dispersion significantly. Obviously, this one period is not a viable solution for any but the structures dominated by the first-mode. On the other hand, the introduction of another spectral value, to form a vector or an appropriate scalar combination of two periods, might prove better.

## 6.4 Using a vector of two spectral values

The use of more than one discrete spectral value necessitates the development of a framework for the use of vector *IMs*. While the definitions set forth in Vamvatsikos and Cornell (2002a) (Chapter 2) do provide for a vector *IM*, up to now, there has been no formal framework developed on how to postprocess and summarize such IDAs. So, before we proceed with our spectral shape investigation, we will propose a methodology to deal with vector *IMs*.

### 6.4.1 Postprocessing IDAs with vector *IMs*

The most important thing that we must keep in mind is that the IDA per se remains unchanged, and no need exists to rerun the results that we have acquired; this is all about postprocessing, as explained in Chapter 3. On the other hand, there are some conceptual differences between a scalar and a vector of *IMs*. Since the *IM* must in both cases represent the scaling of the ground motion record, the scalar *IM* had to be scalable, i.e., be a function of the scale factor of the record (Vamvatsikos and Cornell, 2002a, Chapter 2). However, for a vector of *IMs* it would be redundant and often confusing if more than one of the elements were scalable. Hence, we will focus on vectors where only one of the elements can be scaled, while the others are scaling-independent. That is not to say, for example, that when we have  $S_a(T_1, 5\%)$  in a vector, other spectral values are not acceptable. Rather, we will replace such extra spectral values by their ratio over  $S_a(T_1, 5\%)$  (and similarly normalize any other scalable *IM*); thus, we convey only the additional information that the new elements in the vector bring in with respect to our primary scalable (scalar) *IM*. In this case it is quite precise to speak of this additional information (one or more additional spectral ratios) as reflecting the influence of spectral shape (rather than the amplitude of the record).

Following a similar procedure as for a single scalable *IM*, we will use splines to interpolate the discrete IDA runs for each record versus the scalable *IM* from the vector (Vamvatsikos and Cornell, 2002a, Chapter 2). Then, we can plot the IDA curves for all records versus the elements of the vector, as in Figure 6.14 for the 5-story braced frame and a vector of  $S_a(T_1, 5\%)$  (scalable) and the spectral ratio  $R_{sa}(1.5, T_1) = S_a(1.5T_1, 5\%) / S_a(T_1, 5\%)$  (non-scalable). Contrary to the usual

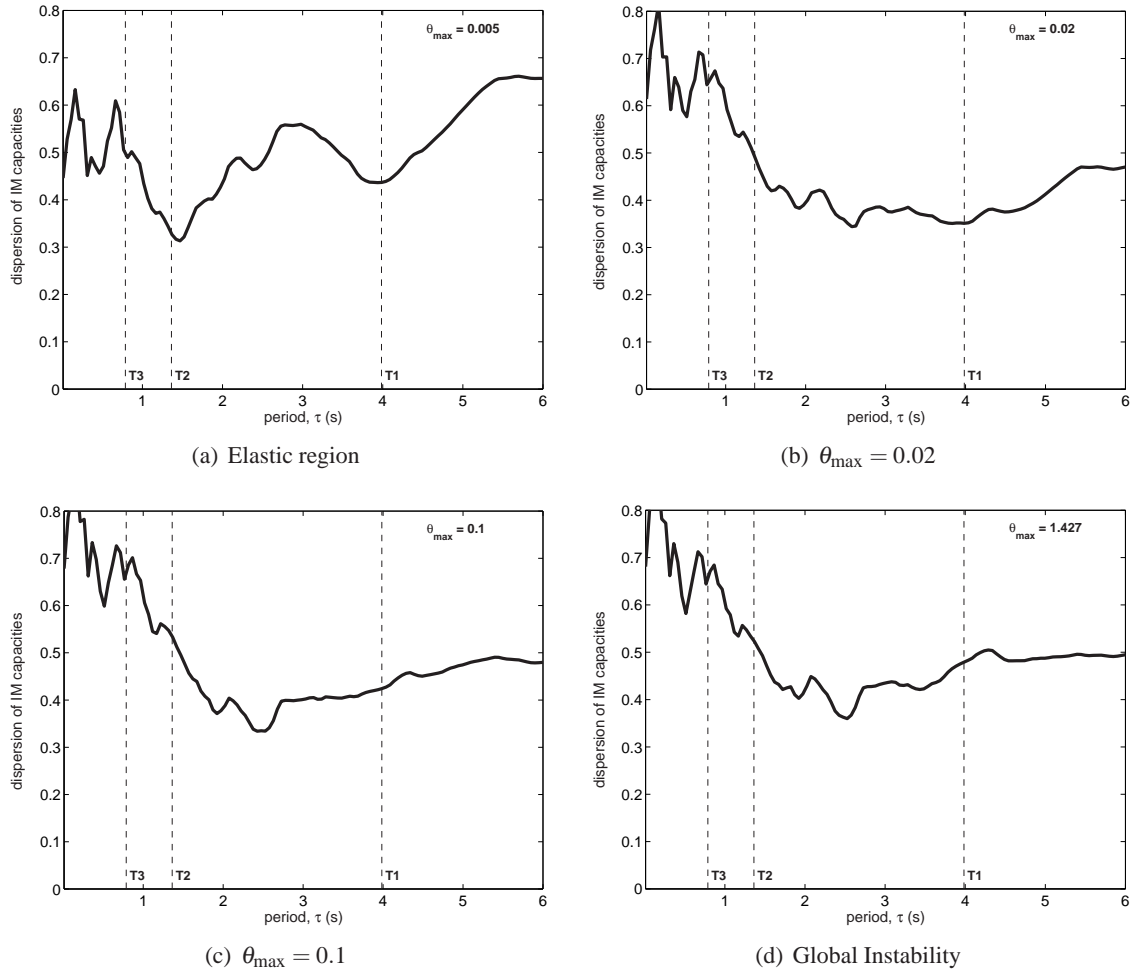


**Figure 6.10:** Dispersion of the  $S_a^c(\tau, 5\%)$ -values versus period  $\tau$  for four limit-states of the 20-story building.

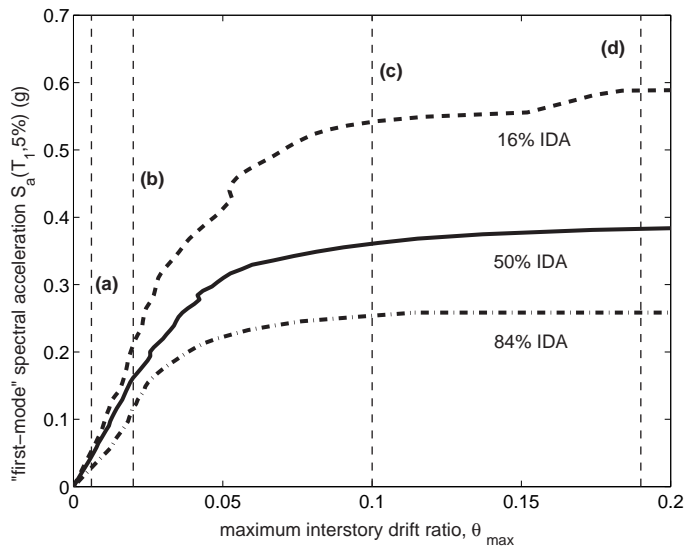


**Figure 6.11:** The fractile IDA curves and capacities for four limit-states (Figure 6.10) of the 20-story building.

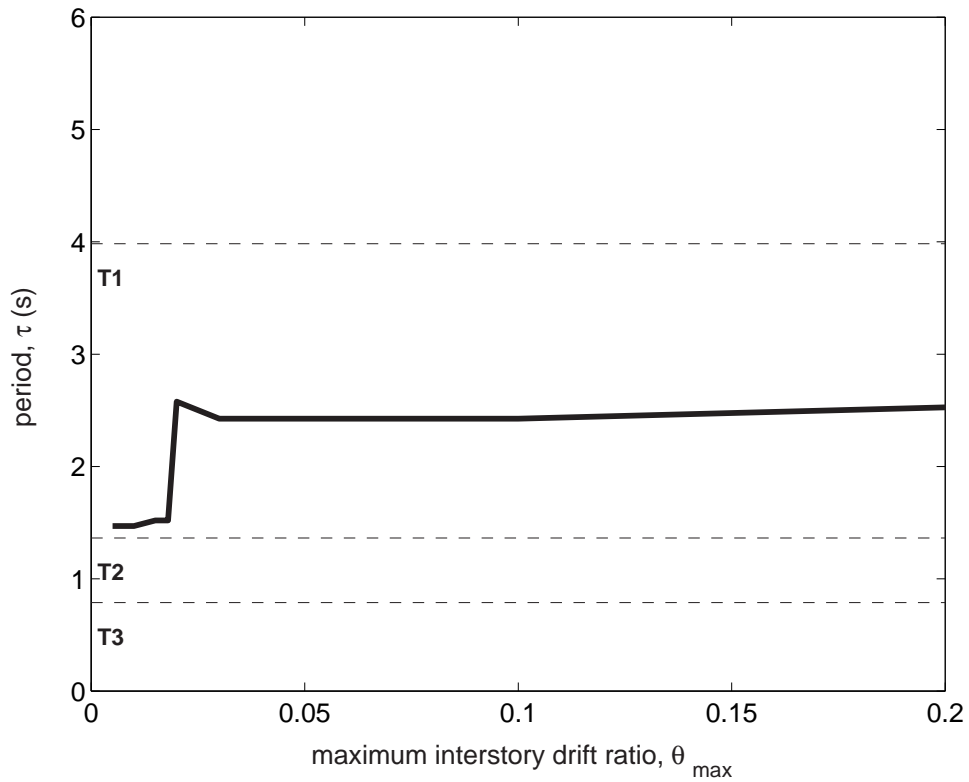


Figure 6.12: The optimal period  $\tau$  as it evolves with  $\theta_{\max}$  for the 20-story building.

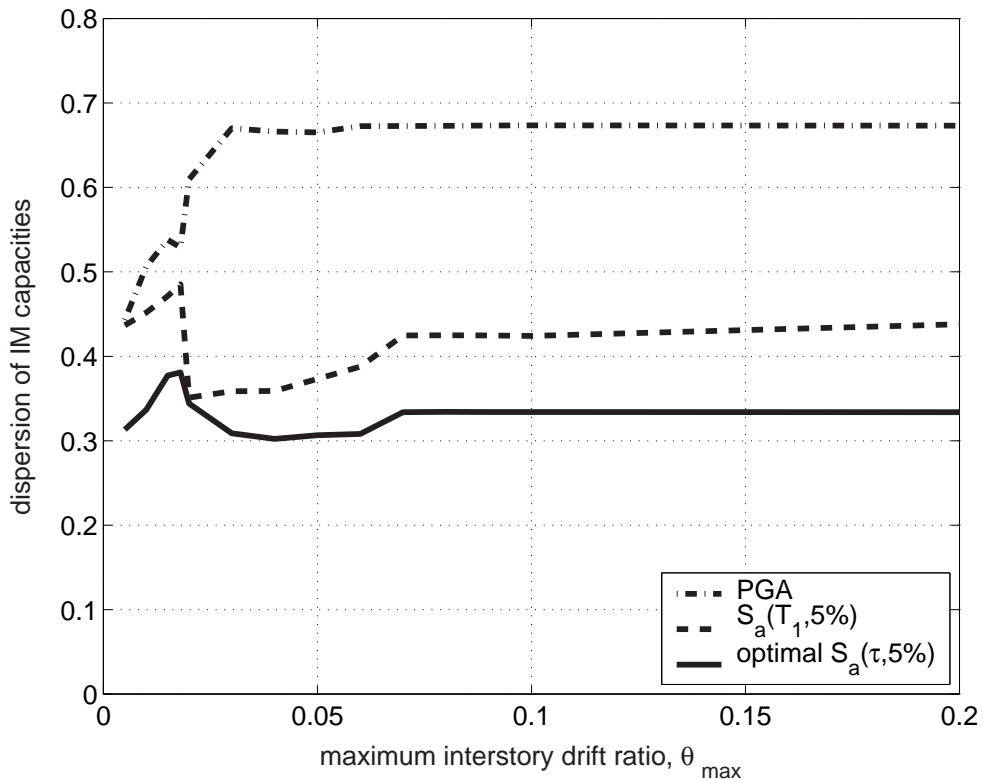
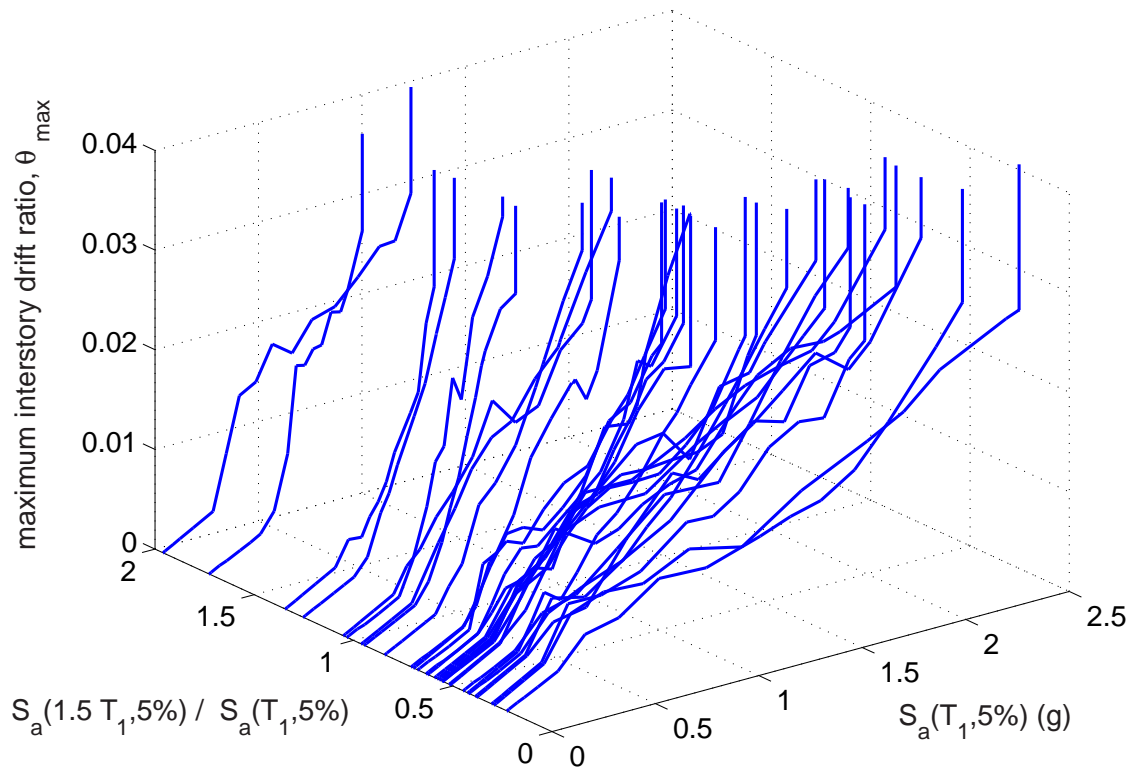
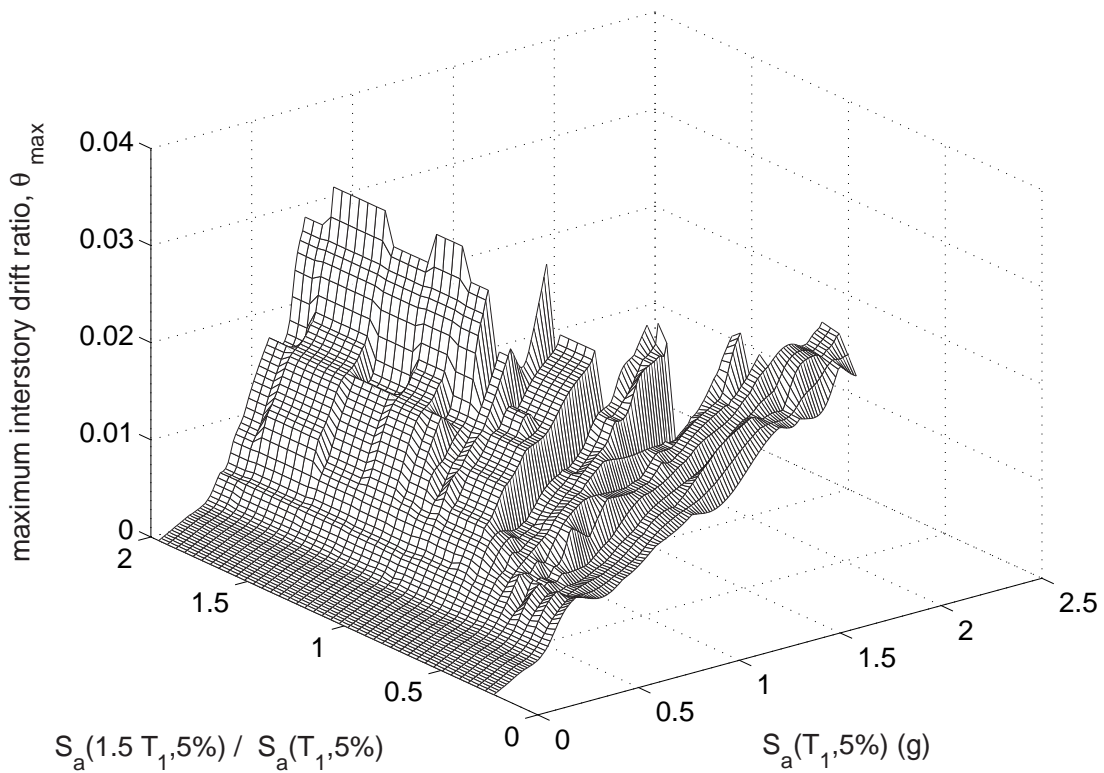


Figure 6.13: The dispersion for the optimal  $S_a(\tau, 5\%)$  compared to  $S_a(T_1, 5\%)$  and PGA, versus the limit-state definition,  $\theta_{\max}$ , for the 20-story building.



**Figure 6.14:** The thirty IDA curves for the 5-story building in  $S_a(T_1, 5\%)$  and  $R_{sa}(1.5, T_1)$  coordinates.



**Figure 6.15:** The median IDA surface for the 5-story building in  $S_a(T_1, 5\%)$  and  $R_{sa}(1.5, T_1)$  coordinates.

practice of plotting the *IM* on the vertical axis, we will now plot both *IMs* on the two horizontal axes and put the *DM* on the vertical one, to visually separate the “input” from the “output”. As a consequence, the flatlines are now vertical lines, rather than horizontal ones.

Still, we are able to interpolate for only the scalable *IM*, while for the non-scalable one we are left with separate, discrete curves. We need to take an extra step here and make the results continuous in the other *IM* as well, which is why we will introduce summarization at this point. However, we are not able to use cross-sectional fractiles, as we did for single *IMs* in Chapter 3. That would require several values of *DM* at each level of the non-scalable *IM*, practically impossible with a limited number of records. However, we can use symmetric-neighborhood running fractiles (Hastie and Tibshirani, 1990) with a given window length to achieve the same purpose. The optimal window length can be chosen, e.g., through cross-validation (Efron and Tibshirani, 1993), or by adopting a reasonable fraction of the sample size. In our case, we selected 30% of the sample size, i.e., used the  $0.3 \times 30 = 9$  symmetrically closest records to approximate the fractile value for each level of the non-scalable *IM*. The resulting median IDA *surface* appears in Figure 6.15.

Now is the time to define limit-state capacities. It can be easily done using *DM*-based rules for all limit-states, with  $\theta_{\max} = +\infty$  resulting in the flatlines for global instability. Imagine horizontal planes, each for a given *DM*-value, cutting the IDA surface. The results can be easily visualized as contours of the fractile IDA surface, seen in Figure 6.16 for the median. Obviously, now the median capacity for a given limit-state is not a single point, as for scalar *IMs*, rather a line, as the ones appearing in Figure 6.16. As an example, we are showing in Figure 6.17 the 16%, 50% and 84% capacity lines for a limit-state at  $\theta_{\max} = 1.6\%$ , close to the onset of global instability. These correspond to our best estimate of the 16%, 50% and 84% vector *IM*-value of the limit-state capacity. For example, if several records had  $R_{sa}(1.5, T_1) = 1.2$ , then if scaled to  $S_a(T_1, 5\%) \approx 0.5g$  (to reach the 16% capacity line) only 16% of them would cause the structure to violate the limit-state, and they would have to be scaled to only  $S_a(T_1, 5\%) \approx 0.6g$  for 84% of them to cause limit-state exceedance. On the other hand, if another set of records were comparatively less rich in the longer periods, e.g., if  $R_{sa}(1.5, T_1) = 0.5$ , they would have to be scaled to  $S_a(T_1, 5\%) \approx 1g$  to cause 50% of the records to violate this same limit-state.

In retrospect, notice that we have slightly altered the “standard” IDA post-processing, as defined by Vamvatsikos and Cornell (2002a, 2004a) (Chapters 2 and 3). For scalar *IMs*, we would first define limit-states points on each IDA, and then summarize, while for vector *IMs* it is advantageous to reverse these steps. Keep in mind though that if we are using only *DM*-based rules for the definition of limit-states, as we do here, then we can similarly reverse these steps for the scalar *IM*. The results will be exactly the same, as explained in Chapter 3: the  $(100 - x)\%$ -fractile IDA limit-state capacities for Immediate Occupancy and Global Instability (and all other *DM*-based limit-states) reside on the  $x\%$ -fractile IDAs. On the other hand, this is not the case for the FEMA-350 (FEMA, 2000a) definition of the Collapse Prevention limit-state. It is partially based on the change of the slope of the IDA (Vamvatsikos and Cornell, 2002a) (Chapter 2), therefore it is clearly not a simple *DM*-based limit-state.

As a final note, it is important to observe how we were forced to introduce summarization over windows rather than stripes. By introducing an extra *IM*, we may have explained some of the variability in the capacities but we have also increased the dimensionality of the sample space, thus the data is more sparse. Where we used to have 30 points for each level (stripe) of the scalable *IM*, we now have only a few points for whole regions of the unscalable *IM*. Obviously, we cannot keep introducing extra dimensions, otherwise we will be facing extreme lack-of-data problems.

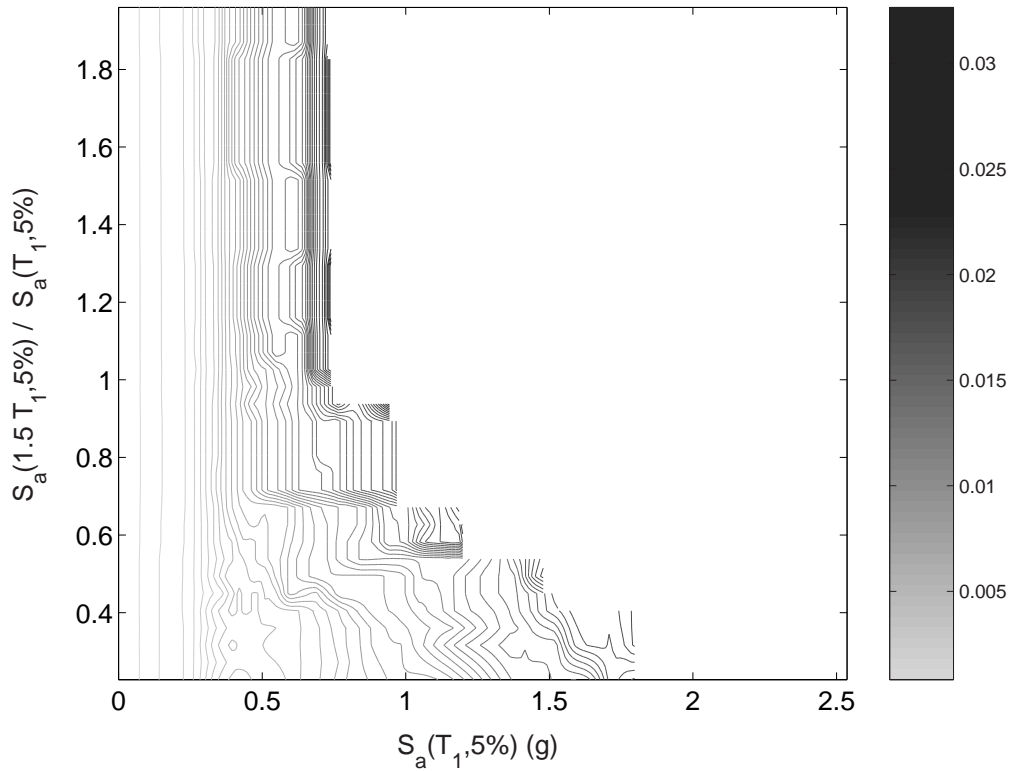


**Figure 6.16:** Median contours for thirty IDA curves for the 5-story building in  $S_a(T_1, 5\%)$  and  $R_{s_a}(1.5, T_1)$  coordinates. Their color indicates the level of  $\theta_{\max}$  as shown in the color bar.

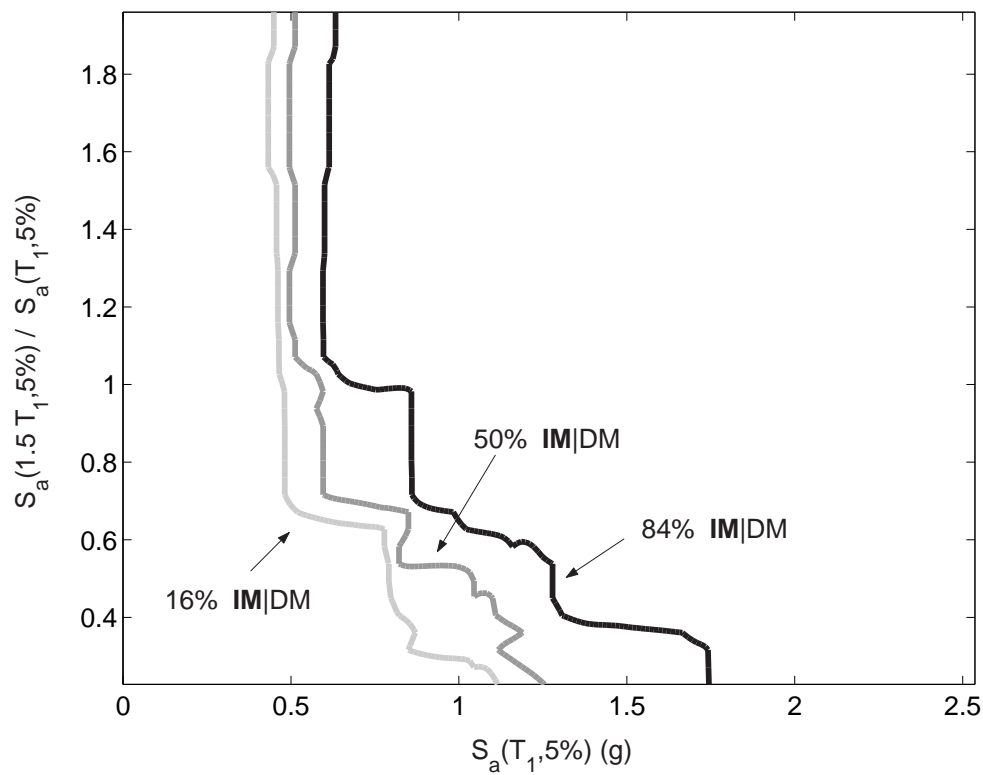


**Figure 6.17:** The 16%, 50% and 84% capacity lines at the limit-state of  $\theta_{\max} = 0.016$  for the 5-story building.

### 6.4.2 Collapsing a vector to a scalar

By observing the contours in Figure 6.16 it becomes obvious that a power law relation can be employed to approximate each one:

$$S_a^c(T_1, 5\%) \approx aR_{sa}(1.5, T_1)^b \quad (6.1)$$

where  $a$ ,  $b$  are the fitted coefficients.

Even though the  $b$ -value is not consistent for all limit-states, as the contours have higher curvature for higher  $DM$ -values, we can still specify some reasonable  $b$ -value that will be adequate for several of them. In that case, we can rewrite Equation (6.1) as

$$a \approx S_a^c(T_1, 5\%) \cdot R_{sa}(1.5, T_1)^{-b} \quad (6.2)$$

and interpret it as follows: by multiplying  $S_a^c(T_1, 5\%)$  capacity values by  $R_{sa}(1.5, T_1)^{-b}$ , we can bring them closer, almost to an (arbitrary) constant. In other words,  $S_a(T_1, 5\%)R_{sa}(1.5, T_1)^{-b}$  is a scalar  $IM$  that will retain much of the vector  $IM$ 's ability to reduce dispersion in limit-state capacities. How much reduction it will achieve will depend on our ability to select a proper  $b$ -value and the goodness-of-fit of Equation 6.1 to the contour.

Not surprisingly, it is such a form that Shome and Cornell (1999), Mehanny and Deierlein (2000) and Cordova et al. (2000) have used to create a new, more effective scalar  $IM$ . While the idea there was mostly driven by the need to be able to use existing attenuation laws to create hazard curves for the new  $IM$  (Cordova et al., 2000), they have come very close to an accurate approximation to the contour shape, at least for this first-mode-dominated structure.

### 6.4.3 Investigating the vector of two spectral values

Clearly, for the 5-story building with negligible higher modes, using a vector instead of a scalar  $IM$  produces very impressive results. The introduction of  $R_{sa}(1.5, T_1)$  provides significant insight to the seismic behavior of the 5-story, as seen in Figure 6.16; when  $R_{sa}(1.5, T_1) > 1$ , as its period lengthens, the damaged structure falls in a more aggressive part of the spectrum and is forced to fail at earlier  $S_a(T_1, 5\%)$  levels, exhibiting rapid softening. On the other hand, if the ratio is less than one, the period lengthening helps to relieve the structure allowing the IDA to harden and reach higher flatlines (in terms of the  $S_a(T_1, 5\%)$ ). Actually, the less aggressive the record is (lower  $R_{sa}(1.5, T_1)$ ) the more the IDA hardens. The introduction of the extra  $IM$  has helped explain some of the record-to-record variability in the  $S_a(T_1, 5\%)$  capacities for almost any level of  $DM$ , i.e., for any limit-state.

Additional studies show that such results are not very sensitive to the spectral ratio that we choose to use. At least for the 5-story building, almost any such lengthened period will provide some explanation of the variability in capacity. On the other hand though, it may not be so for other buildings. As shown in Figures 6.18 and 6.19, where  $R_{sa}(1.5, T_1)$  is also used, it yields little or no additional information for the 9-story and 20-story building respectively. If on the other hand, we use another spectral coordinate, at a period lower than  $T_1$ , some additional resolution is gained, but the shape of the contours may no longer be a power-law, as seen in Figure 6.20 for the 20-story when  $R_{sa}(0.5, T_1)$  is used in addition to  $S_a(T_1, 5\%)$  (where  $0.5T_1 \approx 1.5T_2$  for this building). Still, even for these complex buildings, there exist periods that explain well the variability and even show the familiar, power-law shape of the contours, as shown for the 9-story when we use  $R_{sa}(0.7, T_1)$  (where  $0.7T_1 \approx 2T_2$  for the 9-story), Figure 6.21, and even the 20-story when we introduce  $R_{sa}(0.3, T_1)$  in Figure 6.22 (where  $0.3T_1 \approx T_2$  for the 20-story). Clearly, there is great potential in using the power-law form, but the question remains whether the appropriate periods for its use are easy to determine, especially *a priori*.

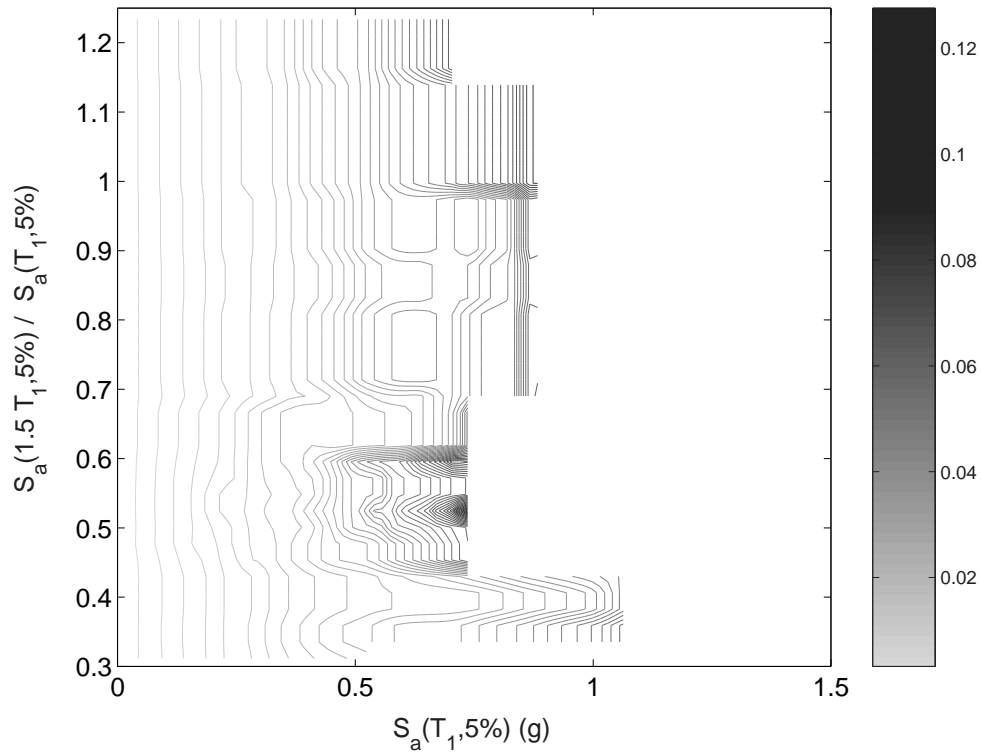


**Figure 6.18:** Median contours for the 9-story building in  $S_a(T_1, 5\%)$  and  $R_{sa}(1.5, T_1)$  coordinates. Little has been gained by using a vector.

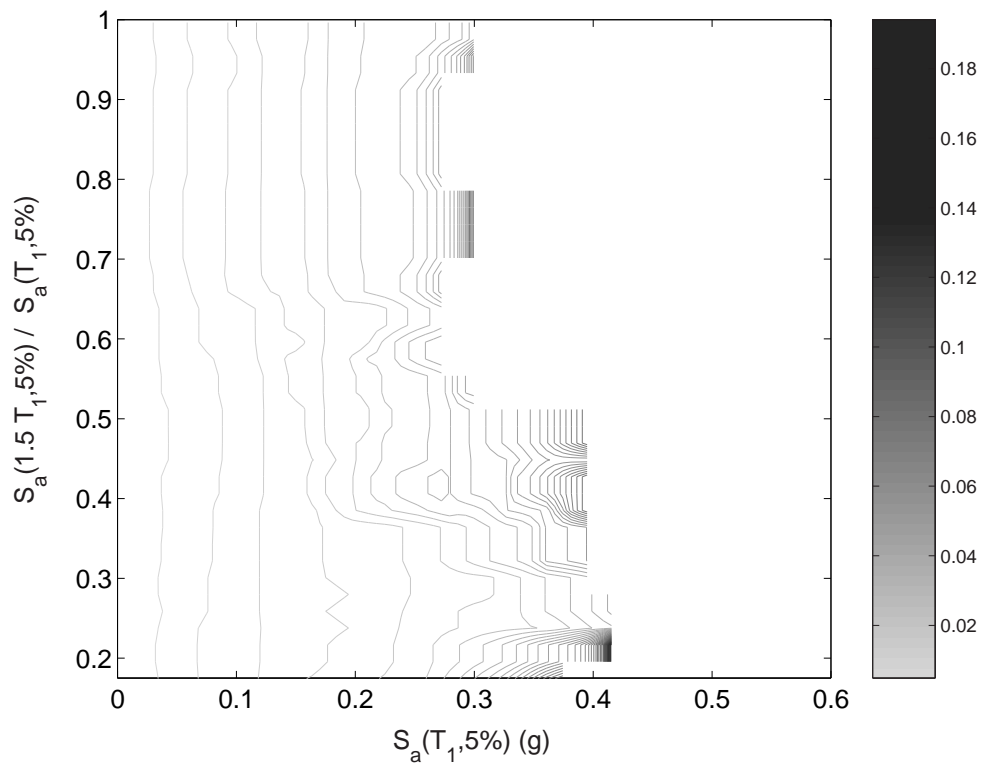


**Figure 6.19:** Median contours for the 20-story building in  $S_a(T_1, 5\%)$  and  $R_{sa}(1.5, T_1)$  coordinates. They are colored by the value of  $\theta_{\max}$ . In this case, the use of a vector has only a small influence.

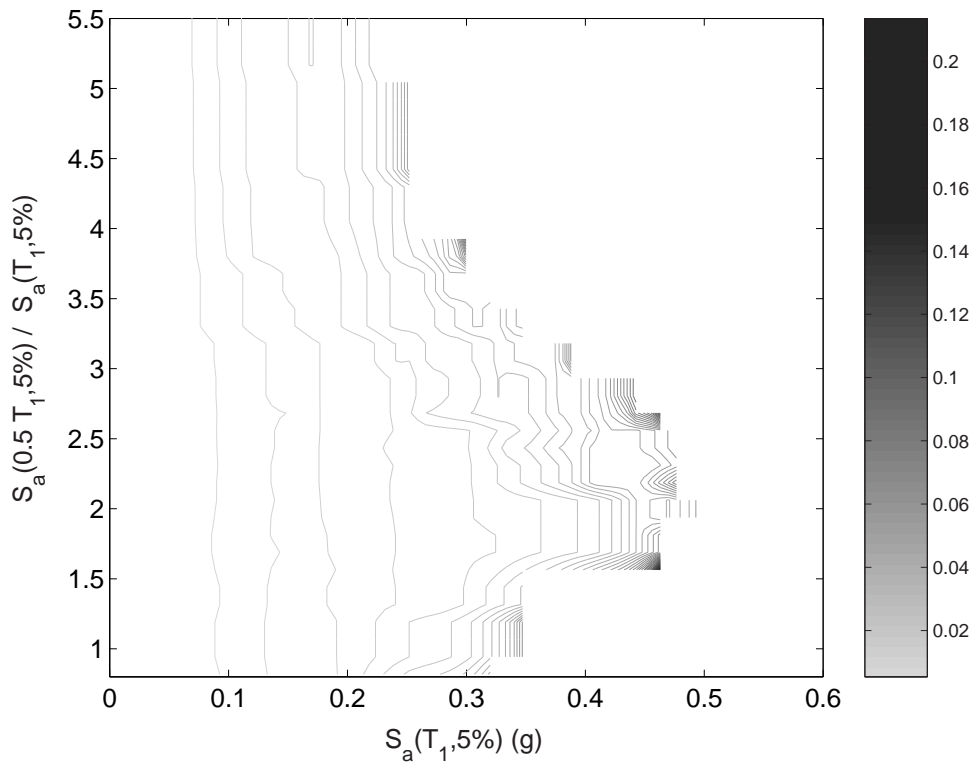


**Figure 6.20:** Median contours for the 20-story building in  $S_a(T_1, 5\%)$  and  $R_{sa}(0.5, T_1)$  coordinates. They are colored by the value of  $\theta_{\max}$ . Some variability is explained but the contours are not simple.

## 6.5 Using a power-law form with two or three spectral values

Motivated by the power-law form that the contours take on many occasions, we have decided to directly investigate its application as an improved *IM*. Formally, we intend to perform a search for the optimally efficient *IM* of the form

$$\begin{aligned} IM &\equiv S_a(\tau_a, 5\%)^{1-\beta} S_a(\tau_b, 5\%)^\beta \\ &= S_a(\tau_a, 5\%) \left[ \frac{S_a(\tau_b, 5\%)}{S_a(\tau_a, 5\%)} \right]^\beta \end{aligned} \quad (6.3)$$

where  $\tau_a$  and  $\tau_b$  are arbitrary periods and  $\beta \in [0, 1]$ . Notice the difference with [Shome and Cornell \(1999\)](#) who constrain both periods to be  $T_1$  and  $T_2$  respectively, or [Mehanny and Deierlein \(2000\)](#) and [Cordova et al. \(2000\)](#), who chose to constrain one of the periods to be  $T_1$ . Instead, we intend to let the optimization find the best values,  $\tau_a$ ,  $\tau_b$  and  $\beta$ .

Additionally, we will investigate a power-law form containing three spectral values or, equivalently, a single spectral value and two spectral ratios:

$$\begin{aligned} IM &\equiv S_a(\tau_a, 5\%)^{1-\beta-\gamma} S_a(\tau_b, 5\%)^\beta S_a(\tau_c, 5\%)^\gamma \\ &= S_a(\tau_a, 5\%) \left[ \frac{S_a(\tau_b, 5\%)}{S_a(\tau_a, 5\%)} \right]^\beta \left[ \frac{S_a(\tau_c, 5\%)}{S_a(\tau_a, 5\%)} \right]^\gamma \end{aligned} \quad (6.4)$$

where  $\tau_a$ ,  $\tau_b$  and  $\tau_c$  are arbitrary periods,  $\beta, \gamma \in [0, 1]$  and  $\beta + \gamma \leq 1$ .

The optimal two periods for the 5-story building appear in [Figure 6.23](#) over a range of limit-states from elasticity to global collapse. At elasticity, the two periods converge to the first mode,  $T_1$ , since the structure has practically no higher mode effects. As damage increases, one of the periods hovers close to  $T_1$ , while the other is increasing and fluctuates about 50% higher. The

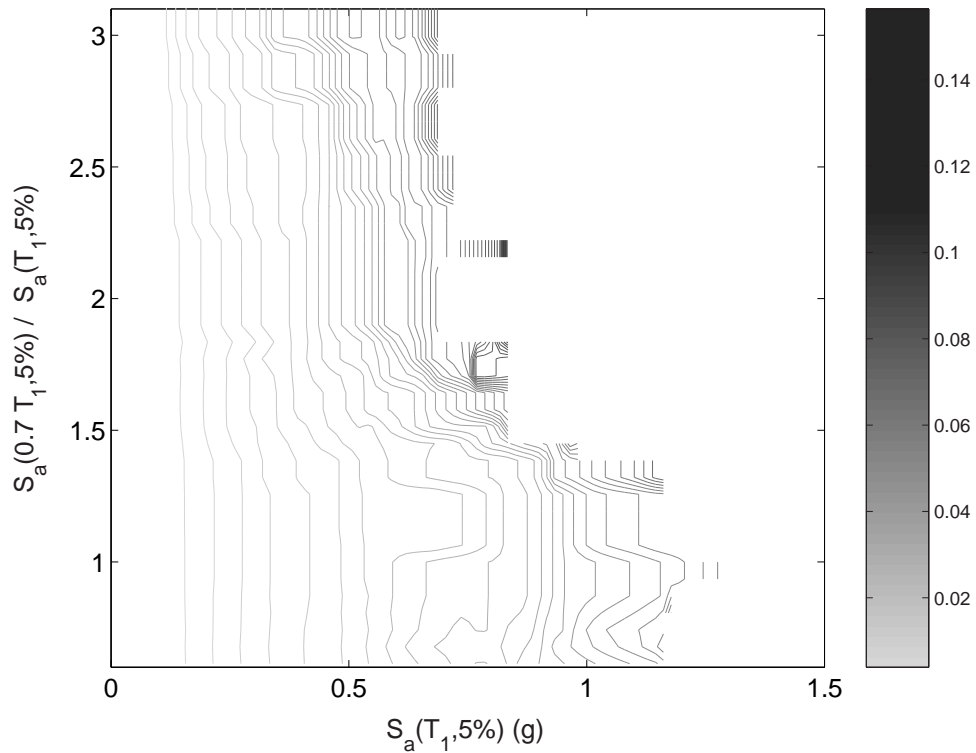


**Figure 6.21:** Median contours for the 9-story building in  $S_a(T_1, 5\%)$  and  $R_{sa}(0.7, T_1)$  coordinates. They are colored by the value of  $\theta_{\max}$ . The use of a vector is beneficial, and the contours have power-law shape.

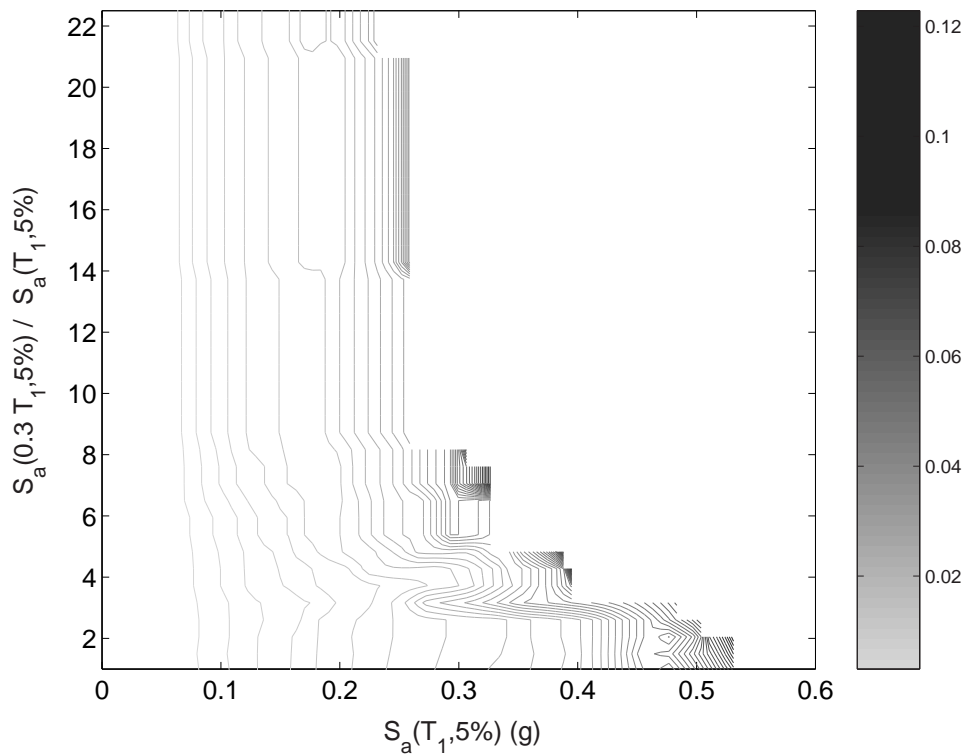


**Figure 6.22:** Median contours for the 20-story building in  $S_a(T_1, 5\%)$  and  $R_{sa}(0.3, T_1)$  coordinates. They are colored by the value of  $\theta_{\max}$ . The use of a vector is beneficial, and the contours have power-law shape.

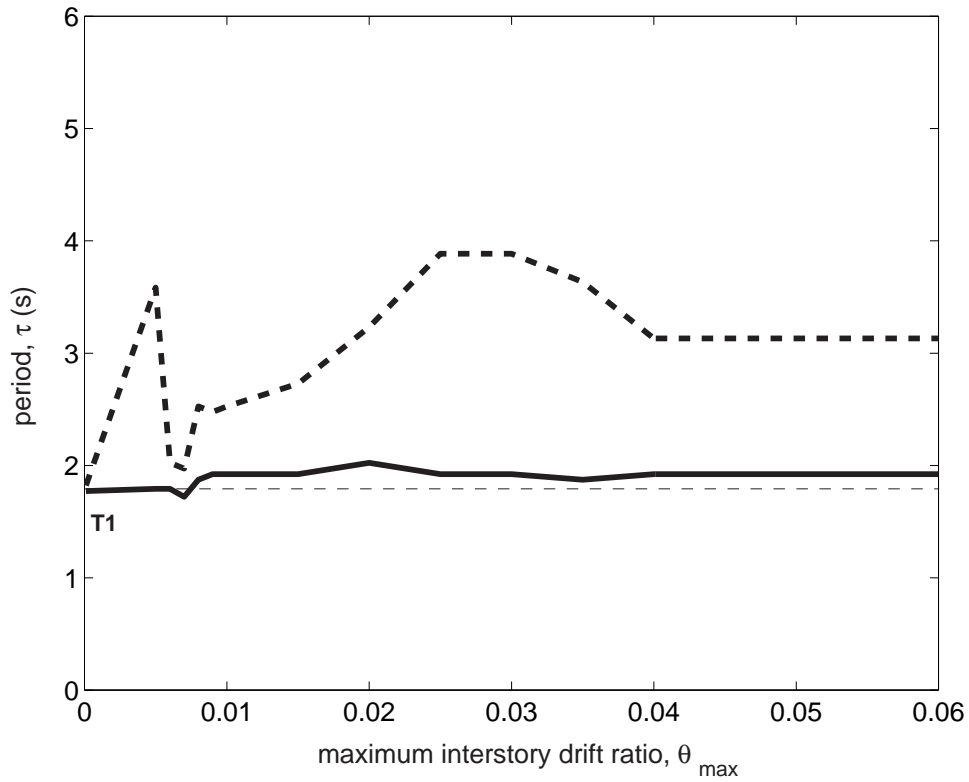


Figure 6.23: The two optimal periods  $\tau_a, \tau_b$  as they evolve with  $\theta_{\max}$  for the 5-story building.

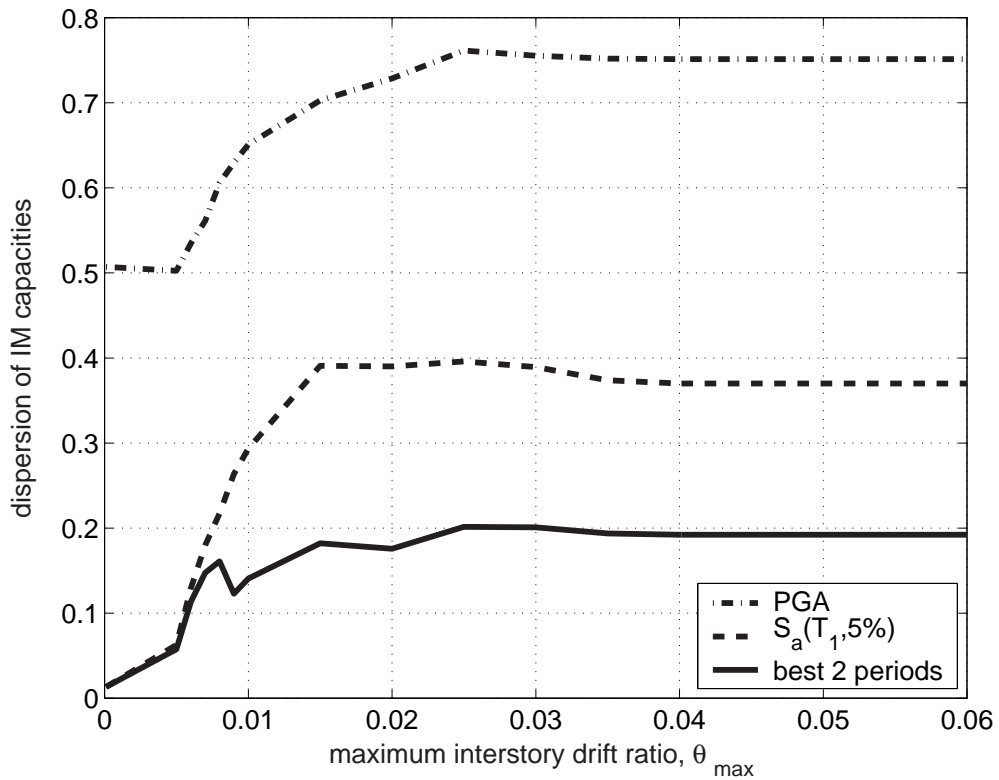


Figure 6.24: The dispersions for optimal  $S_a(\tau_a, 5\%)^{1-\beta} S_a(\tau_b, 5\%)^\beta$  versus  $S_a(T_1, 5\%)$  and PGA for the 5-story building.

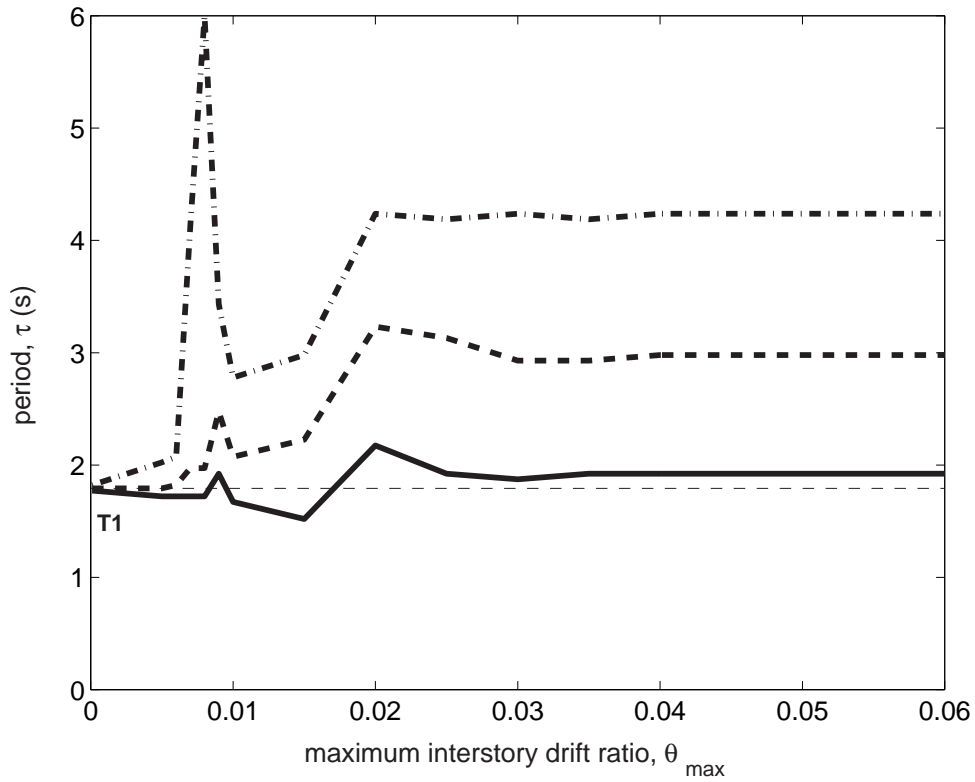


Figure 6.25: The three optimal periods  $\tau_a$ ,  $\tau_b$ ,  $\tau_c$  as they evolve with  $\theta_{\max}$  for the 5-story building.

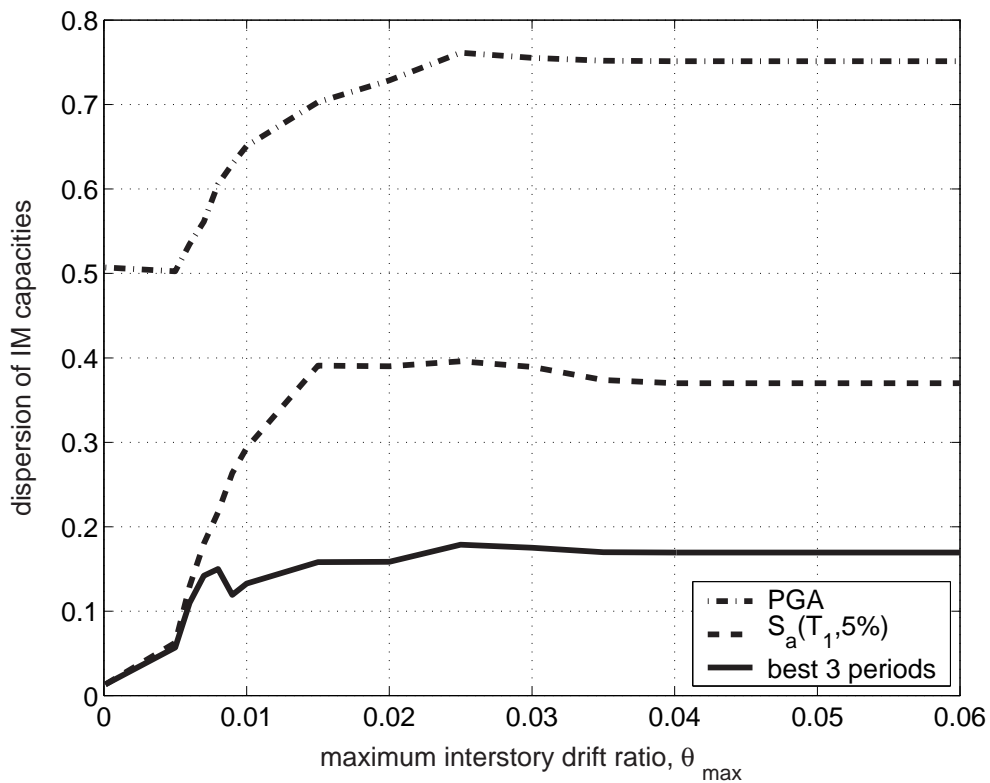
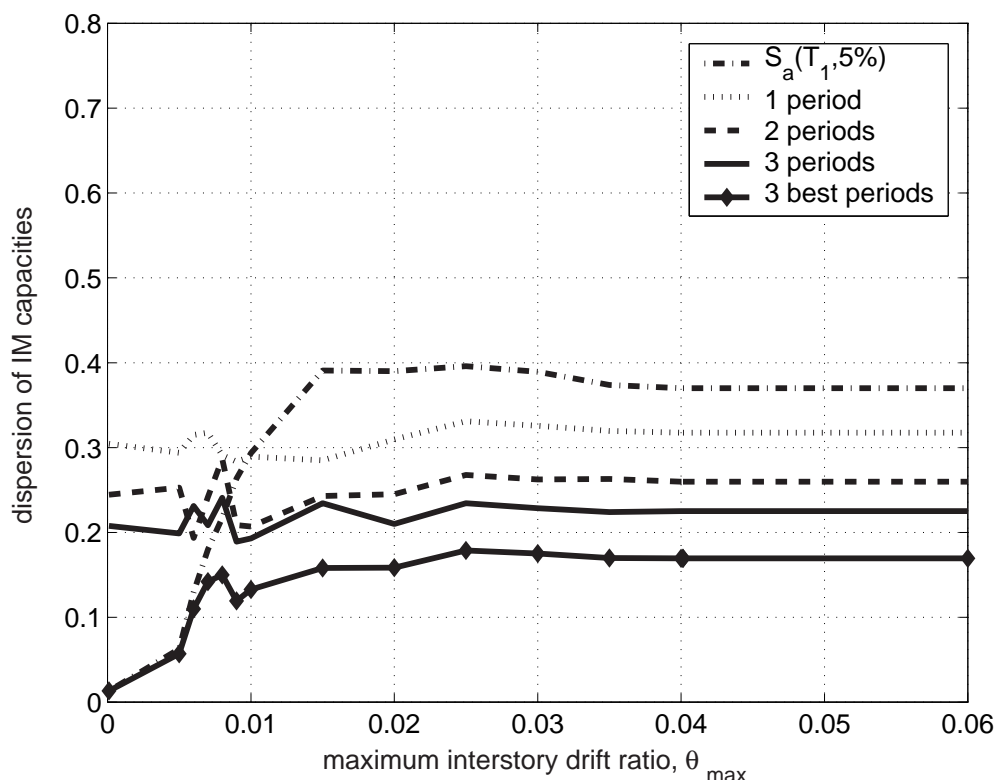


Figure 6.26: The dispersions for optimal  $S_a(\tau_a, 5\%)^{1-\beta-\gamma} S_a(\tau_b, 5\%)^\beta S_a(\tau_c, 5\%)^\gamma$  versus the dispersions for PGA and  $S_a(T_1, 5\%)$  for the 5-story building.



**Figure 6.27:** The 84% fractile of the suboptimal dispersion when using a single spectral value versus a power-law combination of two or three periods for the 5-story building. For comparison, the dispersion achieved by  $S_a(T_1, 5\%)$  and the optimal three-periods power-law is also shown.

optimal value of  $\beta$  is always about 0.5, favoring equal weighting of the two periods. Comparing Figures 6.5 and 6.24 it becomes obvious that the use of two spectral values reduces the capacity dispersion by a small amount relative to the use of a single (optimal) value. While  $S_a(T_1, 5\%)$  would achieve about 40% dispersion and a single optimal period would reduce this to 25%, the use of two periods only brings it down to 20%.

If we introduce a third spectral value for the 5-story through Equation 6.4, then we come up with the three optimal periods shown in Figure 6.25 for a range of damage-states. Again, in elasticity, the three periods converge at  $T_1$  and then they slowly separate. One period stays at about  $T_1$  and the rest gradually increase. When close to global collapse the second one is 50% higher and the third 100% higher than  $T_1$ . Again, equal weighting seems to be the rule for all limit-states since the optimal values are  $\beta \approx \gamma \approx 1/3$ . The dispersion reduction is even less spectacular than before (Figure 6.26), reaching a level of just 18% at global collapse compared to the 20% of the two spectral values. Clearly, we have reached the limits of what the elastic spectral shape can do for this building. As expected, when higher modes are insignificant, one, maybe two, periods will be enough to determine an improved, near-optimal  $IM$ , cutting down dispersion by a factor of two relative to  $S_a(T_1, 5\%)$ . Adding more complexity to the  $IM$  does not seem to help efficiency, as the system is not that complex itself.

When practically implementing such  $IM$ s before the dynamic analyses are performed, it is important that efficiency remains high even when not using the (unknown *a priori*) optimal periods. To investigate the sensitivity of the proposed scalar  $IM$ s we have simulated random user choices for the period(s) used for the single spectral value or the power-law combinations of two or three values. The user is supposed to have picked periods uniformly distributed within  $\pm 20\%$  of the optimal values for each  $IM$  and to have selected equal weighting of spectral values in the power-law (i.e.,  $\beta = 1/2$  or  $\beta = \gamma = 1/3$ ). Such simulations are repeated numerous times for each

limit-state (i.e., value of  $\theta_{\max}$ ) and the achieved suboptimal dispersion is calculated for each *IM*. In Figure 6.27 we are plotting the 84%-fractile of the suboptimal dispersion for the single period and the two power-law combinations versus the  $\theta_{\max}$  definition of each limit-state; i.e., we are focusing on a worse-than-average scenario. For comparison, the dispersion when using  $S_a(T_1, 5\%)$  and when using the optimal three periods power-law is also shown. Obviously, the largest effect for the 5-story is in the elastic region, where not using  $T_1$  is a very bad choice in all cases. In the nonlinear range, missing the optimal period seriously degrades the performance of a single *IM*, bringing its dispersion to about 30%, a fact also observed in Figure 6.2. On the other hand, the two and three period combinations perform relatively well, managing to keep a dispersion of about 25% and 20%. Again, just as when using a vector of two spectral values, the power-law form is quite stable, even more so than using a single spectral value, hence relatively large changes away from the optimal periods do not significantly influence the dispersion reduction of the power-law *IM*. Practically, in the post-yield region, using the first mode plus e.g., a 50% increased period, with  $\beta = 0.5$  (i.e., equal weight on both spectral values) will in general produce good results. Actually these conclusions are quite in agreement with Cordova et al. (2000).

In the case of the 9-story building, the two optimal periods appear in Figure 6.28 and the three best in Figure 6.30. In the first case, the smaller period seems to stay at  $T_2$  while the higher one starts from  $T_1$  and increases to some higher value, only to return back to  $T_1$  again. For the three periods, the results seem to favor one period at  $T_1$ , another at  $T_2$  and a third at about twice  $T_1$ . Similarly to the 5-story, equal weighting is the optimal strategy for both *IMs* and almost all limit-states. With either two or three periods, as seen in Figures 6.29 and 6.31, the dispersion reduction is about the same. Actually, the dispersion drops from 40% for one optimal period (or even for just  $S_a(T_1, 5\%)$ ), to less than 25–30% when two or more periods are used. Again, it seems that two spectral values are enough for this first-mode-dominated building and clearly better than just one.

What is of more value though is that the efficiency of the two or three-element *IM* is very stable relative to the choices of the periods and the  $\beta$ ,  $\gamma$  weights. In Figure 6.32 we plot the results of the previously described sensitivity analysis for the 9-story. Clearly, using only one (suboptimal) period is often worse or at most as good as when using  $S_a(T_1, 5\%)$ , as observed in Figure 6.6 as well. On the other hand, with two or three periods, equally weighted in a power-law form, the *IM* is considerably more robust and relatively reasonable efficiency is maintained. If we follow our observations and set one value around  $T_1$ , another at about  $T_2$  and maybe a third 50% or 100% higher than  $T_1$ , then weigh them equally ( $\beta = 1/2$  or  $\beta = \gamma = 1/3$ ), a dispersion of about 30% is easily achieved in contrast to the elusive single optimal period.

Figure 6.33 shows the best two periods for the 20-story building. One seems to stay somewhere in the middle of  $T_2$  and  $T_3$  while the other is a lengthened version of the first mode, perhaps by 30–50%. The picture is clearer for the three best periods in Figure 6.35, where each seems to be a (roughly) 50% lengthened version of one of the three elastic modes,  $T_1$ ,  $T_2$  and  $T_3$ . The optimal weights are roughly equal for all two or three periods. The dispersion reduction is significant in both cases, reaching down to 25% versus the 35% achieved by a single optimal period or the 40% of  $S_a(T_1, 5\%)$  (Figure 6.34, 6.36). While the use of three periods rather than two seems to offer little benefit, actually it makes the *IM* quite easier to define. Additionally the results of the sensitivity analysis in Figure 6.37 suggest that efficiency remains relatively high when three suboptimal periods are employed, versus two or one. Simply by increasing all three elastic periods by some reasonable percentage and employing equal weights ( $\beta = \gamma = 1/3$ ) works fine for all limit-states, achieving dispersions in the order of 30%.

In conclusion, it seems that the use of the power-law form with two or three spectral values helps even when the higher modes are significant. Actually, the more significant they are, the more periods we might want to include. The benefit is not so much in the reduction of dispersion, rather in the robustness of the *IM* and the ability to identify it *a priori*. Further investigation of more structures is needed before some concrete proposals are made, but the concept looks promising.

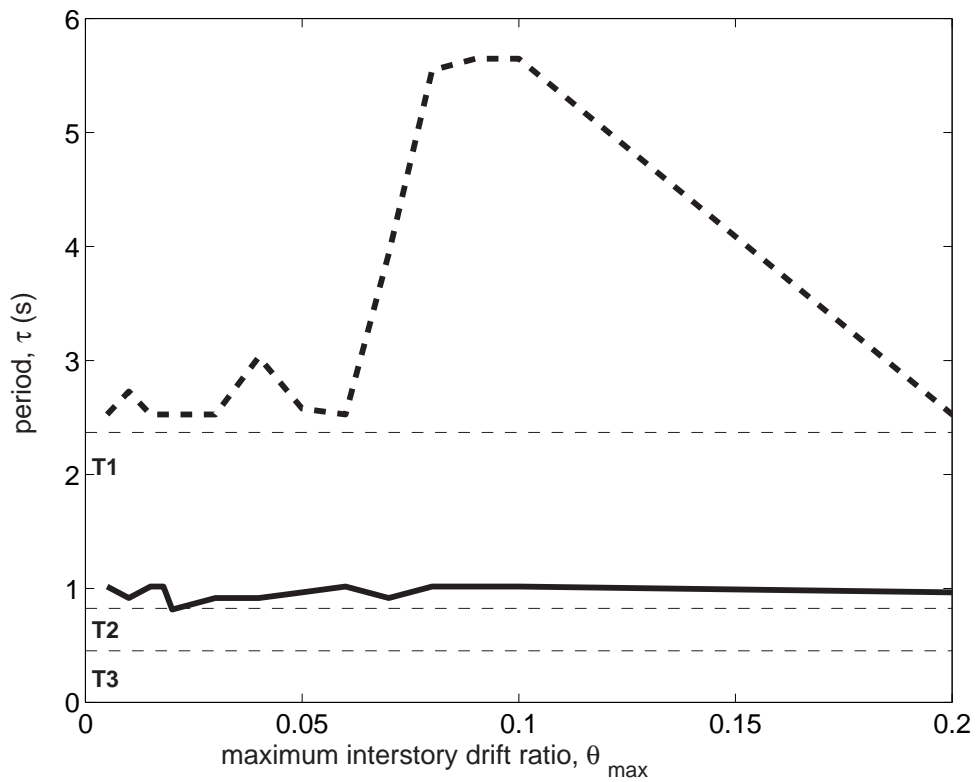


Figure 6.28: The two optimal periods  $\tau_a$ ,  $\tau_b$  as they evolve with  $\theta_{\max}$  for the 9-story building.

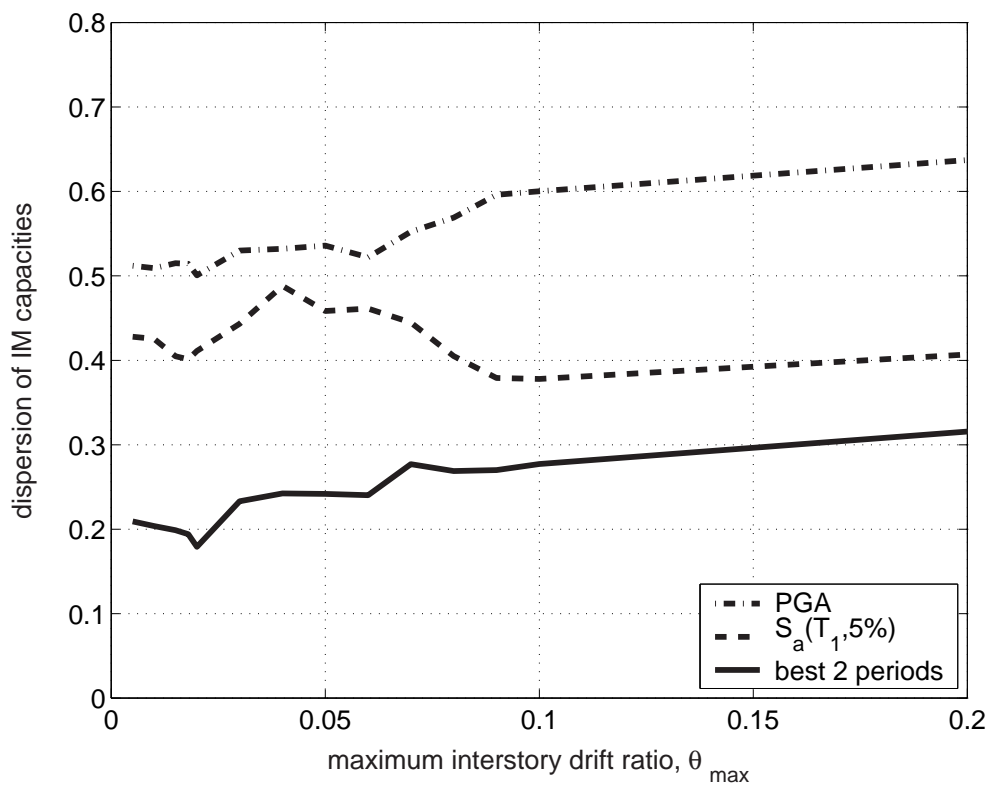


Figure 6.29: The dispersions for optimal  $S_a(\tau_a, 5\%)^{1-\beta} S_a(\tau_b, 5\%)^\beta$  versus  $S_a(T_1, 5\%)$  and PGA for the 9-story building.

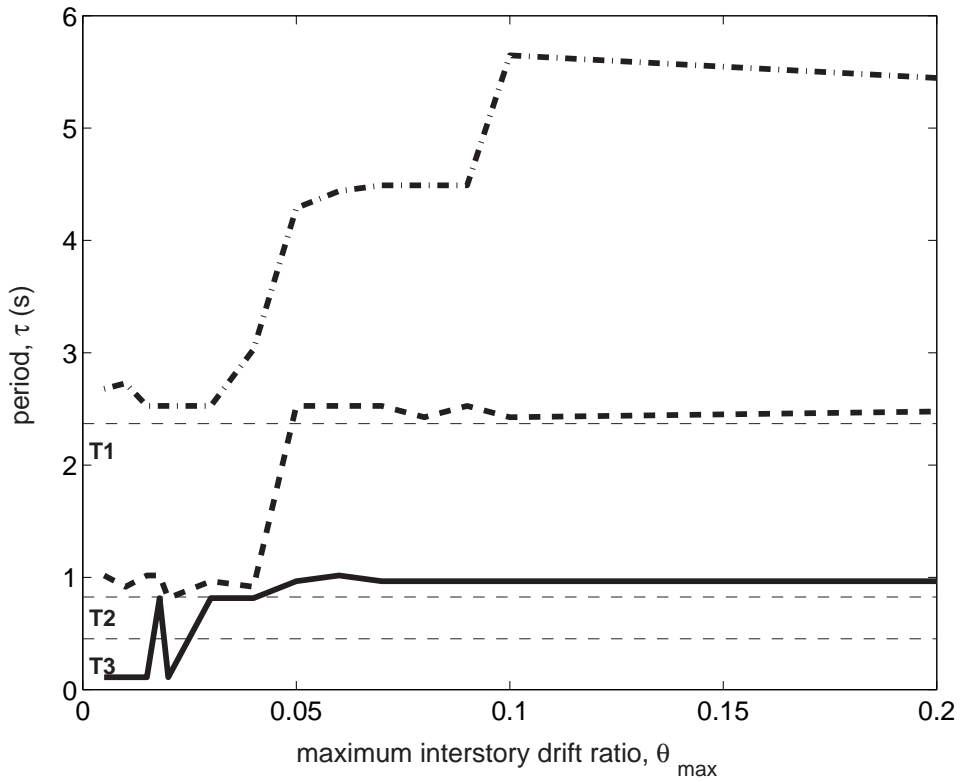


Figure 6.30: The three optimal periods  $\tau_a$ ,  $\tau_b$ ,  $\tau_c$  as they evolve with  $\theta_{\max}$  for the 9-story building.

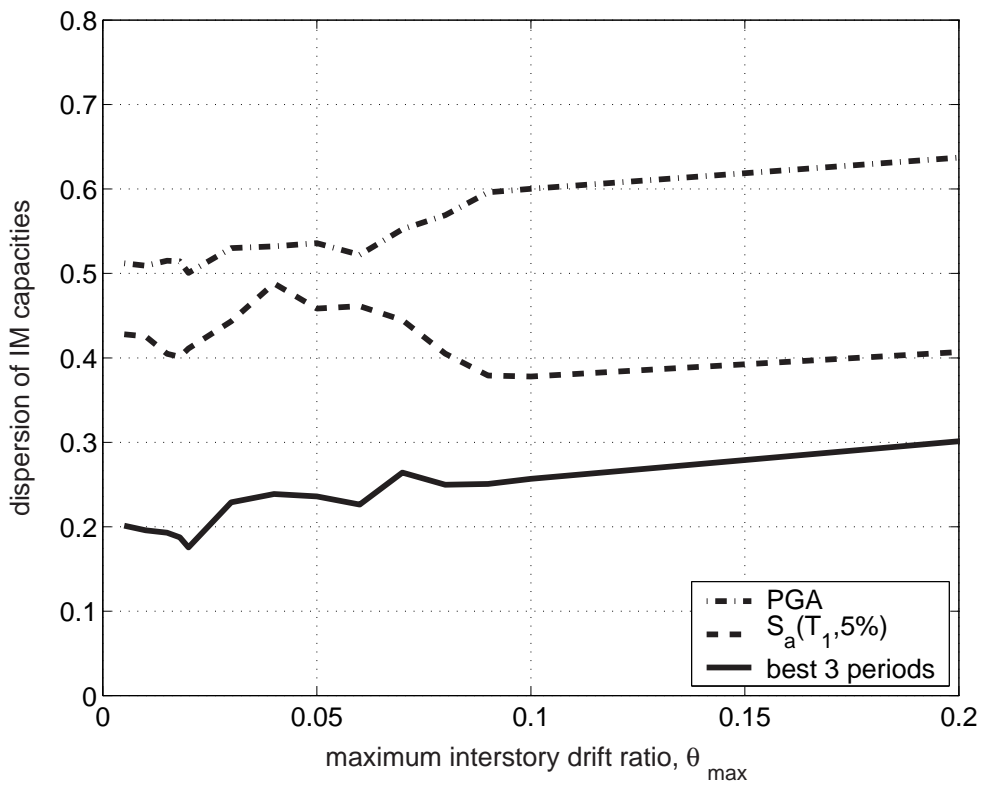
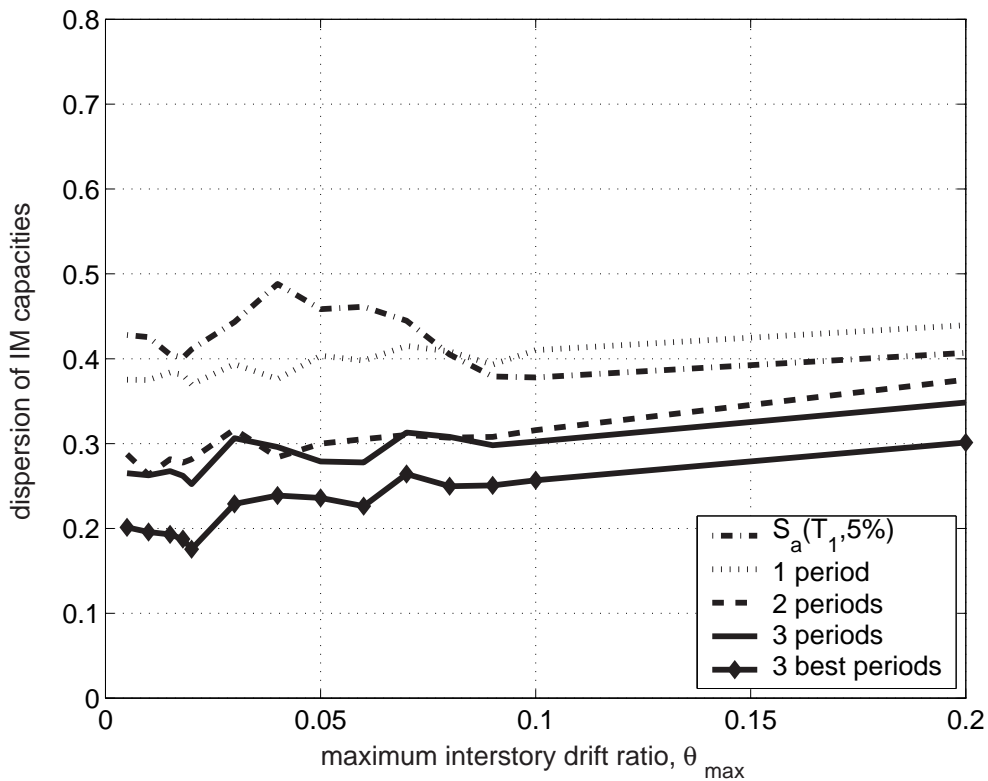


Figure 6.31: The dispersions for optimal  $S_a(\tau_a, 5\%)^{1-\beta-\gamma} S_a(\tau_b, 5\%)^\beta S_a(\tau_c, 5\%)^\gamma$  versus the dispersions for PGA and  $S_a(T_1, 5\%)$  for the 9-story building.



**Figure 6.32:** The 84% fractile of the suboptimal dispersion when using a single spectral value versus a power-law combination of two or three periods for the 9-story building. For comparison, the dispersion achieved by  $S_a(T_1, 5\%)$  and the optimal three-periods power-law is also shown.

## 6.6 Using all spectral values

The problems encountered with all previous attempts to use the spectral shape mainly stem from the fact that we were looking for distinct “perfect” periods. This in part made the problem quite more difficult, as we were trying to describe the full spectral shape with only one or two values. We might want to use more information from the spectral shape than just two discrete values, and this hopefully will open up some easier paths. Still, visualizing such a vector would be hard, and it would be equally difficult to have enough data to fill the extra dimensions. On the other hand, the collapsed form of the vector to a scalar suggests an easier way to approach this problem. Including more spectral coordinates in Equation (6.1) is relatively straightforward, while finding the right  $\beta$ ,  $\gamma$ -coefficients may be handled by standard linear regression methods, penalized to reflect the sample size limitations.

Taking one step further, there exist methods in statistics that can treat each record’s spectrum as a single, functional predictor, thus taking into consideration the shape of the full spectrum and use it as a predictor for limit-state capacity. In formal terms we are proposing the use of a functional linear model (Ramsay and Silverman, 1996) that will use each record’s spectrum to predict a scalar response, i.e., its limit-state  $S_a^{c,i}(T_1, 5\%)$ -capacity derived from the IDA curve of that  $i$ -th record. In essence, we are proposing the use of the linear functional model

$$\ln S_a^{c,i}(T_1, 5\%) = \alpha + \int_{t_s}^{t_e} \beta(\tau) \ln \left[ \frac{S_a(\tau, 5\%)}{S_a(T_1, 5\%)} \right] d\tau + \varepsilon_i \quad (6.5)$$

where  $\alpha$  is the regression intercept,  $\beta(\tau)$  is the regression coefficient function,  $t_s$  and  $t_e$  are the starting and ending periods that bound the spectral region of interest and, finally,  $\varepsilon_i$  are the independent and normally distributed errors (with a mean of zero).

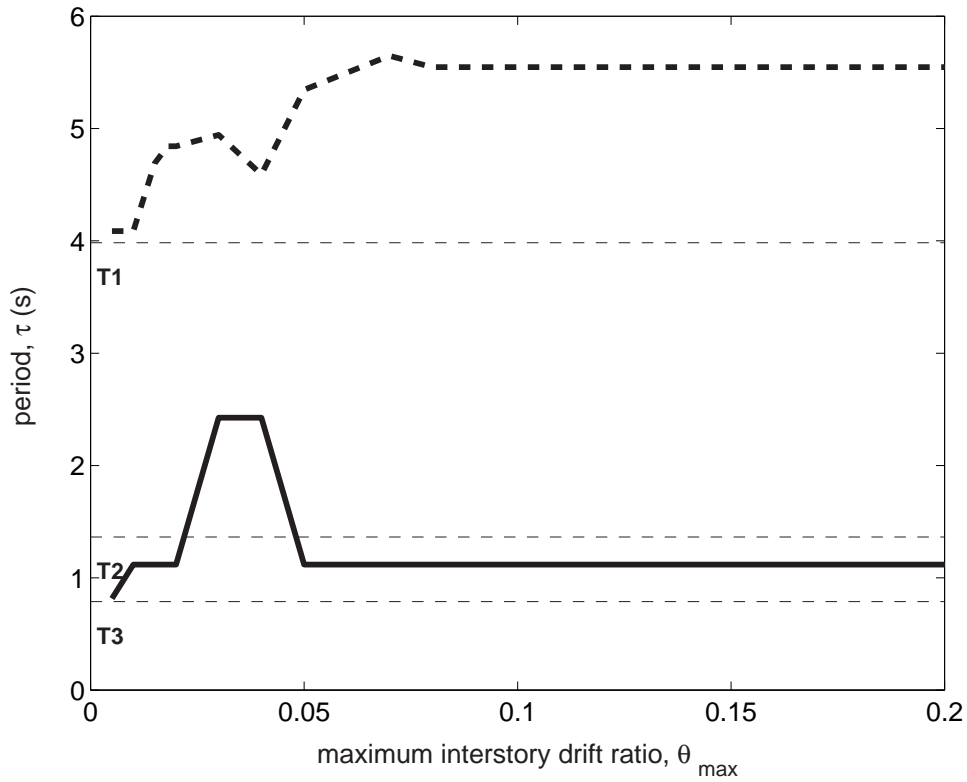


Figure 6.33: The two optimal periods  $\tau_a$ ,  $\tau_b$  as they evolve with  $\theta_{\max}$  for the 20-story building.

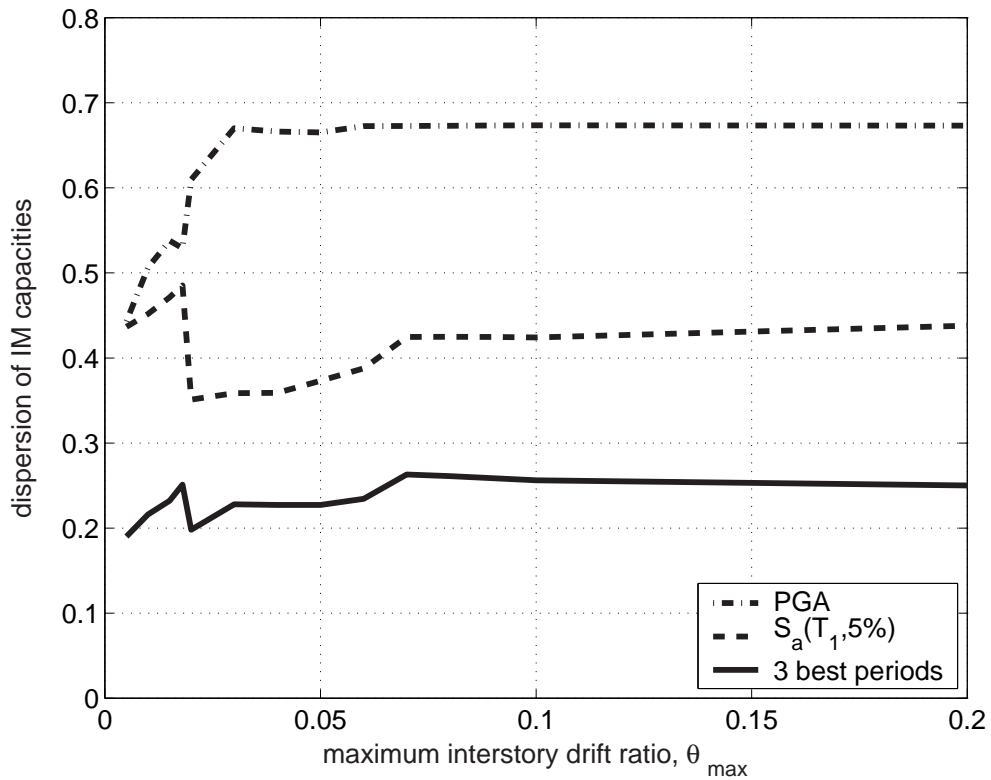


Figure 6.34: The dispersions for optimal  $S_a(\tau_a, 5\%)^{1-\beta} S_a(\tau_b, 5\%)^\beta$  versus  $S_a(T_1, 5\%)$  and PGA for the 20-story building.

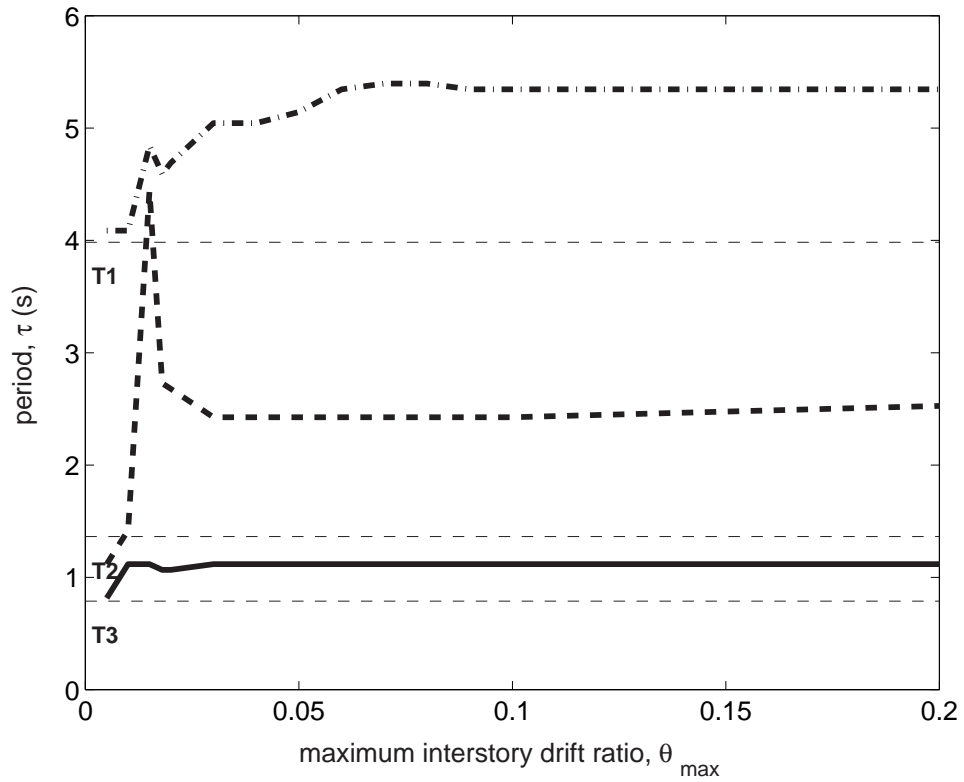


Figure 6.35: The three optimal periods  $\tau_a$ ,  $\tau_b$ ,  $\tau_c$  as they evolve with  $\theta_{\max}$  for the 20-story building.

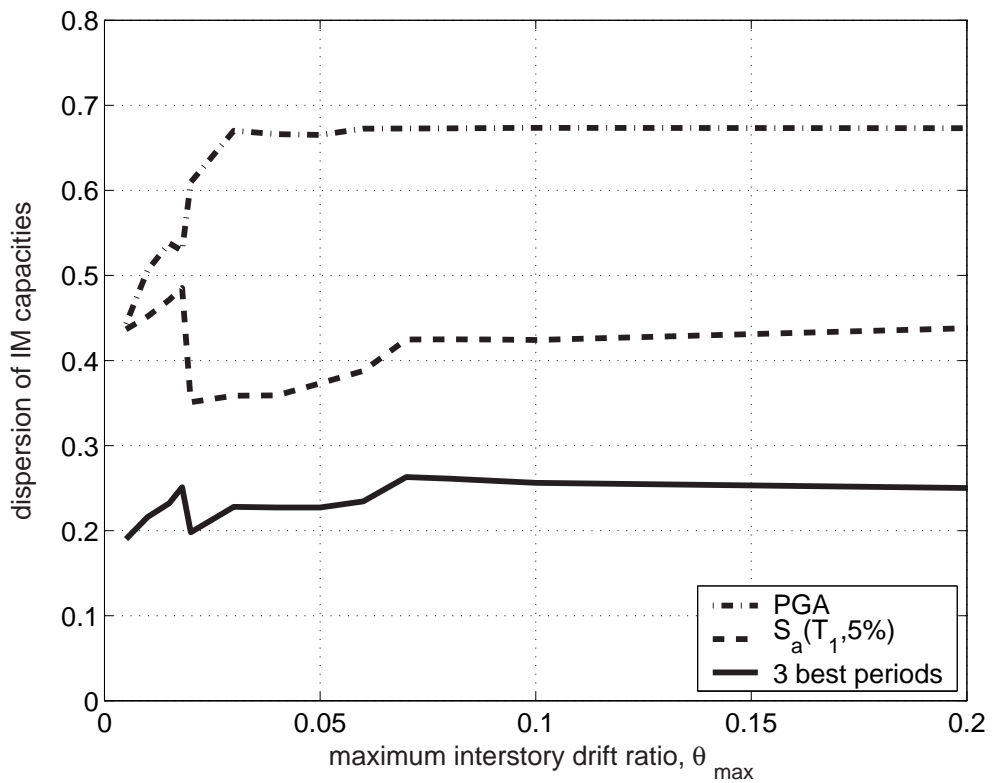
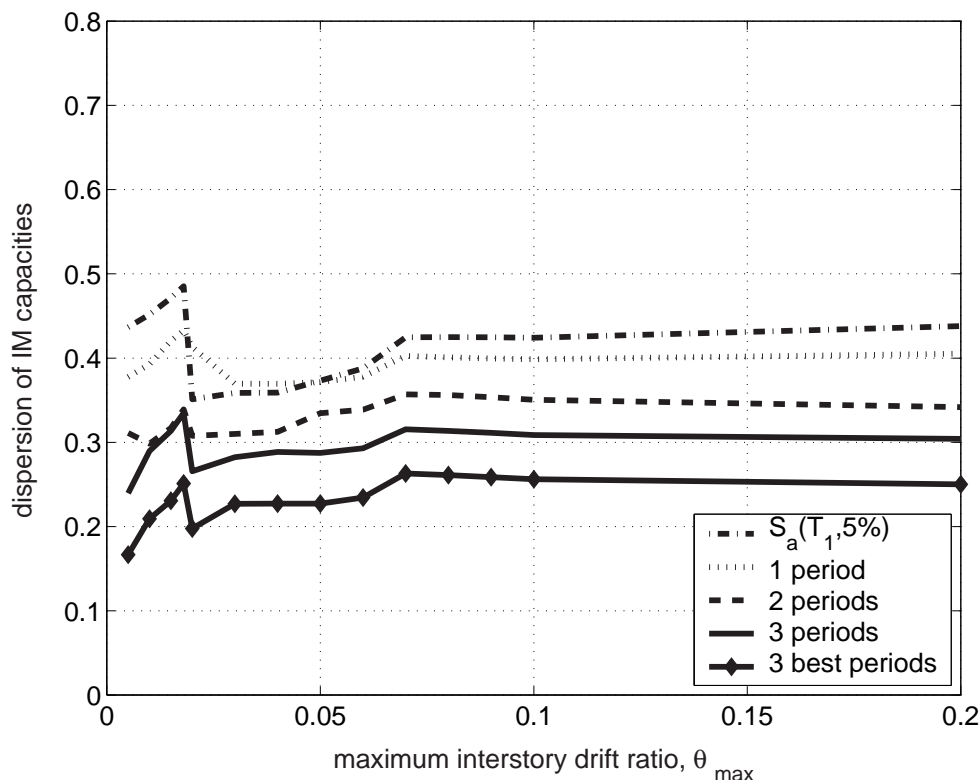


Figure 6.36: The dispersions for optimal  $S_a(\tau_a, 5\%)^{1-\beta-\gamma} S_a(\tau_b, 5\%)^\beta S_a(\tau_c, 5\%)^\gamma$  versus the dispersions for PGA and  $S_a(T_1, 5\%)$  for the 20-story building.



**Figure 6.37:** The 84% fractile of the suboptimal dispersion when using a single spectral value versus a power-law combination of two or three periods for the 20-story building. For comparison, the dispersion achieved by  $S_a(T_1, 5\%)$  and the optimal three-periods power-law is also shown.

This can be thought as a conventional multivariate linear regression model, only we can have an infinite number of predictors, or degrees of freedom, in our fitting. Of course, having infinite parameters and only a finite number of responses, allows such a model to actually interpolate the responses, if we choose so. This would not provide a meaningful estimator, but can be remedied by sufficiently smoothing the coefficient function  $\beta(\tau)$  at a level easily found through cross-validation. We end up with a model to predict limit-state capacities, that can be easily imagined to be of the same power-law form as the one we have introduced to collapse the vector of two *IM*s into a scalar in Equation (6.1). If we use a trapezoidal rule to perform the integration, then we can write Equation (6.5) as:

$$\begin{aligned} \ln S_a^{c,i}(T_1, 5\%) &\approx \alpha + \sum_{j=1}^n \beta(\tau_j) \ln \left[ \frac{S_a(\tau_j, 5\%)}{S_a(T_1, 5\%)} \right] \Delta\tau && \Leftrightarrow \\ S_a^{c,i}(T_1, 5\%) &\approx e^\alpha \prod_{j=1}^n \left[ \frac{S_a(\tau_j, 5\%)}{S_a(T_1, 5\%)} \right]^{\beta(\tau_j) \Delta\tau} && \Leftrightarrow \\ e^\alpha &\approx S_a^{c,i}(T_1, 5\%) \prod_{j=1}^n \left[ \frac{S_a(\tau_j, 5\%)}{S_a(T_1, 5\%)} \right]^{-\beta(\tau_j) \Delta\tau} && (6.6) \end{aligned}$$

Equation (6.6) allows us to define a new *IM*, of similar form to Equation (6.2), that now uses practically the whole spectrum to explain (and reduce) the record-to-record variability. Similarly to the collapsed vector form, as described in Cordova et al. (2000), it is expected that hazard curves can be easily determined for such an *IM* without the need of new attenuation relationships.

But why expand to such a complicated *IM*? We have performed such a functional linear fit for the global instability capacities of the 20-story building, for the spectral coordinates within  $t_s =$

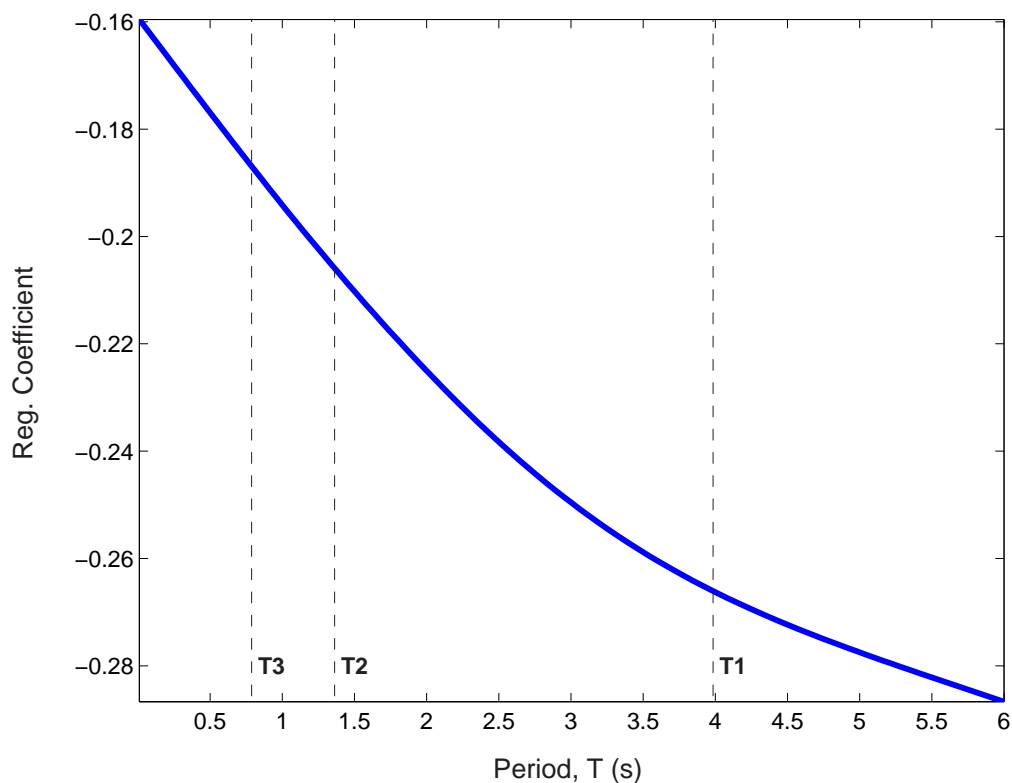


**Figure 6.38:** The regression coefficient function  $\beta(\tau)$  at global dynamic instability for the 20-story building.

0.1s and  $t_e = 6$ s, and have plotted the coefficient function  $\beta(\tau)$  in Figure 6.38; it precisely explains the influence of every spectral coordinate on the flatline capacity. We can think of  $\beta(\tau)$  as a weight function, where its absolute value at each period provides us with the degree of the period's significance to capacity. As it appears, the importance of spectral coordinates is highest for periods longer than the first mode (high  $|\beta(\tau)|$ -values), while it decreases rapidly for periods lower than the second mode (low  $|\beta(\tau)|$ -values). The simplicity of the shape suggests that we can probably provide some general *a priori* suggestions for the coefficient function that will provide relatively efficient *IMs*. Note, that we need not match the actual values of the coefficient function, only its shape, as we are not interested in capacity-prediction, only in capacity dispersion reduction.

Again, the realized gains may not lie as much with dispersion reduction as with robustness. The *IM* suggested by the fit reduces all capacity dispersions for all limit-states by approximately 50% relative to  $S_a(T_1, 5\%)$ , almost to similar amounts as the power-law form with three periods. Only further investigations can prove whether this functional model will prove more useful or robust than the simpler power-law form. Still, it may help us identify spectral regions of interest and characterize structures in a very simple way.

## 6.7 Conclusions

Providing more efficient Intensity Measures (*IMs*) is a useful exercise, both in reducing the number of records needed for PBEE calculations but also in improving our understanding of the seismic behavior of structures. The observed record-to-record dispersion in the limit-state *IM*-capacities can be practically halved by taking advantage of elastic spectrum information. Several methods exist to incorporate elastic spectral values in *IMs*. One could use a single optimally selected spectral value, a vector of two or a power-law combination of several spectral values. While all candidates seem to achieve similar degrees of efficiency, not all of them are suitable for use *a priori*;

it may be quite difficult to select the appropriate periods (or spectral values) before we complete our dynamic analyses. Using a single optimal spectral value is practical only for buildings with insignificant higher modes. On the other hand, when the influence of higher modes is significant, spectral *shape* becomes important. Then, using two or even three spectral values seems to help both the efficiency and the robustness of the *IM* to the suboptimal selection of periods. Still, before such *IMs* are adopted, significant work remains to be done; we need to investigate more structures and more ground motion records, probably ones with important local spectral features, e.g., soft soil or directivity influence. Thus we will be able to better select the appropriate *IM* that will be both efficient and sufficient for a given structure and site.

# Conclusions

## 7.1 Summary

In the preceding chapters we have defined Incremental Dynamic Analysis (IDA) and used it to investigate various aspects of the seismic performance of structures.

Chapter 2 provides a concrete theoretical basis for IDA, fully describing the process of performing multiple nonlinear dynamic analyses under a suite of multiply-scaled ground motion records. The Intensity Measure (*IM*) was introduced to quantify the scaling of a ground motion record and the Damage Measure (*DM*) was used to record its response, generating an IDA curve for each record in the *IM*, *DM* plane. Observing such curves revealed large record-to-record variability but also several interesting aspects of structural behavior. The equal displacement rule was found to be applicable for moderate and long period structures in the near elastic region. Additionally the phenomena of non-monotonic behavior, discontinuities, hardening, softening, flatlining and even resurrection behavior were observed in individual curves. On each IDA curve limit-states were defined using a variety of methods or rules. Using cross-sectional fractiles the IDA curves were summarized into the 16%, 50% and 84% IDA curves, and the capacities were summarized into their 16%, 50% and 84% *DM* or *IM* values. Further we have addressed the question of “legitimacy” of scaling records and the relationships between IDAs and *R*-factors as well as between IDAs and the Static Pushover (SPO) Analysis. A significant connection appeared between the IDA and the SPO; individual segments of the SPO (e.g., elastic, positive-stiffness, negative-stiffness, residual plateau) correspond to unique segments of the IDA (e.g., elastic, equal displacement, softening, secant at reduced stiffness). Finally, algorithms were presented that can significantly reduce the number of nonlinear runs per record. All in all, IDA was shown to provide useful intuition into the seismic behavior of structures.

In Chapter 3 we looked into the practical application of IDA to a 9-story steel moment-resisting frame, using the methods presented in the previous chapter to produce a complete example and commentary for applying IDA to PBEE. Publicly available software is used to perform the analysis, interpolate the IDA curves, estimate limit-state capacities and summarize the results into a format that can be easily integrated with modern PBEE frameworks. The final goal is estimating the mean annual frequency of exceeding certain limit-states. We pay special attention to the details of the practical implementation: how many records, how many runs per record, how the curves are interpolated, the use of approximations in the probabilistic calculations. These are just some of the subjects that we investigate, and they are all found to influence the accuracy of the final IDA results. The methods that have been presented are designed to strike a favorable compromise between speed and accuracy and thus resolve such issues. Perhaps, the single most important thing to remember is the wealth of information that can be found in IDA if only we take advantage of ever-cheaper computing power and automated methods to investigate the structure’s behavior.

In Chapter 4 the SPO2IDA tool was developed to provide rapid estimation of the seismic performance of oscillators with complex backbones and arbitrary periods. The investigated backbone shapes range from simple bilinear to complex quadrilinear with an elastic, a hardening and a negative-stiffness segment plus a final residual plateau that terminates with a drop to zero strength. Using a suite of thirty ground motion records, IDA was performed for numerous such backbone shapes and the summarized IDA curves were extracted for each individual case, yielding interesting observations. Long hardening segments are found to significantly improve performance, while their slope has only a small effect. On the other hand, the steeper the slope of the negative-stiffness segment, the higher the demands and the lower the capacities past the peak of the backbone. Residual plateaus that are higher in terms of strength or longer in terms of ductility, both benefit the post-peak performance. Finally, the oscillator period significantly influences the effect of all segments except the hardening one in the moderate or long period ranges. Several different backbone shapes were found to produce similar dynamic behavior. Thus, the required number of backbone shapes to be investigated is drastically reduced, allowing the effect of a complete quadrilinear backbone to be captured with only a handful of regressions. In accordance, a number of equations have been proposed, defining a flexible, publicly available, software tool (SPO2IDA) for performing fast assessments of the (median and dispersion of) demand and capacity of virtually any oscillator. Using SPO2IDA we can effortlessly get accurate estimates of the performance of the oscillator without having to perform the costly analyses, providing ready insights into the relative advantages and disadvantages of possible design or retrofit alternatives.

In Chapter 5 we employed SPO2IDA in conjunction with the SPO for direct approximation of the MDOF seismic behavior. This method can estimate the seismic demands and capacities of first-mode-dominated MDOF structures for their entire range of behavior, from elasticity to global dynamic instability. Based on the SPO and building upon software able to accurately predict the Incremental Dynamic Analysis (IDA) curves for SDOF systems, it can estimate, with reasonable accuracy, the fractile IDA curves of first-mode-dominated MDOF systems. Similar existing methodologies usually employ bilinear oscillators. The use of SPO2IDA enables us to extend them well beyond the peak of the SPO. Several novel concepts are derived in the process, perhaps the most important being the worst-case, most-damaging SPO. Sometimes, carefully selected load patterns are needed to estimate it, but the worst-case SPO best captures the path that leads to global collapse. Thus it allows accurate prediction of the IDA results. Equally interesting is the apparent “simplification” that occurs in MDOF systems near global collapse. This permits SDOF systems with appropriate backbones to capture the onset of global dynamic instability even for higher-mode-influenced structures. Combining all these observations, we can conclude that simply by using the appropriate SPO curve plus, perhaps, a few elastic response spectrum analyses, the engineer-user is able to generate accurate predictions of the seismic behavior of complex MDOF structures within a fraction of the time needed for a full IDA.

Finally, in Chapter 6, the limit-state capacities estimated by IDA were used as a tool to research the effect of the elastic spectrum on structural performance and its ability to improve *IM*-efficiency. Providing more efficient Intensity Measures (*IMs*) is a useful exercise, both in reducing the number of records needed for PBEE calculations but also in improving our understanding of the seismic behavior of structures. The observed record-to-record dispersion in the limit-state *IM*-capacities can be practically halved by taking advantage of elastic spectrum information. Several methods exist to incorporate elastic spectral values in *IMs*. We chose to use a single optimally selected spectral value, a vector of two or a power-law combination of several spectral values. While all candidates seem to achieve similar degrees of efficiency, not all of them are suitable for use *a priori*; it may be quite difficult to select the appropriate periods (or spectral values) before we complete our dynamic analyses. Using a single optimal spectral value is practical only for buildings with insignificant higher modes. On the other hand, when the influence of higher modes is significant, spectral *shape* becomes important. Then, using two or even three spectral

values seems to help both the efficiency and the robustness of the *IM* to the suboptimal selection of periods. Still, before such *IMs* are adopted, significant work remains to be done; we need to investigate more structures and more ground motion records, probably ones with important local spectral features, e.g., soft soil or directivity influence. Thus we will be able to better select the appropriate *IM* that will be both efficient and sufficient for a given structure and site.

## 7.2 Limitations and Future Work

All the work presented revolves around IDA and is limited in all the ways that IDA is. Thus, the single most important issue is the concept of ground motion record scaling. There certainly exist structures for which scaling is “legitimate”, e.g., moderate period buildings in sites with no directivity when  $S_a(T_1, 5\%)$  is the *IM* (Shome and Cornell, 1999). Still the issue is far from resolved. Structures that have short or long fundamental period, have significant higher modes or exist in sites influenced by near-fault directivity, are candidates for causing problems. That is not to say that in these case the results coming from IDA over a given suite of records will not be legitimate, rather that care should be taken to remove the dependence on record characteristics other than the *IM* used.

The obvious way to do so is to properly select the ground motion records a priori, before performing IDA. Another, easier-to-implement method would be the introduction of a sufficient *IM*, as attempted by Luco and Cornell (2004) and Cordova et al. (2000). A sufficient *IM* would be able to remove the possible bias, bringing together the results from records with different characteristics, like magnitude or forward-directivity. Or, one could try to properly weigh each record according to its contribution to the total hazard, as found by disaggregation; thus, record-selection can be exercised a posteriori. Obviously, there are several candidate methods and more work needs to be directed to this area before the scaling issue is resolved.

IDA is also limited by the very structural model, analysis algorithms and element models that it uses and all the assumptions incorporated therein. Therefore, it has the unique advantage of growing as the power of our modeling and our computational abilities evolve, but it is also hampered by their limits. For example, in many of the results shown herein, there exist damaged but still stable structures at roof drifts in excess of 5%. This is a conclusion that many professionals and researchers may seriously question. It is important to understand that this is exactly what current models can predict. Only the comparison with better models, observations in the field and lab experiments will prove or refute them. But the point is that we are focusing only on the method, and we anticipate that it will remain unchanged as the models improve.

Thus, we await with great anticipation structural models that will include all the important factors that we have left out: the introduction of soil-structure interaction, the expansion of models to three-dimensional structures simultaneously subjected to more than one component of ground motion and the inclusion of more structural elements (e.g., stairwell and partitions) or improved element models that can show e.g., axial failure of columns and shear failure of beams. Until then, IDA will be limited to what has been incorporated to structural models so far.

The approximation of IDA by SPO2IDA is hampered by several additional problems. At the SDOF-level, it is the consideration of directivity, soft soil and the characteristics of the hysteretic model that limit its application, as explained in detail in Chapter 4. In the MDOF case, we have also inherited the limitations of the SPO, especially its inability to capture the influence of higher modes. These further constrain the accuracy we can achieve with SPO2IDA in the near elastic and nonlinear region, although, remarkably, not in the global collapse domain. Also, further work is needed to test and maybe modify the methodology for buildings with stiffness or strength irregularities along their height or within a story. One could easily assume that it may become quite challenging to find the worst-case SPO, or some equivalent SPO that would give the best prediction.

Finally, the use of the elastic spectral shape to reduce the dispersion of capacities in the non-linear range carries all the problems of using elastic information to predict inelastic results. The inelastic spectral shape will probably be a better bet in the long-term, but the cost comes in the face of the building-specific attenuation laws needed.

### 7.3 Overall Conclusions

IDA has proved a useful tool, and can be part of both the short and long-term future of PBEE. It helps quantify the seismic performance of structures, and in the form of the summarized IDA curves and the *IM*-capacities it provides a remarkably useful foundation to develop important intuition and create new approaches to PBEE. Built upon this very foundation, the SPO2IDA tool has proven both accurate and useful for understanding how a structural design may help or hinder the seismic performance both for SDOF but also for MDOF structures. In a similar way we have developed the investigation of the elastic spectral shape. Its potential to explain the record-to-record variability in capacity is promising and can help resolve many problems. Naturally, these methods have limitations but they are not insurmountable and we anticipate that future research will address them appropriately.

# Bibliography

- Al-Sulaimani, G. J. and Roessett, J. M. (1985). Design spectra for degrading systems, *ASCE Journal of Structural Engineering*, **111**(12): 127–136.
- Ang, A. H. S. and De Leon, D. (1997). Determination of optimal target reliabilities for design and upgrading of structures, *Structural Safety*, **19**(1): 19–103.
- Antoniou, S., Pinho, R., and Rovithakis, A. (2002). Development and verification of a fully adaptive pushover procedure, *Proceedings of the 12th European Conference on Earthquake Engineering*, Paper No. 822, London, UK, 1–10.
- ATC (1996). Seismic evaluation and retrofit of concrete buildings, *Report No. ATC-40*, Applied Technology Council, Redwood City, CA.
- Baez, J. I. and Miranda, E. (2000). Amplification factors to estimate inelastic displacement demands for the design of structures in the near field, *Proceedings of the 12th World Conference on Earthquake Engineering*, Paper No. 1561, New Zealand, 1–8.
- Bazzurro, P. and Cornell, C. A. (1994a). Seismic hazard analysis for non-linear structures. I: Methodology, *ASCE Journal of Structural Engineering*, **120**(11): 3320–3344.
- Bazzurro, P. and Cornell, C. A. (1994b). Seismic hazard analysis for non-linear structures. II: Applications, *ASCE Journal of Structural Engineering*, **120**(11): 3345–3365.
- Bazzurro, P., Cornell, C. A., Shome, N., and Carballo, J. E. (1998). Three proposals for characterizing MDOF nonlinear seismic response, *ASCE Journal of Structural Engineering*, **124**: 1281–1289.
- Benjamin, J. R. and Cornell, C. A. (1970). *Probability, Statistics, and Decision for Civil Engineers*, McGraw-Hill, New York.
- Bertero, V. V. (1977). Strength and deformation capacities of buildings under extreme environments, *Structural Engineering and Structural Mechanics*, K. S. Pister, ed., Prentice Hall, Englewood Cliffs, NJ, 211–215.
- Carballo, J. E. and Cornell, C. A. (2000). Probabilistic seismic demand analysis: Spectrum matching and design, *Report No. RMS-41*, RMS Program, Stanford University, Stanford, CA, [Feb 12th, 2004].  
URL <http://www.stanford.edu/group/rms/Reports/RMS41.pdf>
- Chopra, A. K. (1995). *Dynamics of Structures: Theory and Applications to Earthquake Engineering*, Prentice Hall, Englewood Cliffs, NJ.
- Chopra, A. K. and Chintanapakdee, C. (2001). Comparing response of SDF systems to near-fault and far-fault earthquake motions in the context of spectral regions, *Earthquake Engineering and Structural Dynamics*, **30**(12): 1769–1789.

- Cordova, P. P., Deierlein, G. G., Mehanny, S. S., and Cornell, C. A. (2000). Development of a two-parameter seismic intensity measure and probabilistic assessment procedure, *Proceedings of the 2nd U.S.-Japan Workshop on Performance-Based Earthquake Engineering Methodology for Reinforced Concrete Building Structures*, Sapporo, Hokkaido, 187–206.
- Cornell, C. A., Jalayer, F., Hamburger, R. O., and Foutch, D. A. (2002). The probabilistic basis for the 2000 SAC/FEMA steel moment frame guidelines, *ASCE Journal of Structural Engineering*, **128**(4): 526–533.
- Cornell, C. A. and Krawinkler, H. (2000). Progress and challenges in seismic performance assessment, *PEER Center News*, **3**(2), (accessed: June 18th, 2002).  
URL <http://peer.berkeley.edu/news/2000spring/index.html>
- Cuesta, I. and Aschheim, M. A. (2001). Inelastic response spectra using conventional and pulse R-factors, *ASCE Journal of Structural Engineering*, **127**(9): 1013–1020.
- De Matteis, G., Landolfo, R., Dubina, D., and Stratan, A. (2000). Influence of the structural typology on the seismic performance of steel framed buildings, *Moment resistant connections of steel frames in seismic areas*, F. M. Mazzolani, ed., E & FN Spon, New York, 513–538.
- Dubina, D., Ciutina, A., Stratan, A., and Dinu, F. (2000). Ductility demand for semi-rigid joint frames, *Moment resistant connections of steel frames in seismic areas*, F. M. Mazzolani, ed., E & FN Spon, New York, 371–408.
- Efron, B. and Tibshirani, R. J. (1993). *An Introduction to the Bootstrap*, Chapman & Hall/CRC, New York.
- Fajfar, P. and Fischinger, M. (1988). N2 — a method for non-linear seismic analysis of regular structures, *Proceedings of the 9th World Conference on Earthquake Engineering*, Tokyo-Kyoto, Japan, 111–116.
- Fajfar, P. and Gaspersic, P. (1996). The N2 method for the seismic damage analysis for RC buildings, *Earthquake Engineering and Structural Dynamics*, **25**(1): 23–67.
- Farin, G. (1990). *Curves and Surfaces for Computer Aided Geometric Design: A Practical Guide*, 2nd edn., Academic Press, San Diego, CA.
- FEMA (1997). NEHRP guidelines for the seismic rehabilitation of buildings, *Report No. FEMA-273*, Federal Emergency Management Agency, Washington DC.
- FEMA (2000a). Recommended seismic design criteria for new steel moment-frame buildings, *Report No. FEMA-350*, SAC Joint Venture, Federal Emergency Management Agency, Washington DC.
- FEMA (2000b). Recommended seismic evaluation and upgrade criteria for existing welded steel moment-frame buildings, *Report No. FEMA-351*, SAC Joint Venture, Federal Emergency Management Agency, Washington DC.
- Foutch, D. A. and Shi, S. (1998). Effects of hysteresis type on the seismic response of buildings, *Proceedings of the 6th U.S. National Conference on Earthquake Engineering*, Paper No. 409, EERI, El Cerrito, CA, Seattle, WA, 1–12.
- Gupta, B. and Kunnath, S. K. (1998). Effects of hysteretic model parameters on inelastic seismic demands, *Proceedings of the 6th U.S. National Conference on Earthquake Engineering*, Paper No. 358, EERI, El Cerrito, CA, Seattle, WA, 1–12.
- Gupta, B. and Kunnath, S. K. (2000). Adaptive spectra-based pushover procedure for seismic evaluation of structures, *Earthquake Spectra*, **16**(2): 367–391.
- Hastie, T. J. and Tibshirani, R. J. (1990). *Generalized Additive Models*, Chapman & Hall, New York.
- Jalayer, F. and Cornell, C. A. (2002). A technical framework for probability-based demand and capacity factor (DCFDF) seismic formats, *Report No. RMS-43*, RMS Program, Stanford University, Stanford, CA.
- Krawinkler, H. and Seneviratna, G. D. P. K. (1998). Pros and cons of a pushover analysis of seismic performance evaluation, *Engineering Structures*, **20**(4-6): 452–464.

- Lee, E. (1989). Choosing nodes in parametric curve interpolation, *Computer Aided Design*, **21**(6): 363–370.
- Lee, K. and Foutch, D. A. (2002). Performance evaluation of new steel frame buildings for seismic loads, *Earthquake Engineering and Structural Dynamics*, **31**(3): 653–670.
- Lee, L. H., Han, S. W., and Oh, Y. H. (1999). Determination of ductility factor considering different hysteretic models, *Earthquake Engineering and Structural Dynamics*, **28**(9): 957–977.
- Luco, N. and Cornell, C. A. (1998). Effects of random connection fractures on demands and reliability for a 3-story pre-Northridge SMRF structure, *Proceedings of the 6th U.S. National Conference on Earthquake Engineering*, Paper No. 244, EERI, El Cerrito, CA, Seattle, WA, 1–12.
- Luco, N. and Cornell, C. A. (2000). Effects of connection fractures on SMRF seismic drift demands, *ASCE Journal of Structural Engineering*, **126**: 127–136.
- Luco, N. and Cornell, C. A. (2004). Structure-specific, scalar intensity measures for near-source and ordinary earthquake ground motions, *Earthquake Spectra*, in review.
- Macrae, G. A. and Kawashima, K. (1997). Post-earthquake residual displacements of bilinear oscillators, *Earthquake Engineering and Structural Dynamics*, **26**(7): 701–716.
- Mahin, S. A. and Lin, J. (1983). Construction of inelastic response spectra for single-degree-of-freedom systems: computer program and applications, *Report UCB/EERC-83/17*, Earthquake Engineering Research Center, University of California, Berkeley, CA.
- Mehanny, S. S. and Deierlein, G. G. (2000). Modeling and assessment of seismic performance of composite frames with reinforced concrete columns and steel beams, *Report No. 136*, The John A. Blume Earthquake Engineering Center, Stanford University, Stanford, CA.
- Miranda, E. (1993). Evaluation of site-dependent inelastic seismic design spectra, *ASCE Journal of Structural Engineering*, **119**(5): 1319–1338.
- Miranda, E. (2000). Inelastic displacement ratios for structures on firm sites, *ASCE Journal of Structural Engineering*, **126**(10): 1150–1159.
- Miranda, E. (2001). Estimation of inelastic deformation demands of SDOF systems, *ASCE Journal of Structural Engineering*, **127**(9): 1005–1012.
- Nassar, A. A. and Krawinkler, H. (1991). Seismic demands for SDOF and MDOF systems, *Report No. 95*, The John A. Blume Earthquake Engineering Center, Stanford University, Stanford, CA.
- Newmark, N. M. and Hall, W. J. (1982). *Earthquake Spectra and Design*, Earthquake Engineering Research Institute, Berkeley, CA.
- Prakash, V., Powell, G. H., and Filippou, F. C. (1992). DRAIN-2DX: Base program user guide, *Report No. UCB/SEMM-92/29*, Department of Civil Engineering, University of California, Berkeley, CA.
- Press, W. H., Flannery, B. P., Teukolsky, S. A., and Vetterling, W. T. (1986). *Numerical Recipes*, Cambridge University Press, Cambridge.
- Psycharis, I. N., Papastamatiou, D. Y., and Alexandris, A. P. (2000). Parametric investigation of the stability of classical columns under harmonic and earthquake excitations, *Earthquake Engineering and Structural Dynamics*, **29**: 1093–1109.
- Rahnama, M. and Krawinkler, H. (1993). Effects of soft soils and hysteresis model on seismic demands, *Report No. 108*, The John A. Blume Earthquake Engineering Center, Stanford University, Stanford, CA.
- Ramsay, J. O. and Silverman, B. W. (1996). *Functional Data Analysis*, Springer, New York.
- Riddell, R. and Newmark, N. M. (1979). Statistical analysis of the response of nonlinear systems subjected to earthquakes, *Structural Research Series No. 468*, University of Illinois at Urbana-Champaign, Urbana, IL.

- Ruiz-Garcia, J. and Miranda, E. (2003). Inelastic displacement ratios for evaluation of existing structures, *Earthquake Engineering and Structural Dynamics*, **32**(8): 1237–1258.
- SEAOC (1995). *Vision 2000: A Framework for Performance Based Design*, vol. I–III, Structural Engineers Association of California, Sacramento, CA.
- Seneviratna, G. D. P. K. and Krawinkler, H. (1997). Evaluation of inelastic MDOF effects for seismic design, *Report No. 120*, The John A. Blume Earthquake Engineering Center, Stanford University, Stanford, CA.
- Shi, S. and Foutch, D. A. (1997). Connection element (type 10) for DRAIN-2DX, *Technical Report No. 468*, Department of Civil and Environmental Engineering, University of Illinois at Urbana-Champaign, Urbana, IL.
- Shome, N. and Cornell, C. A. (1998). Normalization and scaling accelerograms for nonlinear structural analysis, *Proceedings of the 6th U.S. National Conference on Earthquake Engineering*, Paper No. 243, EERI, El Cerrito, CA, Seattle, WA, 1–12.
- Shome, N. and Cornell, C. A. (1999). Probabilistic seismic demand analysis of nonlinear structures, *Report No. RMS-35*, RMS Program, Stanford University, Stanford, CA, [Feb 12th, 2004].  
URL <http://www.stanford.edu/group/rms/Thesis/NileshShome.pdf>
- Shome, N. and Cornell, C. A. (2000). Structural seismic demand analysis: Consideration of collapse, *Proceedings of the 8th ASCE Specialty Conference on Probabilistic Mechanics and Structural Reliability*, Paper No. 119, Notre Dame, 1–6.
- Stear, J. D. and Bea, R. G. (1999). A simplified structural analysis method for jacket-type platforms in seismically-active regions, *Report to Joint Industry Project sponsors*, Marine Technology and Management Group, Department of Civil and Environmental Engineering, University of California, Berkeley, CA.
- Vamvatsikos, D. (2001). SPO2IDA software for moderate periods, [Feb 12th, 2004].  
URL <http://tremble.stanford.edu/cgi-bin/spo2ida-mt.pl>
- Vamvatsikos, D. (2002). SPO2IDA software for short, moderate and long periods, [Feb 12th, 2004].  
URL <http://tremble.stanford.edu/nausika/software/spo2ida-allt.xls>
- Vamvatsikos, D. and Cornell, C. A. (2002a). Incremental dynamic analysis, *Earthquake Engineering and Structural Dynamics*, **31**(3): 491–514.
- Vamvatsikos, D. and Cornell, C. A. (2002b). Tracing and post-processing of IDA curves: Theory and software implementation, *Report No. RMS-44*, RMS Program, Stanford University, Stanford, CA.
- Vamvatsikos, D. and Cornell, C. A. (2004a). Applied incremental dynamic analysis, *Earthquake Spectra*, **20**(2): 523–553.
- Vamvatsikos, D. and Cornell, C. A. (2004b). Direct estimation of the seismic demand and capacity of MDOF systems through incremental dynamic analysis of an SDOF approximation, *ASCE Journal of Structural Engineering*, in review.
- Vamvatsikos, D. and Cornell, C. A. (2004c). Direct estimation of the seismic demand and capacity of oscillators with multi-linear static pushovers through incremental dynamic analysis, *Earthquake Engineering and Structural Dynamics*, in review.
- Vamvatsikos, D. and Cornell, C. A. (2004d). Direct estimation of the seismic demand and capacity of oscillators with multi-linear static pushovers through incremental dynamic analysis, *Earthquake Engineering and Structural Dynamics*, in review.
- Veletsos, A. S. and Newmark, N. M. (1960). Effect of inelastic behavior on the response of simple systems to earthquake motions, *Proceedings of the 2nd World Conference on Earthquake Engineering*, Tokyo, Japan, 895–912.

- Vidic, T., Fajfar, P., and Fischinger, M. (1994). Consistent inelastic design spectra: Strength and displacement, *Earthquake Engineering and Structural Dynamics*, **23**(5): 507–521.
- Weisberg, S. (1985). *Applied Linear Regression*, 2nd edn., John Wiley & Sons, New York.
- Yun, S. Y., Hamburger, R. O., Cornell, C. A., and Foutch, D. A. (2002). Seismic performance evaluation for steel moment frames, *ASCE Journal of Structural Engineering*, **128**(4): 534–545.